2001

Theoretical studies of the nucleation and growth of thin metal films: a focus on Ag deposited on Ag(100)

Kyle John Caspersen
Iowa State University

INFORMATION TO USERS

This manuscript has been reproduced from the microfilm master. UMI films the text directly from the original or copy submitted. Thus, some thesis and dissertation copies are in typewriter face, while others may be from any type of computer printer.

The quality of this reproduction is dependent upon the quality of the copy submitted. Broken or indistinct print, colored or poor quality illustrations and photographs, print bleedthrough, substandard margins, and improper alignment can adversely affect reproduction.

In the unlikely event that the author did not send UMI a complete manuscript and there are missing pages, these will be noted. Also, if unauthorized copyright material had to be removed, a note will indicate the deletion.

Oversize materials (e.g., maps, drawings, charts) are reproduced by sectioning the original, beginning at the upper left-hand corner and continuing from left to right in equal sections with small overlaps.

Photographs included in the original manuscript have been reproduced xerographically in this copy. Higher quality 6" x 9" black and white photographic prints are available for any photographs or illustrations appearing in this copy for an additional charge. Contact UMI directly to order.

ProQuest Information and Learning
300 North Zeeb Road, Ann Arbor, MI 48106-1346 USA
800-521-0600

UMI®

Theoretical studies of the nucleation and growth of thin metal films: A focus on Ag deposited on Ag(100).

by

Kyle John Caspersen

A dissertation submitted to the graduate faculty

in partial fulfillment of the requirements for the degree of

DOCTOR OF PHILOSOPHY

Major: Physical Chemistry

Program of Study Committee:
James W. Evans, Co-major Professor
Mark S. Gordon, Co-major Professor
John J. Kozak
Gordon J. Miller
Jacob W. Petrich

Iowa State University

Ames, Iowa

2001

Graduate College
Iowa State University

This is to certify that the doctoral dissertation of

Kyle John Caspersen

Has met the requirements of Iowa State University

Signature was redacted for privacy.

Committee Member

Signature was redacted for privacy.

Committee Member

Signature was redacted for privacy.

Committee Member

Signature was redacted for privacy.

Co-major Professor

Signature was redacted for privacy.

Co-major Professor

Signature was redacted for privacy.

For the Major Program

Dedicated to my family

TABLE OF CONTENTS

1. GENERAL INTRODUCTION

1. Interfaces in the World

Properties of interfaces control much of the world around us. For instance, whether or not our cells are permeable depends on the cell wall. The strength and scope of earthquakes is controlled by the nature of contact zone between the two tectonic plates. Even the peculiar structure of snowflakes is an interfacial property. The primary factor that controls the properties of interfaces is their structure (obviously along with composition). The passage of a molecule into a cell is allowed if a chiral receptor on the cell wall recognizes the molecule and allows it to pass. A factor that determines the strength and frequency of earthquakes is how rough or smooth the two contacting plates are. And differences in atmospheric temperature and pressure, during the formation of the ice crystal, stabilize different crystallographic faces of water at different times creating the famous dendridic structure [1]. Therefore the ability to control and understand the structure of interfaces is of critical importance.

Controlling the structure of solid interfaces has enormous technological ramifications. The demand for faster more powerful computers has increased, the desire to create smaller and smaller microchips has sky rocketed, and the ability to make small chips is linked to the ability to create very smooth Silicon and Germanium surfaces [2]. Therefore controlling the surface structure of these semi-conductors has been an active area of research for many years. However the last 15 years have seen an explosion in research in not only the Silicon and Germanium surfaces but on other surfaces as well. This is due to the development and proliferation of the Scanning Tunneling Microscope (STM) (as well as the Atomic Force

Microscope (AFM)), in which electric current is passed through a metal tip (usually Tungsten) to a conductive surface where the height is controlled to keep either the current or voltage constant [3]. This technique then allows the resolution of individual molecules. Previously mostly reciprocal space techniques, such as Low Energy Electron Diffraction (LEED) and Reflected High Energy Electron Diffraction (RHEED), were used to investigate the surface morphology. Diffraction techniques gave researchers insight into quantities such as the average feature separation and average feature shape. STM now allowed researchers access to the real space surface structures in great detail. About the time the STM was invented, computer power had progressed to the point where it was now possible to run simulations that mimicked the real experiments. These two techniques together allowed researchers to look at the surface, speculate on the properties that were responsible for the surface structure, develop a model that incorporated the proposed properties, use computers to simulate the surface, and then compare the simulation to the STM data.

One type of metal surface that was studied by these methods was the surface generated under epitaxial metal film growth, in which a metal surface is bombarded with atoms and eventually enough atoms are deposited so that a thin film begins to grow. There are two types of epitaxy, homoepitaxy and heteroepitaxy. In homoepitaxy the same substance that the surface is composed of is deposited. Conversely, in heteroepitaxy a different substance is deposited on the surface. In the study of a vast number of these systems very complicated behavior was observed for which an explanation of the processes proved problematic. Even the simplest epitaxial systems show remarkably complex behavior. This thesis focuses on one of these "simple" systems, notably the homoepitaxial deposition of silver onto the (100) facet of silver under Molecular Beam Epitaxy (MBE).

The focus is on the development of lattice gas models that are believed to contain the relevant physical processes. These models are then implemented using Kinetic Monte-Carlo (KMC) simulations and compared with experimental data.

The rest of this introduction focuses on background concepts in film growth. The equation that describes the morphology of growing films is introduced. A brief discussion of the critical scaling of growing films is presented. Different types of growth are introduced. Finally, KMC and the lattice gas modeling employed here are discussed. If the reader has previous background in these areas he or she is advised to skip to the bulk of the text where the details are presented.

2. The Growth Equation

Commonly in the study of film growth a coarse-grained approach is used, where the morphology of the surface is represented by a continuous function, $h(\underline{x},t)$, of position ($\underline{x}$) and time (t). A particular area on the surface will grow depending on the local environment, where $h(\underline{x},t)$ obeys the partial differential equation called the growth equation, Equation 1.

$$\partial h(\underline{x},t)/\partial t = F/\rho + \nabla J + \eta(\underline{x},t) \tag{1}$$

F is the atomic flux, ρ is the density of film (for a film with no void defects ρ=1), J is the lateral mass flux, and $\eta(\underline{x},t)$ is a random noise term that represents the deposition source. The type of η considered here is uncorrelated in space and time, i.e.

$$\langle \eta(\underline{x},t) \rangle = 0 \tag{2}$$

$$\langle \eta(\underline{x}',t')\, \eta(\underline{x}'',t'') \rangle = 2D\delta^{d}(\underline{x}'-\underline{x}'')\delta(t'-t'') \tag{3}$$

for which d is the surface dimension. The J term in (1) is nontrivial and is dependent on the type of growth considered, as shown below.

3. Scaling Concepts

Growing surfaces often display asymptotic scaling, where after a long enough time (depends on the specific system) average characteristics of the growing film obey power laws. The main characteristic considered for growing films is the roughness (W), where

$$W = \langle h^2 \rangle - \langle h \rangle^2 \tag{4}$$

There will be four power laws for the types of epitaxial surfaces described here. A schematic of a typical W vs. time (and hence coverage (θ), for θ=F·t) plot for a finite system size is shown in Fig.1, where the log(W) increases linearly with log(t) for beginning times but then transitions to a regime where $\delta W/\delta t=0$. If t is small then W follows the scaling relation

$$W \sim t^{\beta} \text{ (or also } W \sim \theta^{\beta}) \tag{5}$$

β is called the *growth exponent*. Not surprisingly, as W increases with time the length scale over which heights are correlated laterally along the surface increases as well. This means when the growing lateral correlation length reaches the lateral system size (L) the correlation length can not grow any further and hence W can not become any larger, or W has reached its saturation value, W_{sat}. W_{sat} is dependent on L, where W_{sat} obeys the *roughness exponent*, α, through

$$W_{sat} \sim L^{\alpha} \tag{6}$$

Furthermore, how long it takes for the system to reach W_{sat} (this time is noted t_x) is dependent on L through the *dynamical exponent*, z, by

$$t_x \sim L^{z} \tag{7}$$

Together these three relations suggest the dynamical scaling relation [4]

$$W(L,t) \sim L^{\alpha} f(t/L^{z}) \tag{8}$$

f is a scaling function with the properties that if $t/L^z<1$ then $f=t^\beta$ and if $t/L^z>1$ then f =constant. It is also easy to show that if Equation 8 is valid then one recovers a relation between α, β, and z that is shown in Equation 9.

$$z=\alpha/\beta \tag{9}$$

The three types of scaling associated with α, β, and z occur for most epitiaxial growing interfaces. Now the fourth power law mentioned above only exists for growing interfaces with features that have an average lateral size (L_{av}) and obey

$$L_{av} \sim t^n \text{ (or } L_{av} \sim \theta^n) \tag{10}$$

Where n is termed the *coarsening exponent*. Cases where features have a selected slope, as will be shown, there exists a very simple relation between β and n, notably β=n.

The reader should understand that there is one important proviso to these scaling relations, which is that these relations only exist when the film is in the scaling regime. For a number of epitaxial systems there exist a substantial preasymptotic, or transient, regime. And it is important to realize that for a film that has not reached its scaling regime, these scaling concepts mentioned above are completely invalid.

4. Growth Modes

It is probably not hard to imagine that films grow in a vast number of ways depending on the parameters of the system. Examples of these parameters are crystal structure, surface structure, substrate temperature, angle of deposition, nature of deposition (Molecular Beam Epitaxy (MBE), Chemical Vapor Deposition (CVD), Electrochemical Deposition (ED), etc.), type of deposition (Homoepitaxy or Heteroepitaxy), etc. Therefore a discussion of a few growth modes, or patterns, should prove useful. Four growth modes are discussed here: Poisson Growth; Self-Affine Growth; Correlated Growth; and Layer-By-Layer Growth.

There exist many other growth modes, but as relates to the bulk of this thesis, these four are the most relevant. In fact only two, Self-Affine and Correlated, are directly applicable to the type of growth features seen in the rest of this thesis, however the other two (Poisson and Layer-By-Layer) are useful constructs and hence are discussed here.

4.1 Poisson Growth

Poisson Growth, sometimes called Random Deposition, is conceivably the simplest type of growth (with perhaps the exception of Layer-By-Layer). It is simply the deposition of particles on to a lattice site, Fig.2, which results in columns that grow without any dependence on height of the neighboring columns. The feature of no lateral motion in Poisson Growth means that there is no lateral mass flux and therefore the very simple growth equation

$$\partial h(\underline{x},t)/\partial t = F + \eta(\underline{x},t). \tag{11}$$

This simple equation, not surprisingly, has the simple solution

$$h(\underline{x},t) = Ft + \int \eta(\underline{x},t')dt'. \tag{12}$$

Now using Equations 2 and 3 it is easy to show that

$$\langle h \rangle = Ft \tag{13}$$

$$\langle h^2 \rangle = (Ft)^2 + 2Dt, \tag{14}$$

and use of Equation 4 immediately yields [5]

$$\beta = 1/2. \tag{15}$$

Since the columns grow independently there can be no lateral correlations or feature size that means that α, z, and n do not exist for the Poisson Growth mode.

4.2 Self-Affine Growth

The term Self-Affine means that a "structure" is self-similar under some rescaling. This means for some function, h(x), as x is rescaled like $x \rightarrow bx$, then for the function to remain self-similar h must be rescaled like $h \rightarrow b^{\alpha}h$, where α is the aforementioned *roughness* exponent. The properties imply the scaling relation $h(x) \sim b^{-\alpha}h(bx)$ [5]. An example of a Self-Affine function is the one-dimensional random walk, Fig.3, where in order for the system to remain statistically self-similar the function must be rescaled anisotropically with $\alpha=1/2$. A special case of Self-Affinity is when $\alpha=1$, this is the well-known case of self-similar fractals.

Poisson Growth, where particles are deposited randomly with no post-deposition diffusion, does not generate Self-Affine structures due to the fact that there are no lateral correlations. Self-Affine Growth is achieved by allowing particles to relax, by making small lateral moves to local stable sites, where the degree of relaxation determines α. This small movement results in a nontrivial mass flux term in the growth equation. The Self-Affine growth discussed in the bulk of this text falls into two universality classes; the Edwards-Wilkinson (EW) and Kardar-Parisi-Zhang (KPZ) universality classes.

4.2.1 The Edwards-Wilkinson Universality Class [6]

An example of the growth described by EW scaling consists of random deposition of particles on to an initially flat substrate with a relaxation toward the bulk such that there are no overhangs formed. An example of this, called Downward Funneling (DF) [7], is shown in Fig.4. Where this lateral motion is akin to a particle sliding down a facet, therefore it should not be surprising that the amount of this lateral motion should depend on the slope. For EW growth $J=F\nu\nabla h$. This causes the Growth Equation to become the EW equation, Equation 16. (Provided the prefactor, ν, does not have a position dependence.)

$$\partial h(x,t)/\partial t = F + F\nu\nabla^2 h(x,t) + \eta(x,t) \tag{16}$$

Noting that this lateral motion produces a curvature dependence term, which acts likes a surface tension. Furthermore, if F and η are ignored then the EW equation reduces to the well known Diffusion Equation. Therefore this local relaxation acts like a surface tension and tends to smooth the surface. By intuition this would mean that β would be smaller than EW Growth than in Poisson Growth.

To examine the behavior of the EW equation the most straightforward method is to perform a scaling analysis, as shown below. The essential elements of the scaling analysis are self-affine scaling relations

$$x \rightarrow bx \tag{17}$$

$$h \rightarrow b^{\alpha} h \tag{18}$$

$$t \rightarrow b^{z} t. \tag{19}$$

Using these scaling relations transforms the EW equation into

$$b^{\alpha-z}\partial h/\partial t = b^{\alpha-2}F\nu\nabla^2 h + b^{-\alpha/2-d/2}\eta, \tag{20}$$

where the term in front of the noise term is generated using the relations $\delta^d(ax)=a^{-d}\delta^d(x)$ and $<\eta(x,t)\eta(x',t')>=2D\delta^d(x-x')\delta(t-t')$ by realizing that

$$<\eta(bx,b^z t)\eta(bx',b^z t')> = 2D\delta^d(b(x-x'))\delta(b^z(t-t')) = b^{-d-z}2D\delta^d(x-x')\delta(t-t'), \tag{21}$$

which means that

$$<\eta(bx,b^z t)\eta(bx',b^z t')>=b^{-d-z}<\eta(x,t)\eta(x',t')>, \tag{22}$$

and therefore the relation

$$\eta(bx,b^z t)=b^{-d/2-z/2}\eta(x,t) \tag{23}$$

is realized. Now dividing both sides of Equation 22 by $b^{\alpha-z}$ gives the scaled EW equation

$$\partial h/\partial t = b^{z-2}F\nu\nabla^2 h + b^{z/2-d/2-\alpha}\eta \tag{24}$$

The requirement that the EW equation be invariant upon this rescaling means that the exponents of b in Equation 24 be exactly zero. Using this fact allows the solution of the exponents by solving the system of equations z-2=0 and z/2-d/2-α=0 (and also z=α/β), where this scaling analysis gives the exponents to be

$$z=2 \tag{25}$$

$$\alpha=(2-d)/2 \tag{26}$$

$$\beta=(2-d)/4 \tag{27}$$

(Note: the exact solution also gives these exponents [8]). A peculiarity in the exponents for the EW equation comes when d=2, where β=0. This does not mean that the surface does not roughen, it simply means that the surface roughness grows logarithmically rather than by a power law.

4.2.2 The Kardar-Parisi-Zhang Universality Class [9]

The type of growth described by the KPZ universality class is a generalization of EW growth where particles still relax, however the relaxation does not have to be as complete as EW growth, so voids and overhangs can be produced. In other words, growth can proceed along a local normal direction, therefore the film grows with voids and overhangs, or ρ<1. Now ρ can be written as the gradient expansion

$$\rho = \rho_0 + \rho_1|\nabla h|^2 + \rho_2\nabla^2 h + \ldots \tag{28}$$

Truncating this expansion and placing this ρ into the Growth Equation gives

$$\partial h(x,t)/\partial t = F(\rho_0 + \rho_1|\nabla h|^2)^{-1} + F\nu\nabla^2 h(x,t) + \eta(x,t). \tag{29}$$

Performing a Taylor Expansion on the ρ term reveals

$$F(\rho_0 + \rho_1|\nabla h|^2)^{-1} = F\rho_0^{-1}\Sigma(-1)^n(\rho_1\rho_0^{-1}|\nabla h|^2)^n, \tag{30}$$

truncating the expansion after two terms (small slope approximation) gives the final form for growth of Self-Affine systems with voids and overhangs

$$\partial h(x,t)/\partial t = F\rho_0^{-1} + \lambda|\nabla h|^2 + F\nu\nabla^2 h(x,t) + \eta(x,t). \quad (31)$$

Equation 31 is the KPZ equation, where $\lambda = F\rho_1\rho_0^{-2}$. The nature of the non-linearity makes the KPZ equation very difficult to solve analytically. At present, the scaling exponents have only been found analytically for d=1 using a Renormalization Group approach [9,10], where $\alpha=1/2, \beta=1/3$, z=3/2. For d>1 only numeric solutions for the exponents have been found where for d=2 $\beta\approx0.24$ [11]. (Note: The scaling analysis that was used for the EW equation does not work for KPZ, for it appears that λ, ν, and D do not rescale independently.)

One important feature of the KPZ equation, unlike the EW equation, is the presence of a phase transition. For d>2 if the non-linearity is sufficiently weak (i.e. a small λ) then the solutions of the KPZ equation crossover to EW scaling [5].

4.3 Correlated Growth

In the two previous growth modes, the feature of no significant lateral surface diffusion caused the surface morphology to be of a random, or fractal, nature. For the Correlated Growth mode surface diffusion is active and the morphology created is quite different. (Note: For diffusion to be active means that the diffusion rate must be fast *relative* to the particle flux.) Lateral diffusion produces compact instead of fractal structures. Also along with lateral diffusion comes the possibility of enhanced barriers toward interlayer diffusion (i.e. diffusion over steps) relative to terrace diffusion. These enhanced barriers cause growth instabilities, manifested by "mounds," to be formed. This lateral diffusion is also the source for long correlation lengths.

One of the key features that produces the mounded surface morphology is this enhanced barrier for particles to diffuse over steps. This barrier is called the Erlich-Schwoebel, or Step-Edge, barrier (E_{se}) [12]. This Step-Edge barrier is a small increase in the transition state energy of a particle when hopping over an edge relative to the terrace diffusion barrier (E_d) Fig.5. This causes particles that approach a step from above to be preferentially reflected away from the step-edge rather than diffuse over it, and is termed Step-Edge Reflection (SER) [13]. This SER process forces particles to remain on top of one particle high "islands" longer making the nucleation of new islands on top of preexisting islands easier. This process of enhanced nucleation on top of islands leads to "wedding cake" type growth instabilities, or mounds.

In terms of the Growth Equation, SER induces a lateral mass flux in the uphill direction, J_{up}. The exact functional form of J_{up} is not known (although there are numerous speculations [14]), however the shape of function versus the average local slope (M) of the mounds is known, and is shown in Fig.6. For M=0 then $J_{up}=0$ by symmetry. Then as M increases the number of steps becomes large heightening the probability for SER thus enlarging J_{up}. However, as M increases further the average diffusion length of the particles decreases, due to shrinking terraces, and since J_{up} is dependent on the extent of mass transport this causes a maximum and then a decrease, where as $M\rightarrow\infty$ then $J_{up}\rightarrow 0$. There is a lateral process that competes with SER and that is the particle relaxation during deposition of EW growth, or more precisely the Downward Funneling that is shown in Fig.4. The lateral mass flux for this process is termed J_{down}, where $J_{down}=F\nu\nabla h$. Clearly J_{down} is linear in M, Fig.6a, combining both J_{up} and J_{down} into the total mass flux (J_{total}) gives the functional form shown in Fig.6b. Fig.6b an "attractive fixed point" is observed, where for slopes smaller

than the fixed point J_{total} is positive and the slope increases, and for slopes larger than the fixed point J_{total} is negative and the slope decreases. This feature is termed slope selection and the fixed point is called the selected slope. Slope selection causes β to equal n. Simply saying that there is a specific slope where the effect of SER is completely negated by Downward Funneling.

4.4 Layer-By-Layer Growth

Layer-By-Layer Growth is conceptually the easiest growth mode. In Layer-By-Layer Growth all diffusion pathways are significantly active such that the surface finds its equilibrium configuration in the time frame of deposition. In other words the surface grows by one perfectly flat particle layer on top of another.

5. Lattice Gas Modeling

The type of atomistic models described in this thesis is termed lattice gas modeling. A lattice gas is a collection of "particles" that occupy discrete positions in space, and perform some action depending on the local environment. Probably the most well known lattice gas is the Ferromagnetic Ising Model, where particles are refered to as spins. In this model a periodic lattice is constructed of plus and minus spins, where these spins flip with some rate dictated by neighboring spins. This model is at equilibrium, therefore the rates are constructed from some Hamiltionan and must obey detailed balance. This model's most famous feature is a first order phase transition, where at high temperatures there is no spontaneous magnetization, however for temperatures below some critical value there is a spontaneous magnetization.

The modeling here, while still lattice gas modeling, is quite different. Here atoms are deposited randomly on to a lattice, in this case a (100) facet of a Face Centered Cubic (FCC)

Crystal. The rate at which atoms are deposited, called the Flux (F), is set to be consistent with the experimental value, typically on the order of 10^{-2} monolayers (ML) per second (S). During deposition the atom may land directly on an adsorption site, or the atom may have to relax (via DF) to reach an adsorption site. Once deposited the atom may diffuse on the surface, where the rate for a particular diffusion process is dependent on the local environment and given by Arrhenius rate law with an energy barrier for diffusion and an attempt frequency. (The attempt frequency is typically on the order of a lattice vibration). Fig.7 shows a schematic of this kind of lattice gas model. Comparing experimental data and various model predictions (generated using KMC) it is possible to extract a view of the relevant processes that dominate the growing morphology.

6. Kinetic Monte-Carlo Simulations

The accuracy of the lattice gas models that were developed was tested using KMC simulations. Monte-Carlo Simulations [15] are an extremely powerful technique in statistical mechanics. It allows one access to nearly every statistical quantity as well as being able to probe much larger systems and longer times than Molecular Dynamics (MD) Simulations. (However this is not to say the MD is not a powerful tool also.)

KMC works by converting rates of a specific event occurring into a probability of that event occurring with respect to all other possible events, and then using a random number generator to choose a process out of a list of probabilities. For example, there are two possible processes that can occur, A and B. Process A occurs with a rate R_A, likewise Process B occurs with a rate R_B. Then the probability of A (P_A) and B (P_B) occurring relative to each other are

$$P_A = R_A/(R_A+R_B) \tag{32}$$

$$P_B = R_B/(R_A+R_B) \quad (33)$$

Then using a random number generator one of the processes is chosen, where the time step for each successive movement is $1/(R_A+R_B)$.

7. Dissertation Organization

This thesis consists of six chapters, all of which are separate papers that have been published, or submitted for publication. This thesis also contains three appendices, two of which are published papers and one of which is a description of a morphology analysis technique. Chapter 2 is a paper published in Physical Review B, which studies multilayer growth of thin films at extremely cold temperatures. Chapter 3 is a paper to be submitted to Physical Review B, which studies the post-deposition time dependence of submonolayer island density. (Note: This paper was a collaboration between an experimental and theory group, where KJC was the lead contributor for the theory.) Chapter 4 is a paper published in Physical Review B, which studies the temperature dependence of 25 monolayer Ag films. Chapter 5 is a paper to be submitted to surface science, which studies the effect the step-edge barrier has on one monolayer films as well as films deposited at different temperatures. Chapter 6 is a paper to be submitted to Physical Review Letters, which studies the temperature dependence of coarsening. Chapter 7 is a paper accepted in the 2001 Proceedings of the North Atlantic Treaty Organization's Workshop for Advanced Research-Atomic Aspects of Epitaxial Growth, which studies the temperature dependence of coarsening. In Chapter 8 there are some general conclusions. Appendix A is a paper published in Physical Review Letters, which studies the temperature dependence of 25 monolayer Ag films. Appendix B is a paper published in Volume 619 of the Symposium Proceedings of the Materials Research Society, which studies film growth at extremely cold

temperatures. Appendix C is a description of a morphology analysis technique, which divides the surface into the individual features.

References

[1] J.M. Adams, Phys. Rev. **35**, 113 (1930).

[4] F. Family and P.M. Lam, Physica A **205**, 272 (1994).

[2] C.R.M Grovenor, Microelectronic Materials, 1ed (IOP Publishing Ltd., Bristol, 1989).

[3] C.J. Chen, Introduction to Scanning Tunneling Microscopy, 1ed, (Oxford University Press, New York, 1993).

[5] A.L. Barabasi and H.E. Stanley, "Fractal Concepts in Surface Growth," 1ed (Cambridge University Press, New York, 1995).

[6] S.F. Edwards and D.R. Wilkinson, Proc. R. Soc. London A **381**, 17 (1982).

[7] J. W. Evans, D. E. Sanders, P. A. Thiel, and A. E. DePristo, Phys. Rev. B **41**, 5410 (1990).

[8] T. Nattermann and L.-H. Tang, Phys. Rev. A 45, 7156 (1992).

[7] M. Kardar, G. Parisi, and Y.-C. Zhang, Phys. Rev. Lett. **56**, 889 (1986).

[9] D. Foster, D. Nelson, and M. Stephen, Phys. Rev. A **16**, 732 (1977).

[11] B.M. Forrest and L. Tang, J. Stat. Phys. **60**, 181 (1990).

[12] G. Ehrlich and F.G. Hudda, J. Chem. Phys. **44**, 1039 (1966); R.L. Schwoebel and E.J. Shipsey, J. Appl Phys. **37**, 3682 (1966).

[13] J. Villain, J. Phys I **1**, 19 (1991).

[14] M. D. Johnson, C. Orme, A. W. Hunt, D. Graff, J. Sudijono, L. M. Sander, and B. G. Orr, Phys. Rev. Lett. **72**, 116 (1994). P. Politi and J. Villain, Phys. Rev. B **54**, 5114(1996).

[15] D. Chandler, "Introduction to Modern Statistical Mechanics," Oxford University Press (1987).

Figure Captions

Figure 1. A schematic of a typical W vs. time plot for a finite size system, where both W_{sat} and t_x labeled.

Figure 2. A schematic of Poisson Growth.

Figure 3. An example of Self-Affine scaling. A one-dimensional surface generated from the position and time of a one-dimensional random walk.

Figure 4. A diagram of the Downward Funneling model, which is also an example of a system which follows the scaling of the Edwards-Wilkinson Universality Class.

Figure 5. A description of the Erlich-Schwoebel (or step-edge) barrier.

Figure 6. A qualitative picture of the up and downhill currents, and there relationship with each other, notably feature of slope selection.

Figure 7. A schematic of the type of lattice gas modeling done in this thesis. The arrows represent possible atomic motion (though some of these pathways will be inactive for the modeling here), F represents the atomic flux, and E_d and E_{se} represent the terrace diffusion and step-edge barriers respectively. (Note: the placement of E_d and E_{se} is meant to show that the rates for these processes depend on E_d and E_{se})

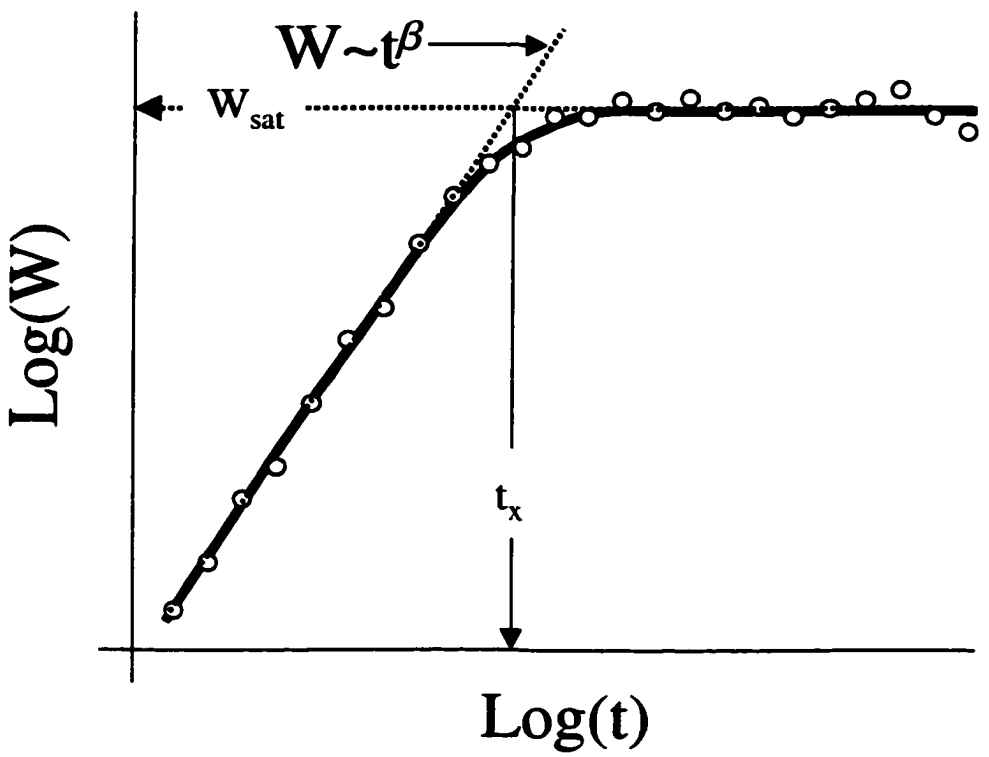

Figure 1

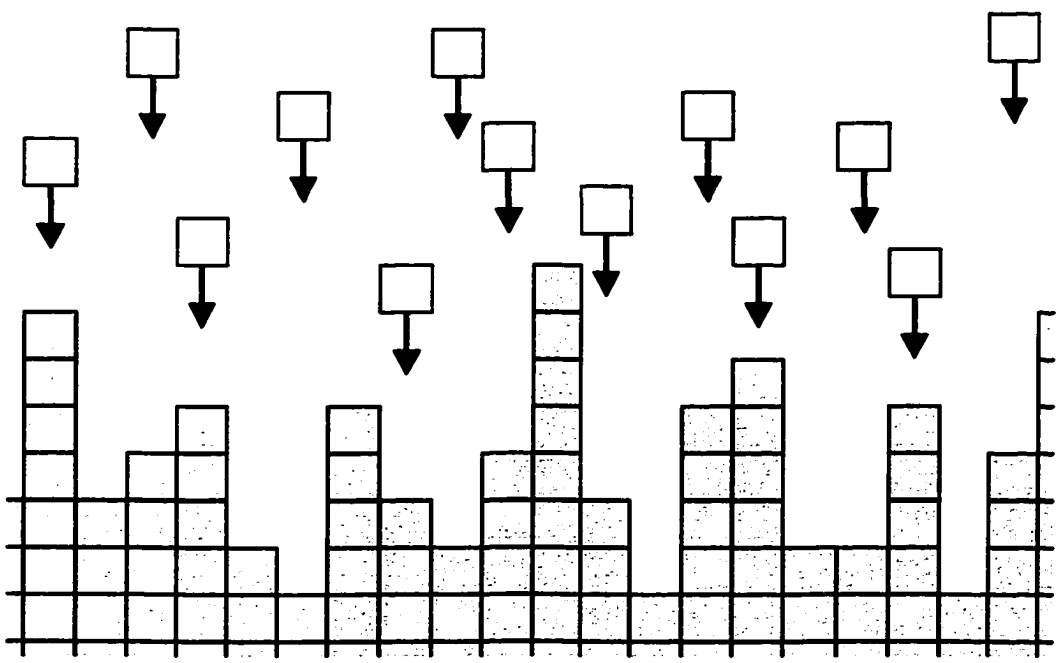

Figure 2

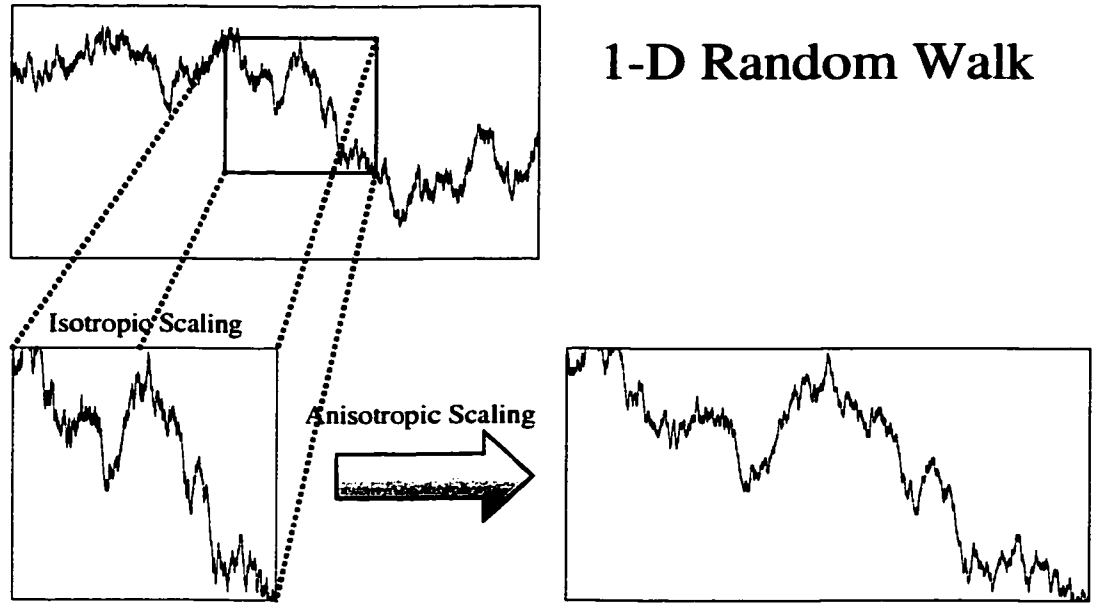

Figure 3

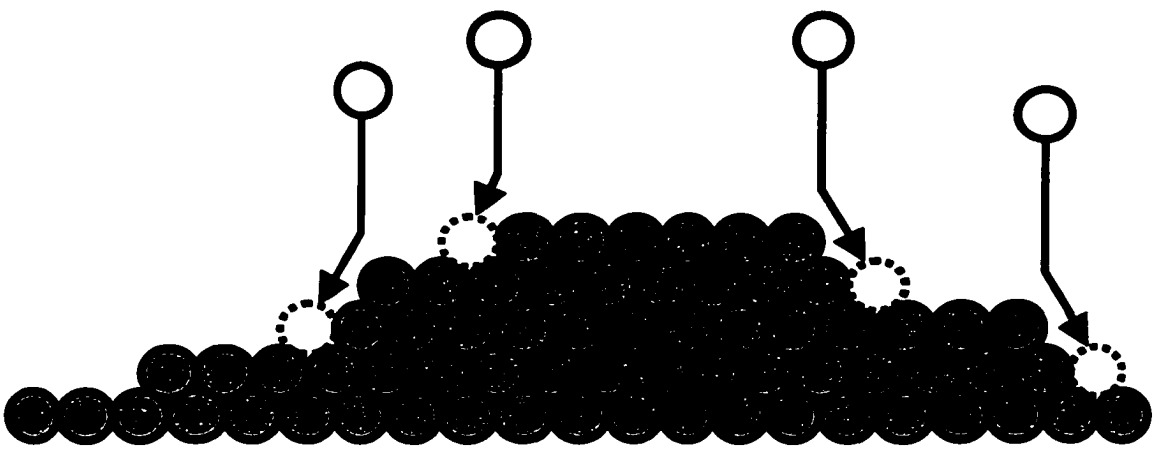

Figure 4

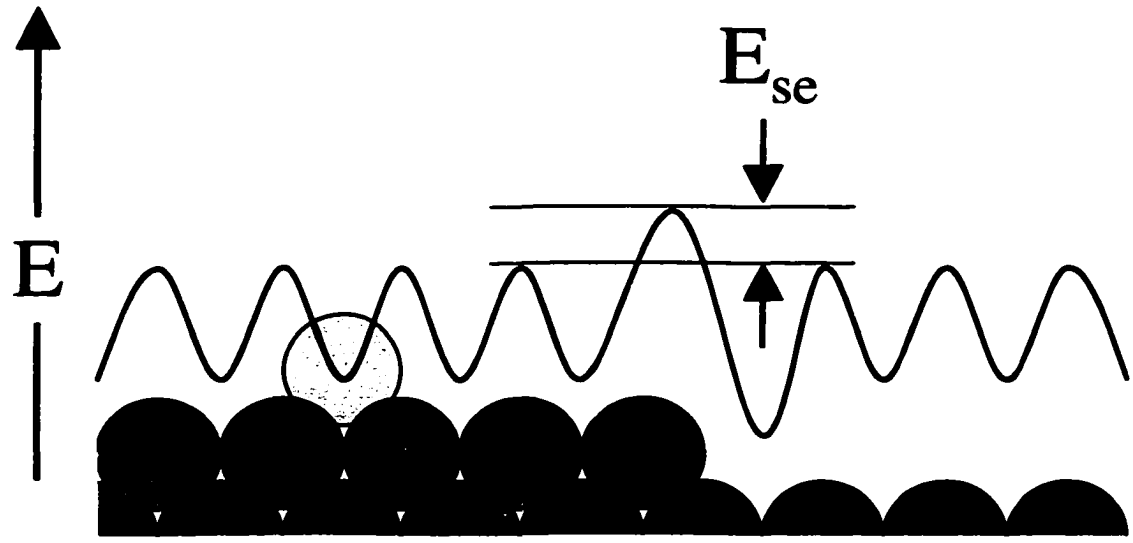

Figure 5

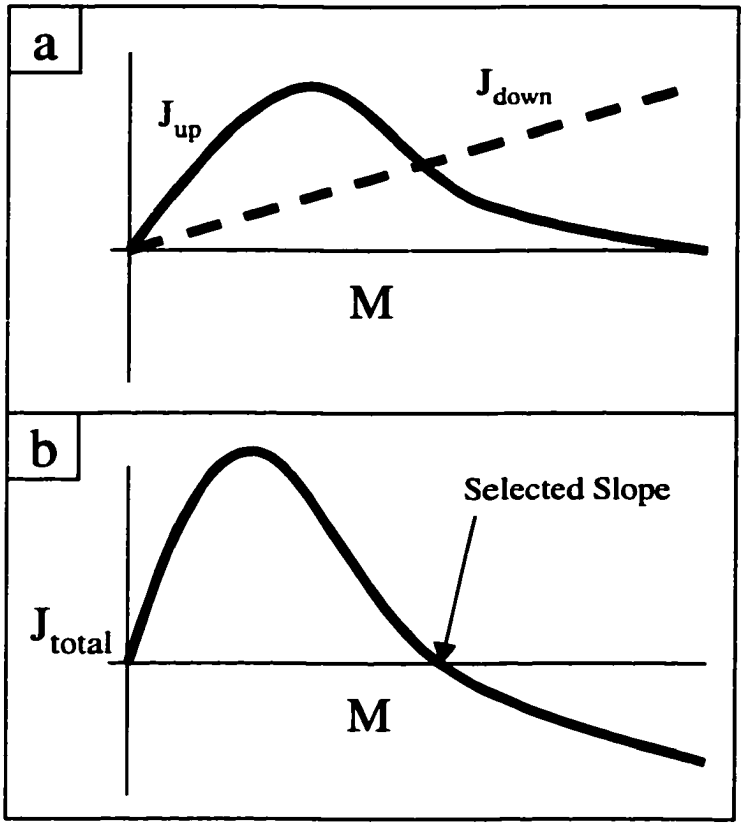

Figure 6

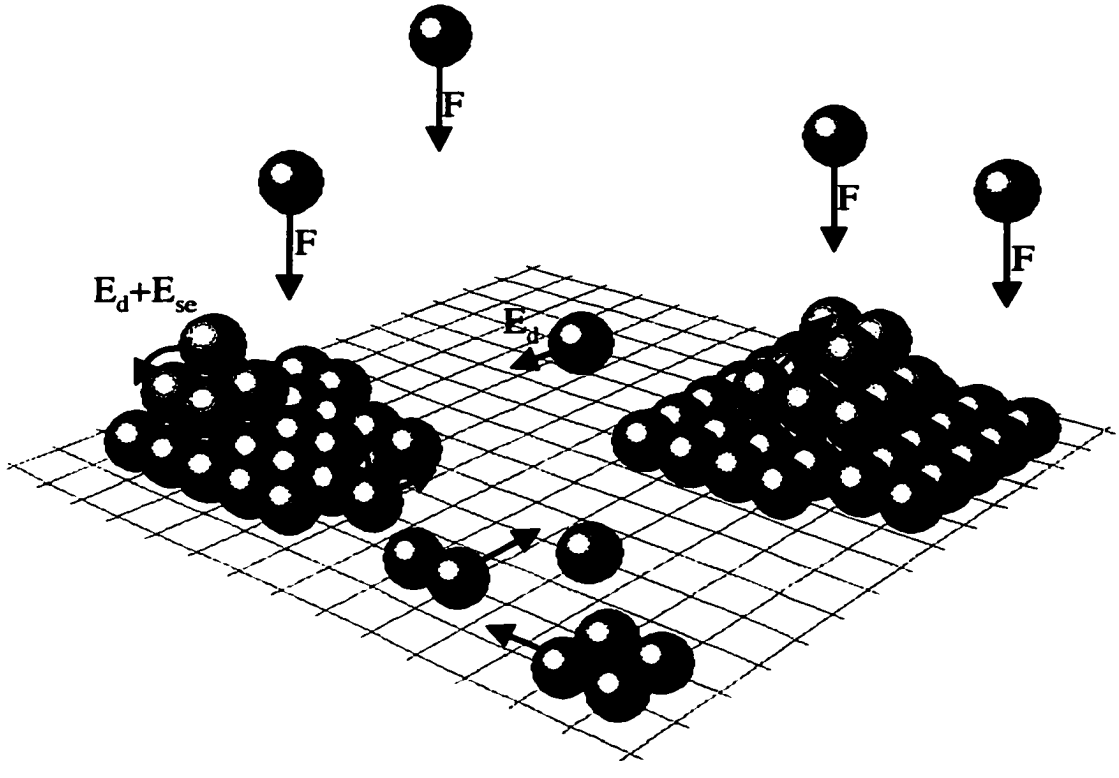

Figure 7

2. METAL HOMOEPITAXIAL GROWTH AT VERY LOW TEMPERATURES: LATTICE-GAS MODELS WITH RESTRICTED DOWNWARD FUNNELING

A paper published in Physical Review B.

K.J. Caspersen and J.W. Evans

Abstract

We develop and analyze 1+1d and 2+1d models for multilayer homoepitaxial growth of metal films at low temperatures (T), where intralayer terrace diffusion is inoperative. This work is motivated by recent variable-temperature scanning tunneling microscopy studies of Ag/Ag(100) homoepitaxy down to 50K. For growth at 0K, we introduce a "restricted downward funneling" model, wherein deposited atoms can be trapped on the sides of steep nanoprotrusions rather than funneling down to lower adsorption sites (which are bridge sites in our 1+1d models, and four-fold hollow sites for our 2+1d models for fcc(100) or bcc(100) surfaces). This leads to the formation of *overhangs* and *internal defects* (or *voids*), and associated "rough" growth. Upon increasing T, we propose that a series of interlayer diffusion processes become operative, with activation barriers below that for terrace diffusion. This leads to "smooth" growth of the film for higher T (but still in the regime where terrace diffusion is absent), similar to that observed in models incorporating "complete downward funneling."

1. Introduction

A traditional expectation for homoepitaxial growth is that the roughness of deposited films of a given thickness should increase with decreasing deposition temperature (T), due to enhanced kinetic barriers to smoothing [1,2]. However, unexpected "smooth growth" has been observed in diffraction studies [3,4] of metal(100) homoepitaxial growth at liquid nitrogen temperatures where terrace diffusion is inoperative. This behavior was initially associated with "transient mobility" of "hot" deposited adatoms [3]. However, such transient mobility was not observed in molecular dynamics (MD) studies. An alternative proposal was that the smooth growth was due to "downward funneling" (DF) of depositing atoms from the point of impact to lower four-fold hollow sites in the fcc(100) crystal geometry [5]. It should be noted however that the DF model does not explain the narrow diffraction profiles (i.e., long-range lateral spatial correlations) observed in the submonolayer regime [6].

Recent variable-temperature Scanning Tunneling Microscopy (VTSTM) studies [7-9] of the morphology of 25ML-30ML Ag films deposited on Ag(100) do in fact find "re-entrant" smooth growth. Specifically, the roughness increases as the deposition temperature is lowered from room temperature to 210K, but then decreases again until about 140K. The smooth growth observed at 140K is consistent with the earlier diffraction studies [3,4]. Furthermore, the measured roughness is just slightly above that predicted by the downward funneling model with no thermal diffusion processes [5] (at least if one corrects the continuous STM height distribution to account for discrete atomic layers [9]). However, the VTSTM studies in Ref.s [7] and [9] examine roughness down to 50K, and reveal a previously unobserved rougher growth for these "very low" T. The latter behavior cannot be explained by the downward funneling model without thermal diffusion processes (for which

there is no temperature-dependence), and suggests that in some growth regimes, this model oversimplifies the atomistic dynamics.

Thus, our goal in this paper is the development and analysis of a refined model which can describe the observed novel growth behavior for low-T where terrace diffusion is inoperative. Motivated by Molecular Dynamics studies [5,10,11], we propose that "rough growth" at 0K can be described by a "restricted downward funneling" (RDF) model, where deposited atoms get caught on the sides of steep nanoprotrusions (which are prevalent below 120K). As a result, overhangs and internal defects or voids can form in the growing film. These models are then extended to describe growth for a range of "low" T>0K, where terrace diffusion of isolated adatoms is still inoperative, by incorporating various thermally activated interlayer atomic hopping processes with barriers lower than that for terrace diffusion. Apart from physical 2+1 dimensional (2+1d) system of interest, we also present corresponding 1+1d model as it is easy to implement, and the behavior is instructive. The emphasis in this work is not on asymptotic behavior, but rather on experimentally relevant properties of thin films and their variation with T.

In Sec.2, we provide some background on the characterization of film morphology for the relevant (non-simple-cubic) crystalline geometries. Then, in Sec.3, we develop and analyze RDF models for 0K growth. Next, in Sec.4, we develop and analyze models for growth in low-T regime where low-barrier interlayer diffusion processes, but not terrace diffusion, are operative. Some general discussion of observed behavior in the context of coarse-grained continuum modeling is provided in Sec.5, and brief concluding remarks are presented in Sec.6.

2. Crystalline Geometry and Morphological Characterization of Films

Most lattice-gas modeling of epitaxial growth is based on an unphysical simple-cubic (sc) crystalline geometry. For growth of defect free films with such sc geometries, adsorption sites are chosen as "on-top" sites. In other models incorporating defects, such as ballistic deposition [12], atoms can also stick at unsupported sites adjacent to film atoms (which is somewhat artificial), thus creating overhangs. In both cases, atoms in the film are arranged in columns, and the "surface atoms" at the top of each column are completely exposed.

The situation is very different for 2+1d homoepitaxial growth on fcc(100) or bcc(100) substrates. In typical the situation of defect-free growth, the "natural" adsorption sites are four-fold hollow sites supported by four atoms in the layer beneath. Similarly, in the 1+1d analogues of these physical geometries, the "natural" adsorption sites are bridge sites, supported by two atoms in the layer beneath. In our growth models, although deposited atoms will be restricted to epitaxial sites, they will not be constrained to sit at natural adsorption sites [i.e., they can have less than four supporting atoms in the 2+1d models, and less than two in 1+1d models]. In any case, atoms in the film are arranged in vertical columns, and we describe the atoms at the top of these columns as "surface atoms". Atoms in each column are either in layers of even height, or of odd height (in contrast to sc geometries), and columns of atoms with even and odd height alternate. Also differing from sc geometries is the feature that surface atoms can be partially covered by γ=1-4 atoms in one of the higher layers in 2+1d models (or by γ=1-2 atoms in 1+1d models), or completely exposed (γ=0). See Fig.1. Thus, surface atoms are naturally labeled by α. Below, we define the standard quantities used to characterize the film surface [12] in terms of the locations of these

surface atoms, thereby incorporating refinements necessary to account for non-sc geometries, and for possible internal defects in the growing film.

To characterize vertical structure of the film, let $P_{j\gamma}$ denote the fraction of surface atoms which are in layer j and have type γ, so that $\Sigma_j \Sigma_\gamma P_{j\gamma} = 1$. It is natural to weight the significance of surface atoms in determining film roughness, etc., according to the degree to which they are covered (i.e., their type γ), as determined by a factor $f_\gamma \leq 1$ with $f_0=1$. Then, $P_j = \Sigma_\gamma f_\gamma P_{j\gamma}$ is the effective population of surface atoms in layer j (i.e., the discrete film height distribution), and in general $\Sigma_j P_j$ depends on film structure. Below, we shall utilize the normalized height distribution, $P'_j=P_j/\Sigma_j P_j$. Of course, the choice of f_γ is somewhat arbitrary, but one natural possibility is to set $f_\gamma=(2n-\gamma)/(2n)$ for n+1 dimensional systems. Then f_γ varies between unity for fully exposed surface atoms ($\gamma=0$), and zero for the maximum α. Furthermore, for films with no overhangs or defects, one has the familiar result, $2P_j=\theta_j-\theta_{j+1}$, analogous to behavior for the sc geometry [13].

The following quantities characterizing the vertical structure of the film surface are primary interest: the mean film height, j_{av}; the interface width, W (both in units of the vertical interlayer spacing); the skewness, κ; and the kurtosis, Q, of the film height distribution. We define these quantities by

$$j_{av} = \Sigma_j \; j \, P'_j, \;\; W^2 = \Sigma_j \, (j-j_{av})^2 \, P'_j, \; \kappa = W^{-3}\Sigma_j \, (j-j_{av})^3 \, P'_j, \text{ and } Q= W^{-4}\Sigma_j \, (j-j_{av})^4 \, P'_j \; -3. \quad (2.1)$$

Since the P'_j are based on surface atoms, these quantities effectively ignore any enclosed voids. W measures roughness of the film surface, κ gives a measure of vertical asymmetry, and Q measures the weight of the height distribution in the tail relative to a Gaussian (where Q=0). One has that $j_{av} \geq Ft=\theta$, where F is the deposition flux in ML/unit time, t is the time

since deposition was initiated (on a perfect substrate), and θ is the coverage in monolayers (ML). The strict inequality applies in the case of internal voids. Also, one generally expects that for a system of linear size L (with periodic boundary conditions), that $W(L,t) \sim L^{\alpha} f(t/L^{z})$, where $f(x<<1) \sim x^{\beta}$, with $\beta=\alpha/z$, and $f(x>>1) \sim$ constant [12]. Thus, for $L \rightarrow \infty$, one has $W \sim t^{\beta}$ for large t, corresponding to "kinetic roughening" of the growing film (for $\beta>0$). In some models, one has slower roughening where $W^2 \sim \ln(t)$, for which one usually identifies $\beta=0$. For $t \rightarrow \infty$, the saturation roughness in a finite system satisfies $W \sim L^{\alpha}$. The behavior of κ and Q will be discussed below for specific models.

It is also appropriate to characterize the lateral structure of the film surface. To his end, one introduces a height-height correlation function, $H(\underline{r})$. This quantity gives the mean square height difference for lateral separations, $\underline{r}$, and is defined by

$$H(\underline{r}) = \Sigma_{j\,k}\, (j-k)^2\, P'_{j\,k}(\underline{r}). \qquad (2.2)$$

Here, $P'_{j\,k}(\underline{r})$ is pair probability for surface atoms in layers j and k to separated laterally by $\underline{r}$, normalized so that $\Sigma_{j\,k}\, P'_{j\,k}(\underline{r}) = 1$. We incorporate the same weighting of surface atoms as in the height distribution. For a specific $\underline{r}$, we emphasize that for non-zero $P'_{j\,k}$, the difference in layer labels, j-k, is either constrained to even values (these $\underline{r}$ are denoted $\underline{r}_+$), or to odd values (these $\underline{r}$ are denoted $\underline{r}_-$). Thus, we have $P'_{j\,k}(\underline{r}_+)=0$ for j-k odd, and $P'_{j\,k}(\underline{r}_-)=0$, for j-k even. This complicates the standard analysis of asymptotic behavior for large r [12]. Nonetheless, one can show that

$$H(\underline{r}_\pm) \rightarrow 2[W^2 \pm M_2\, M_0 \pm (M_1)^2]/[1 \pm (M_0)^2], \text{ for } r=|\underline{r}_\pm| \rightarrow \infty, \qquad (2.3)$$

where $M_k = (\Sigma_{j\ even} - \Sigma_{j\ odd})\ j^k\ P'_j$ ($\sim W^{k-1}$ in some situations) [14]. See the Appendix. Thus, one has $H(\underline{r}) \rightarrow 2W^2$ except for a "small" correction, for large W. This mimics standard behavior for sc geometries where $H(\underline{r}) \sim r^{2\alpha}$ for $r<<\xi\sim t^{1/z}$, and $H(\underline{r}) \approx 2W^2$ for $r>>\xi$ [12].

3. "Restricted Downward Funneling" Models for Growth at 0K

For temperatures at or very close to 0K, all thermal diffusion processes are inactive, so the structure of growing films (and specifically their surface morphology), is controlled by the deposition dynamics. As noted in Sec.1, a commonly accepted view is that smooth growth for fcc(100) metal homoepitaxy at low-T derives from the downward funneling (DF) of atoms depositing at step edges and the sides of nanoprotrusions to lower four-fold hollow adsorption sites in the fcc(100) crystal geometry [5,15]. For DF, deposited atoms require the maximum possible number (four) of support atoms, and if the impact a site that has fewer, they deflect or funnel downward until reaching such a site. Indeed, models for growth at higher T do reveal "re-entrant" smooth growth at lower T if DF deposition dynamics is incorporated [7,9,16,17]. However, as also indicated in Sec.1, experimental W-values for 25ML Ag/Ag(100) films around 50K (and presumably for lower T) are significantly higher than DF values. We believe that these high W values can only be described by modifying the DF deposition dynamics. Thus, we introduce the concept of "Restricted Downward Funneling" (RDF) deposition dynamics: atoms depositing on the sides of nanoprotrusions do not necessarily funnel down to lower four-fold-hollow sites, but rather can adhere to or get stuck at "trap sites" on these sides that do not necessarily have four support atoms. Specifically, after impact, one checks to see if the site is a specified trap site; if not the atom funnels downward to an available adjacent site in the next lower layer, checking again for a trap site, and continuing this process until such a site is reached. These models are motivated

by Molecular Dynamics studies which reveal the trapping of adatoms depositing on {111} facets forming the sides of nanopyramids placed on a fcc(100) surface [10]. One consequence of this breakdown of funneling is the possibility of forming overhangs and internal defects in the growing film, a feature which is incorporated into our modeling, and which has also been observed in Molecular dynamics studies of film growth at low T [11].

While detailed analysis of experiments requires a model with the correct dimensionality (2+1d), we will also discuss analogous 1+1d models involving adsorption at bridge sites (see Fig.1a). The DF model in 1+1d has been implemented previously [5,15,18], and modification to incorporate RDF is natural and straightforward. The lower dimensional models can provide insight into behavior for the physically relevant higher dimension. Before proceeding, it is convenient to introduce a simple notation to characterize trap sites in the various RDF (or DF) models. They will be labeled by ns\nn, where ns number of support atoms, and nn is the minimum number of adjacent in-layer atoms (for the specified ns) needed to trap a deposited atom. Thus, for the DF model, the only trap sites are 4\0 in 2+1d, and 2\0 in 1+1d. Below, we present detailed results from Kinetic Monte Carlo simulation of RDF models, and compare behavior with that of DF models.

3.1 1+1 Dimensional Models

Trap sites in our RDF model are naturally designated as either 2\0 or 1\1 sites, as compared with only 2\0 sites for DF. See the schematic in Fig.2a. Also shown in Fig.2b and 2c are examples of 25ML films simulated in these models. Simulation results related to the first few moments of the height distribution are shown in Fig.3. Perhaps of primary interest is behavior of the roughness, W. For a large system, RDF and DF models show the same behavior for low θ until significant higher layer population is achieved, then distinct behavior

emerges, and asymptotic scaling behavior is achieved fairly quickly after $\theta \approx 10$ML. We find that $\beta=0.31(\approx 1/3)$ for RDF, and $\beta=0.25(\approx 1/4)$ for DF. This is consistent with expectations from coarse-grained continuum treatments of these models, which indicate that Kardar-Parisi-Zhang (KPZ) behavior will be observed for RDF, and Edwards-Wilkinson (EW) behavior for DF (see Sec.5). From the saturation roughness versus system size, $L \geq 100$ (lattice constants), we find the expected values for roughness exponents of $\alpha=0.50\pm0.02$ for RDF, and $\alpha=0.500\pm0.001$ for DF (see Sec.5). Another basic quantity for RDF is the defect density (per site), which we simply define as $\rho_d=(j_{av}-\theta)/j_{av}$. Initially, ρ_d increases slowly (since building a void requires several deposited atoms), and then approaches monotonically its asymptotic value of about 0.18.

Next, we discuss the θ-dependence of κ and Q. For both models, one has $\kappa \sim \theta^{-1/2}$ and $Q \sim \theta^{-1}$, for $\theta \ll 1$, corresponding to initial population of effectively only the first layer. For DF, κ decreases monotonically to zero (as expected for EW), although rather slowly. Details of this behavior may reflect the sensitivity of odd moments of the height distribution like κ to our choice of f_γ quantifying surface atom exposure [19]. For RDF, κ decreases until about 10ML then increases towards the asymptotic KPZ value of 0.28 [20]. Where the initial decrease reflects the feature that RDF initially has difficulty filling all surface sites leaving large crevasses on the surface (decreasing κ). Eventually, overhangs and protrusions form covering the crevasses, and leading to an increase in κ. For both models, Q shows the same features: an initial decrease in Q to a minimum value (reflecting limitations on building micro-protrusions at low θ), and then approaches its asymptotic EW value of 0 for DF, and KPZ value of 0.12-0.16 for RDF [20].

Finally, in the top frames of Fig.4, we show examples of the behavior of H(r) versus r (in units of the surface lattice constant) for the 1+1d DF and RDF models. Note the appearance of "oscillations" (which are most clear for small W), consistent with (2.3).

3.2 2+1 Dimensional Models

Our 2+1d studies are performed for a crystalline geometry corresponding to an fcc(100) surface. Thus, the only trap site for DF model is the 4\0 (four-fold hollow) site. In contrast, for RDF, we allow 3\0 trap sites with only three support atoms, 2\1 trap sites with two support atoms, provided they had at least one in-layer nearest neighbor, and even 1\2 trap sites with one support atom and at least two in-layer nearest neighbors [21]. A schematic of these trap sites for the DF and RDF models are shown in Fig.5a, along with a cross-section of simulated 25ML films in Fig.5b and 4c. Simulation results related to the first few moments of the height distribution are shown in Fig.6. Behavior is qualitatively similar to 1+1d, but there are some significant quantitative differences. Increased pathways for funneling, and constraints in population of higher layers, creates smoother surfaces for both models. The effective β (around 10^3 ML) is significantly reduced to about 0.06. This is expected for DF in 2+1d where EW with β=0 applies. The RDF model does not exhibit asymptotic KPZ behavior where $\beta \approx 0.24$ [12], an issue to be discussed further in Sec.5. For RDF (DF), effective values for α decrease from 0.13 (0.14) for L=15-35 to 0.10 (0.11) for L=35-70 for RDF. This should be compared with asymptotic values of α=0 for EW, and α=0.4 for KPZ, although lower values down to 0.2 often emerge from simulations for the latter [12]. For RDF, the defect density, again defined as $\rho_d = (j_{av}-0)/j_{av}$, increases

monotonically (slowly initially) as in 1+1d, achieving an asymptotic value of about 0.29 (although more quickly than in 1+1d).

For DF, oscillations appear in κ and Q reflecting sensitivity of these quantities to the initial quasi-layer-by-layer growth, and then these quantities decay quickly to around zero (as expected for EW). For RDF, the development of a "large" negative κ and positive Q achieved at $\theta \approx 8$ML reflect the development of deep crevasses, and the limited inability of growth to cover these by developing micro-protrusions and overhangs. For larger θ, both quantities decrease in amplitude which might be compared with asymptotic EW values of zero [22].

Finally, in the bottom two frames of Fig.4, we show examples of the behavior of $H(\underline{r})$ versus $\underline{r}$ for the 2+1d DF and RDF models. Solid lines correspond to the [100] direction along diagonal rows of surface atoms, where atoms in adjacent columns alternate between even on odd layers. These reveal the appearance of "oscillations" (for small W), consistent with (2.3). Dashed lines correspond to $\underline{r}$ in the [110] direction, where atoms in the relevant columns are either all in even or all in odd layers, so there are no oscillations in $H(\underline{r})$.

4. Growth at Low Temperatures: Low-Barrier Interlayer Diffusion

In this section, we will discuss deposition at temperatures above 0K, but still below the threshold for activation of the terrace diffusion of isolated adatoms. Why should there be any temperature dependence to growth? We argue that typically there should exist a family of low-barrier interlayer thermal diffusion processes that are active, and which combined with the deposition dynamics control film growth in this low-T regime. These low-barrier processes consist of diffusion from the low coordination sites that are created as a result of the RDF deposition dynamics. Our motivation for this model comes from consideration of

the Ag/Ag(100) system, where the barrier for diffusion across {100} terraces equals $E_d^{(100)}$ ≈0.4eV [23], so this process is inactive below about 130K. However, the barrier for diffusion across {111} micofacets of $E_d^{(111)}$ ≈0.1eV [24] is much lower, leading to activation of this process around 40K. Atoms landing on the side of pyramidal micro-protrusions are, in actuality, landing on {111} facets, so their diffusion leads to interlayer transport potentially smoothing the film above 40K. In the rest of this section, we present results of the Kinetic Monte-Carlo simulations, in which we incorporate certain low-barrier diffusion processes into our previously describe RDF models in 1+1d and 2+1d. Using parameters for Ag/Ag(100) in the 2+1d model, we shall see that activation of these interlayer diffusion processes leads to smoother film growth as T is increased from 0K to around 100K, consistent with experimental observations [7,9].

4.1 1+1 Dimensional Models

In our model, atoms are randomly deposited via RDF dynamics at a rate F ML/unit time, and then certain lower-coordination atoms undergo interlayer hopping to adjacent sites until reaching designated trapping sites (such as 2\0 bridge sites). A detailed specification of hopping is naturally given in terms of the (initial) coordination, m_i=1-6, of deposited atoms in this 1+1d geometry. Atoms with m_i=1 are specified to hop instantaneously, consistent with low barrier expected for these sites. Atoms with m_i=2 (except those at 2\0 sites with both support atoms) are given a finite hop rate h/unit time (per direction). All other atoms (m_i>2 or 2\0) are not allowed to diffuse, consistent with the high barriers expected for high coordination, and emulating the feature of the 2+1d system that terrace diffusion is inactive in the temperature range of interest. Atoms were only allowed to hop to one of the six

unoccupied nearest-neighbor (final) destination sites, in which the coordination satisfied $m_f>0$. This last requirement ensures that diffusing atoms do not leave the surface.

We designate the above prescription as the "Up and Over" (U&O) Model, since atoms can climb from the sides to the top of mesas through a $m_f=1$ "transition state" site (as shown in Fig.7a). The corresponding process in physical 2+1d systems is expected to have a substantial barrier (see Sec.4.2), so we are motivated to also consider a modified "Up and Back" (U&B) model where this process is inoperative (see Fig.7a). This modification is achieved by simply imposing the restriction that $m_f>1$, blocking atoms from hopping into the above mentioned transition state.

As there is only a single finite hopping rate, h, in our models, film structure (for a given θ) is determined entirely by the ratio h/F. Fig.7b and Fig.8 show the variation with h/F of key features of 25ML films generated from KMC simulations in the 1+1d U&O and U&B models. Below we describe the observed behavior for various regimes of h/F:

(i) *Negligible diffusion.* For h/F below 10^{-1}, deviations from 0K RDF growth are negligible.

(ii) *Onset of diffusion.* For h/F around 10^{-1} - 10^{0}, diffusion becomes active on the time scale of deposition, but each diffusing atom hops approximately only once before it is stabilized. We now discuss the observed deviations or perturbations of the 0K RDF morphology. Diffusion of atoms to trap sites in higher or lower layers has the effect of increasing not just the width (W) of the height distribution, but also the relative population in the upper and lower extremes or tails (i.e., increasing Q). The significant increase in W is not surprising for the U&O model (allowing for climbing on top of mesas), but a small increase occurs even for U&B dynamics. The change in skewness, κ, is less dramatic. An initial slight decrease in κ for U&B dynamics may reflect an initial bias towards lower trap sites, whereas the initial

increase in κ for U&O dynamics reflects the possibility of populating higher trap sites by climbing on top of mesas.

(iii) *Significant diffusion.* The range 10^0-10^1<h/F<10^3-10^4 is characterized by a complex interplay between RDF (creating voids and overhangs), and the increased diffusivity (filling in voids). Increased diffusivity allows atoms to more easily find higher coordinated trap sites, eliminating of voids and overhangs, and decreasing in W. More surprising is the non-monotonic behavior of κ and Q. Apparently for h/F<20, the combined effect of RDF and diffusion is to produce a few broad protrusions while reducing W. These contribute to the upper extreme of the height distribution, thus increasing κ as well as Q. For h/F>20, diffusion is sufficiently fast to preclude RDF from building many of these protrusions, thus decreasing κ and Q.

(iv) *Rapid diffusion (asymptotic regime)* For h/F>10^3-10^4, diffusion is so rapid that deposited atoms can effectively always find a trap site without interference from subsequent deposited atoms. In this regime, U&O dynamics reduces to model in which atoms are immediately placed at one of the trap-sites on either side of the deposition site, whether it be above or below. In contrast, the restriction that m_f>1 for the U&B model means that it reduces to the DF model in this regime (see Fig.7b and 8). In both cases, the films have no overhangs or voids.

4.2 2+1 Dimensional Models

One complication in incorporating interlayer diffusion processes into the 0K 2+1d RDF model is the vast number and variety of configurations with low coordination from which interlayer hopping (with low barrier) may be possible. Furthermore, it is likely that a spectrum of activation barriers, E_d, and thus Arrhenius hopping rates, will apply. Thus, we

make some reasonable, simple choices for these barriers based partly on the coordination of the atom, as well as on known results for the Ag system. Adatoms in sites with a very low (initial) coordination of m_i=1 or 2 likely have an extremely low barrier towards diffusion, and thus are prescribed to hop instantaneously. Some adatoms with m_i=3 are on the {111} micro-faceted sides of pyramidal micro-protrusions on the {100} surface, and thus have E_d=0.10eV corresponding to terrace diffusion of Ag on Ag(111) [24]. In fact, we assign E_d=0.10eV to all sites with m_s=3, except for 3\0 sites. The latter more resemble 4\0 sites, which have a high barrier, and are therefore assign E_d=0.15eV. Hopping of adatoms from some sites with m_s=4 resembles dimer scission on a Ag(111) surface where E_d≈0.25eV [25], so sites with m_i=4 (except 4\0 sites) were assigned this barrier. Hopping of adatoms from some sites with m_i=5 resembles in-channel diffusion of Ag on Ag(110) for which E_d≈0.25eV [26], so sites with m_i=5 (except four-fold hollow sites) were assigned this barrier. Adatoms at sites with $m_i \geq 6$ are not allowed to hop, due to assumed high barriers. A schematic of these diffusion processes is shown in fig.9. The attempt frequency (ν) for all active hopping processes was set to 1×10^{12}/s, consistent estimates for diffusion of Ag on Ag(111) [24]. We also set F=0.04ML/s as in experiment [7], but note that results depend only on the ratio ν/F.

Analogous to 1+1d, in our 2+1d "up and over" (U&O) model, adatoms are allowed to diffuse to any of the 12 unoccupied nearest neighbor sites, provided that the (final) coordination satisfies $m_f \geq 1$. In particular, this means that they can climb up from the (111) micro-faceted sides to the top of pyramidal mesas through low-coordination "transition state" site. However, this corresponds to hopping down from the edge of an island on a Ag(111) surface, for which we know there exists a substantial additional Ehrlich-Schwoebel barrier

[24]. Thus, it is reasonable to examine the effect of precluding this process in a 2+1d "up and back" (U&B) model, where adatoms can only hop to sites with $m_d \geq 3$, thus prevented them from hopping into the above mentioned transition state.

Since there are several rates in the 2+1d models, it is natural to examine behavior as a function of deposition temperature, T (rather than versus some h/F), thus facilitating comparison with experiment. Fig.10 and 11 shows the variation with T of key features of 25ML films generated from KMC simulations in the 2+1d U&B and U&O models. Most dramatic feature of Fig.11 is the step-wise variation of quantities with increasing T; the three steps correspond to the activation of three different classes of diffusion processes with progressively higher barriers (0.10eV, 0.15eV, and 0.25eV). First, we discuss the variation of W with T. For the U&O model, the steps at 40K (activation of diffusion on {111} facets) and at 105K (activation of diffusion for m_i=4 or 5) display a transient increase in W, since the activated process allows adatoms to climb on top of mesas and become trapped on top. In contrast, the step at 60K (activation of diffusion from 3\0 sites) shows no such increase. This is because upward hopping from 3\0 sites is not possible (destination sites would have m_f=0, i.e. no support). Similarly, W decreases monotonically with increasing T for the U&B model, where climbing on top of mesas is precluded. For high T (>120K), effectively all deposited atoms find a trap site without interference from subsequent deposition. Not surprisingly, W(T>120K) for the U&O model is "quite high", as a significant fraction of these trap sites are higher than the deposition site. W(T>120K) for the U&B model is lower, but not as low as for the DF model, contrasting 1+1d behavior. This is because the higher dimensionality allows for limited lateral diffusion to trap sites (along the sides of a micro-protrusion), rather than just downward transport to 4\0 traps as in DF. In both models, as expected, diffusion

processes work to eliminate voids and overhangs, the associated density, $\rho_d=(j_{av}-\theta)/j_{av}$, decreasing step-wise monotonically to be effectively zero for T>120K.

To summarize the overall behavior, one sees that both models deviate smoothly from 0K RDF behavior with increasing T: W decreases towards (but does not achieve) the DF value, κ and Q approach DF-like values, and ρ_d vanishes consistent with the DF. Therefore, the combination of RDF with these very active selected low barrier diffusion process work to produce DF or EW-like behavior for T>120K. Since the actual barrier to climb up on top of mesas is finite, perhaps 0.2-0.3eV for Ag/Ag(100), the optimum prediction behavior for this system may lie between the U&O and U&B models. In any case, considering the simplicity of these models, predicted behavior of W versus T is in good semi-quantitative agreement with experimental results [7,9] for the same deposition flux. See Fig.11.

5. Discussion: Continuum Formulations of Film Growth

To provide some basis for understanding the behavior observed in our RDF models, it is instructive to consider a coarse-grained description of film morphology and growth [12]. Here, one does not resolve atomically discrete lateral or vertical film structure, and thus describes film height and lateral position $\underline{x}$ by a continuous function $h(\underline{x},t)$ (defined here with the units of interlayer spacing or monolayers). Then, $h(\underline{x},t)$ satisfies stochastic continuum evolution equation of the form

$$\partial/\partial t\, h(\underline{x}, t) = F/\rho - \nabla\cdot \underline{J} + \eta \qquad (5.1)$$

where F is the deposition flux in ML/unit time, $\rho=1-\rho_d$ is the film density (normalized to unity for defect free epitaxial growth), and $\underline{J}$ is the conservative lateral mass current across the film surface. Finally, η denotes the shot-noise in the deposition process, and satisfies

$\langle\eta\rangle=0$, and $\langle\eta(\underline{x},t)\eta(\underline{x}',t')\rangle \propto \delta(\underline{x}-\underline{x}')\delta(t-t')$, where $\langle\rangle$ denotes a suitable ensemble average. For our purposes, the lateral mass flux, $\underline{J}$, is naturally decomposed as $\underline{J}=\underline{J}_{DYN}+\underline{J}_{THERM}$, where the component $\underline{J}_{DYN}$ is associated with transient deposition dynamics, and the component, $\underline{J}_{THERM}$, with thermally activated diffusion (for T>0K). Often, one develops expansions in slope (and curvature) for $\underline{J}$ and ρ, and thus for the RHS of (5.1), focusing on the lowest-order terms which control the long-time and long wavelength asymptotic behavior [12].

It is convenient to first consider the standard downward funneling (DF) model for growth at 0K, where $\rho=1$. For surfaces which are fairly smooth locally (small local slopes), it is not surprising that $\underline{J}_{DYN}=\underline{J}_{DF}$ should be proportional to the step density, which in turn is proportional to ∇h, so that $\underline{J}_{DF} \approx -F\nu_{DF}\nabla h$ [15]. In fact, simple calculations give quite reliable estimates of ν_{DF} [17]. Then, equation (4.1) becomes the linear Edwards-Wilkinson (EW) equation

$$\partial/\partial t\, h(\underline{x}, t) \approx F - F\nu_{DF}\nabla^2 h + \eta \tag{5.2}$$

for which $\beta=1/4$ in 1+1d, and $\beta=0$ (logarithmic roughening) in 2+1d [12].

Next, we consider behavior for the restricted downward funneling (RDF) model for growth at 0K. For small local slopes (where surfaces have primarily monoatomic steps), one expects that to a good approximation, $\underline{J}_{DYN}=\underline{J}_{RDF}$ is still proportional to ∇h, so that $\underline{J}_{RDF} \approx -F\nu_{RDF}\nabla h$. The key difference from the DF model is that now $\rho<1$ due to the formation of internal defects, and one expects that ρ can be expanded as

$$\rho = \rho(\nabla h, \nabla^2 h,\ldots) = \rho_0 + \rho_1|\nabla h|^2 + \rho_2 \nabla^2 h + \ldots \tag{5.3}$$

Thus, equation (5.1) becomes the non-linear Kardar-Parisi-Zhang (KPZ) equation

$$\partial/\partial t\, h(\underline{x}, t) \approx F(\rho_0)^{-1} - F\rho_1(\rho_0)^{-2}|\nabla h|^2 - F[\nu_{RDF}+\rho_2(\rho_0)^{-2}]\,\nabla^2 h + \eta \tag{5.4}$$

for which $\beta=1/3$ in 1+1d, and $\beta\approx1/4$ in 2+1d for sufficiently strong non-linearity.

Some insight into the strength of the non-linearity comes from studies of the RDF model for vicinal substrates with a range of prescribed slopes, ∇h_0. Specifically, we monitor the variation in the steady-state defect density with ∇h_0, and find a nearly quadratic variation of the form $\rho(\nabla h_0) \approx \rho_0 + \rho_1|\nabla h_0|^2$. From simulations, we determine that $\rho \approx 0.183 + 0.29|\nabla h_0|^2$ in 1+1d, and $\rho \approx 0.284 + 0.065|\nabla h_0|^2$ in 2+1d. Thus, one finds a remarkably weak non-linearity in 2+1d (certainly compared with 1+1d). This likely explains the slow roughening with $\beta\approx0.06$ in 2+1d over the observed coverage range. One possibility is that asymptotic behavior is not relevant in the experimentally accessed regime, consistent with other models incorporating defects which reveal a very slow crossover to true asymptotic behavior [27]. Another perspective comes from numerical studies of KPZ models in 2+1d revealing an apparent kinetic phase transition to a regime of smooth EW growth for sufficiently weak non-linearity [12,28]. Later work suggested that 2+1d was the lower critical dimension for this phase transition [29], implying that the numerical studies were in fact seeing extremely slow crossover to KPZ behavior. This situation could apply for the RDF model.

We note that there are other standard (on- or off-lattice) "ballistic deposition" models which incorporate internal defects, and which do reveal KPZ behavior [12], similar to our RDF model in 1+1d. It is also know that introducing some restructuring in these models can significantly modify (and produce ambiguous) asymptotic scaling behavior [27,30].

In conventional models for growth at T>0K incorporating thermally activated terrace diffusion, the associated mass flux is written in Mullins form as $\underline{J}_{THERM}=\nabla\mu$, where $\mu = F[\mu_0$

+ $\nu' \nabla^2 h + \ldots]$ denotes a generalized chemical potential [12]. Stroscio *et al.* [31] suggest replacing $\nabla^2 h$ with $\nabla^4 h$ for systems where terrace diffusion leads to irreversible capture at step edges. The presence of step-edge barriers can lead to additional destabilizing uphill currents [12]. In all these cases, terrace diffusion is operative leading to the possibility of large lateral characteristic lengths for any film thickness. However, the "limited" interlayer thermal diffusion in our models is fundamentally different, being restricted to sloping portions of the film surface, and thus being unable to generate these large lateral characteristic lengths. Thus, the form of $\underline{J}_{THERM}$ is expected to be different from above. For example, in U&B models for high T, RDF plus thermal diffusion together mimic DF, so $\underline{J}_{THERM} = -F\nu_{TH}\nabla h$ (a stabilizing downhill current), where $\nu_{RDF} + \nu_{TH} \approx \nu_{DF}$.

6. Conclusions

We have developed 2+1d models (and their 1+1d analogues) for metal(100) homoepitaxial growth at 0K controlled by "restricted downward funneling" deposition dynamics. These were extended to describe low-T growth, where terrace diffusion is inoperative, but various low-barrier interlayer diffusion processes may be active. The 2+1d models are quite successful in describing the variation with T (below 130K) of the roughness of 25ML Ag/Ag(100) films as observed in recent experiments [7,9]. In particular, they predict the transition from "smooth growth" around 115K-130K (effectively described by the simple downward funneling model), to rougher growth at lower T. Furthermore, they predict the incorporation of internal voids or defects in growing metal(100) homoepitaxial films at low T. Indeed, recent experimental evidence for a low density of such defects in Ag/Ag(100) film growth at 100K was provided by surface-sensitive X-ray scattering studies [32].

Our models are certainly idealized both in the treatment of the deposition dynamics, and of thermally activated diffusion processes. One possible variation in the deposition dynamics is to include "knock-down" effects, where for example depositing atoms could knock downhill adatoms caught on the sides of {111} microfacets. Another variation is to implement less restricted funneling, so atoms deposited on sites without four supporting atoms can make at least one downward hop before becoming trapped. Then, behavior would be closer to standard funneling model. Possible variations in the treatment of thermal diffusion include incorporation of more precise and more varied barriers for interlayer diffusion processes, and also consistent incorporation of low-barrier intralayer step-edge diffusion processes [30]. The latter will perhaps not much affect W (the main focus of this study), but step-edge diffusion processes should increase the lateral correlation length [16], and possibly reduce the density of internal voids. This would likely describe more precisely actual experimental behavior.

Acknowledgements

This work was supported by NSF Grant CHE-0078596, and performed at Ames Laboratory which is operated for the USDOE by Iowa State University under Contract No. W-7405-Eng-82. We also thank Joachim Krug and A. Laszlo Barabasi, and our experimental collaborators, Conrad Stoldt and Patricia Thiel, for useful discussions.

Appendix: Height-Height Correlation Functions

Let $P'_{j\,k}(\underline{r})$ denote the normalized pair probability for surface atoms in layers j and k to separated laterally by $\underline{r} = \underline{r}_+$ or $\underline{r}_-$, defined as in the text. The independence of film height for two points with an asymptotically large separation implies that $P'_{j\,k}(\underline{r}_+) \rightarrow c_+ P'_j P'_k$ (or 0), for j-k even (or odd), as $|\underline{r}_+| \rightarrow \infty$. Also, one has that $P'_{j\,k}(\underline{r}_-) \rightarrow c_- P'_j P'_k$ (or 0), for j-k odd (or

even), as $|\underline{r}_-|\to\infty$. Given the normalization condition on $P'_{j\,k}(\underline{r})$, it should be clear that the constants of proportionality in these relations are non-trivial, and satisfy

$$(c_+)^{-1}=\Sigma_{j-k\ \text{even}}\, P'_j\, P'_k \text{ and } (c_-)^{-1}=\Sigma_{j-k\ \text{odd}}\, P'_j\, P'_k \tag{1}$$

Setting $M_k = (\Sigma_{j\ \text{even}} - \Sigma_{j\ \text{odd}})\, j^k\, P'_j$, one can show that

$$(c_+)^{-1} = \tfrac{1}{2} + \tfrac{1}{2}\,(M_0)^2 \text{ and } (c_-)^{-1} = \tfrac{1}{2} - \tfrac{1}{2}\,(M_0)^2 \tag{2}$$

Next, we introduce a height-height correlation function, $H(\underline{r})$, for lateral separations, $\underline{r}$, defined by

$$H(\underline{r}\,)= \Sigma_{j\,k}\,(j-k)^2\, P'_{j\,k}(\underline{r}\,) \tag{3}$$

The above mentioned constraint on non-zero $P'_{j\,k}(\underline{r}\,)$ complicates the analysis of $H(\underline{r}\,)$. Nonetheless, for asymptotically large $\underline{r}$, one can show that

$$H(\underline{r}_e) \to (c_+)^{-1}\,\Sigma_{j-k\ \text{even}}\,(j-k)^2\, P'_j\, P'_k = 2[W^2 + M_2\, M_0 + (M_1)^2]/[1+ (M_0)^2] \tag{4a}$$

$$\text{and } H(\underline{r}_o) \to (c_-)^{-1}\,\Sigma_{j-k\ \text{odd}}\,(j-k)^2\, P'_j\, P'_k = 2[W^2 - M_2\, M_0 - (M_1)^2]/[1- (M_0)^2] \tag{4b}$$

Finally, we mention another formulation (not used here) for $H(\underline{r}\,)$ in non-sc geometries which recovers some of the simpler behavior familiar in sc geometries. The idea is simply to redefine $\underline{r}$ in a convenient way. For $\underline{r}=\underline{r}_+$ separating columns with atoms in both even or both odd layers, the standard definition is used as above. For $\underline{r}=\underline{r}_-$ separating atoms in even and odd layers, $\underline{r}_-=\underline{0}$ is reassigned to correspond to adjacent columns in a certain direction. Then for each specific $\underline{r} = \underline{r}_+$ or $\underline{r}_-$ take the same set of discrete values, and there is no constraint on j-k being even or odd as above. Thus, the analysis of $H(\underline{r}\,)$ mimics that for an sc geometry, but now $H(\underline{0})>0$ [15].

References

[1] *Morphological Organization in Epitaxial Growth and Removal*, edited by Z. Zhang and M.G. Lagally (World Scientific, Singapore, 1998)

[2] Another misconception (see Ref.[1]) is that smoother growth at low T is simply due to the presence of smaller islands from which deposited atoms can more easily descend.

[3] W.F. Egelhoff and I. Jacob, Phys. Rev. Lett. **62**, 921 (1989).

[4] D.K. Flynn-Sanders, J.W. Evans, and P.A. Thiel, Surf. Sci. **289**, 77 (1993); J. Vac. Sci. Technol. A **7**, 2162 (1989).

[5] J.W. Evans, D.E. Sanders, P.A. Thiel, and A.E. DePristo, Phys. Rev. B **41**, 479 (1990).

[6] Long-range correlations have been attributed to intralayer "clumping" of atoms deposited nearby other adatoms, facilitated by low-barrier edge diffusion processes. See M.C. Bartelt and J.W. Evans, Surf. Sci. **423**, 189 (1999); G. Vandoni, C. Felix, R. Monot, J. Buttet, W. Harbich, Surf. Sci. **320**, L63 (1994); M. Breeman, unpublished.

[7] C.R. Stoldt, K.J. Caspersen, M.C. Bartelt, C.J. Jenks, J.W. Evans, and P.A. Thiel, Phys. Rev. Lett. **85**, 800 (2000).

[8] G. Constantini, F. Buatier de Mongeot, C. Boragno, and U. Valbusa, Surf. Sci. **459**, L487 (2000).

[9] K.J. Caspersen, C.R. Stoldt, A.R. Layson, M.C. Bartelt, P.A. Thiel, and J.W. Evans, Phys. Rev. B, **63**, Feb. 15 (2001).

[10] D.E. Sanders and J.W. Evans, in *Structure of Surfaces III* edited by S.Y. Tong, *et al.* (Springer, Berlin, 1991); D.M. Halstead and A.E. DePristo, Surf. Sci. **286**, 275 (1993).

[11] C. Kelchner and A.E. DePristo, Surf. Sci. **393**, 72 (1997).

[12] A.L. Barabasi and H.E. Stanley, *Fractal Concepts in Surface Growth* (Cambridge U.P, Cambridge, 1995).

[13] See Appendix in J.W. Evans, Phys. Rev. B **39**, 5655 (1989) which normalized P_j to the number of atoms in a complete layer. Here, we normalize to the number of columns (twice as large), hence the extra factor of 2 relating P's and θ's.

[14] If $P'_j \sim W^{-1} f(j/W)$, and $h=W^{-1}$, then $\Sigma_{j\ odd}\ j^k\ P'_j \sim W^k\ [h\Sigma_{x=jh\ (j\ odd)}\ x^k\ f(x)]$, and similarly with j even. If expressions in parenthesis approximate an integral with error O(h), then $M_k \sim W^{k-1}$.

[15] H.C. Kang and J.W. Evans, Surf. Sci. **271**, 321 (1992)

[16] M.C. Bartelt and J.W. Evans, Phys. Rev. Lett. **75**, 4250 (1995).

[17] M.C. Bartelt and J.W. Evans, Surf. Sci. **423**, 189 (1999).

[18] P. Meakin, *Fractals, Scaling and Growth Far From Equilibrium* (Cambridge UP, Cambridge, 1998). See Fig.5.8b for an alternative realization of DF in 1+1d.

[19] Our non-symmetric choice of $f_\gamma=(2n-\gamma)/(2n)$ for n+1 dimensions, atoms at the top ($\gamma=0$) and at the bottom ($\gamma=2n$) of saw-tooth profiles are not weighted equally. A symmetric choice with $f_0=f_{2n}$ would produce modified behavior, perhaps more like in sc geometries.

[20] J. Krug, Adv. Phys. **46**, 139 (1997).

[21] We have checked that behavior of a modified RDF model with only 4\0, 3\0, and 2\1 trap sites is similar to that of the RDF model analyzed here.

[22] For the 2+1d ballistic deposition (single-step) model [12], κ reaches about 0.7 (-1.3), and Q reaches about 0.3 (0.3) at 10^3 ML. These models have KPZ scaling.

[23] P.A. Thiel and J.W. Evans, J. Phys. Chem. B **104**, 1663 (2000).

[24] K. Bromann, H. Brune, H. Roder, and K. Kern, Phys. Rev. Lett. **75**, 677 (1995).

[25] J.W. Evans and M.C. Bartelt in [1] estimate 0.13eV for the Ag_2/Ag(111) pair bond energy.

[26] C. Motel, R. Ferrando, F. Hontinfinde, and A.C. Levi, Surf. Sci. **402-404**, 286 (1998).

[27] M. Schimschak and J. Krug, Phys. Rev. B **52**, 8550 (1995); S. Das Sarma, C.J. Lanczycki, S.V. Ghaisas, and J.M. Kim, Phys. Rev. B **49**, 10693 (1994).

[28] Y.P. Pelligrini and R. Jullien, Phys. Rev. Lett. **64**, 1745 (1990); H. Yan, D. Kessler, and L.M. Sander, *ibid*, **64**, 26 (1990); J.G. Amar and F. Family, *ibid*, **64**, 543 (1990).

[29] T. Natterman and L.-H. Tang, Phys. Rev. A 45, 7156 (1992).

[30] P. Meakin and R. Jullien, J. Physique **48**, 1651 (1987).

[31] J.A. Stroscio, D.T. Pierce, M. Stiles, A. Zangwill, and L.M. Sander, Phys. Rev. Lett. **75**, 4246 (1995).

[32] W.C. Elliott, P.F. Miceli, and P.W. Stevens, Bull APS **44**, 1604 (1999).

[33] B.D. Yu and M. Scheffler, Phys. Rev. Lett. **77**, 1095 (1996).

FIGURE CAPTIONS

Figure 1. Schematic of different types of surface atoms (labeled by γ in a subset of cases) for: (a) 1+1d (where one example of a bridge site is above the left-most atom labeled γ=2); (b) 2+1d (where four-fold hollow sites are above all atoms labeled by γ=4).

Figure 2. (a) Schematic of DF and RDF dynamics in 1+1d. Hatched sites are final trap sites (which are labeled for RDF in the central inset). Simulated 25ML films in 1+1d for: (b) RDF; (c) DF.

Figure 3. W, κ, Q, and ρ_d versus θ for the RDF model (thick solid line) and the DF model (thin solid line) for 0K growth in 1+1d. All quantities are dimensionless (and ρ_d=0 for DF).

Figure 4. Top frames: H(r) versus r in the 1+1d DF and RDF models. Bottom frames: H($\underline{r}$) versus $\underline{r}$ in the 2+1d DF and RDF models. The solid (dashed) lines correspond to the [110] ([100]) directions. In all cases, behavior for four coverages (1, 5, 25, 100 ML from bottom to top) are shown. H($\underline{r}$) is dimensionless (based on units of the interlayer spacing), r and $\underline{r}$ are dimensionless (units of surface lattice constant). Horizontal dotted lines give values of $2W^2$.

Figure 5. (a) Schematic of trap sites (open circles) for RDF in 2+1d. Support atoms are dark circles, and in-layer neighbors are gray. Simulated 25ML films in 2+1d for: (b) RDF; (c) DF.

Figure 6. W, κ, Q, and ρ_d versus θ for the RDF model (thick solid line) and the DF model (thin solid line) for 0K growth in 2+1d. All quantities are dimensionless (and ρ_d=0 for DF).

Figure 7. (a) Schematic of U&O and U&B models in 1+1d. The inset shows the key "transition state" accessible only in the U&O model. (b) Simulated 25ML films for $h/F = 10^{-1}, 10^{0}, 10^{3}$ (shown).

Figure 8. W, κ, Q, and ρ_d versus h/F for 25ML films for the U&O model (small open symbols) and the U&B model (small closed symbols) in 1+1d. All quantities are dimensionless.

Figure 9. Schematic of low-barrier interlayer hops in 2+1d, together with the associated barriers.

Figure 10. Simulated 25ML films for 20K, 50K, 80K, 130K (shown) for the U&O and U&B models in 2+1d.

Figure 11. W, κ, Q, and ρ_d versus T for 25ML films for the U&O model (open small symbols) and the U&B model (closed small symbols) in 2+1d. Experimental data for Ag/Ag(100) is also shown (large closed circles). All quantities are dimensionless.

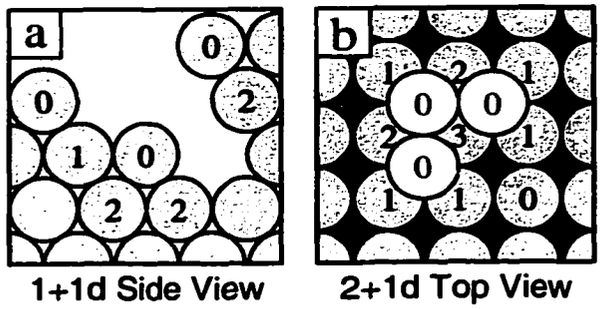

Figure 1

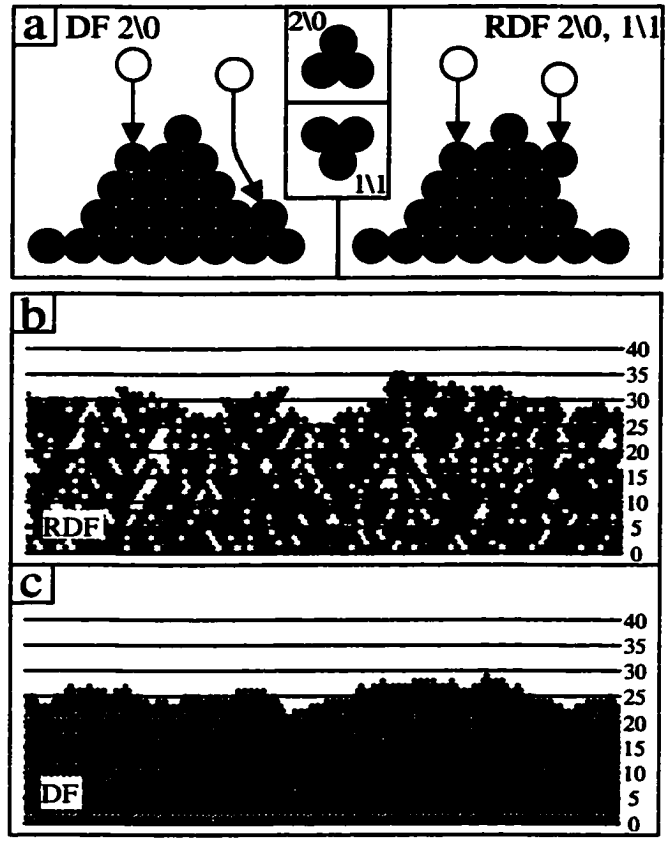
a
DF 2\0
2\0
1\1
RDF 2\0, 1\1
b
40
35
30
25
20
15
10
5
0
RDF
c
40
35
30
25
20
15
10
5
0
DF

Figure 2

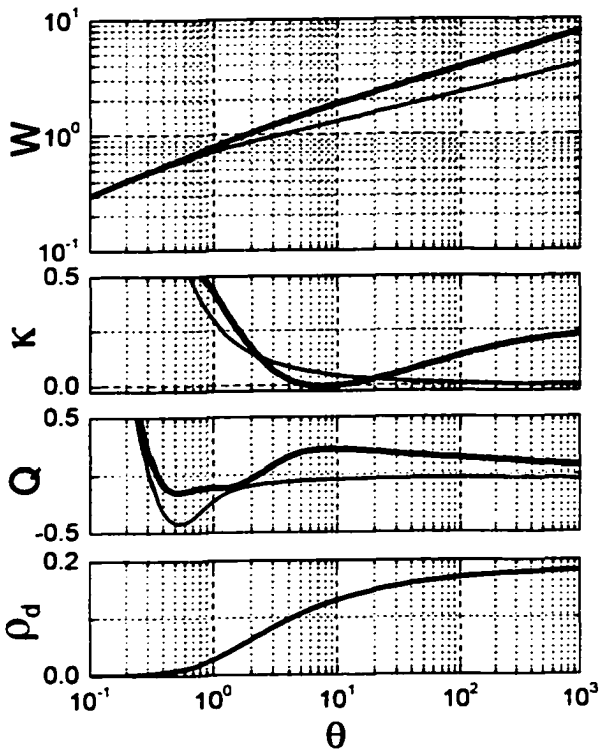

Figure 3

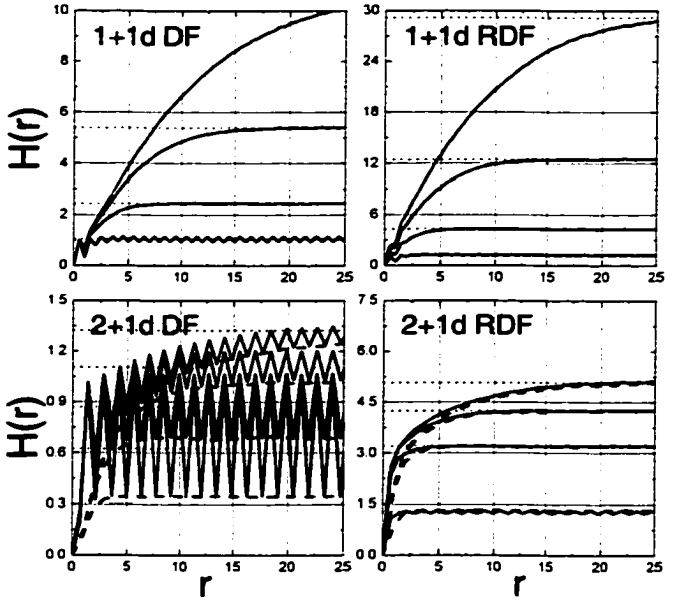

Figure 4

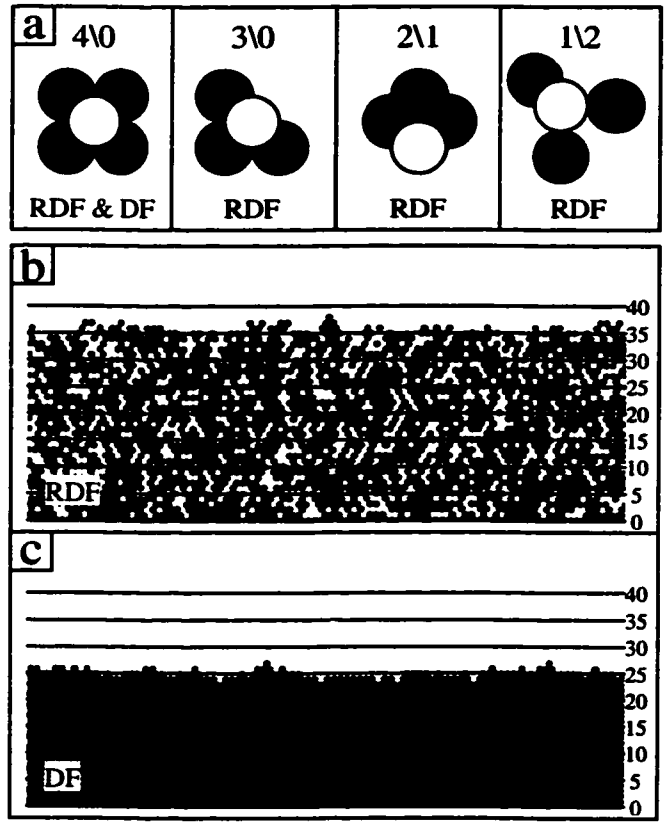
a
4\0
3\0
2\1
1\2
RDF & DF
RDF
RDF
RDF
b
40
35
30
25
20
15
10
5
0
RDF
c
40
35
30
25
20
15
10
5
0
DF

Figure 5

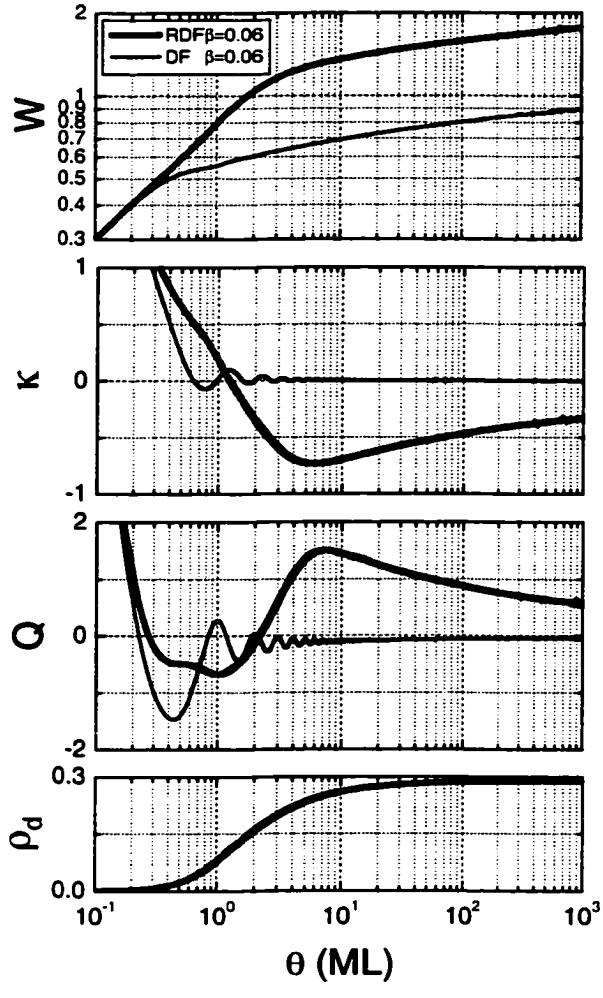

Figure 6

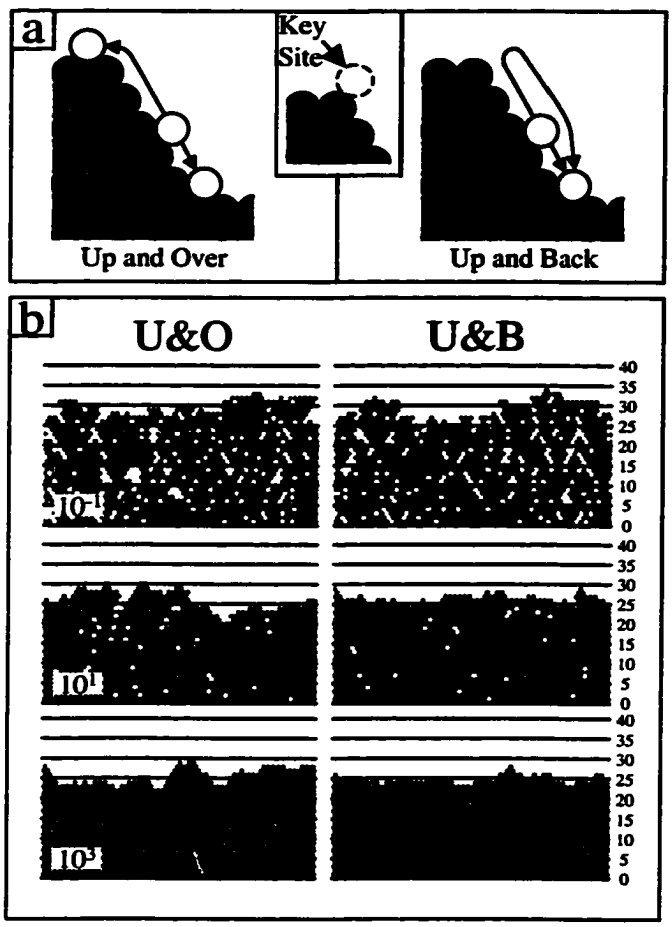
a
Key
Site
Up and Over
Up and Back
b
U&O
U&B
10-1
10-2
10-3
40
35
30
25
20
15
10
5
0

Figure 7

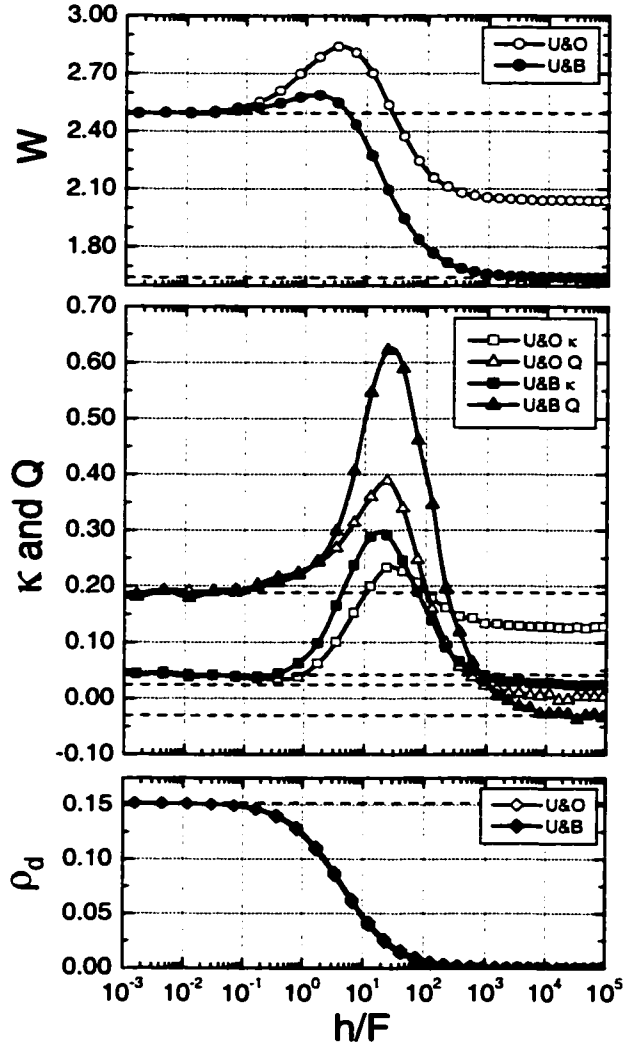
3.00
2.70
2.40
2.10
1.80
W
U&O
U&B
0.70
0.60
0.50
0.40
0.30
0.20
0.10
0.00
-0.10
κ and Q
U&O κ
U&O Q
U&B κ
U&B Q
0.15
0.10
0.05
0.00
ρd
U&O
U&B
10-3 10-2 10-1 100 101 102 103 104 105
h/F

Figure 8

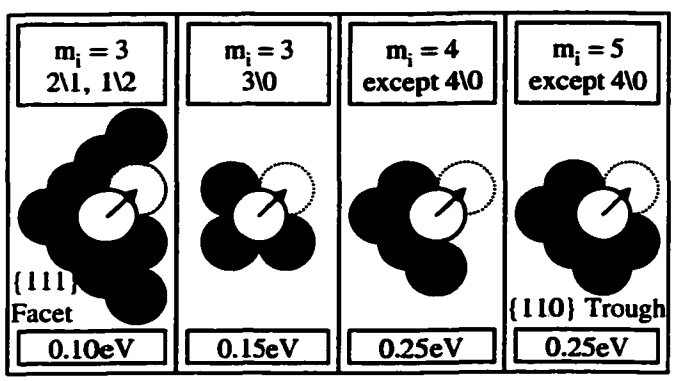
$m_i = 3$
2\1, 1\2
$m_i = 3$
3\0
$m_i = 4$
except 4\0
$m_i = 5$
except 4\0
{111}
Facet
{110} Trough
0.10eV
0.15eV
0.25eV
0.25eV

Figure 9

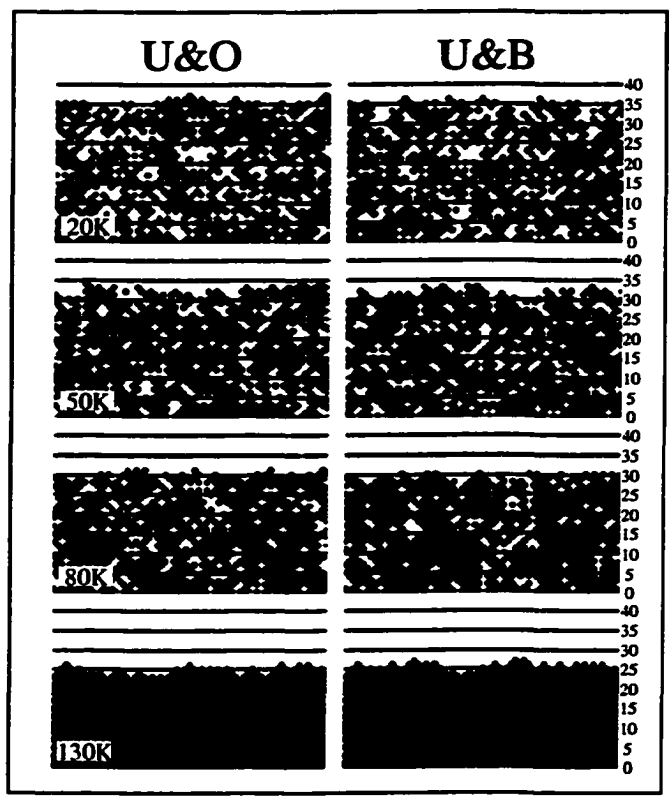

Figure 10

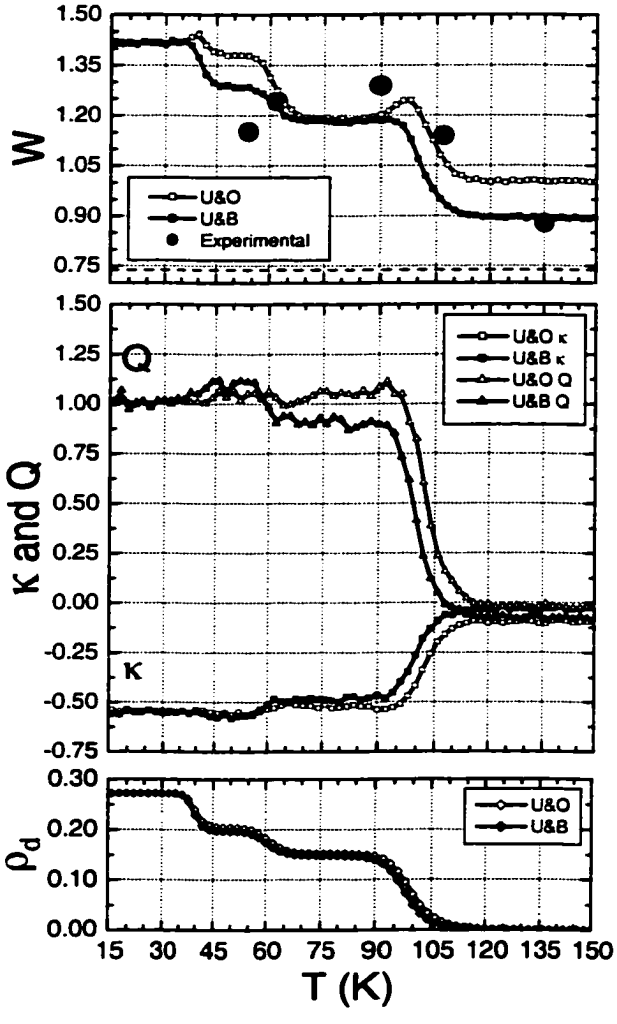

Figure 11

3. APPROACHING THE LOW TEMPERATURE LIMIT IN NUCLEATION AND GROWTH OF FCC(100) METAL FILMS – AG/AG(100).

A paper submitted to Physical Review B.

S. Frank, H. Wedler, and R.J. Behm

J. Rottler and P. Maass,

K.J. Caspersen, C.R. Stoldt, P.A. Thiel, and J.W. Evans

Abstract

We analyze the formation of two-dimensional Ag islands following deposition of about 0.1 ML of Ag on Ag(100) between 125K and 300K. Particular emphasis is placed on the post-deposition dynamics at lower temperatures, where the saturation island density is not reached at the end of the deposition and nucleation and aggregation processes continue with adatoms from the remaining adatom gas. Our analysis combines VT-STM experiments with Kinetic Monte Carlo simulation of appropriate atomistic models. The only adjustable parameters in the model are the terrace diffusion barrier and prefactor, which can be determined from island density behavior near room temperature. Other processes such as rapid edge diffusion, and "easy" nucleation and aggregation of diagonally adjacent adatoms, are treated as instantaneous. Nonetheless, the model excellently reproduces all aspects of behavior at low temperatures, demonstrating that nucleation and growth processes can be described in one consistent scheme, down to the regime of almost immobile adatoms.

1. Introduction

The early stages of nucleation and growth of ultrathin metal films have been investigated with increasing detail over the last decade (see [1,2]). Atomistic properties such as hopping barriers for isolated adatoms, and the influence of adjoining steps, corners, or adatom-adatom interactions on these barriers, have been determined from a quantitative analysis of island densities, sizes and shapes as a function of deposition temperature, flux, and coverage. Such experimental studies mostly utilize Scanning Tunneling Microscopy (STM). These results are interpreted by comparison with predictions from theoretical models.

Traditionally, theoretical modeling begins by considering the formation of islands with a critical island size i, i.e., aggregates composed of more than i adatoms are stable. The time evolution of the mean island density, N, is given by a set of mean-field rate equations (see, e.g., ref. [3]). Such modeling has its limitations: monomers are usually assumed to be the only mobile species; longer-range attraction of adatoms to island edges are neglected: island sizes and shapes are accounted for only approximately in the capture numbers for diffusing adatoms (or only via the coverage dependence of the average capture number), key correlations in the island distribution are not incorporated, etc. Recently, a variety of realistic lattice gas models have been analyzed in great detail using Kinetic Monte Carlo (KMC) simulations [2]. Such modeling can readily incorporate such features as dimer mobility [4,5], longer-range attractions [6], and adatom detachment from larger islands of all sizes [7], or explicitly model island shapes by including adatom mobility along island edges and around corners [8-10]. They allow an increasingly more realistic characterization of the actual film

growth process, which correctly describes subtle correlations between island sizes and separations, as well as the island size distribution [11].

Somewhat neglected, however, were the effects that come into play when the growth process approaches the limit of low temperatures (T). This occurs when the adatom mobility is slowed down so much that the supersaturation density of adatoms (due to deposition) is not reduced to its equilibrium value until long after deposition ceases, and saturation of the island density during deposition is reached only at relatively high coverages. Traditionally, this regime is excluded by limiting the studies to the regime of sufficient adatom mobility, as determined by the condition $h/F>10^5$, with h denoting the hop rate for terrace diffusion, and F the adatom deposition rate [1]. Brune and coworkers recently reported on these low temperature effects in Ag/Pt(111) [6] and Cu/Ni(100) [12] heteroepitaxy, and also performed theoretical analyses.

These authors introduced the terms post-deposition nucleation and post-deposition growth [13]. In the former case, some monomers still present after the end of the deposition will undergo further nucleation events, increasing the number of stable islands after deposition is finished, while the rest of the monomers aggregate with existing islands. In the latter case, all these monomers attach to existing islands, so the monomer density will decay with time, with the island density remaining constant. We note that post-deposition nucleation is connected in a simple way to saturation of the island density. If this density has saturated during deposition, further nucleation is insignificant for continuing deposition, and even more so if deposition is terminated (at least for constant T). Hence, post-deposition nucleation is only possible if the deposit has not reached its saturation island density, unless T is lowered after deposition.

In the present paper, we report and discuss results of a combined experimental and theoretical study on low temperature effects on the homoepitaxial growth on Ag(100). We employ variable temperature scanning tunneling microscopy (VT-STM), as well as KMC simulations. Specifically, we present a detailed quantitative investigation of the post-deposition dynamics (absent in previous studies), incorporating the effects of a post-deposition temperature quenching, and highlighting the sensitivity of this dynamics to the terrace diffusion rate. The Ag/Ag(100) system has been extensively studied in the past [14], testing fundamental ideas about submonolayer nucleation [15], multilayer kinetic roughening [16,17], and post-deposition relaxation [18-20]. Thus, basic aspects of the growth process are established [15]: island formation during deposition is irreversible (i=1) below 320 K; dimer diffusion does not play a significant role in this process; and the activation energy and prefactor for terrace diffusion were determined (although new data in this study allows the most accurate assessment of these key parameters). This information provides a rigorous test for the present study, since any physically reasonable modeling of the low temperature behavior must also reproduce the higher temperature growth characteristics (cf. ref.[21]).

The paper will be organized as follows. After a brief account of the experimental and calculational procedures, we first illustrate temperature effects on the nucleation behavior in the temperature range between 125 K and 300 K with a sequence of STM images. We then focus on the relaxation of the monomer and island density with time, after deposition was stopped. This reveals the time scale of the relaxation process as compared to typical experimental times, in particular the time between the end of deposition and the start of the STM measurement. In the next section, we follow the evolution of monomer and island densities with coverage in order to obtain reliable measures of the minimum coverage

required for the island densities to saturate at 125K. We then evaluate the temperature dependence of the island density, including possible effects due to subsaturation coverages or post-deposition growth and post-deposition nucleation. The results will be discussed in light of KMC simulation results for a fairly simple atomistic model, which nonetheless successfully captures all the essential features of the deposition and relaxation processes.

2. Experimental and Model Details

University of Ulm, which is described in detail elsewhere [22]. In brief, it is equipped with a home-built beetle type STM designed for operation at various temperatures in the range from 115 K up to 500 K, and standard techniques for surface preparation and characterization. These include Low Energy Electron Diffraction (LEED), X-ray Photoelectron Spectroscopy (XPS), Auger Electron Spectroscopy (AES) and low energy Ion Scattering Spectroscopy (ISS). Liquid N2 cooling and radiative heating of the sample back face allowed the sample temperature to be varied between 115 and 500 K while tunneling, with the temperature being directly measured at the sample.

STM images were recorded at constant current, typically at tunnel currents around 1 nA and tunnel voltages between 0.5 and 1 V. This way tip induced effects are minimized, which is particularly important for small islands. Island sizes and coverages were generally determined by using the FWHM of the islands. For comparison, other methods were also employed in selected cases. Although this procedure removes tip effects in STM imaging to a large extent, it may slightly overestimate the size of small islands. STM images are presented as gray level top view presentations, with brighter shades corresponding to higher levels. Absolute heights are accessible from the mostly monolayer height steps.

The Ag(100) single crystal was prepared by repeated cycles of Ar^+ ion sputtering (1.2 keV) and subsequent annealing at temperatures of about 850 K, until STM images revealed a well ordered topography with terraces of several hundred angstroms width, and no contaminants could be detected spectroscopically or in STM. Ag was evaporated from a Knudsen cell, typically using a flux of about 0.006 ML/s [1 ML (monolayer) is equivalent to a full (1×1) layer], which were calibrated against STM-determined coverages of submonolayer Ag films.

The simulations were performed both at the University of Konstanz and Iowa State University, using models that are slightly different in detail, but which agree in their basic characteristics [23-25]. The common philosophy is the use of models which are as simple as possible, but yet capture the essential features of the physical process (as determined from previous experiments [15]). Specifically, they incorporate irreversible (or effectively irreversible) nucleation and growth of islands mediated by terrace diffusion of atoms deposited on the substrate, and by direct deposition of atoms on top of islands. Mobility of dimers and other small clusters is neglected, as it is not significant during deposition. Island growth was described by placing adatoms which land on top of islands, or which diffuse across the substrate to island edges, immediately at an edge site of highest coordination. Although this computationally efficient scheme does not incorporate the distinct finite rates for various edge diffusion processes, it does accurately describe island structure and growth since edge mobility in this system is far higher than terrace mobility [26]. Specifically, it leads to the observed compact island shapes, and avoids the formation of ramified island structures, which have a higher propensity for capturing mobile adatoms.

Various refinements to the above modeling are possible. For example, we will typically allow adatoms reaching sites either nearest-neighbor (NN) or diagonal (i.e., next) nearest-neighbor (NNN) to other adatoms to immediately nucleate or aggregate (whereas NN sites must be reached in the "canonical" models above). This choice reflects the feature that according to semi-empirical studies of energetics in metal(100) homoepitaxial systems, the activation barrier for hopping from NNN to NN sites is far below the barrier, E_h, for terrace diffusion [27-29]. The above can be regarded as a specialized version of "easy attachment" at island edges utilized in modeling of the Ag/Pt(111) system by Brune et al. [6]. In that system, hopping towards step edges was considered to be enhanced. In our case only attachment at corners is enhanced, since the above semi-empirical studies indicate no significant reduction in the activation barrier for hopping towards step edges (from sites two lattice constant away). It should also be remarked that enhanced nucleation is perhaps more important than enhanced attachment in our model. In any case, we emphasize that the behavior in our model is controlled by a single parameter h/F. In fact, the behavior right at the end of deposition can be extracted from previous studies [23], although refined simulations which continue to model surface diffusion processes after deposition has stopped are required to fully explore post-deposition effects. Based on previous room-temperature studies of Ag/Ag(100) growth [15], we write the hop rate (per direction) for terrace diffusion as $h=\nu\cdot\exp[-E_h/(k_B\cdot T)]$, and choose $E_h=0.40$ eV and $\nu=5\cdot10^{12}$ sec^{-1} [30].

A contrasting philosophy is adopted by Furman et al. [29,31], who utilize more complex models for submonolayer deposition incorporating a large set of hopping barriers from semi-empirical analysis (or incorporating some reduced version of these). However, for metal(100) homoepitaxial systems in the regime of irreversible formation of compact islands,

the actual values of most of these parameters are not important. Thus, we prefer our simpler modeling approach that focuses on the essential processes and parameters (estimating the latter by comparison with experimental observations).

3. Results

The influence of temperature on the submonolayer growth behavior in Ag(100) homoepitaxy below room temperature is illustrated in a sequence of STM images in Fig.1. The images were recorded after deposition at various temperatures (T) between 180 K and 300 K, at a deposition rate of 0.006 ML/sec, and subsequent quench to 120 K. The deposit amounts to 0.1 monolayers (ML) as determined by STM. In all cases, the islands are of a monolayer height, with no evidence for any second layer nucleation. As expected, the island size increases with temperature, while the island density decreases. In the medium and higher T range, the islands assume pronounced square shapes. However, for the small islands obtained below 200K, the islands are still compact, but their shapes are no longer well resolved. Their somewhat frizzy appearance is not likely due to temperature-induced fluctuations in the island edge positions at this low T. Instead, their appearance is probably caused by interaction with the tip.

A quantitative evaluation of the island density is presented in Fig.2, where the logarithm of the island density, derived from a large number of similar images, is plotted against the inverse deposition temperature. The broken line, with a slope equivalent to the hopping barrier of Eh = 0.40 eV determined previously, represents an excellent fit to the data points above 180K, while at lower temperatures the experimental values bend over to lower island densities than expected. Hence, traditional mean-field nucleation theory using parameters determined previously from behavior for higher T provides a good description for

the growth behavior above 180K. The deviations at lower temperatures are tentatively assigned (primarily) to post-deposition effects. These lead to low T deviations in the island density similar to those observed for other systems [1,6,12]. The extent of these deviations, however, has to be quantified, and should be consistent with the high T growth behavior and with the atomistic quantities derived previously.

In order to assess the time scale of the relaxation processes possible after the deposition was stopped, we followed the evolution of the island and monomer density with time, during deposition and for 3600 s after deposition. The KMC simulations in Fig.3 show the island density (dashed line) and the combined island-plus-monomer density (full line) as a function of time for two different deposition temperatures, 152 K (Fig.3a) and 128 K (Fig.3b). The monomer density is given by the difference between these two curves. Experimental data are included as filled points. In both cases, T was kept constant after deposition. A dotted vertical line marks the end of the deposition. At T=152 K, the simulations show that the monomer density declines rapidly and has effectively vanished after 50 sec. The island density, on the other hand, does not vary much during this time, causing the island-plus-monomer density to decline slightly during the first 50 sec., and then stay constant. Hence, the monomers still present after deposition largely attach to existing islands. The time dependence found in these simulations fits well to the experimental data obtained in a sequence of STM images, which show that the experimentally determined island density is practically constant over the time it was recorded, starting about 30 min after deposition. (Fluctuations in the data result from the fact that for each data point only a single STM image could be evaluated.) Thus, at 152 K, the monomer decay after deposition occurs

practically exclusively via attachment to existing islands, i.e., via post-deposition growth processes.

The behavior for the lower deposition temperature of 128 K looks quite different. After deposition (t_{dep}=12 sec, F=0.0042 ML/sec, θ_{dep}=0.1 ML), the monomer density decays much more slowly, in agreement with expectations. Now the monomer decay leads to a significant increase in island density, by a factor of roughly two. Hence, a significant fraction of the monomers were engaged in nucleation events (about 50% based on simulations), the remaining fraction being consumed by growth of existing or new islands. Correspondingly, at these temperatures, post-deposition nucleation plays an important role. The decay in island-plus-monomer density in the later stages of growth is reflected also by the experimental data points, which were again taken starting about 30 min after deposition was stopped. Despite the scatter in the data (see above), this combined density exhibits a clear downward trend, roughly by about a factor of two over the observation period of 30 min. Also, in this case, much of the monomer diffusion had occurred before the STM observations was started, but even after that monomer mobility still leads to appreciable changes in the film morphology. Most important, in both cases experimental data agree with simulations of atomistic models using parameters based on high temperature growth characteristics.

In a next step, we want to evaluate the influence of post-deposition processes also in the intermediate temperature range between 180 K (where the high temperature limit seems to be reached), and around 120 K (where time-resolved STM measurements can resolve the changes in island-plus-monomer density in these processes). This was done by mirroring the experimental process in the simulations: deposition was performed at a specified T_{dep}, and

after deposition, the temperature was lowered to a final lower T_{fin}, mimicking the quench process. The temperature decay was modeled by an exponential decay function, $T(t)=T_{fin}+(T_{dep}-T_{fin})\cdot\exp(-k\cdot t)$, with the decay constant being $k=0.008$ sec^{-1} in order to reproduce the average cooling behavior.

Using this temperature program, the growth process was simulated in the same way as described before for the simulations at constant temperature in Fig.3. The temporal evolution of the island density (dashed curves), and island-plus-monomer density (full curves) for different deposition temperatures between 125 K and 180 K is shown in Fig.4 (F=0.006 ML/sec, θ_{dep}=0.1 ML). Upon decreasing T, two trends become apparent: the time-scale for post-deposition processes increases strongly, and the island density by the end of deposition remains well below its saturation value.

The nature of the post-deposition dynamics is readily understood. Consider first the simpler cases of an infinitely fast quench or no quench, where the only process active in the temperature regime considered is monomer hopping at a constant rate, h. The characteristic time, t_c, for relaxation is such that the monomer diffusion length, $(ht_c)^{1/2}$, equals the mean distance, L_{NN}, to the or island nearest monomer. (L_{NN} is controlled by the mean island separation except for very low T where the monomer density is high, so their separation is low.) Changing the temperature, in the absence of deposition, just slows down or enhances the monomer mobility, but will not affect the relative rates of competing processes (within the limits of the present model). Hence, the temperature quench leads to a distortion of the time scale, as compared to an infinitely fast or no quench, but does not alter the final outcome of the relaxation process.

Another effect to be considered in low temperature deposition is the increasing coverage required for reaching the saturation island density. Hence, a coverage of 0.1 ML, which is experimentally convenient because the islands are still well separated, may be too low to reach the saturation island density at the low T considered here. This question can be answered by looking at the simulation data shown in fig. 4. In the high T limit, the increase of the island density with coverage becomes very small (which is equivalent to being close to or at the saturation island density). However, this is no more the case at temperatures $\leq$ 160 K. The steep slope of the island density at 0.1 ML clearly indicates that under these conditions the saturation island density is not reached, leading to deviations from the 'ideal' high temperature behavior as observed in Fig.2.

Comparison with experimental data can be made in a set of experiments, where increasing amounts of Ag, up to 0.09 ML, were deposited at temperatures around 125 K and at a fixed, rather low, deposition rate (F=0.000695 ML/sec). The resulting island-plus-monomer densities are given as filled dots in Fig.5. For the related simulations, we considered that after deposition, the sample remained practically at the deposition temperature, and was analyzed between 1 and 4 hours later. Therefore, the simulations included a waiting time of 1 hour after the deposition was stopped, at the temperature of the respective experiment (In reality, the sample may cool down slightly during that waiting time to temperatures between 125 K and 120 K. Because of the ill-defined final temperature, we did not include this in the simulations.) The deposition/measurement temperatures and coverage values are tabulated in Table 1. Incorporating NNN (rather than just NN) attachment, as described in the experimental and modeling section, the simulation data provide an excellent fit to the observed island density, given the statistical uncertainty. (The

latter can be assessed from the distance between the two experimental points at 0.054 ML, where the deposition conditions were identical.) Overall, the different tests described so far yielded very good agreement between experimental data and simulations, which allowed for post-deposition effects, but otherwise used the same parameters and model characteristics as used previously for describing the higher temperature nucleation and growth behavior.

Based on these results we finally return to the analysis of the temperature-dependence of the experimental island-plus-monomer densities (Fig.2), which are replotted in Fig.6 as filled dots. These densities were simulated: a) directly after deposition (dashed curves in Fig.6); and b) after a waiting time of 3600 sec where the sample was allowed to cool down, following the temperature-time relation described above (solid curves in Fig.6). We also compare simulation results for NNN aggregation (thick curves), and just NN aggregation (thin curves). Also shown in the inset are the simulation results for the maximum island density (dashed line) obtained by continued deposition [32]. It is clear that the deviation of experimental data from the Arrhenius line starting at temperatures < 180K is mainly attributable to post-deposition effects, specifically to a decrease in the island-plus-monomer density due to aggregation of monomers. The data which do include post-deposition processes represent an almost ideal fit to the experimental data (for either NN or NNN aggregation). For very low temperatures, the deviation from Arrhenius behavior reflects a transition to statistical growth behavior (i.e., a random distribution of occupied sites): the solid horizontal line represents the corresponding value of the island-plus-monomer density at 0.1 ML.

4. Discussion

The high-quality STM data presented above provides the most comprehensive and precise picture available of submonolayer nucleation and growth at low T in the Ag/Ag(100) system. The observations are entirely consistent with a previous high-resolution LEED study of island distributions formed by depositing 0.3 ML of Ag on Ag(100) between 170 K and 295 K [33]. However, noise in the diffracted intensity data limited the accuracy of the assessment of the Arrhenius behavior, and the availability of only reciprocal-space information inhibits a precise assessment of real-space island densities, particularly at lower T.

The fairly simple atomistic modeling above is very successful in providing a coherent description of both the high T behavior and of various aspects of the low T behavior. Modeling is simplified by two features of the Ag/Ag(100) system: the irreversible island formation is in the entire T range, and the insignificant dimer mobility, so the single controlling parameter is h/F. The model results do depend on choices such as the specific rule for aggregation. However, this can be selected based on semi-empirical analyses of the energetics, which show that most processes are either very active or inactive, so actual values of activation barriers are not important.

It is appropriate to note the strong sensitivity of the post-deposition dynamics to temperature. A difference of only 5 K for T around 120 K changes h by a factor of 5, leading to a corresponding rescaling of the relaxation time. For example, there are noticeable differences in the simulated densities in Fig.5 if one allows a post-deposition quench to 120 K. In general, one could ask, how sensitive are the post-deposition processes of diffusion-mediated nucleation and aggregation to fluctuations. Studies of such processes for an initial

random distribution of adatoms have focused on the low-density regime, and reveal anomalous fluctuation-dominated behavior only for reversible island formation (i>1) [34], conditions which are not relevant to our low-T studies.

Another issue of much current interest is the shape of the island size distributions for different nucleation processes. However, most studies suffer from limited experimental statistics, and also from misperceptions regarding theoretical predictions. The density of islands of size s is usually written as $N_s \propto f(s/s_{av})$. A commonly assumed monomodal form [35] of $f \propto x \cdot \exp[-0.27x^{3.7}]$ has f(0)=0, whereas simulations [23] and an exact theory [11] show that f(0)>0. Furthermore, analysis of experiments is complicated by the feature that small islands can disappear quickly after deposition, leading to distributions with $f(0) \approx 0$ [36]. Analysis of rather noisy data for Ag/Ag(100) finds f(0) negligible at higher T (cf. Ref.[15,36]), but increasing significantly by 160 K. This trend towards monotonically decreasing f vs. x with decreasing T has been seen in previous studies, and attributed to post-deposition effects [1]. However, it should be noted that the same trend is clearly apparent in simulations without post-deposition relaxation, being due to deviations for lower h/F from the asymptotic scaling form [23].

Various refinements are still possible in the analysis and modeling. We have neglected dimer mobility during deposition based on asymptotic flux scaling experiments at high T (300 K) [15]. Introducing significant dimer mobility into the modeling one could likely maintain the quality of the fit to the experimental data in Fig.6. This could be achieved by increasing the barrier for monomer diffusion and at the same time introducing dimer (or trimer) diffusion), so as to maintain the measured island density at 300 K. In that case one would also have to consider the effect of dimer mobility for post-deposition processes, but its

effect should be less significant than during nucleation. For test purposes we have inhibited corner rounding of atoms at island edges to explore the effects of more ramified islands [25], but this is found to have little effect in the present system. Finally, one could incorporate a possible T-dependence in the prefactor for adatom hopping, but this dependence is expected to be weak [37].

5. Conclusions

Based on comparative VT-STM experiments and KMC simulations of a simple atomistic model for metal-on-metal epitaxy, we have shown for a test system, Ag/Ag(100), that the basic processes and parameters derived for modeling high temperature growth give a correct description also of the behavior in the low temperature limit, close to adatom immobility. The considerable deviations of the island-plus-monomer densities obtained at these low temperatures from a simple Arrhenius behavior can be quantitatively explained by properly accounting for post-deposition processes, specifically post-deposition nucleation and post-deposition growth. Time-dependent variations in the low temperature island-plus-monomer density, and the evolution of these properties with coverage, can also be quantitatively reproduced by simulations. This extends the regime accessible for nucleation and growth studies far beyond the regime of $h/F>10^5$ considered in most previous studies. It allows the description of nucleation and growth processes in one consistent scheme, down to the regime of almost immobile adatoms.

Acknowledgements

SF gratefully acknowledges a fellowship of the Deutsche Forschungsgemeinschaft (DFG) within the Graduiertenkolleg 'Molekulare Organisation und Dynamik an Grenz- und Oberflächen', and P.M. thanks the DFG for a Heisenberg fellowship. Financial support for

the work in Konstanz came from the DFG via Sonderforschungsbereich 513 (Nanostrukturen an Grenz- und Oberflächen). CRS, KJC, PAT and JWE were supported for this work by NSF Grant CHE-0078596. Their work was performed in the facilities of the Ames Laboratory, which is operated for the U.S. Department of Energy (U.S. DOE) by Iowa State University under Contract No. W-7405-Eng-82.

References

[1] H. Brune, Surf. Sci. Rept. **31**, 121 (1998).

[2] Morphological Organization in Epitaxial Growth and Removal, Z. Zhang and M.G. Lagally, eds. (World Scientific, Singapore, 1998)

[3] J.A. Venables, Philos. Mag. **27**, 697 (1974); S. Stoyanov, K. Kaishiev, Curr. Topics Mater. Sci. **7**, 69 (1981).

[4] S. Liu, L. Bönig, H. Metiu, Phys. Rev. B. **52**, 2907 (1995).

[5] M.C. Bartelt, S. Günther, E. Kopatzki, R.J. Behm, J.W. Evans, Phys. Rev. B **53**, 4099 (1996).

[6] H. Brune, G.S. Bales, J. Jacobsen, C. Boragno, K. Kern, Phys. Rev. B **60**, 5991 (1999).

[7] C. Ratsch, A. Zangwill, P. Smilauer, D.D. Vvedensky, Phys. Rev. Lett. **72**, 3194 (1994).

[8] M. Hohage, M. Bott, M. Morgenstern, Z. Zhang, T. Michely, G. Comsa, Phys. Rev. Lett. **76**, 2366 (1996).

[9] H. Brune, H. Röder, K. Bromann, K. Kern, J. Jacobsen, P. Stoltze, K. Jacobsen, J. Norskov, Surf. Sci. **349**, L115 (1996).

[10] A. Bogicevic, J. Strömquist, B.I. Lundqvist, Phys. Rev. Lett. **81**, 637 (1998).

[11] M.C. Bartelt, J.W. Evans, Phys. Rev. B **54**, R17359 (1996).

[12] B. Müller, L. Nedelmann, B. Fischer, H. Brune, K. Kern, Phys. Rev. B **54**, 17858 (1996).

[13] These authors used the term post-nucleation rather than post-deposition nucleation.

[14] P.A. Thiel, J.W. Evans, J. Phys. Chem. **104**, 1663 (2000).

[15] C.-M. Zhang, M.C. Bartelt, J.-M. Wen, C.J. Jenks, J.W. Evans, P.A. Thiel, Surf. Sci. **406**, 78 (1998).

[16] W.C. Elliott, P.F. Miceli, T. Tse, P.W. Stephens, Phys. Rev. B **54**, 17938 (1996).

[17] C.R. Stoldt, K.J. Caspersen, M.C. Bartelt, C.J. Jenks, J.W. Evans, P.A. Thiel, Phys. Rev. Lett. **85**, 800 (2000).

[18] J.-M. Wen, J.W. Evans, M.C. Bartelt, J.W. Burnett, P.A. Thiel, Phys. Rev. Lett. **76**, 652 (1996).

[19] W.W. Pai, A.K. Swan, Z. Zhang, J.F. Wendelken, Phys. Rev. Lett. **79**, 3210 (1997).

[20] C.R. Stoldt, A.M. Cadilhe, C.J. Jenks, J.-M. Wen, J.W. Evans, P.A. Thiel, Phys. Rev. Lett. **81**, 2950 (1998).

[21] M. Bott, M. Hohage, M. Morgenstern, T. Michely, G. Comsa, Phys. Rev. Lett. **76**, 1304 (1996).

[22] S. Günther, Ph.D. dissertation, Universität Ulm (1995).

[23] M.C. Bartelt, J.W. Evans, Surf. Sci. **298**, 421 (1993).

[24] S. Heinrichs, J. Rottler, P. Maass, Phys. Rev. B **62**, 8338 (2000).

[25] K.J. Caspersen, C.R. Stoldt, A.R. Layson, M.C. Bartelt, P.A. Thiel, J.W. Evans, Phys. Rev. B, **63**, 085401 (2001).

[26] B.D. Yu, M. Scheffler, Phys. Rev. Lett. 77, 1095 (1996); Phys. Rev. B 55, 13916 (1997).

[27] A.F. Voter, Proc. SPIE **821**, 214 (1987)

[28] M. Langelaar, Ph.D. dissertation, University Groningen (1998).

[29] H. Mehl, O. Biham, I. Furman, M. Karimi, Phys. Rev. B **60**, 2106 (1999).

[30] We previously set =11013 s-1 [14, 25] which slightly better matches higher temperature behavior, but either choice is consistent with data here.

[31] I. Furman, O. Biham, J.-K. Zuo, A.K. Swan, J.F. Wendelken, Phys. Rev. B **62**, R10649 (2000).

[32] By monitoring the density of islands (islands plus monomers) versus coverage for the NNN aggregation model, we determine the coverage, max, of maximum density for each T or h/F. We use a percolation theoretic analysis of densities based on NN connectivity. For just islands, we find that max= 0.26 at 100 K, decreasing to 0.16 at 185 K, and slowly increasing to 0.20 by 300 K. For islands-plus-monomers, one has max= 0.19 at 100K, decreasing to 0.15 at 160K, and slowly increasing to 0.20 by 300 K.(, 2000)

[33] L. Bardotti, C.R. Stoldt, C.J. Jenks, M.C. Bartelt, J.W. Evans, P.A. Thiel, Phys. Rev. B **57**, 12544 (1998).

[34] J. Li, G. Rojo, L.M. Sander, Phys. Rev. Lett **78**, 1747 (1997).

[35] J.G. Amar, F. Family, Phys. Rev. Lett **74**, 2066 (1995).

[36] C.R. Stoldt, C.J. Jenks, P.A. Thiel, A.M. Cadilhe, J.W. Evans, J. Chem. Phys. **111**, 5157 (1999).

[37] U. Kürpick, T.S. Rahman, Phys. Rev. B **57**, 2482 (1998).

Table Captions

Table 1. Coverage, island density and deposition/measurement temperature for the measurements and simulations displayed in fig. 5.

Figure Captions

Figure 1. Sequence of STM images of size 25×25 nm^2 recorded after deposition at the temperatures indicated (F=0.006 ML/sec, θ_{dep}=0.1 ML).

Figure 2. Experimentally determined island-plus-monomer densities (•) at different temperatures. The broken line indicates the Arrhenius slope of $E=E_h/3$, for E_h=0.40 eV and a critical cluster size of i = 1 (F=0.006 ML/s, θ_{dep}=0.1 ML).

Figure 3. Simulated time evolution of the island density (dashed curve), and island-plus-monomer density (full line) at two different temperatures, comparing simulations for the model with NNN aggregation with experimentally determined island-plus-monomer densities (points). a) Deposition (ca. 0.1 ML, t_{dep}=16.6 sec, so F=0.006 ML/s) and subsequent STM measurement at 152 K; b) deposition (0.05 ML, t_{dep}= 12 sec, so F=0.0042 ML/sec) and STM measurements at 128 K.

Figure 4. Simulated time evolution of the island density (dashed curve), and island-plus-monomer density (full curve) for the model with NNN aggregation for deposition at different temperatures, between 120 K and 180 K (F=0.006 ML/sec, t_{dep}=16.6 sec, θ_{dep}=0.1 ML), and subsequent quench to 120 K. During the quench the temperature evolution was modeled by an exponential decay, with $T(t)=T_{fin}+(T_{dep}-T_{fin})\cdot\exp(-k\cdot t)$, with T_{dep} being the temperatures before the quench, T_{fin}=120 K, and k set to 0.0008 sec^{-1}.

Figure 5. Comparison of simulated (x) and experimental (•) island densities at a constant deposition rate F = 0.000695 ML/sec for different coverages and varying deposition/measurement temperatures around 125 K, accounting for post-deposition processes during a waiting period of 3600 sec at the deposition temperature. Exact coverages and temperatures are indicated in Table 1. The above simulations with varying T include

NNN aggregation. The corresponding results for fixed temperature of 125K are shown as a full curve, and for NN aggregation as a dashed curve.

Figure 6. Comparison of experimental (•) and simulated island-plus-monomer densities at different temperatures (F=0.006 ML/sec, θ_{dep}=0.1 ML): a) directly after deposition (dashed curves); and b) after a waiting time of 3600 sec where the sample was allowed to cool down, following the temperature-time relation described in the text (full curves). We furthermore compare simulation results for NNN aggregation (thick curves), and just NN aggregation (thin curves). The horizontal line corresponds to statistical growth. The inset compares the island-plus-monomer density directly after deposition of 0.1ML (solid curve - corresponding to thick dashed line in the main plot) with its maximum value obtained by continued deposition (dashed curve) for different temperatures in the NNN aggregation model (F=0.006 ML/sec).

Coverage (ML)	Island Density ($Site^{-1}$)	Temperature (K)
4.87E-03	4.10E-03	124
9.38E-03	7.70E-03	121
1.81E-02	1.56E-02	121
1.81E-02	1.42E-02	128
2.71E-02	1.74E-02	126
2.71E-02	1.80E-02	125
3.61E-02	2.31E-02	121
5.42E-02	3.30E-02	124
5.42E-02	3.00E-02	124
7.51E-02	3.89E-02	126
9.04E-02	2.67E-02	128
9.04E-02	4.61E-02	124

Table 1

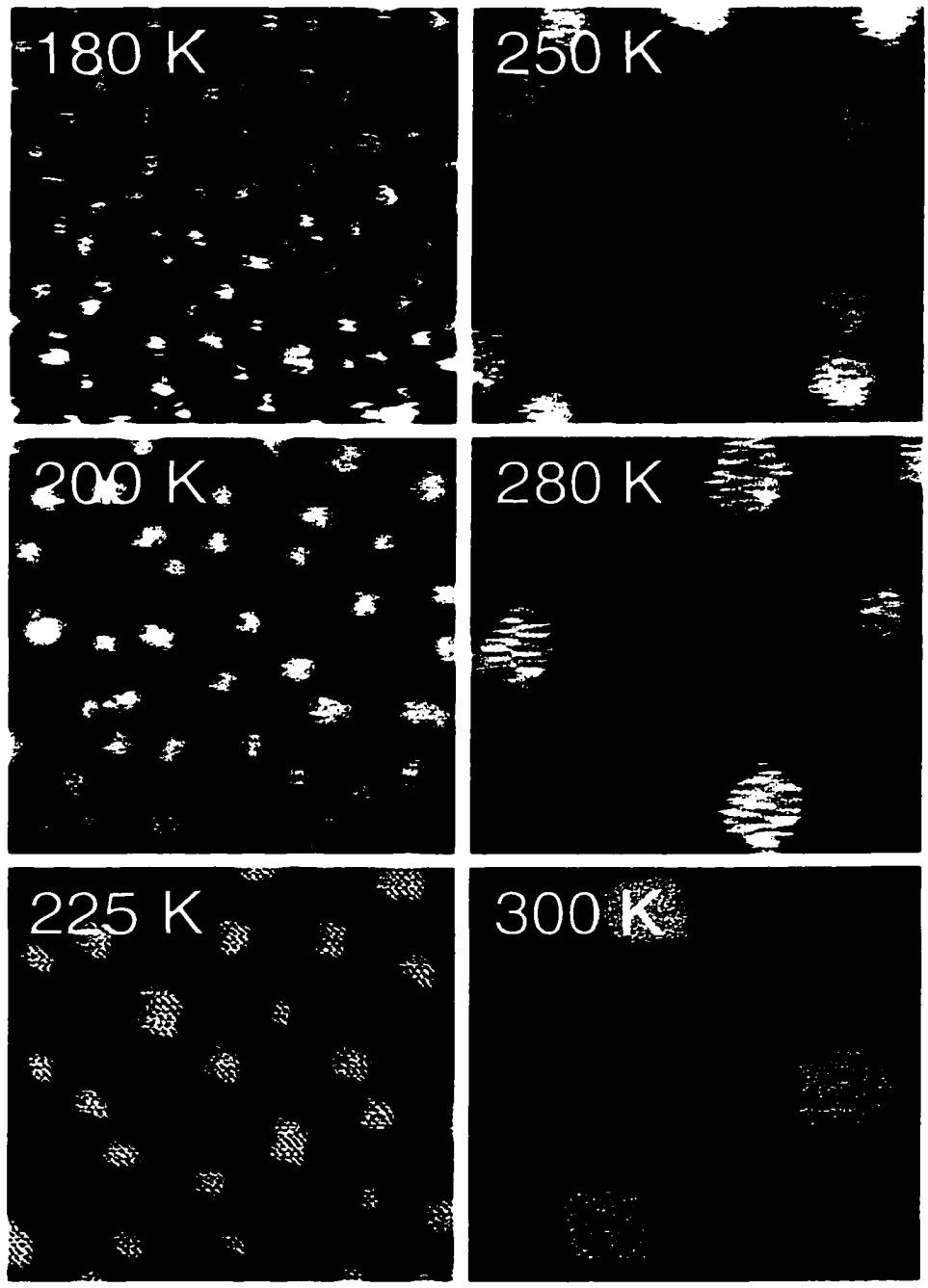

Figure 1

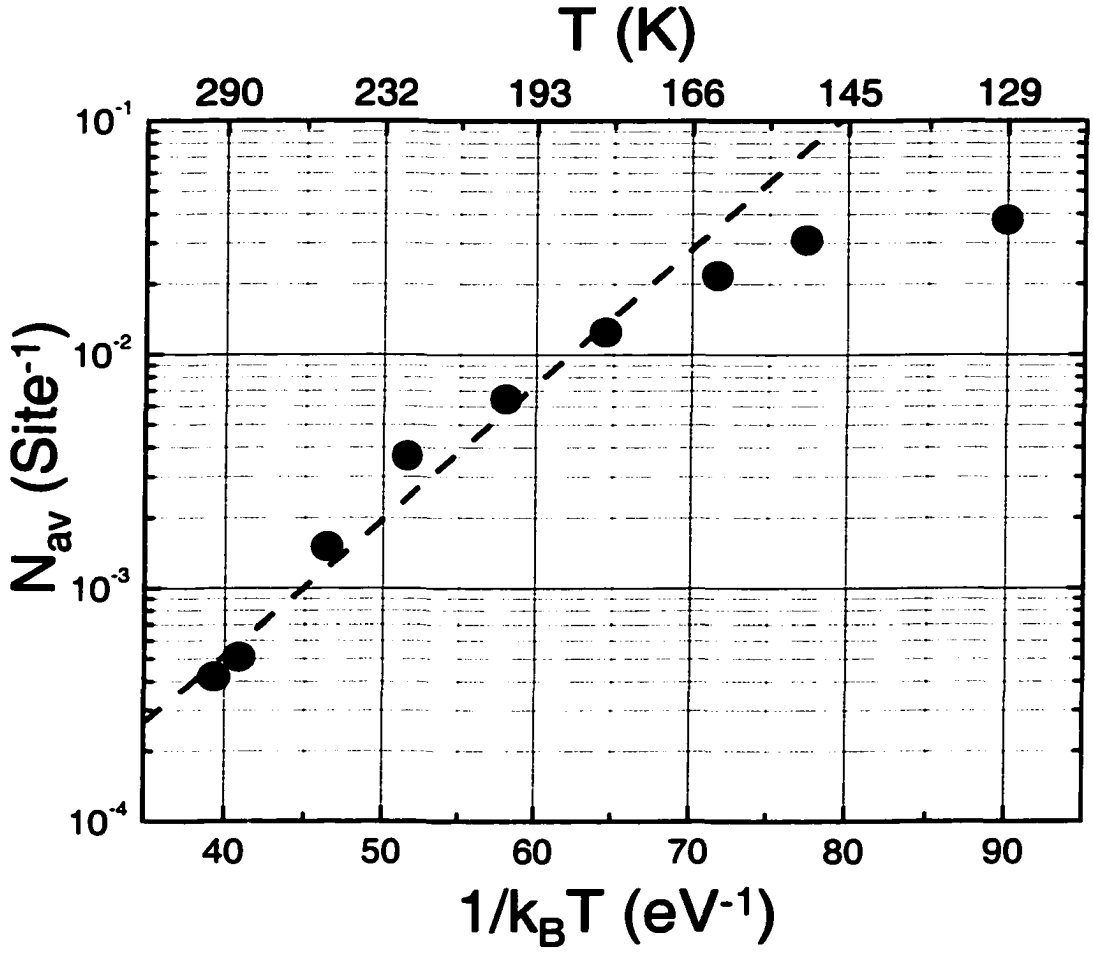
T (K)
290
232
193
166
145
129
10^{-1}
10^{-2}
10^{-3}
10^{-4}
N_{av} (Site^{-1})
40
50
60
70
80
90
$1/k_BT$ (eV^{-1})

Figure 2

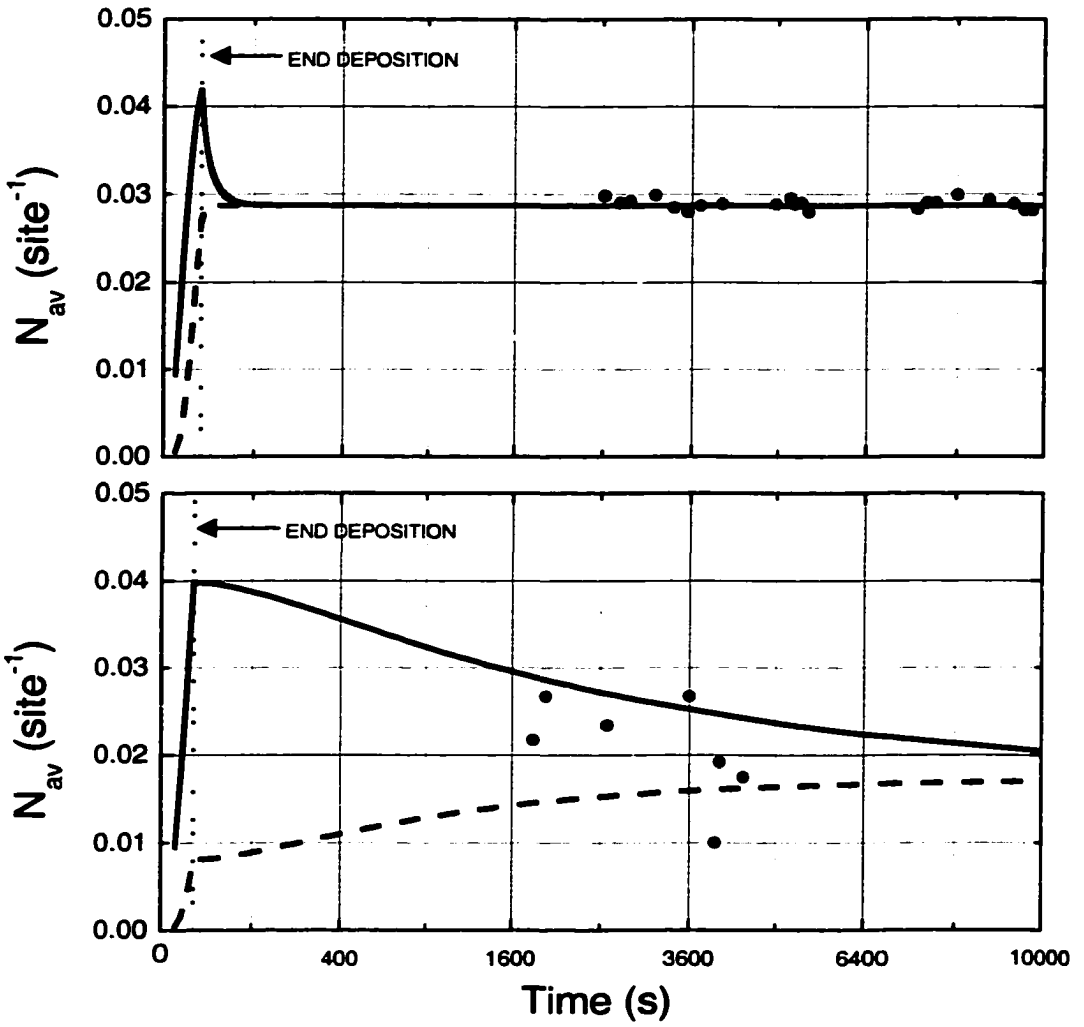
0.05
0.04
0.03
0.02
0.01
0.00
END DEPOSITION
N_{av} (site^{-1})
0.05
0.04
0.03
0.02
0.01
0.00
END DEPOSITION
N_{av} (site^{-1})
0
400
1600
3600
6400
10000
Time (s)

Figure 3

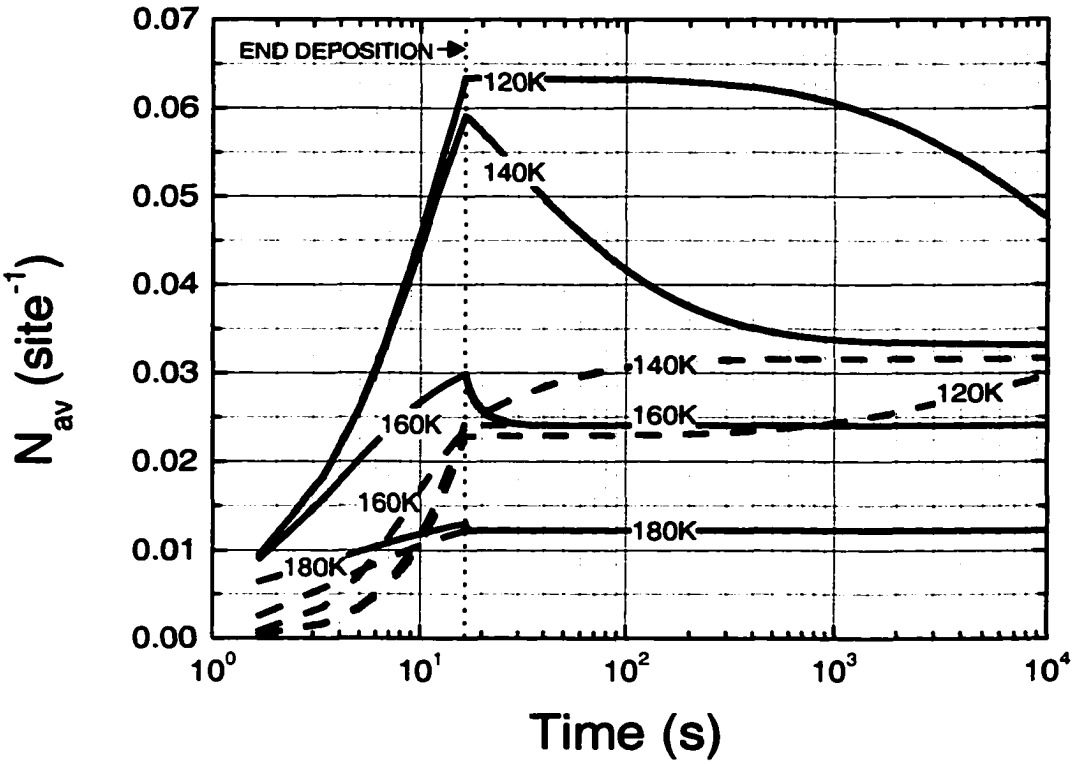
0.07
0.06
0.05
0.04
0.03
0.02
0.01
0.00
N_{av} (site^{-1})
END DEPOSITION
120K
140K
140K
120K
160K
160K
160K
180K
180K
10^0
10^1
10^2
10^3
10^4
Time (s)

Figure 4

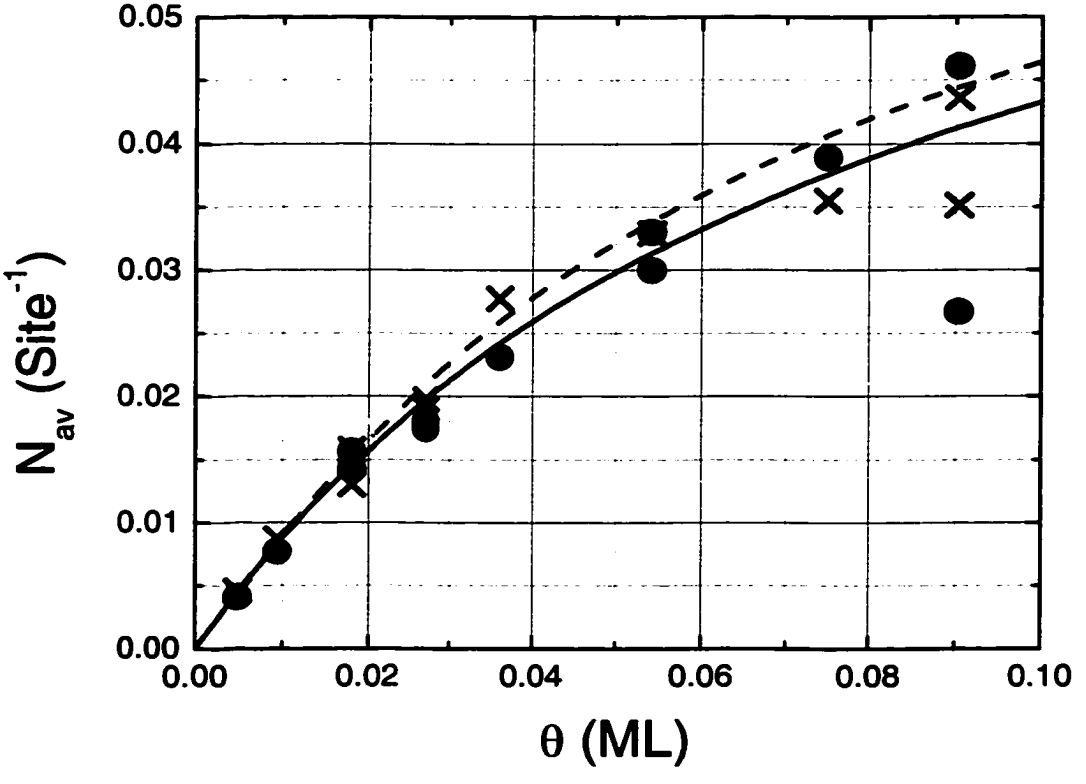

Figure 5

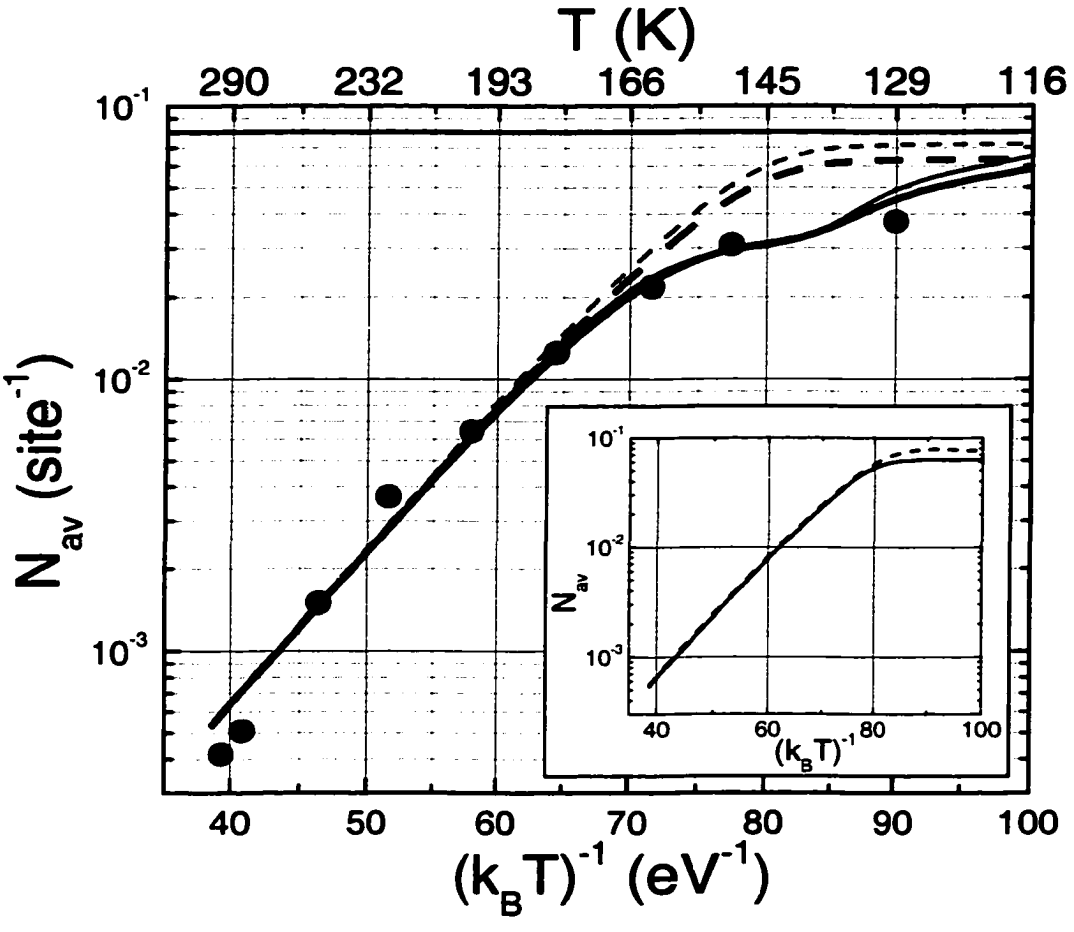
T (K)
290
232
193
166
145
129
116
10^{-1}
10^{-2}
10^{-3}
N_{av} (site^{-1})
40
50
60
70
80
90
100
$(k_BT)^{-1}$ (eV^{-1})
N_{av}
$(k_BT)^{-1}$

Figure 6

4. MORPHOLOGY OF MULTILAYER AG/AG(100) FILMS VERSUS DEPOSITION TEMPERATURE: STM ANALYSIS AND ATOMISTIC LATTICE GAS MODELING

A paper published in Physical Review B.

K.J. Caspersen, C.R. Stoldt, A.R. Layson, M.C. Bartelt, P.A. Thiel, and J.W. Evans

Abstract

Scanning Tunneling Microscopy is used to analyze the nanoscale morphology of 25ML films of Ag deposited on Ag(100) at temperatures (T) between 55K and 300K. A transition from self-affine growth to "mound formation" occurs as T increases above about 140K. The roughness decreases with increasing T up until 140K in the self-affine growth regime, and then increases until about 210K before decreasing again in the mounding regime. We analyze mounding behavior via a lattice-gas model incorporating: downward funneling of depositing atoms from step edges to lower four-fold hollow adsorption sites; terrace diffusion of adatoms with a barrier of 0.40 eV leading to irreversible island formation in each layer; efficient transport of adatoms along island edges to kink sites; and downward thermal transport of adatoms inhibited by a step-edge barrier of 0.06-0.07 eV along close-packed step edges (but with no barrier along kinked or open steps). This model reasonably recovers the T-dependence of not just the roughness, but also of the mound slopes and lateral dimensions above 190K. To accurately describe lateral dimensions, an appropriate treatment of the intralayer merging of growing islands is shown to be critical. To describe behavior below 190K, one must account for inhibited rounding of kinks by adatoms at island edges, as this

controls island shapes, and thus the extent of open steps and of easy downward transport. Elsewhere, we describe the low-T regime of self-affine growth (with no terrace diffusion) accounting for a breakdown of the simple downward funneling picture.

1. Introduction

The kinetic roughening of growing films has been a topic of intense interest in the statistical physics community since the mid-1980's [1]. The emphasis in such studies was primarily on long-time asymptotic properties for generic growth models, where often noise-induced roughening produced self-affine film morphologies. In 1991, Villain [2] recognized that a rather different growth mode occurs in the presence of an additional Ehrlich-Schwoebel step-edge barrier [3], which inhibits downward thermal transport of adatoms relative to intralayer transport. This barrier produces a growth instability resulting in the formation of "mounds", a scenario which is common in homoepitaxial growth [4]. However, the current understanding of such unstable growth processes is incomplete, and theoretical investigations continue with the goal of elucidating kinetic roughening in terms of mound coarsening and possible slope selection [4,5]. Experimental studies have also become common, particularly in the 1990's, often comparing measured growth exponents with theoretical values predicted for various universality classes [1,4]. In homoepitaxial growth, mound formation has been observed in several metal and semiconductor systems, and attempts made to extract exponents both for roughening and mound coarsening [4]. Of particular relevance here are studies of metal(100) homoepitaxy, where kinetic roughening and mound formation has been observed for Cu [6], Fe [7], and Ag [8,9,10].

However, often for applications of thin films, it is not the asymptotic behavior of roughening which is relevant, but rather the morphology of films which have a thickness of a

few layers to a few dozen layers. Desired magnetic properties, conductivity, catalytic activity, etc., often depend sensitively on film morphology, and in particular on roughness [11]. It is thus natural to explore how the morphology of such films depends on deposition conditions (substrate temperature, T, and deposition flux, F). In fact, a basic goal of nanotechnology, and a desired outcome of such studies, is the ability to "tune" nanoscale film morphology by suitable control of deposition conditions. In fact, there are surprisingly few studies which consider the temperature dependence of film growth (let alone provide a systematic analysis). Furthermore, such studies could be instructive for analysis of asymptotic roughening behavior. Most system specific modeling of roughening is based on (and potentially over interprets) limited data, typically for growth at a only single temperature [4], where one is often not even sure if asymptotic behavior has been achieved. Availability of data for a range of temperatures would help offset these problems.

Another basic goal is to develop atomistic models for growth which are sufficiently realistic to have quantitative predictive power. The development of such models also greatly promotes our understanding of the key atomistic processes controlling the morphology of the growing film. Some success has been obtained in modeling Fe/Fe(100) growth at room temperature [12,13], and also Pt/Pt(111) growth [14]. However, the potential of such modeling to predict the T-dependence of growth has not yet been fully tested. Such a test is provided by the present comprehensive study of the T-dependence of Ag/Ag(100) film growth, which extends our previous more limited analysis [9].

In Sec.2, we briefly review the details of the experimental component of our study, which utilizes Variable-Temperature Scanning Tunneling Microscopy (VTSTM). A comprehensive analysis is presented in Sec.3 of our experimental data for 25ML Ag/Ag(100)

films deposited at temperatures between 50K and 300K. A general discussion of the atomistic mechanisms underlying the observed growth is presented in Sec.4. Based on this discussion, detailed atomistic models are presented in Sec.5 for growth above about 135K, where mound formation is observed. The predictions of these models are presented in Sec.6, and a detailed comparison is made with experiment. Our findings are summarized and future work discussed in Sec.7.

2. Experimental Details

Thin films of Ag were deposited on an Ag(100) single crystal surface held at temperatures (T) between 55K and 300K with a flux of F≈0.02 ML/s. The epitaxial adsorption sites on perfect terrace on this fcc(100) surface form a square array with a lattice constant of a=2.89 Å The crystal was mounted in an ultra-high vacuum (UHV) chamber with a base pressure below 1×10^{-10} Torr. The deposition source was an Omicron EFM3 UHV evaporator containing pure Ag. The morphology of the thin films was examined using an Omicron VTSTM. Liquid nitrogen was used for cooling of the substrate down to 135K, while liquid helium was used to achieve lower T down to 55K. The temperature during deposition and subsequent imaging remained fixed to within ±5K. The morphology of the deposited film was analyzed above the central portions of broad atomically flat terraces on the substrate. In this way, we minimize the influence of steps and other defects on the observed morphology of the deposited film. Images are taken as soon as possible after deposition (15-30min.) to limit post-deposition restructuring or smoothing, but we believe that these effects are small (and, in fact, negligible below 260K). Fig. 1 shows typical VTSTM images for films deposited at four different temperatures.

3. Analysis of STM Data for 25ML Ag/Ag(100) Films

3.1 Film Height Distribution

The key quantity characterizing vertical structure is the film height distribution. Clearly, the heights of atoms (and terraces) in growing homoepitaxial films take a periodic set of discrete values separated by the interlayer spacing, $b=a/\sqrt{2}=2.04$Å, for Ag(100). However, line scans from the VTSTM produces a quasi-continuous distribution, Φ_h, of heights, h. This distribution is normalized via $\int dh \Phi_h=1$, and describes the fraction of the apparent surface (as probed by the STM tip) at a specific height, h. Also, the first moment $\int dh\, h\Phi_h=h_{av}$ gives the mean film height. In the distributions, Φ_h, regularly separated peaks are typically evident. The positions of the peaks correspond to the heights of atomic layers, so the separation between them must coincide with b (and, in fact, this observation is used to achieve precise calibration of the vertical scale in the STM line scans). The observed continuous height distribution reflects various features of the STM probe: the tip tracks the electronic (rather than physical) topography in a way that depends on tip shape; the response of the tip to height changes is not instantaneous; etc..

From Φ_h, it is natural to extract a discrete height distribution, Φ_j, which describes the fraction of surface atoms in discrete layer j [15], and which is more appropriate for comparison with results from atomistic modeling. This was accomplished by deconvoluting Φ_h using a specified fitting function, G^j_h, for the contributions from layer j. Here, G^j_h has the properties $\int dh\, G^j_h = \Phi_j$, $\int dh\, hG^j_h / \int dh\, G^j_h = jb$, and $\Phi_h \approx \Sigma_j G^j_h$. It follows that $\Sigma_j \Phi_j=1$ and $\Sigma_j\, j\Phi_j=j_{av}$, where $h_{av} \approx j_{av} b$. The most appropriate form for the G's depends on the exact nature of the deviation of Φ_h from a discrete distribution, which involves non-trivial issues mentioned

above, such as the tip shape, tip current, substrate morphology, etc.. Thus, a simplification was made by choosing all G^j_h to be a Gaussians. The deconvolution of Φ_h was performed via a linear least-squares fit of multiple Gaussians (one per peak), with the only constraint being that the Gaussian centers were equally separated. Fig. 2 gives examples of Φ_h, and the corresponding G's, for two temperatures.

Next, we determine the key moments of the height distributions, Φ. Below, to facilitate comparison between continuous and discrete distributions, we always measure h in units of *b*. The most important quantity is the surface roughness, W (the root-mean-square width of the film height distribution), where $W_c^2 = \int dh\ (h-h_{av})^2\ \Phi_h$ and $W_d^2 = \Sigma_j\ (j-j_{av})^2\Phi_j$, for continuous (c) and discrete (d) distributions, respectively [1]. Fig. 3 shows both these values of W for 25ML Ag/Ag(100) films deposited over a temperature range from 54K to 300K. Note that the former values are larger, except at higher T where terraces are so broad that Φ_h effectively reduces to a discrete distribution. The variation of W with T shows remarkable structure, for W increases from 300K to 205K, then decreases from 205K to 135K, and then increases again for temperatures lower than 135K (at least to 55K). We elucidate this behavior in later sections.

From the same experimental Φ, we also calculated the skewness of the film height distribution, $\kappa_c = W_c^{-3} \int dh\ (h-h_{av})^3\ \Phi_h$ and $\kappa_d = W_d^{-3}\ \Sigma_j\ (j-j_{av})^3\Phi_j$. These quantities give a measure of the lack of vertical reflection symmetry in the film surface. In addition, we determined the kurtosis of the height distribution, $Q_c = W_c^{-4} \int dh\ (h-h_{av})^4\ \Phi_h - 3$, and $Q_d = W^{-4}\ \Sigma_j\ (j-j_{av})^4\Phi_j - 3$. This quantity, Q, measures the weight of the height distribution contained in the tail, relative to a Gaussian distribution (where Q=0). Fig. 4 shows the variation of both κ and Q with T. Despite the uncertainty in the data, there is a clear decrease from positive to

negative values of κ with increasing T above about 110K (and small systematic difference between κ_c and κ_d). The data for Q is noisier, but reveals systematically non-zero values.

3.2 Other Aspects of the Film Morphology

For a more complete description of film morphology beyond its vertical structure (characterized by Φ and its moments), the lateral structure should also be quantified. For this purpose, we use primarily the height-height correlation function, $H(\underline{r})$. In a continuous representation of the height of the film surface, $H(\underline{r})$ gives the mean-square height difference for two points on the film surface separated laterally by a displacement, $\underline{r}$. It follows that $H(\underline{r})$ vanishes for zero separation, and $H(\underline{r})$ can be shown to approach $2W^2$ for large separations [1,15]. Also, $H(\underline{r})$ exhibits other general features depending on the nature of the film morphology [1]: **(i)** If the film surface has a fractal-like self-affine structure (characterized by a continuous spectrum of length scales), then $H(\underline{r})$ is monotonically increasing with $r=|\underline{r}|$. It has the form $H(\underline{r})-r^{2\alpha}$ before reaching its saturation value of $2W^2$, where α is a roughness exponent. **(ii)** If the film surface is characterized by a somewhat ordered array of protrusions or "mounds" with a well-defined characteristic lateral size, then H(r) displays damped oscillations towards its asymptotic value of $2W^2$. The value, R_{av}, of $r=|\underline{r}|$ at the first maximum of $H(\underline{r})$ represents one measure of the average mound radius, while the value, D_{av}, at the first minimum represents a corresponding measure of the average mound diameter (so one expects that $D_{av} \approx 2R_{av}$).

Fig. 5a shows typical $H(\underline{r})$ behavior (measured in the direction along close-packed [110] step edges) at various temperatures. The key feature is that strong oscillations in $H(\underline{r})$ occur for $T \geq 175K$, but the oscillations are negligible or absent for $T \leq 135K$. This suggests a transition from mounding to self-affine growth somewhere between 175K and 135K. The

existence of a transition is further supported by examination the T-dependence of the roughness exponent, α [1]. Rather than using H(r), it is more convenient to estimate α from the (restricted) film roughness, $W_L \sim L^{\alpha}$, observed in a finite L×L "observation window" produced by STM line scans of length L [16]. Fig. 6 shows that for $T \geq 175$ K, one has $\alpha \approx 1$, which is consistent with mounding morphologies, while for $T<135$K, one has $\alpha \approx 0.5$, which is consistent with self-affine morphologies. Further indirect evidence for the existence of a transition in growth mode around 135K comes from our analysis of the local surface slopes, described below.

In the mounding regime, the two quantities, D_{av} and R_{av}, decrease rapidly with decreasing temperature down to approximately 190K, then remain virtually constant for lower temperatures. The relation $D_{av} \approx 2R_{av}$ is satisfied to within the experimental uncertainty. An Arrhenius analysis (Fig. 5b) of R_{av} and D_{av} for $T \geq 190$K yields an energy of $E_c \approx 0.074$eV. Below, we argue that the physical significance of E_c is in its relationship to the terrace diffusion barrier, E_d [here for Ag on Ag(100)] via $E_d \approx 6E_c$.

We also determined the typical surface slope using a variety of prescriptions. Of course, the slope provides a connection between the vertical roughness (W) and lateral characteristic lengths (R_{av} or D_{av}). In our analysis, we first determine the local slope, S, for each pixel in the VTSTM image by fitting a quadratic (second order) surface to its neighboring environment. From this local slope, S, two slope distributions were formed as shown in Fig.7a, one from the entire surface, and the other only from a restricted portion of the surface near mound sides. To characterize the latter, consider the "slope surface" obtained by plotting S as a function of lateral position. We identify the sides of mounds as

locations where at least one of the two principal curvatures of this "slope surface" is negative [17].

Upon examination, we find that the peaks of the distributions are slightly smaller than the averages. This is somewhat surprising since it was generally believed that the peak of these distributions would correspond to the slope of the mound sides [18], and the mound sides having the greatest slope would cause the peak to be greater than the average. However, we believe that the peak of the histograms partly reflects the substantial transition region between mound sides and tops, and between mound sides to the valley floor. These are the regions in greatest abundance in a "birds eye" view of the VTSTM images.

Fig. 8 shows the variation with T of various definitions of typical slopes (obtained from the peaks and averages of the full and restricted slope distributions). All of these increase as T is lowered from 300K to roughly 200K, and then remain virtually flat until 135K, and finally increase again as T decreases below 135K. This apparent non-analytic slope discontinuity at 135K provides further indication of the existence of a transition from mounding to self-affine growth at that temperature.

Also shown in Fig.8 is another common measure of mound slope [19]: the inverse tangent of W/R_c, where R_c is the lateral separation for which H(r) first achieves $2W^2$. The traditional motivation for this selection was presumably that W provides an estimate of mound height, and R_c of mound radius. R_c is clearly smaller than our alternative estimate, R_{av}, of mound radius (but see below), however it seems that W generally underestimates height, actually resulting in the ratio giving a smaller estimate of mound slope than produced by our direct estimates.

3.3 Tessellations for the Mound Distribution

In systems where mounds are well developed with fairly steep slopes [20], their identity is unambiguous. However, this is not necessarily the cases for 25ML Ag/Ag(100) films, especially for higher T. Thus, we developed a systematic definition or identification of mounds based on a prescibed decomposition or tessellation of the surface. This approach makes possible an unambiguous determination of the mound density, as well as a numerous other quantities characterizing mound structure. In this tessellation, boundaries between adjacent mounds are defined to be the bottom of the "valleys" on the film surface, or more exactly curves where the direction of maximum principal curvature, and the gradient vector, ∇h, for the film surface, are orthogonal (Fig.9a). Such curves can include the valleys of "flutes" on the sides of mounds (which terminate at points), as well as boundaries separating mounds. Any such terminating flute curves are removed from the tessellation. To determine these principle curvature and gradient vectors, we fit the film surface obtained from VTSTM images with the same fitting functions as used in the determination of the slopes. Small gaps or discontinuities in the resulting domain boundaries, caused by the imperfect fitting procedure and noise in the data, were then filled in by hand. Fig. 9b shows these domain boundaries superimposed a VTSTM image of the surface of a 25ML Ag/Ag(100) film deposited at 230K. The above procedure is effective and can be applied for various T between 175K and 260K, where mounds are visually evident. The mound density, N_m, was thus extracted, and the behavior of the corresponding measure of the mean mound separation, $L_m=(N_m)^{-1/2}$, is shown in Fig.5b to be consistent with D_{av} and R_{av}. We emphasize that there is no simple precise relationship between these quantities. One might roughly equate L_m with D_{av}. However, making a new estimate of mound radius, R'_{av}, equating $\pi(R'_{av})^2$ to the mean

area per mound, $(N_m)^{-1}$, yields $D'_{av}=2R'_{av}=2\pi^{-1/2}L_m\approx 1.13L_m$. From Fig.5b, one sees that D'_{av} seems to approach D_{av} only for higher T (but recall that the interpretation of D_{av} as the mean mound diameter is not precise either).

4. Discussion of Atomistic Process Underlying Growth

Before presenting in detail the model that we employ to describe Ag/Ag(100) film growth, it is useful to discuss more generally the possible atomistic processes that could underlie our experimental observations. Over the experimental temperature range, the films grow with one of two distinct modes. As noted above, for "high" T above about 140K, the film morphology is characterized by partially ordered array of protrusions or mounds (the "mounding regime"). Conversely, for "low" T below about 140K, the morphology assumes a random fractal-like self-affine structure (the self-affine regime). In the Ag/Ag(100) system, it is known that the activation barrier for terrace diffusion is $E_d\approx 0.40$eV with an attempt frequency of $\nu\approx 10^{13}$/s [21]. Thus, one can conclude that terrace diffusion is active in the mounding regime (at least above 150K), but effectively inoperative in the self-affine regime.

First, we discuss the mounding regime. As a preliminary observation, we note that the presence of terrace diffusion leads to the diffusion-mediated nucleation and growth of two-dimensional islands in each layer. Furthermore, for the Ag/Ag(100) system, these processes are known to be effectively irreversible below about 320K [22]. From traditional nucleation theory, it is known that the mean island separation, L_{av}, scales like $L_{av} \approx 1.8(\nu/F)^{1/6}\exp[-E_d/(6k_BT)]$ (measured in units of surface lattice constant, a) for coverages around 0.1ML [23,24]. The scaling of the mean island density, $N_{av} = (L_{av})^{-2}$ automatically follows from this result.

With regard to mound formation, as noted in Sec.1, Villain [2] made the fundamental observation that this type of "unstable growth" is induced by the presence of an additional Ehrlich-Schwoebel barrier (E_{se}) at step edges which inhibits downward transport (with total barrier E_d+E_{se}) relative to terrace diffusion (with barrier E_d) [3]. Such step-edge barriers can be due to the reduction of the coordination in the transition state for an atom hopping over an edge. These barriers cause some atoms to be reflected from descending steps, and produces biased incorporation at ascending steps. This "step edge reflection" (SER) produces a net lateral mass current, $\underline{J}_{up}$, in the uphill direction, which in turn produces a growth instability (manifested by the formation of mounds). The step-edge barrier also enhances nucleation of islands in upper levels, and hence increases the population of atoms in higher levels. It should be noted that other mechanisms can produce a growth instability and mounding. These include attraction of diffusion atoms towards step edges [25], and diffusion along step edges [26]. However, we have no evidence that these dominate the growth instability in the Ag/Ag(100) system, so we will attribute mounding primarily to the existence of a step-edge barrier.

Another key element of the film growth is the existence of downward funneling (DF) or deflection of atoms deposited at step edges (and perhaps at other microprotrusions) to lower four-fold hollow (4FH) adsorption sites corresponding to homoepitaxy in fcc(100) systems [27]. It is clear that such DF produces a net lateral mass current, $\underline{J}_{down}$, in the downhill direction, and in fact increases the population of lower levels in the growing film. In general, there is a delicate interplay between the effects of the step-edge barrier and DF during growth. For a perfect flat (singular) fcc(100) substrate, after some initial island formation, the uphill current, $\underline{J}_{up}$, will typically dominate resulting in the development of

mounds, such that the slopes of the mound sides increase with time or film thickness. However, as these slopes increase, so does the step density, and thus the amount of downward funneling and the magnitude of the downhill current, $\underline{J}_{down}$. Eventually a slope is selected where the currents balance, i.e., $\underline{J}_{up}+\underline{J}_{down}\approx\underline{0}$ [12,28]. However, the film thickness required for slope selection, and the value of the selected slope, θ_s, depends on the deposition parameters. For higher T, where larger islands and lateral structures formed in the initial stages of growth, it would take longer to achieve slope selection if θ_s was independent of T. However, θ_s generally decreases with increasing T, partly countering this trend.

With the above background, the following overview of the growth process in the mounding regime can be developed. The relatively large smooth features that dominate the morphology at 300K are the result of both the interlayer and intralayer diffusion processes being active. As the temperature is lowered to 200K intralayer diffusion slows creating features with a smaller lateral length, also the E_{se} inhibits the interlayer diffusion process causing W to increase. For T below 200K (down to 130K) the inhibition of interlayer diffusion and the slowing of intralayer diffusion produce small features, such that the number of step-edges becomes very large. Then the smoothing DF process dominates reducing W (down to 130K). This non-monotonic "re-entrant" smooth growth was first predicted in atomistic simulations for metal(100) homoepitaxy [12,28].

Finally, we comment on the scaling of lateral mound sizes at least above 190K. Since mounds are built upon a base of a few submonolayer islands, one can imagine that the mean mound separation (and thus the diameter and radius) should scale like the mean submonolayer island separation, L_{av}. This explains our contention in Sec.II that $E_c\approx E_d/6$ (implying that $E_d \approx 0.44$ eV consistent with previous estimates [21]). The assumption in the

above analysis is that the number of islands per mound is independent of T, a feature which is not clear given the varying influence of the step-edge barrier. However, analysis of our experimental and simulation data indicates that D_{av}/L_{av} =2.7, 2.9, 2.4 for T=175K, 225K, 260K, respectively, is roughly constant.

Second, we briefly discuss the self-affine regime, where an appropriate characterization of the deposition dynamics is key to understanding behavior. Even in the earliest Molecular Dynamics (MD) studies of deposition dynamics, it was recognized that atoms depositing on larger microprotrusions can get caught on the sides rather than funneling all the way down to lower 4FH sites [29]. While such larger microprotrusions have a negligible population at higher T, they become more prevalent at low T, so restrictions to downward funneling become an issue. For growth at extremely low T (near 0K), no thermal diffusion process are active, thus the film morphology is completely controlled by the deposition dynamics, which we describe as "restricted downward funneling" (RDF). The possibility for depositing atoms to get caught or trapped on the sides of microprotrusions in RDF leads to the formation of overhangs, and even internal voids or defects. This scenario was in fact observed in MD simulations of low T growth [30], and its consequences discussed elsewhere [28,31,32]. RDF also produces the growth of rougher films, consistent with the low-T data in Fig. 3.

Next, we consider behavior as T is increased above 0K, but still in the regime where terrace diffusion is inoperative. Note that the trap sites for RDF are frequently of low coordination, and hence the activation barriers for interlayer diffusing out of these sites can be low. One example is for atoms trapped on the sides of {111} microfacets, the activation barrier for diffusion is only 0.1eV (in contrast to 0.4eV for terrace diffusion). As a result, as

T is raised above 0K, these low barrier diffusion process become increasingly active. Since most of the high coordination sites are in lower levels, the result is typically a net downward flow of atoms that works to make growth smoother. Thus, the drop in W from 50K to140K in Fig. 3 is attributed to these low barrier diffusion pathways becoming operative at T is increased. In fact, for large enough T (around 130K), these diffusion pathways become so active that they essentially reproduce the DF behavior. Detailed modeling, described elsewhere [9,31,32], reveals that the density of internal voids vanishes just above 100K. This is consistent with a claim by Miceli *et al* [33], based on surface sensitive X-ray scattering data, that there exists a small population of internal defects in Ag/Ag(100) films grown at 100K.

5. Atomistic Models for Mounding in Ag/Ag(100) Film Growth

We have developed suitably tailored lattice-gas models which we believe effectively capture the essential atomistic processes controlling Ag/Ag(100) film growth in the temperature range above about 135K. These models are analyzed via Kinetic Monte-Carlo (KMC) simulation. For such temperatures, we believe that these key processes are (cf. Sec.4): terrace diffusion; irreversible island formation within each layer; rapid diffusion at island edges; inhibition of downward interlayer diffusion by the Ehrlich-Schwoebel step-edge barrier; and downward funneling of depositing atoms from step-edges and other micro-protrusions to lower 4FH sites.

In our models, we use the appropriate face-centered cubic crystalline geometry, selecting a (100) facet for the initial perfect substrate. Deposition occurs at randomly chosen locations at rate F (per site), and atoms follow DF deposition dynamics. Thus, atoms are allowed to occupy only 4FH sites, and as a consequence no overhangs or internal voids are

formed. Isolated adatoms on flat terraces were then allowed to diffuse with a rate (per direction) given by the Arrhenius expression, $h=\nu_d \exp[-E_d/(k_BT)]$, with an activation barrier of E_d=0.40eV, and a prefactor of $\nu_d = 1\times10^{13}$ s^{-1} [21]. Adatoms hop down a descending step-edge with rate reduced from h by a factor $\exp[-E_{se}/(k_BT)]$, where the additional barrier, E_{se}, can depend on the step structure, as described below [34]. (Thus, we assume a common prefactor, ν_d, for intra- and interlayer diffusion.) An isolated adatom diffuses until meeting another diffusing adatom, after which a new immobile island is irreversibly nucleated, or until irreversibly aggregating with a preexisting island (either by intralayer terrace diffusion, or by downward diffusion at the island edge). In the case of aggregation, the final destination site for mobile adatoms at the island edge is determined by yet to be prescribed edge diffusion processes.

Semi-empirical studies of energetics for diffusion processes [35,36], previous analysis of the sputtering of Ag(100) [37], and our own analysis of our own more extensive experimental data for Ag/Ag(100) film growth up to 100ML [38], suggest that the step-edge barrier, E_{se}, is negligible at kinked step edges (e.g., the open [100] step edge) compared with straight closed-packed [110] step edges. Thus, in our modeling, we assign a step-edge barrier $E_{[100]}=0$ for adatoms descending at kink sites (where the transition state for hopping has roughly three supporting atoms), and a barrier of $E_{[110]}\geq0$ for atoms descending at straight [110] step edges (where the transition state for hopping has two supporting atoms). $E_{[110]}$ will be treated as a free parameter in fitting experimentally observed behavior. We also note that the process of descending from a step edge may actually involve exchange rather than simple hopping [35,36,39].

Finally, we describe in detail our treatment of edge diffusion. Below, we shall distinguish between "local corners" or single-atom high kinks (just referred to as kinks below) at the island edge, and "global corners" (which include the four extremities of the island, and also kinks with multiple height). An edge adatom will be able to round kinks (which is necessary to avoid a shape instability and the development of fractal islands [40,41,42]), but not global corners (so isolated islands exhibit "rectangular fluctuations" from perfect squares, consistent with experiment). When a diffusing adatom aggregates with a pre-existing island, the adatom is bound irreversibly to the island. However, its final destination is determined by accounting for the very rapid edge diffusion that occurs at these temperatures. (The barrier, E_{edge}, for diffusion along straight [110] edges is only about 0.25eV in this system [39].) Since the hop rate along these edges is so much larger than across terraces, we developed an algorithm that treats edge diffusion as instantaneous. After an adatom reaches the step edge, we check along the edge in both directions until a site with more than one occupied neighbor, or a corner site, is found. If one finds two global corners, as in Fig 11f., the atom remains where it impacted the island. Otherwise, the atom was placed in the multiply coordinated site with highest priority (see Fig.11) that was found by the above procedure, rounding a kink site if necessary. We term this treatment of edge diffusion as the Instantaneous Kink Rounding (IKR) Model, since any kink rounding occurs instantaneously on the time scale of aggregation. See Fig. 12 for a schematic overview.

However, it is quite likely that there exists an additional "kink Ehrlich-Schwoebel" barrier, E_{kse}, to round kink sites (Fig.11d), relative to the barrier E_{edge} to hop along straight [110] edges. Then, the total activation barrier for kink rounding is $E_{kr}=E_{edge}+E_{kse}$. Studies using semi-empirical potentials suggest barriers of $E_{kse} \approx 0.25$-0.3eV to hop around corners

[43]. Such barriers have also been used in the modeling of far-from-equilibrium step-edge nanostructures [44]. However, no definitive determination of E_{kse} exists. One should also consider the possibility of kink rounding by exchange [35,44], which one might expect is more likely than exchange at global corners, due to a more favorable transition state [44]. Below, we assign an attempt frequency of $\nu_e \approx 10^{12}$ s^{-1} for edge diffusion processes [44]. Then, the key issue is whether kink rounding at rate [45] $h_{kr} = \nu_e \exp[-E_{kr}/(k_BT)]$ is efficient on the time scale of aggregation of diffusing adatoms with each side of an island. The latter occurs at rate $h_{agg} \approx 4F/N_{av} \sim 1.2\nu_d(F/\nu_d)^{2/3}\exp[-E_d/(3k_BT)]$, using the scaling expression for N_{av} at coverages of around 0.1ML [23,24]. Here, we have assumed that the barrier E_{kr} limits kink rounding, rather than transport to the corner (the latter was assumed in Ref.[40]). Then, corner rounding is efficient if

$E_{kr} < (k_BT)[15.1+2\ (\ln F)/3] + E_d/3$.

Thus, for $F \approx 0.02$ML/s, efficient kink rounding occurs only for T>200K if $E_{kr} \approx 0.35$eV so $E_{kse} \approx 0.1$eV, which is a plausible scenario based on analysis of experimental film morphologies (or for T>250K, if $E_{kr} \approx 0.40$eV so $E_{kse} \approx 0.15$eV). These low values for E_{kse} suggest that kink rounding may occur via exchange. Certainly, kink rounding is effectively inoperative in the lower T-regime of mound formation. With this in mind, we modified the IKR Model to exclude all kink rounding, and describe this as the No Kink Rounding (NKR) Model.

6. Mounded Film Morphology Predicted by Atomistic Models

In the quantitative analysis of simulated film morphologies is presented in this Sec.6, we set E_d=0.40eV, and treat the step-edge barrier $E_{[110]}$ as an adjustable parameter which is

varied to match experimental observations. A common prefactor of $\nu_d=10^{13}s^{-1}$ is assumed for all thermal diffusion process. While the focus of this paper is on the morphology of 25ML Ag/Ag(100) films, it should be noted that considerable insight into the atomistic processes and energetics controlling interlayer transport can be obtained from analysis of initial stages of growth. In Appendix A, we compare model predictions with the observed morphology of 1ML films. Estimates of the step-edge barrier, $E_{[110]}$, can be compared with those obtained below from analysis of 25ML films.

In Fig.13, we show the morphologies of 25ML films predicted from both the IKR and the NKR models for three different temperatures. As expected, the IKR model appears to match well the experimental morphologies shown in Fig.1 at the higher T=230K and 280K, and even does reasonably well at 190K. The 190K morphology from the NKR model is also consistent with the experimental observations (especially given the possibility of some post-deposition restructuring of the lateral morphology may have occurred before STM imaging). However, NKR model morphologies at higher T do not match experiment, and display a shape instability in two-dimensional island growth deriving from the lack of corner rounding [40,41]. Since the IKR Model describes Ag/Ag(100) film growth for most of the T-range of interest, we also present a direct comparison of experimental and simulated film morphologies at 230K (using a three-dimensional representation) in Fig.14.

6.1 Film Height Distribution

In this subsection, we focus on the behavior of W_d, κ_d, and Q_d, which are determined from the film height distribution, $\Phi_j=\theta_j-\theta_{j-1}$, where θ_j is the coverage of layer j. (Note that our simulations do not produce continuous versions of these quantities.) W_d from experiment and for both IKR and NKR models with various $E_{[110]}$ is shown in Fig. 15. For higher T

above 200K, the IKR Model with $E_{[110]}$ =0.06-0.07eV best matches experimental behavior. The match is poor for the IKR Model below 200K. This feature should be expected, since kink rounding is in fact strongly inhibited in this regime. Overactive kink rounding in the IKR Model produces islands that are too compact with an over abundance of the close packed [110] step-edges. Actual island morphologies should be more irregular than predicted by the IKR model, with more kinked step edges, making downward interlayer transport more efficient. To check this contention, we note that the NKR Model does a good job of predicting the observed roughness for lower T around 140K-160K. However, the NKR Model values for W_d deviate significantly from experiment for all higher T. Here, the complete inactivity of kink rounding in the NKR Model produces artificially ramified star-like island shapes (Fig. 11), with an over abundance of kinked step-edges and artificially active downward transport. In summary, for the IKR Model, the over abundance of [110] step-edges with their large E_{se} produces W_d values that were too high at lower T. In the NKR Model, the over abundance of kinked step-edges and their small E_{se} produces W_d values that are too small at higher T. Preliminary analysis shows that a model with finite E_{kse} can universally describe observed W_d behavior. Details will be presented elsewhere.

The simulation results for the higher moments, κ_d and Q_d, are compared with experiment in Fig. 16. Both quantities show significant deviations from experimental values, which we believe can be rationalized as follows. Due to its finite size, the STM tip has difficulty probing the bottoms of valleys of the film surface, this limitation becoming more severe for lower T where characteristic lateral lengths are smaller, and local slopes are greater. This effect produces a height distribution in which the probabilities of the lowest layers are artificially small. These differences are small enough for W_d to be virtually

unaffected. However, κ_d and Q_d, being higher moments, are more sensitive to the shape of the height distribution, and are more greatly affected (particularly the odd moment κ). The simulated κ_d is more positive, and Q_d is more negative than in experiment. Thus, in comparing simulation with experiment, we focus more on comparing trends than matching the quantitative values for each T. Fig. 16 shows that the IKR Model, with $E_{[110]}$ as chosen above, does a reasonable job in this respect, and thus we believe that it accurately describes the basic features of the height distribution, especially for higher T.

6.2 Other Aspects of the Film Morphology

Analogous to Sec.4.2, for a complete analysis of simulated morphologies (and for comparison with experiment), we examine the lateral morphology as characterized by the height-height correlation function, as well as the slope of the film surface. For comparison of lateral lengths, we will focus on only D_{av}. As seen in Fig. 17a, D_{av} for the IKR Model, and even the NKR Model, compare favorably with experiment for a range of values of $E_{[110]}$. This should not be surprising, for the major determining factor for the lateral length of the system is simply the terrace diffusion rate, which is controlled by the same E_d for all models. We emphasize that the mean mound separation, L_m, and diameter, D_{av}, are substantially larger than the mean island separation, L_{av}, in the submonolayer regime (see below). The E_d-value used in our simulations ensures the match to L_{av}. However, there is no apriori guarantee that the simulations will match D_{av} for 25ML films. Indeed, experimental values of D_{av} are <u>not</u> matched if we use our previous simpler "square island" model for metal(100) homoepitaxial growth [9,12,24,28], where square islands within each layer that meet during growth do not restructure, but continue to grow as overlapping squares. See Appendix B. Thus, it is clear that a realistic treatment of the restructuring or merging of islands in the

same layer is critical for describing the increase in lateral correlation length which is associated with mound formation during growth (at least in the case of systems with "small" step-edge barriers).

Next, in Fig.17b, we compare simulated local slopes with experimental values. The simulated slope was obtained by determining the density of step edges (in the direction aligned with [110] step edges), weighting by step height. This corresponds roughly to the experimental local slope averaged over the whole surface, which is also shown in this figure. We see that for T>200K the experimental and simulation slopes match acceptably, however the simulated slopes are too large for lower T. In the IKR Model, this is partly a consequence of the overestimation of W_d. We also expect that the step density may not correspond to the experimental measure of slope at low T, particularly in the NKR Model, which has a large step density due to very irregular island shapes. Note that our modeling does not produce the slope discontinuity around 135K observed in other experimental data. This may be because our models do not incorporate the breakdown in DF necessary to realistically describe the transition to low-T self-affine growth [31,32].

For comparison with the tessellated mound distribution obtained in the experimental STM image for a 25ML Ag/Ag(100) film grown at 230K (Fig.9), we also show the corresponding tessellation for a simulated film morphology using the IKR Model in Fig. 18. The procedure used here is identical to that applied in Fig.9. Qualitative comparison of Fig.9 and Fig.18 indicates that the IKR Model does reproduce the key features of the mound distribution. A comprehensive quantitative analysis of various features of the tessellated mound distribution will be presented elsewhere, but detailed comparison with experiment is inhibited by limited statistics for the latter.

6.3 Effect of Downward Funneling

As a definitive test of the notion that DF is responsible for the drop in W as T decreases from 200K to130K, we implemented the IKR Model, and the NKR Model, for a simple cubic (SC) crystalline geometry (where the initial substrate is a (100) facet). In our implementation in a SC geometry, DF is completely absent, as all deposited atoms adsorb where they impinge at on-top sites directly above film atoms. Fig. 19 shows the results for W_d for the SC models over the same temperature range as the FCC model results in Fig.15. We see that W_d in the SC models do not show the same drop below 200K as in the FCC models. Also, W_d for the SC models are larger for all T's (substantially so for lower T). This should be expected since DF is a smoothing effect, which is amplified for lower T. Also SC models should produce Poisson growth as $T \rightarrow 0$, for which $W_d = \theta^{1/2}$ (so W_d=5 for 25ML films).

That DF controls the drop in W is not unambiguous from the outset. One alternative is that the development below 200K of irregular structures with a high population of kinked step edges (as a result from limited kink rounding) would also naturally enhance downward transport due to the zero step-edge barrier for kinked (versus [110]) step edges. In the SC NKR Model, W_d is indeed much lower than in the IKR Model for a range of T below 200K, so it is possible that W_d could drop somewhat below 200K in a model with a finite corner rounding rate. However, W_d would certainly achieve the same high value as in both the IKR and NKR models for lower T around 135K. Consequently, such a model could not explain experimental observations.

Finally, we note another recently proposed idea [4] that the "re-entrant" decrease in W with decreasing T is simply due to the higher density, and thus decreasing size, of islands

(with decreasing T). More specifically, presumably the idea is that it is easier for atoms deposited on top of small islands to reach the edge and hop down. However, if valid, the decrease in W should appear in the SC models discussed above (and in the SC model described in Appendix B). This is not the case. The reason for the failure of this idea is simply that as T decreases and the islands become smaller, so does the terrace diffusion rate. Thus, it is not necessarily easier for adatoms to reach island edges. Furthermore, one should note that in any SC model, as T decreases and all thermal diffusion processes switch off, very rough Poisson growth must be achieved [9].

7. Summary

In summary, our analysis of VTSTM data for deposited Ag/Ag(100) films provides the most comprehensive analysis to date of the T-dependence of the morphology of deposited metal(100) homoepitaxial films. We note that our results for the T-dependence of Ag/Ag(100) film growth are consistent with recent VTSTM studies of growth between 135K and 300K by the Genova group [10] (who also studied sputtering [46]), and with the earlier observation based on surface-sensitive X-ray scattering of rougher growth at 200K than at 300K [8]. In our analysis, we have considered in detail both vertical and lateral aspects of the morphology, focusing on the regime of mound formation. Our lattice-gas modeling provides insight into the key atomistic processes and energetics controlling growth. For example, we find that a step-edge barrier of $E_{[110]}$=0.06-0.07eV along close-packed [110] step edges (compared with $E_{[100]} \approx 0$eV along kinked or open step edges) is responsible for the mound formation. (This value for $E_{[110]}$ assumes a common prefactor for intra- and interlayer diffusion.) Downward funneling deposition dynamics is shown to be responsible for the re-entrant smooth growth below 200K (at least down to 135K). Also, the post-collision

restructuring of growing islands within the same layer is shown to be a key ingredient in the development of mounds and the determination of their lateral dimension.

It should be emphasized that while our atomistic modeling has been quite successful, the IKR and NKR Models that we have implemented are still rather idealized, being tailored to incorporate just the essential physics. We have already suggested the need to incorporate a finite kink Ehrlich-Schwoebel barrier, E_{kse} [rather that the extremes of E_{kse}=0 for IKR, and E_{kse}=∞ for NKR], in order to describe film morphology over the entire T-range from 135K to 300K. We have also noted that our estimates for the step-edge barrier, $E_{[110]}$, correspond to assuming a common prefactor of $\nu_d=10^{13}s^{-1}$ for intra- and interlayer diffusion. Of course, there will be some difference between the prefactors [36,47], which would modify the estimate of $E_{[110]}$. One could reduce the prefactor for interlayer diffusion (relative to that for terrace diffusion), and increase $E_{[110]}$, so the interlayer diffusion rate is unchanged at 230K, say. Relative to the original model, this would inhibit (enhance) interlayer diffusion, and thus lead to an increase (slight decrease) in W above (below) 230K. However, it is not clear that the fit to experimental data would be much improved, and similar refinements could perhaps be achieved by instead incorporating further variations in step-edge barrier. Another change might include nucleation or aggregation once a diffusing adatom reaches a site diagonally adjacent to (rather than directly adjacent to) another atom or island, a feature reflecting the low barrier to move from the diagonal to the directly adjacent site [43]. These modifications will be considered in future work.

In this paper, we have not discussed the dynamics of kinetic roughening or of mound coarsening (or given values for the associated exponents) for film growth at a fixed temperature. In more extensive experimental studies of Ag/Ag(100) film deposition up to at

least 100ML [38], we find a strong T-dependence of these aspects of film growth, with slow selection of mound slopes for higher T [9], and more rapid selection at lower T. Details will be reported elsewhere.

Acknowledgements

KJC, CRS, ARL, PAT, and JWE were supported for this work by NSF Grant CHE-0078596. Work was performed at Ames Laboratory, which is operated for the U.S. Department of Energy (U.S. DOE) by Iowa State University under Contract No. W-7405-Eng-82. MCB was supported by the U.S. DOE. Lawrence Livermore National Laboratory is operated for the U.S. DOE by the University of California, under contract No. W-7405-ENG-48.

Appendix A: Initial Stages of Multilayer Growth

We have used the IKR Model with E_d=0.40eV, $E_{[110]}$=0.07eV, and $\nu_d=10^{13}s^{-1}$ (and $E_{[100]}$=0eV) to examine the initial stages of growth up to 1ML at room temperature (300K). We set F≈0.055ML/s to match earlier experiments [22]. In Fig.20, we show simulated configurations at this T and F for coverages of 0.25, 0.5, 0.75, 1.0ML. Note that before island coalescence is significant, almost all step edges have the close packed [110] orientation. However, as a result of coalescence, a high population of kinked step edges are generated. Since these step edges have no step-edge barrier, their formation is significant in inhibiting the nucleation and growth of 2nd layer islands. Fig.21 shows the 2nd layer population at 1ML versus $E_{[110]}$.

A single experimental study imaging a 100nm×100nm region revealed a 2nd layer coverage of θ_2≈0.057ML [22]. Then, from Fig.21, we would estimate that $E_{[110]}$≈0.09eV. However, it should be recognized that there is substantial uncertainty in the estimate of θ_2

from a single 100nm×100nm image. Simulations for this size region (with $E_{[110]}$=0.07eV) find a distribution of θ_2-values with a standard deviation of 0.0054ML. Thus, the true (average) experimental θ_2 could be as low as 0.050ML, roughly consistent with a lower estimate of $E_{[110]}$ given in the text.

Appendix B: Comparison with "Square Island" Growth Model

In previous modeling of metal(100) homoepitaxy in this (Ag) and other systems, we focussed on analysis of film roughness using a simpler canonical "square island" model [9,12,22,24,28]. This model enforced square shapes for individual (isolated) islands in each layer, as well as specifying that when growing islands meet, they continued to grow as overlapping square. Thus, there was no restructuring, or formation of dumbbell shapes seen in our more realistic IKR Model (cf. Fig.20). Consequently, in this "square island" model, only [110] step edges are present, so consistently we assume a uniform step-edge barrier. Otherwise, all the ingredients of the models described in the text (terrace diffusion leading to irreversible nucleation and growth of islands; downward funneling deposition dynamics for a fcc(100) crystal geometry) are incorporated.

Fig.22 shows the predictions of the "square island" model with an fcc(100) crystal geometry for W_d versus T for 25ML films deposited with F=0.02ML/s with E_d=0.040eV and $\nu_d=10^{13}$/s. Also the uniform barrier E_{se}=30meV was chosen to best match the experimental data for Ag/Ag(100). As noted in previous studies [9,22], this barrier should be regarded as an effective value. Indeed, our more sophisticated modeling in Sec.6 shows that it corresponds to some sort of average of the values for kinked (or open), and [110] close-packed step edges. Fig.23 shows a snapshot of the predicted morphology of a 25ML film grown at 230K. For comparison, we also show W_d behavior for this model with the same

parameters as above, but for a SC geometry (on-top adsorption sites and no downward funneling). The comparison demonstrates that DF in the model with an fcc(100) geometry produces the decrease in W_d below 200K.

Next, we discuss the predictions of the "square island" model for characteristic lateral lengths (focusing on D_{av}) in 25ML films. One finds that for T=175K, 205K, and 230K, the model predictions of D_{av} = 2.3nm, 5.6nm, and 6.6nm (in the [110] direction), respectively, are much smaller than the experimental values of 7.7nm, 11.9nm, and 13.1nm, respectively. Apparently, the lack of restructuring of island pairs after collision in the model artificially inhibits the development (i.e., the increase) of the lateral correlation lengths. This lack of restructuring may also enhance agreement with experimental W_d for T below 200K, which seems artificially good given the poor description of the lateral lengths.

References

[1] A.L. Barabasi and H.E. Stanley, *Fractal Concepts in Surface Growth* (Cambridge, New York, 1995).

[2] J. Villain, J. Phys. I (France) **1**, 19 (1991).

[3] G. Ehrlich and F.G. Hudda, J. Chem. Phys. **44**, 1039 (1966); R.L. Schwoebel and E.J. Shipsey, J. Appl. Phys. **37**, 3682 (1966).

[4] *Morphological Organization in Epitaxial Growth and Removal*, edited by Z. Zhang and M.G. Lagally (World Scientific, Singapore, 1998).

[5] M. Siegert, Phys. Rev. Lett. **81**, 5481 (1998); J.G. Amar, Phys. Rev. B **60**, R11317 (1999); L.-H. Tang, P. Smilauer, and D.D. Vvedensky, Eur. Phys. J. B **2**, 409 (1998).

[6] H.-J. Ernst, F. Fabre, R. Folkerts, and J. Lapujoulade, Phys. Rev. Lett. **72**, 112 (1994); L.C. Jorritsma, M. Bijnagte, G. Rosenfeld, and B. Poelsema, Phys. Rev. Lett. **78**, 911 (1997); J.-K. Zuo and J.F. Wendelken, Phys. Rev. Lett. **78**, 2791 (1997).

[7] J.A. Stroscio, D.T. Pierce, M. Stiles, A. Zangwill, and L.M. Sander, Phys. Rev. Lett. **75**, 4246 (1995); K. Thürmer, R. Koch, M. Weber, and K.H. Rieder, Phys. Rev. Lett. **75**, 1767 (1995).

[8] W.C. Elliott, P. F. Miceli, T. Tse, and P. W. Stephens, Phys. Rev. B **54**, 17938 (1996).

[9] C.R. Stoldt, K.J. Caspersen, M.C. Bartelt, C.J. Jenks, J.W. Evans, and P.A. Thiel, Phys. Rev. Lett. **85**, 800 (2000); in *Recent Developments in Oxide and Metal Epitaxy: Theory and Experiment*, edited by M. Yeadon, S. Chang, R.F.C. Farrow, J.W. Evans, and O. Auciello, MRS Proceedings **619** (MRS, Pittsburgh, 2000).

[10] G. Constantini, F. Buatier de Mongeot, C. Boragno, and U. Valbusa, Surf. Sci. **459**, L487 (2000).

[11] Special issue on *Magnetism on a Microscopic Scale* [MRS Bull. **20**, No. 10 (1995)]; K.L. Ekinci and J.M. Valles, Phys. Rev. B **58**, 7347 (1998).

[12] M.C. Bartelt and J.W. Evans, Phys. Rev. Lett. **75**, 4250 (1995); in *Evolution of Epitaxial Structure and Morphology*, edited by A. Zangwill, D. Jesson, D. Chambliss, and R. Clarke, MRS Proceedings **399** (MRS, Pittsburg, 19960), p.89.

[13] J.G. Amar and F. Family, Phys. Rev. B **54**, 14071 and 14742 (1996).

[14] J. Jacobsen, K.W. Jacobsen, P. Stoltze, and J.K. Norskov, Phys. Rev. Lett. **74**, 2295 (1995).

[15] For a growing fcc(100) epitaxial film, where atoms sit in four-fold hollow adsorption sites, "surface atoms" can be partially covered by k=0-4 neighboring atoms in the layer

above. Thus, in our definition of the population, Φ_j, of surface atoms, we assign a corresponding weight, $w_k=(4-k)/4$, to each atom reflecting the degree to which it is uncovered. For these w_k, one can show that $\Phi_j=\theta_j-\theta_{j-1}$, where θ_j is the coverage of layer j. See the Appendix of J.W. Evans, Phys. Rev. B **39**, 5655 (1989). For the analysis of height-height correlation functions, $H(\underline{r})$, in an fcc(100) geometry, the same weighting is naturally applied. We note that behavior is not as simple as described in the text for the continuous representation: $H(\underline{r})$ for large $\underline{r}$ in the direction of [110] step edges tends to oscillate between two values both close to $2W^2$. See Ref.[32] for details.

[16] J. Krim, I. Heyvaert, C. Van Haesendonck, and Y. Bruynseraede, Phys. Rev. Lett. **70**, 57 (1993).

[17] Principle curvatures come from diagonalizing the 2×2 matrix with (i,j) entries $\partial^2 S/\partial x_i \partial x_j$.

[18] J.E. Van Nostrand, S. Jay Chey, M.-A. Hasan, D.G. Cahill, and J.E. Greene, Phys. Rev. Lett. **74**, 1127 (1995); See also Stroscio *et al.* in Ref.7.

[19] See Stroscio *et al.* in Ref.7; Zuo and Wendelken in Ref.6.

[20] M. Kalff, P. Smilauer, G. Comsa, and T. Michely, Surf. Sci. **426**, L447 (1999).

[21] P.A. Thiel and J.W. Evans, J. Phys. Chem. B **104**, 1663 (2000).

[22] C.-M. Zhang, M.C. Bartelt, J.-M. Wen, C.J. Jenks, J.W. Evans, and P.A. Thiel, Surf. Sci. **406**, 178 (1998).

[23] J.A. Venables, Philos. Mag. **27**, 697 (1973); S. Stoyanov and K. Kashchiev, Curr. Topics Mater. Sci. **7**, 69 (1981).

[24] M.C. Bartelt and J.W. Evans, Surf. Sci. **298**, 421 (1993).

[25] J. G. Amar and F. Family, Phys. Rev. Lett. **77**, 4584 (1996).

[26] M. V. Ramana Murty and B. H. Cooper, Phys. Rev. Lett. **83**, 352 (1999); O. Pierre-Louis, M. R. D'Orsogna, and T. L. Einstein, Phys. Rev. Lett. **82**, 3661 (1999).

[27] J. W. Evans, D. E. Sanders, P. A. Thiel, and A. E. DePristo, Phys. Rev. B **41**, 5410 (1990).

[28] M.C. Bartelt and J.W. Evans, Surf. Sci. **423**, 189 (1999).

[29] D.E. Sanders and J.W. Evans, in *The Structure of Surfaces III*, edited by S.Y. Tong, M.A. Hove, K. Takayanagi, and X.D. Xie (Spinger-Verlag, Heidelberg, 1991) p.38; D.M. Halstead and A.E. DePristo, Surf. Sci. **286**, 275 (1993).

[30] C.L. Kelchner and A.E. DePristo, Surf. Sci. **393**, 72 (1997).

[31] K.J. Caspersen, C.R. Stoldt, P.A. Thiel, and J.W. Evans, in *Recent Developments in Oxide and Metal Epitaxy: Theory and Experiment*, edited by M. Yeadon, S. Chang, R.F.C. Farrow, J.W. Evans, and O. Auciello, MRS Proceedings **619** (MRS, Pittsburgh, 2000).

[32] K.J. Caspersen and J.W. Evans, Phys. Rev. B, *to be submitted.*

[33] P. Miceli, private communication.

[34] Once an adatom hops over the edge, DF dynamics used to select lower adsorption site for the diffusing adatom. This is correct for monatomic steps. However, one should strictly incorporate the appropriate interlayer thermal diffusion for multiple steps, which could lead to an adatom climbing back on top of the step [31,32]. However, we believe that this scenario is rare, and DF dynamics suffices in the T-range of interest. For example, there is an additional barrier of about 0.1eV (over the facet diffusion barrier of 0.1eV) for an adatom to climb from the sides to the top of a truncated pyramid with {111} facets as sides [31,32].

[35] J. Merikoski, I. Vattulainen, J. Heinonen, and T. Ala-Nissila, Surf. Sci. **387**, 167 (1997).

[36] U. Kurpick and T.S. Rahman, Phys. Rev. B **57**, 2482 (1998).

[37] C. Teichert, C. Ammer, and M. Klaua, Phys. Status Solidi A **146**, 223 (1994).

[38] A.R. Layson, C.R. Stoldt, K.J. Caspersen, M.C. Bartelt, J.W. Evans, and P.A. Thiel, Bull. APS **45**, 203 (2000).

[39] B.D. Yu and M. Scheffler, Phys. Rev. Lett. **77**, 1095 (1996); Phys. Rev. B **55**, 13916 (1997).

[40] M.C. Bartelt and J.W. Evans, Surf. Sci. **314**, L829 (1994).

[41] J. Zhong, T. Zhang, Z. Zhang, and M.G. Lagally, Bull. APS **45**, 506 (2000).

[42] A. Bogicevic, J. Strömquist and B.I. Lundqvist, Phys. Rev. Lett. **81**, 637 (1998).

[43] A.F. Voter, Proc. SPIE **821**, 214 (1987); H. Mehl, O. Biham, I. Furman, and M. Karmi, Phys. Rev. B **60**, 2106 (1999); M. Breeman, G.T. Barkema, and D.O. Boerma, Surf. Sci. **303**, 25 (1993).

[44] C.R. Stoldt, A.M. Cadilhe, C.J. Jenks, J.-M. Wen, J.W. Evans, and P.A. Thiel, Phys. Rev. Lett. **81**, 2950 (1998); A.M. Cadilhe, C.R. Stoldt, C.J. Jenks, P.A. Thiel, and J.W. Evans, Phys. Rev. B **61**, 4910 (2000).

[45] In the modeling of Ref.[44], the prefactor for kink rounding was set to $\nu_e/2$ (versus ν_e for hopping along straight [110] edges). However, an adatom impinging on an island edge (that cannot reach a kink site without corner rounding) can typically avoid nucleating a new layer by rounding one of 2 kinks. This compensates for the factor of ½ in the prefactor (thus justifying the expression for h_{kr} in the text).

[46] G. Constantini, S. Rusponi, R. Gianotti, C. Boragno, and U. Valbusa, Surf. Sci. **416**, 245 (1998) found a non-monotonic dependence of roughness on temperature between 100K and 500K for sputtering of the Ag(100) surface [46], somewhat analogous to behavior observed during growth between 135K and 300K.

[47] K.R. Roos and M.C. Tringides, Phys. Rev. Lett. **85**, 1480 (2000).

Figure Captions

Figure 1. Differentiated $100\times100nm^2$ STM images of 25 ML Ag/Ag(100) films deposited with F≈0.02ML/s at various temperatures (shown). Darker (brighter) regions are lower (higher). Arrows indicating directions are labeled by the surfaces resulting from cleaving orthogonal to the arrows.

Figure 2. Examples of the deconvolution of VTSTM height distributions of 25ML Ag/Ag(100) films deposited at: (a) 230K; and (b) 280K. The thin solid line is the VTSTM distribution. The dotted lines are the individual Gaussian fitting functions, and the thick solid line is their sum.

Figure 3. W vs. T for 25ML Ag/Ag(100) films deposited with F≈ 0.02ML/s obtained from both the continuous (W_c) and discrete (W_d) film height distributions.

Figure 4. κ and Q vs. T for 25ML Ag/Ag(100) films deposited with F≈ 0.02ML/s obtained from both the continuous (κ_c and Q_c) and discrete (κ_d and Q_d) film height distributions.

Figure 5. (a) A family of H(r) curves for various T, displaced vertically for clarity, and normalized by dividing by $2W^2$. Solid (dotted) vertical line segments indicate values of R_{av} (D_{av}). (b) Arrhenius plot of R_{av} (circles), D_{av} (squares), and the average mound separation (triangles) for 175K≤T≤300K for 25ML Ag/Ag(100) films deposited with F≈0.02ML/s. For D_{av} (R_{av}), the slope of the linear fit for 190K≤T≤300K is
-0.075eV (-0.074eV).

Figure 6. α vs. T for 25ML Ag/Ag(100) films deposited with F≈0.02ML/s. The curve is to guide the eye.

Figure 7. Example of the distribution of local slopes for a 25ML Ag/Ag(100) film deposited at 205K with F≈0.02ML/s, for the entire surface and for the "mound sides" (see text).

Figure 8. Values for different prescriptions of local slopes vs. T for 25ML Ag/Ag(100) films deposited with F≈0.02ML/s. Circles correspond to sampling entire surface, whereas squares correspond to sampling mound sides. The solid lines with filled symbols represent the distribution peak, and the dashed lines with open symbols represent the average. Solid triangles show values obtained from the ratio W/R_c.

Figure 9. (a) Schematic of our prescription for construction of tessellations of the film surface into mounds (where K_{max} is the direction of maximum positive curvature). (b) A tessellation of an $80\times80nm^2$ VTSTM image of a 25ML Ag/Ag(100) film deposited at 230K with F≈0.02ML/s.

Figure 10. Schematic of Downward Funneling (DF) and Step-Edge Reflection (SER), as well as the associated induced lateral mass currents.

Figure 11. Schematic of edge diffusion processes. Priority 1 is selected before priority 2, etc. (see text).

Figure 12. Schematic of atomistic processes in the IKR Model. The thicker lines and arrows represent the instantaneous edge diffusion in this model.

Figure 13. $100\times100nm^2$ images for the morphologies of 25ML Ag/Ag(100) films deposited with F=0.02ML/s at various temperatures (shown), as predicted by the IKR Model and the NKR Model.

Figure 14. $50\times50nm^2$ images of 25ML Ag/Ag(100) films deposited at 230K with F=0.032ML/s:

(a) experimental STM image; (b) simulation image fromthe IKR Model. Note that STM imaging

typically produces some "artificial" smoothing of features.

Figure 15. W_d vs. T for 25ML Ag/Ag(100) films deposited with F≈0.02ML/s for experiment (sold circles), the IKR model with $E_{[110]}$=0.07, 0.06, 0.05eV (solid curve, long dashed curve, short dashed curve), and the NKR model with $E_{[110]}$=0.06eV(dotted curve).

Figure 16. κ and Q vs. T for 25ML Ag/Ag(100) films deposited with F≈0.02ML/s for experiment (solid circles), the IKR model with $E_{[110]}$=0.07, 0.06, 0.05eV (solid curve, long dashed curve, short dashed curve), and the NKR model with $E_{[110]}$=0.06eV(dotted curve).

Figure 17. (a) D_{av} and (b) local slope vs. T for 25ML Ag/Ag(100) films deposited with F≈0.02ML/s for experiment (solid circles), the IKR model with $E_{[110]}$=0.07, 0.06, 0.05eV (solid curve, long dashed curve, short dashed curve), and the NKR model with $E_{[110]}$=0.06eV(dotted curve). The local slope is an average over the entire surface for experimental data, and is obtained from the step density in the simulations.

Figure 18. Tessellation of an 80×80nm^2 image generated from the IKR model of a 25ML Ag/Ag(100) film deposited at 230K with F≈0.02ML/s.

Figure 19. W_d vs. T for 25ML Ag/Ag(100) films deposited with F≈0.02ML/s. Solid circles represent experimental data, while solid (open) squares correspond the SC version of the IKR (NKR) model.

Figure 20. 102×102 nm^2 images of simulated film morphologies for initial stages of Ag/Ag(100) growth at 300K with F=0.055ML/s from the IKR model with $E_{[110]}$=0.07eV.

Figure 21. Second layer coverage, θ_2, vs. $E_{[110]}$ in the IKR model for 1ML Ag/Ag(100) films deposited at 300K with F=0.055ML/s.

Figure 22. 35×35nm^2 image of the "square island" model prediction for the morphology of a 25ML Ag/Ag(100) film deposited at 230K with F≈0.02ML/s.

Figure 23. W_d vs. T for 25ML Ag/Ag(100) films deposited with F≈0.02ML/s from experiments (closed circles), the FCC "square island" model (open circles), and the SC "square island" model (open squares).

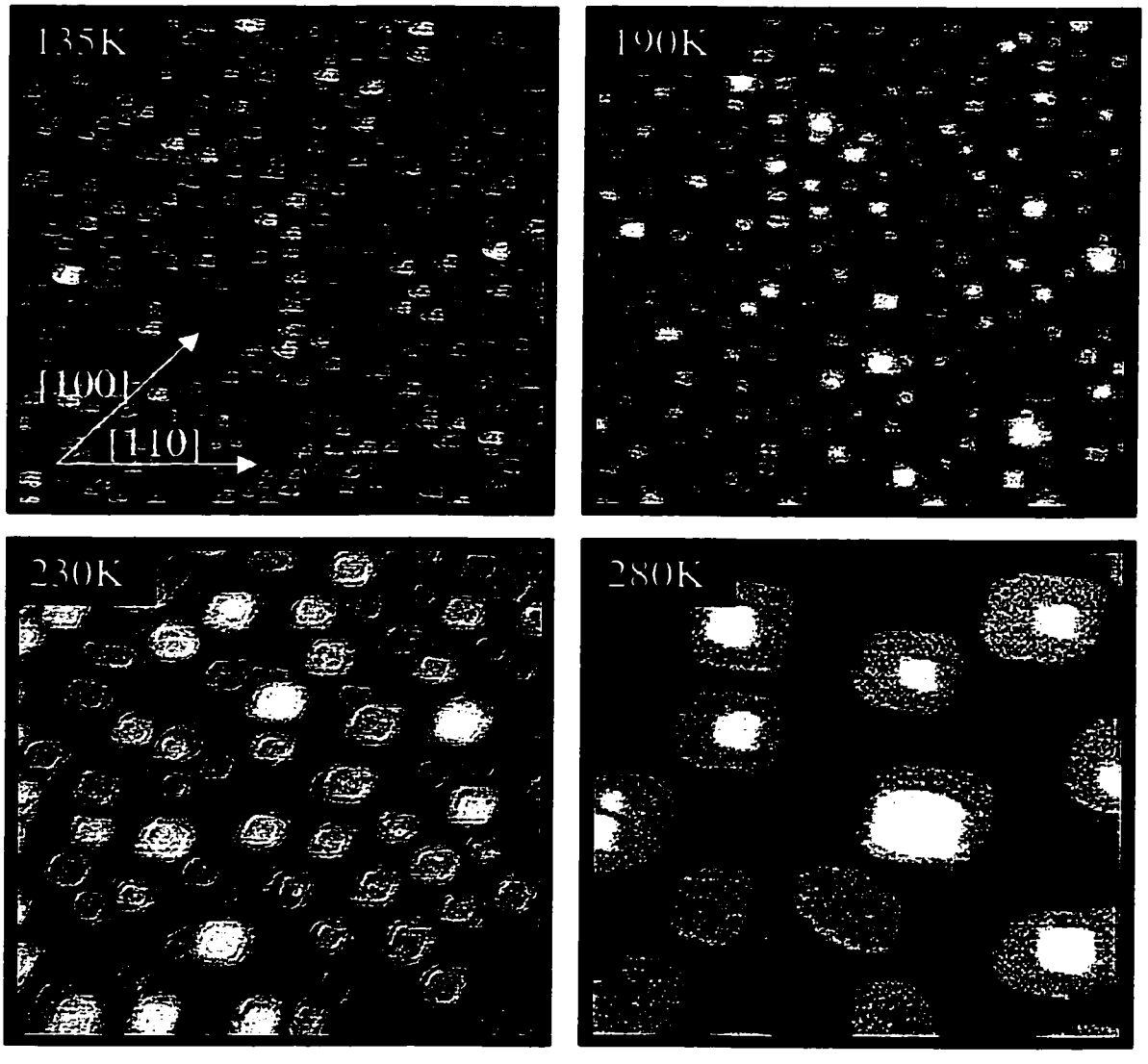

Figure 1

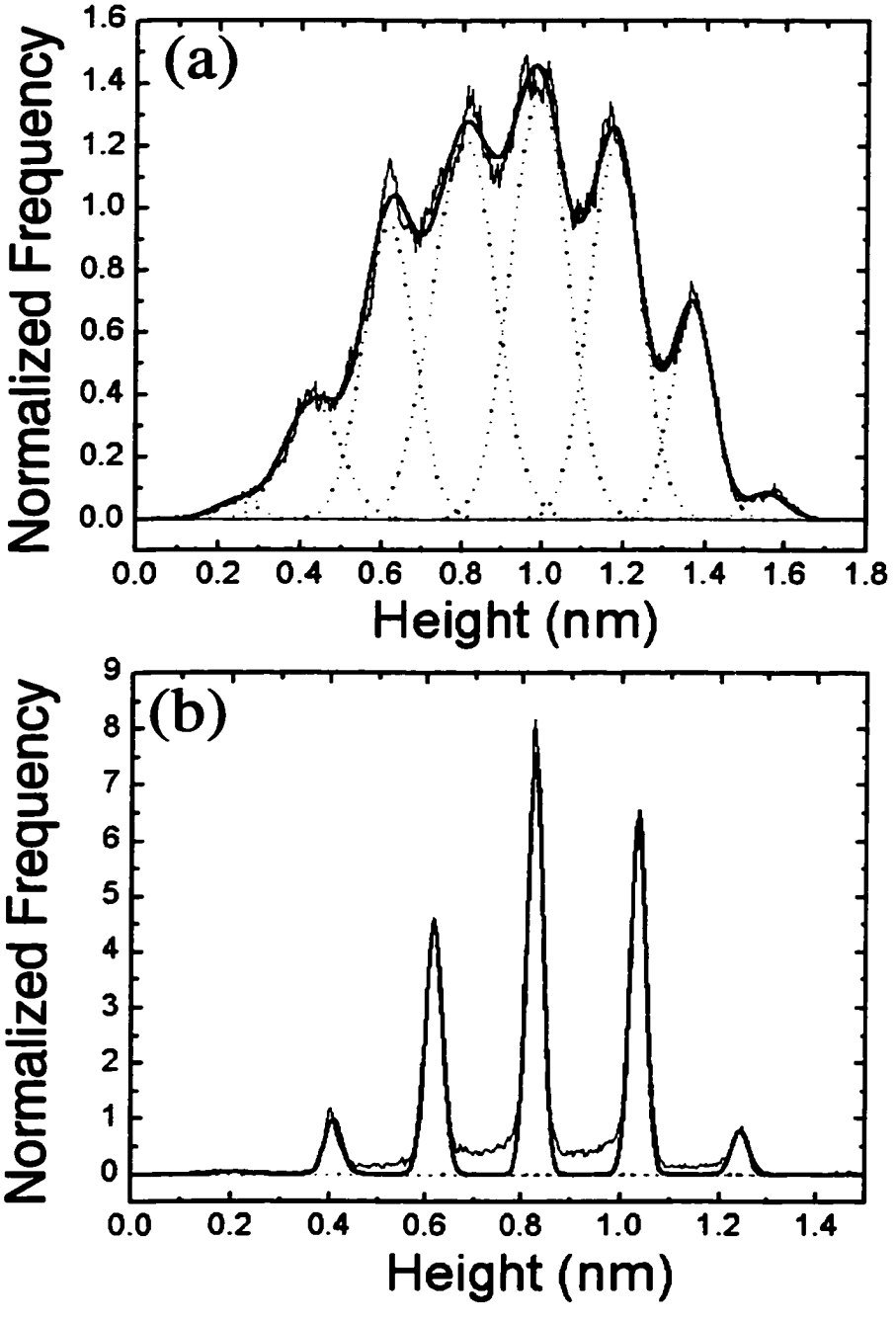
(a)
Normalized Frequency
Height (nm)
(b)
Normalized Frequency
Height (nm)

Figure 2

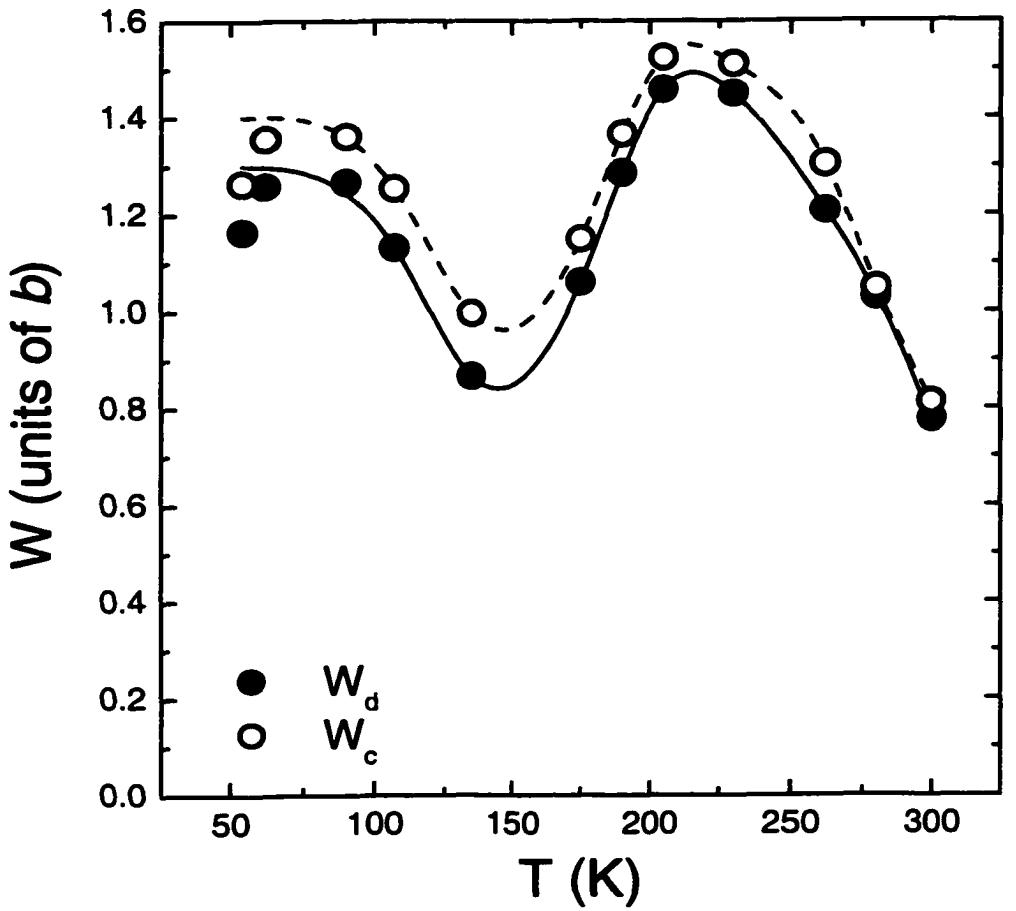
1.6
1.4
1.2
1.0
0.8
0.6
0.4
0.2
0.0
W (units of b)
50
100
150
200
250
300
T (K)
W_d
W_c

Figure 3

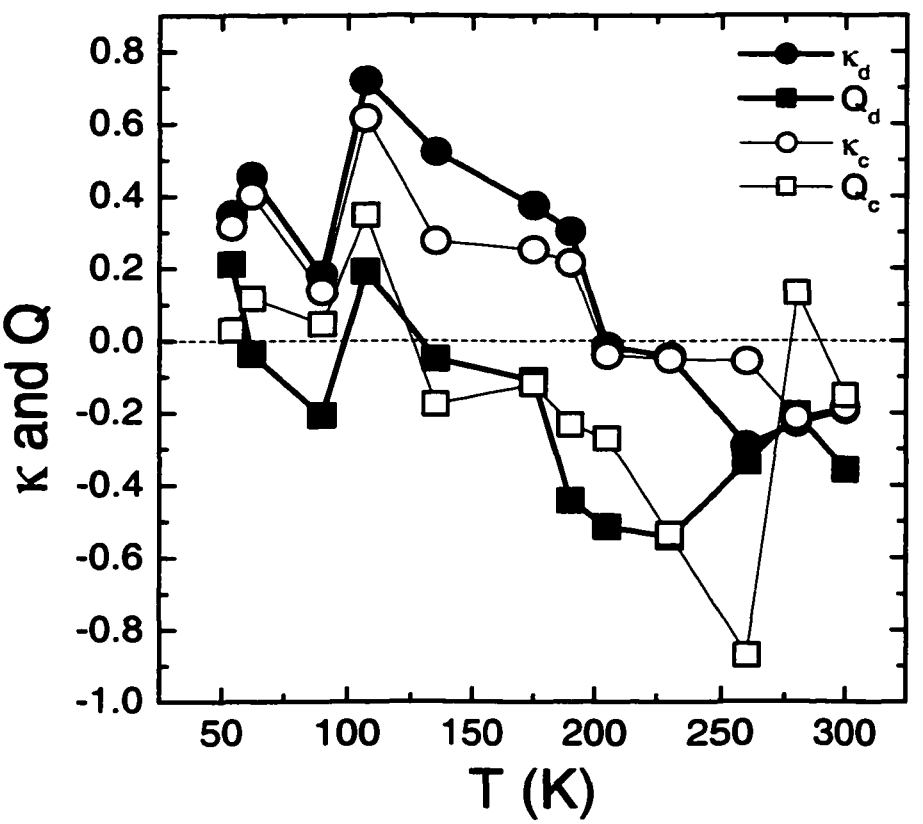
0.8
0.6
0.4
0.2
0.0
-0.2
-0.4
-0.6
-0.8
-1.0
κ and Q
50
100
150
200
250
300
T (K)
κd
Qd
κc
Qc

Figure 4

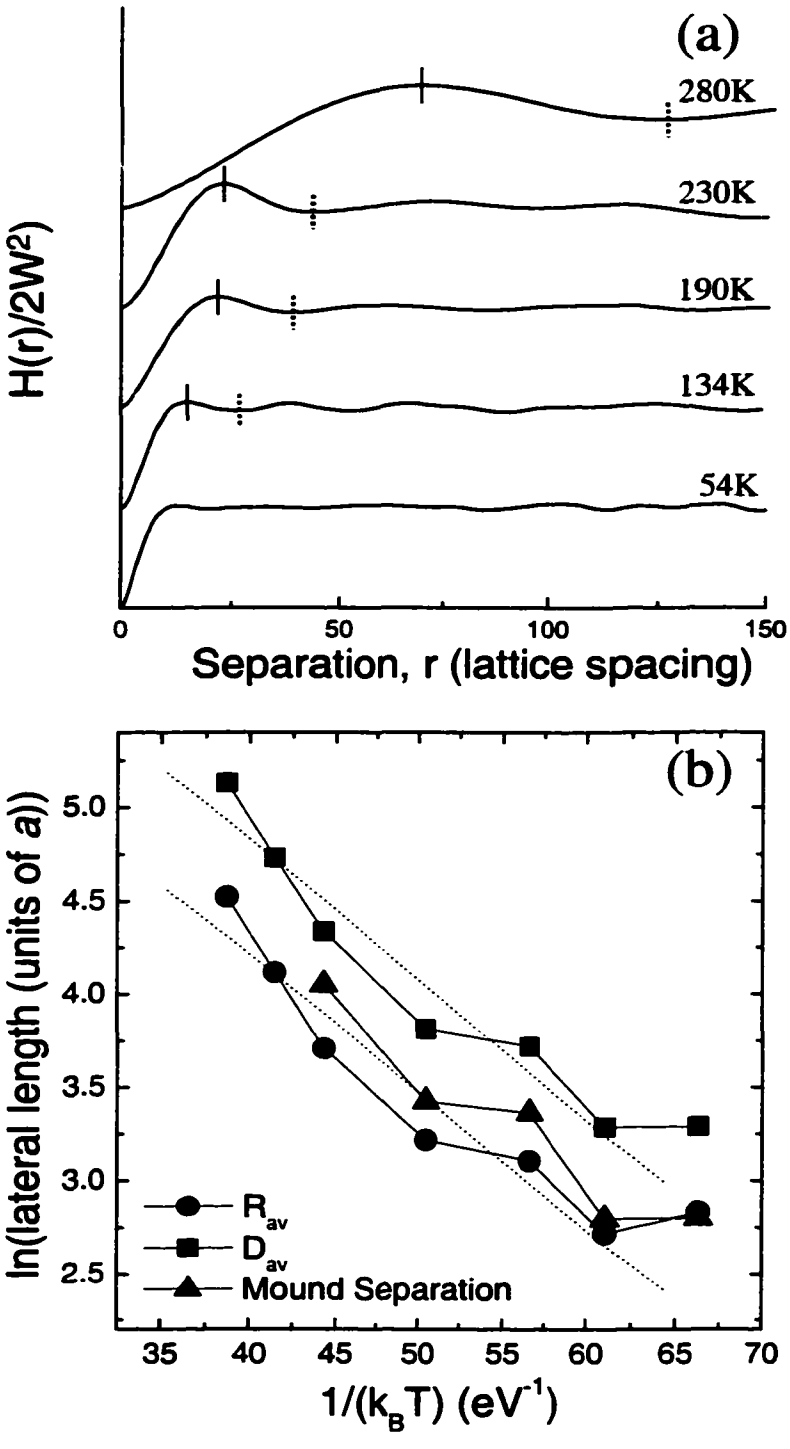
(a)
280K
230K
190K
134K
54K
H(r)/2W²
0
50
100
150
Separation, r (lattice spacing)
(b)
ln(lateral length (units of a))
5.0
4.5
4.0
3.5
3.0
2.5
R_av
D_av
Mound Separation
35
40
45
50
55
60
65
70
1/(k_BT) (eV^-1)

Figure 5

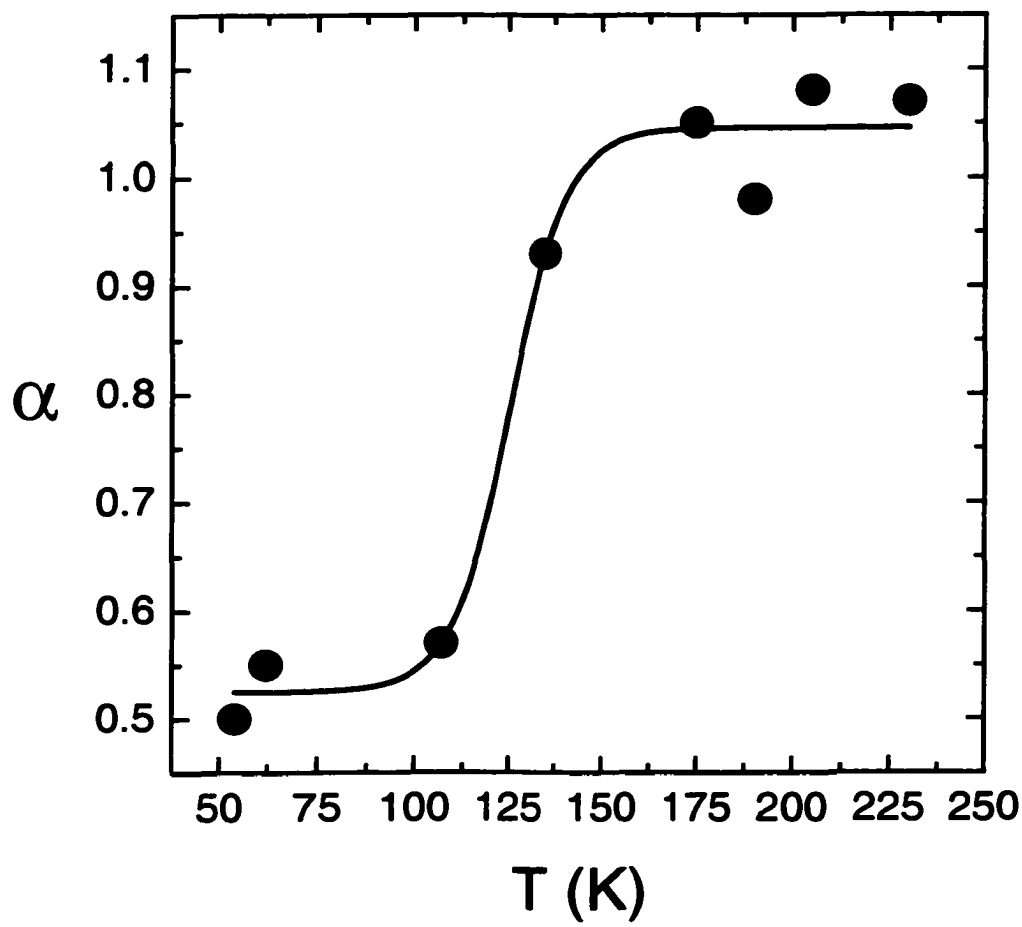

Figure 6

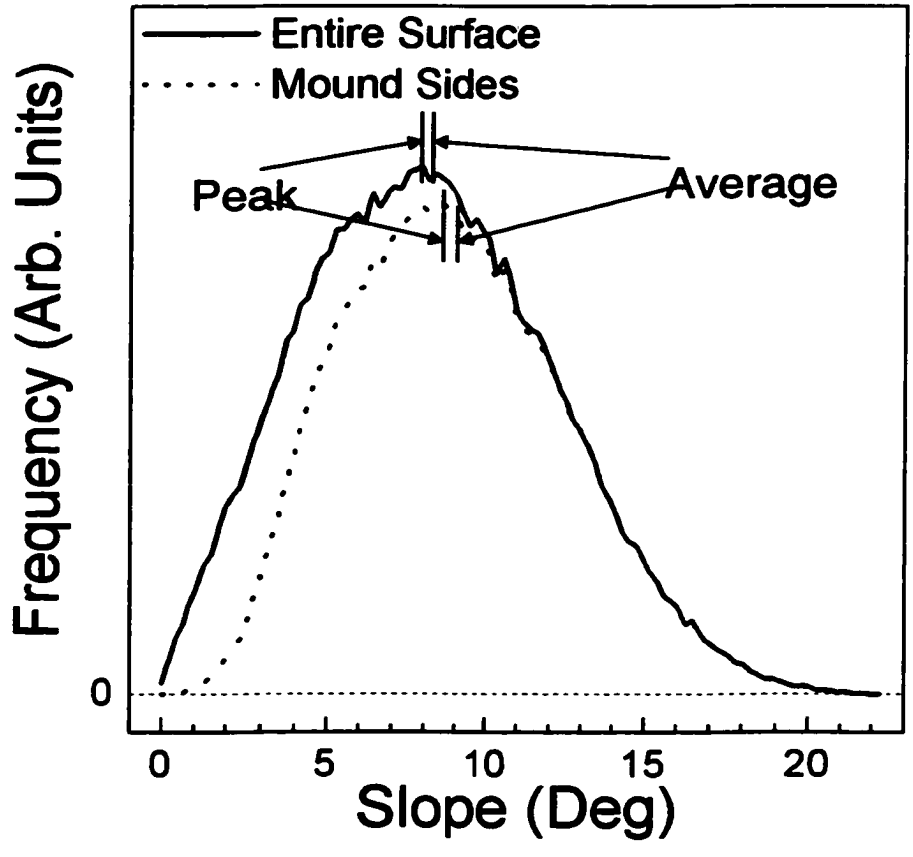
Entire Surface
Mound Sides
Peak
Average
Frequency (Arb. Units)
0
0
5
10
15
20
Slope (Deg)

Figure 7

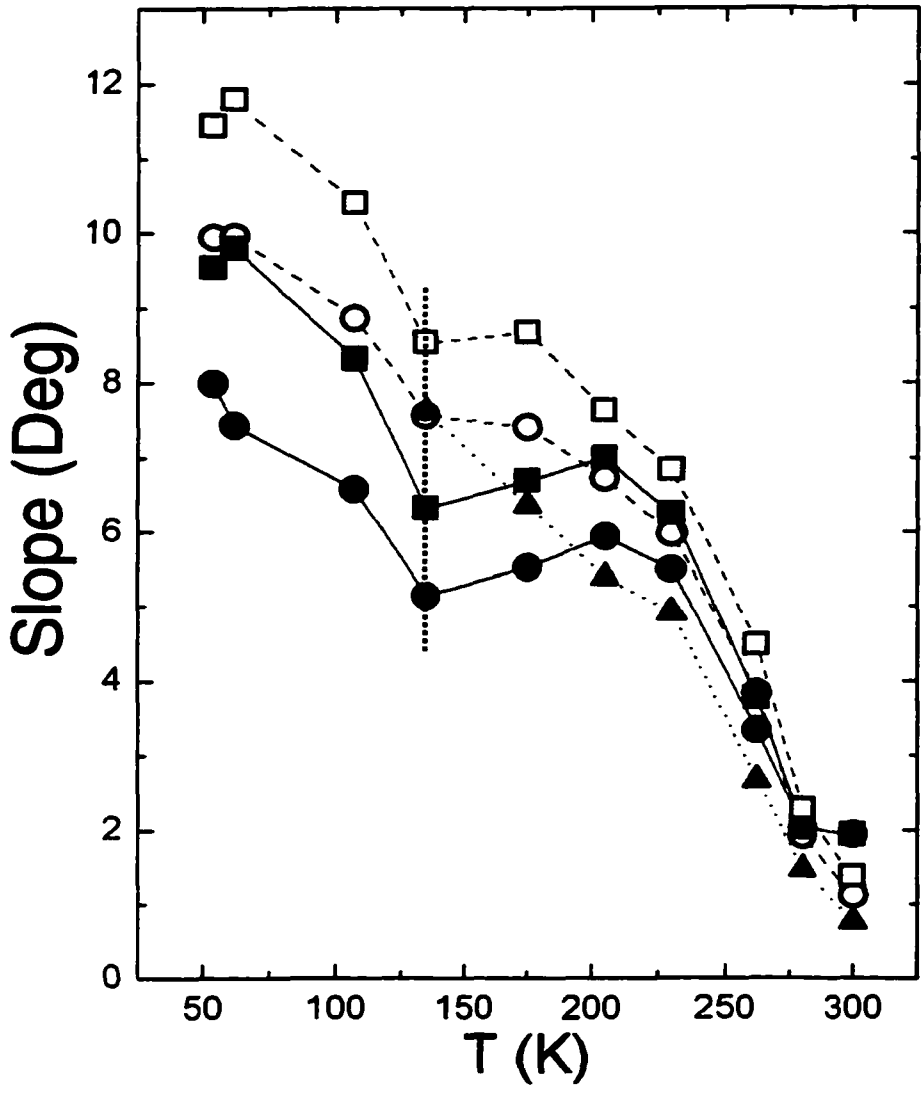

Figure 8

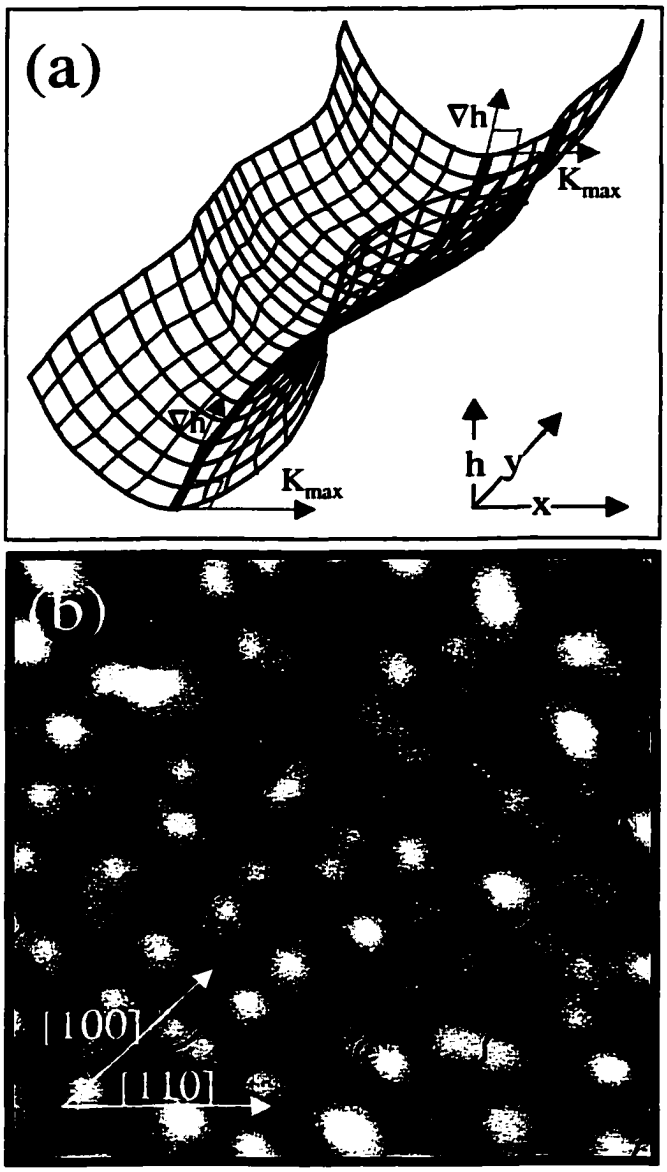

Figure 9

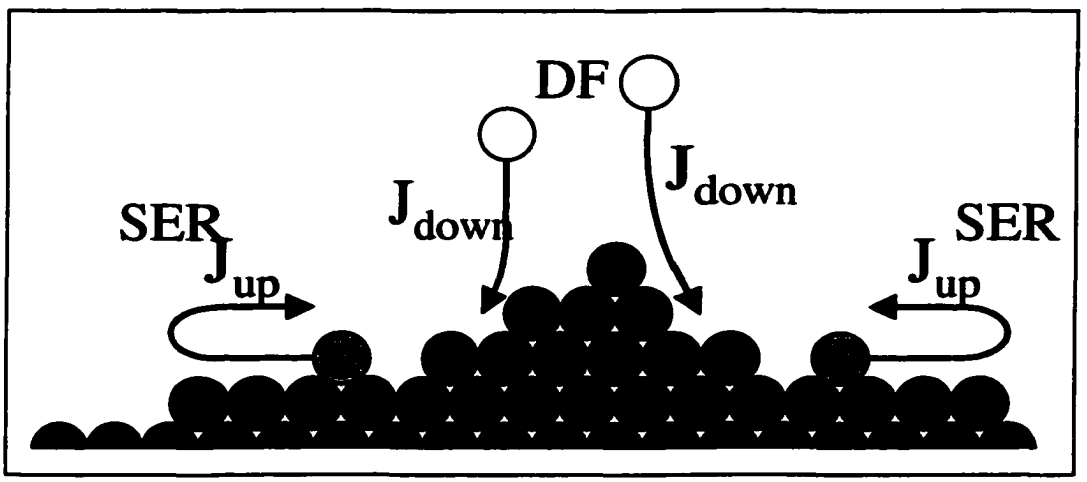

Figure 10

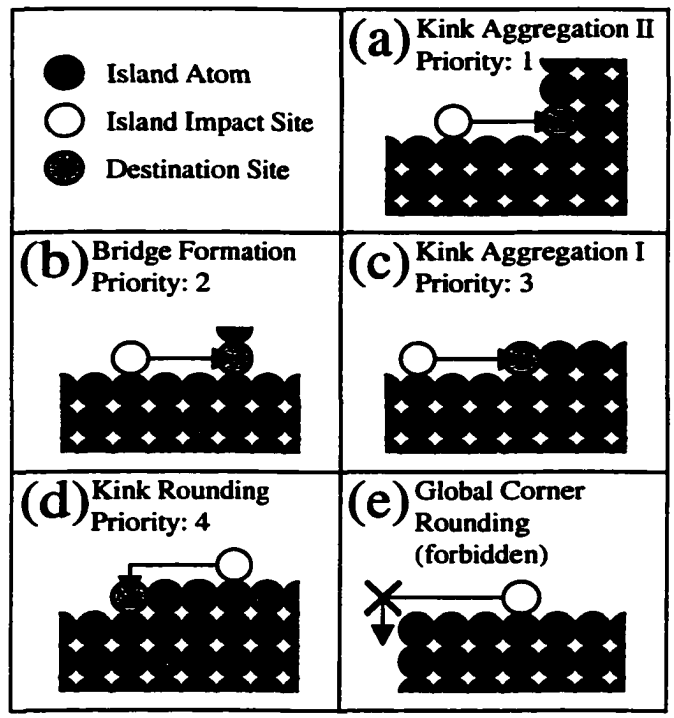
Island Atom
Island Impact Site
Destination Site
(a) Kink Aggregation II
Priority: 1
(b) Bridge Formation
Priority: 2
(c) Kink Aggregation I
Priority: 3
(d) Kink Rounding
Priority: 4
(e) Global Corner
Rounding
(forbidden)

Figure 11

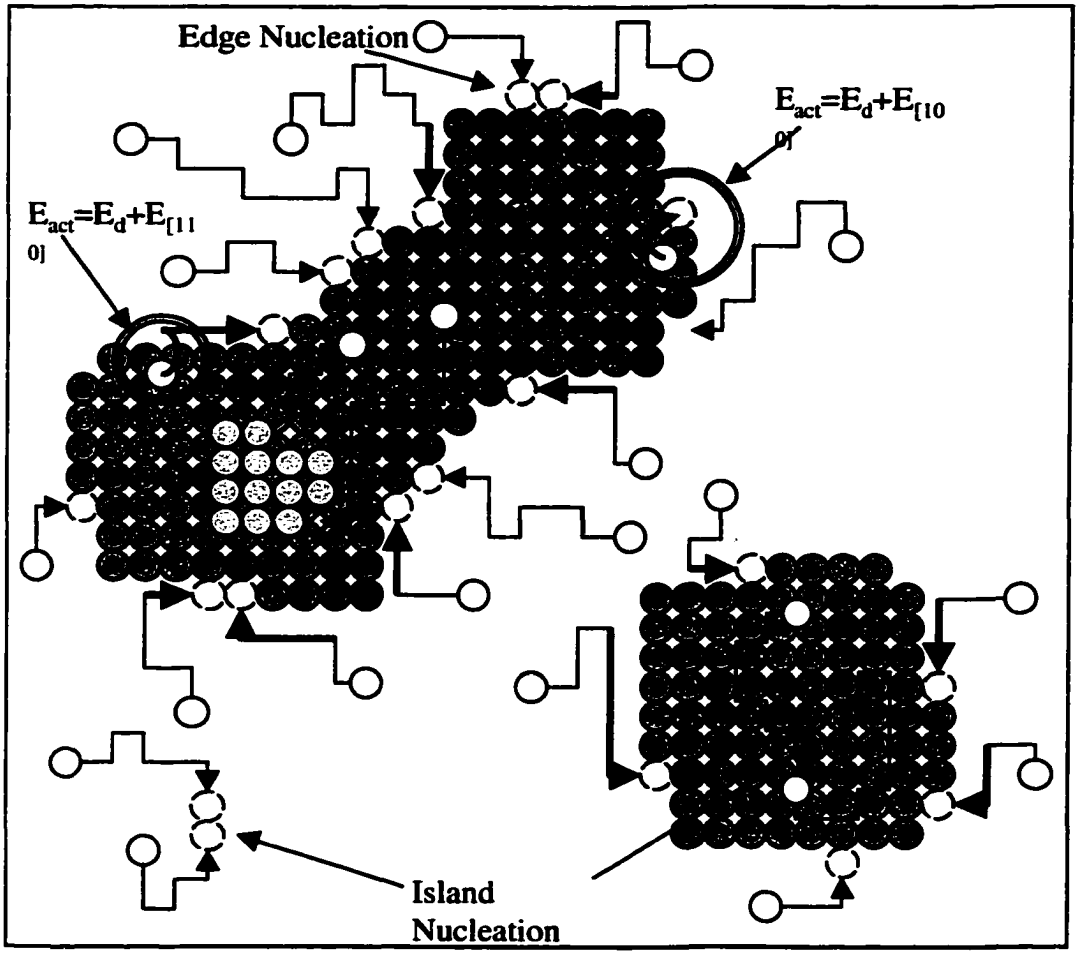
Edge Nucleation
$E_{act}=E_d+E_{[10}$
$0]$
$E_{act}=E_d+E_{[11}$
$0]$
Island
Nucleation

Figure 12

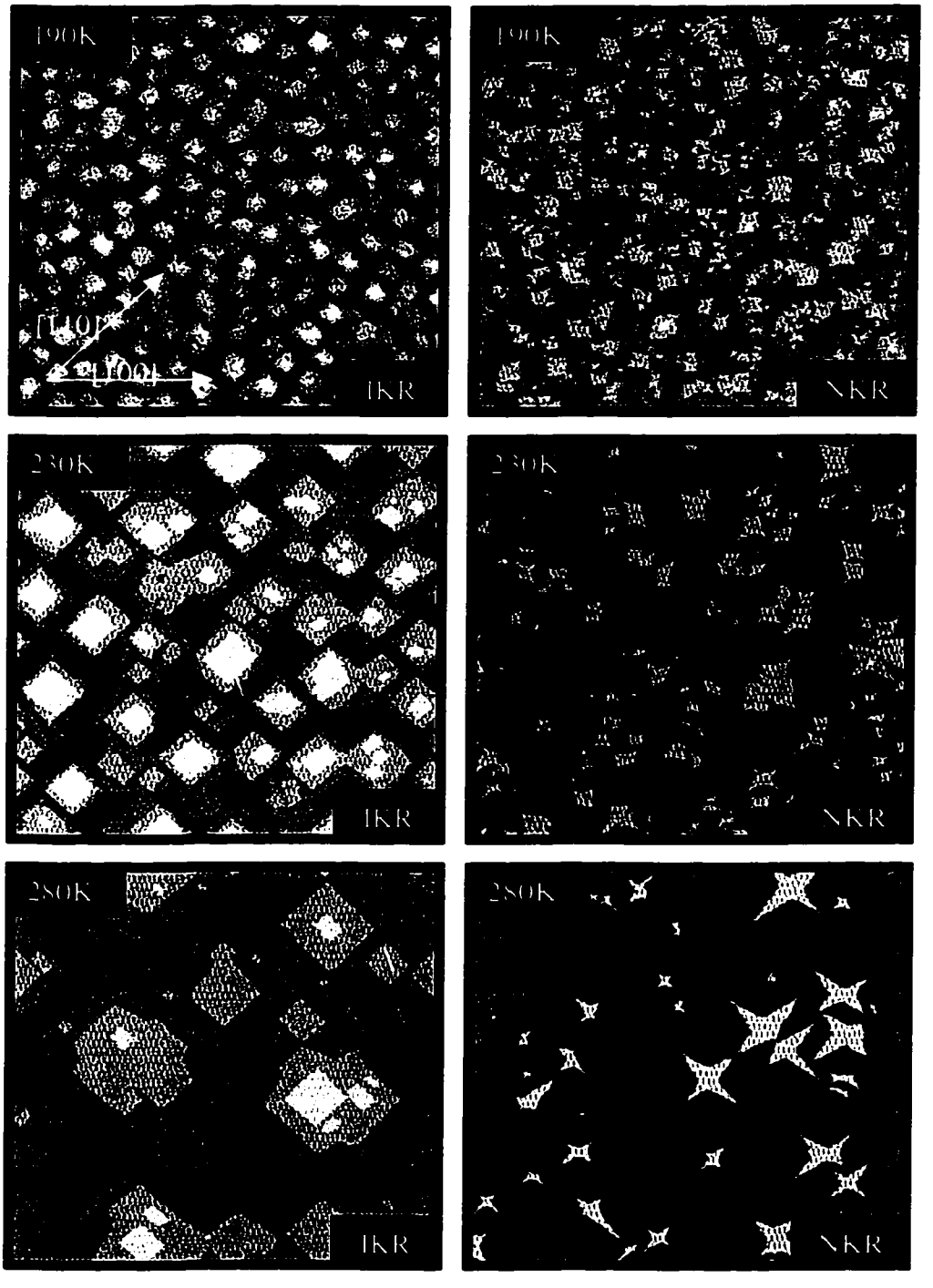

Figure 13

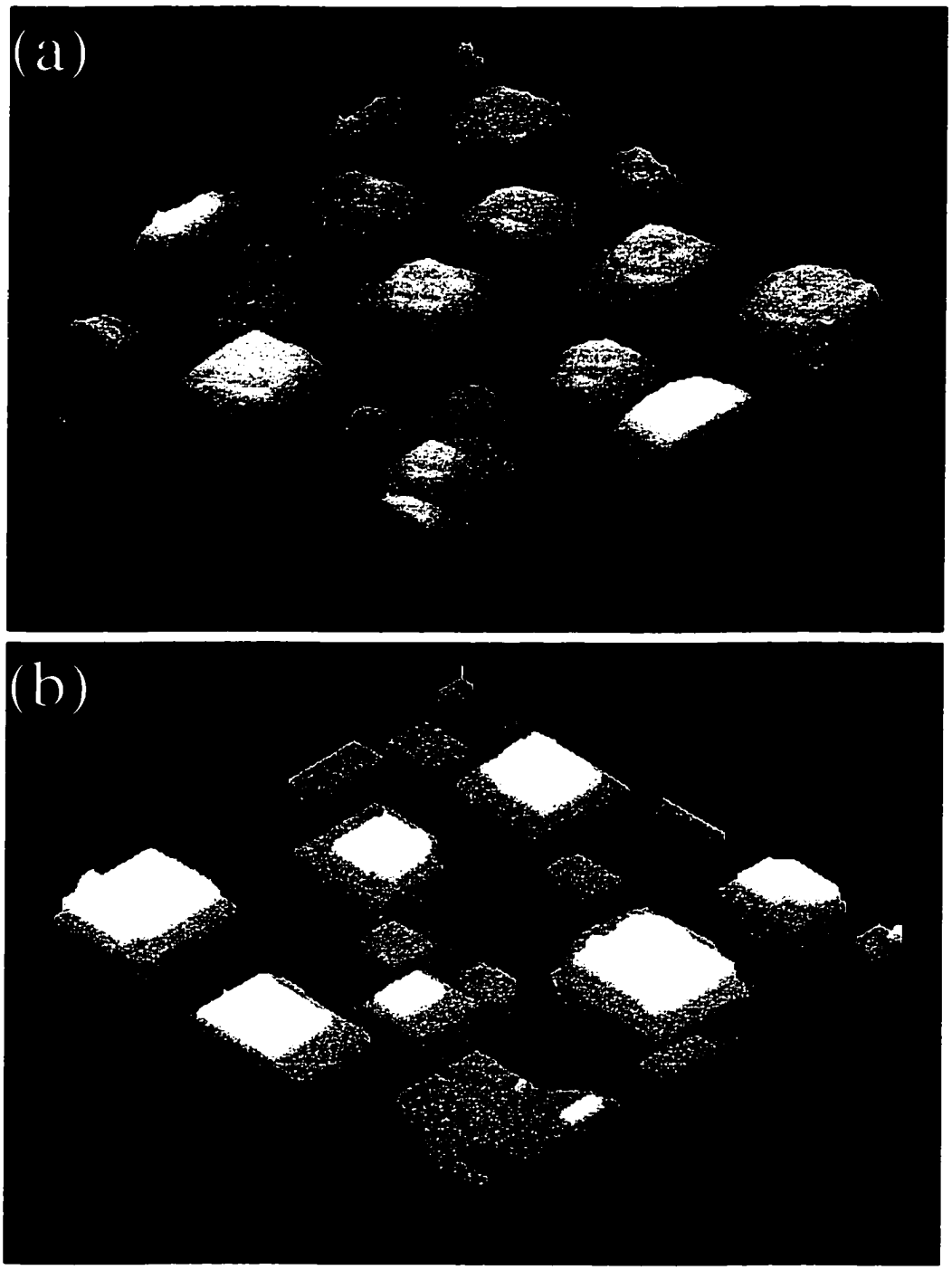

Figure 14

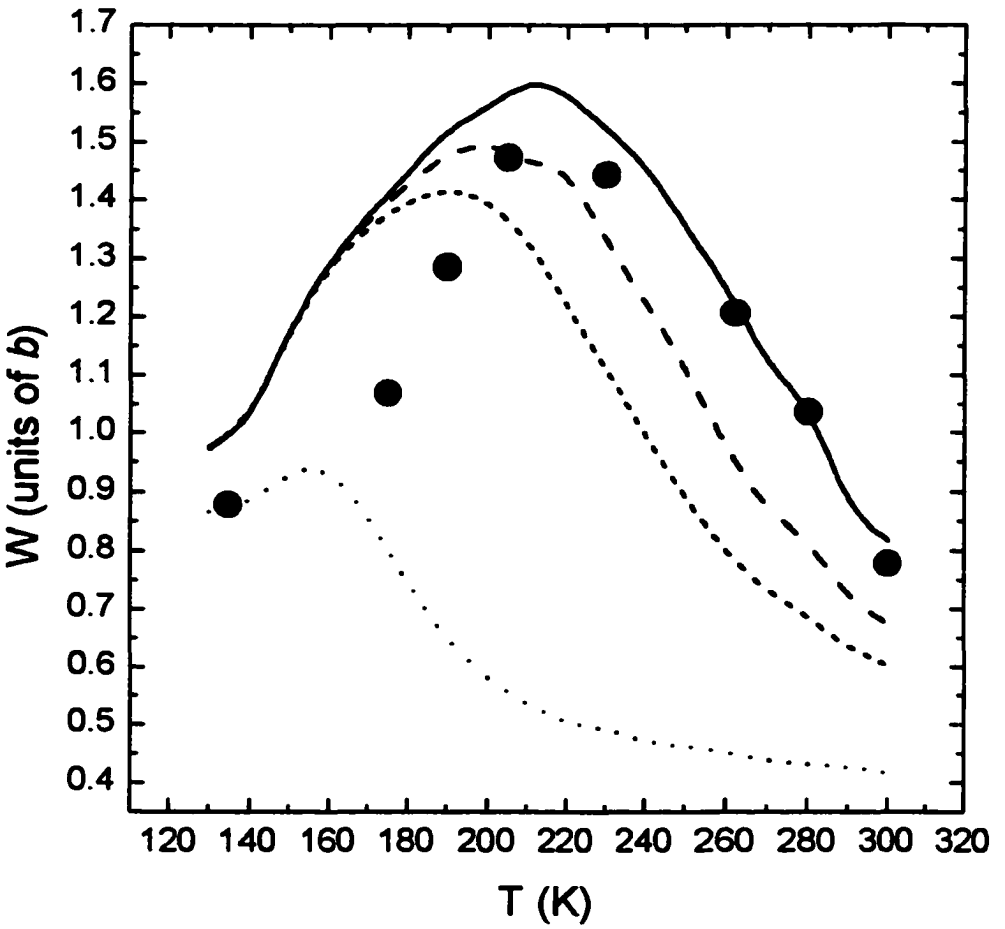
W (units of b)
T (K)
1.7
1.6
1.5
1.4
1.3
1.2
1.1
1.0
0.9
0.8
0.7
0.6
0.5
0.4
120
140
160
180
200
220
240
260
280
300
320

Figure 15

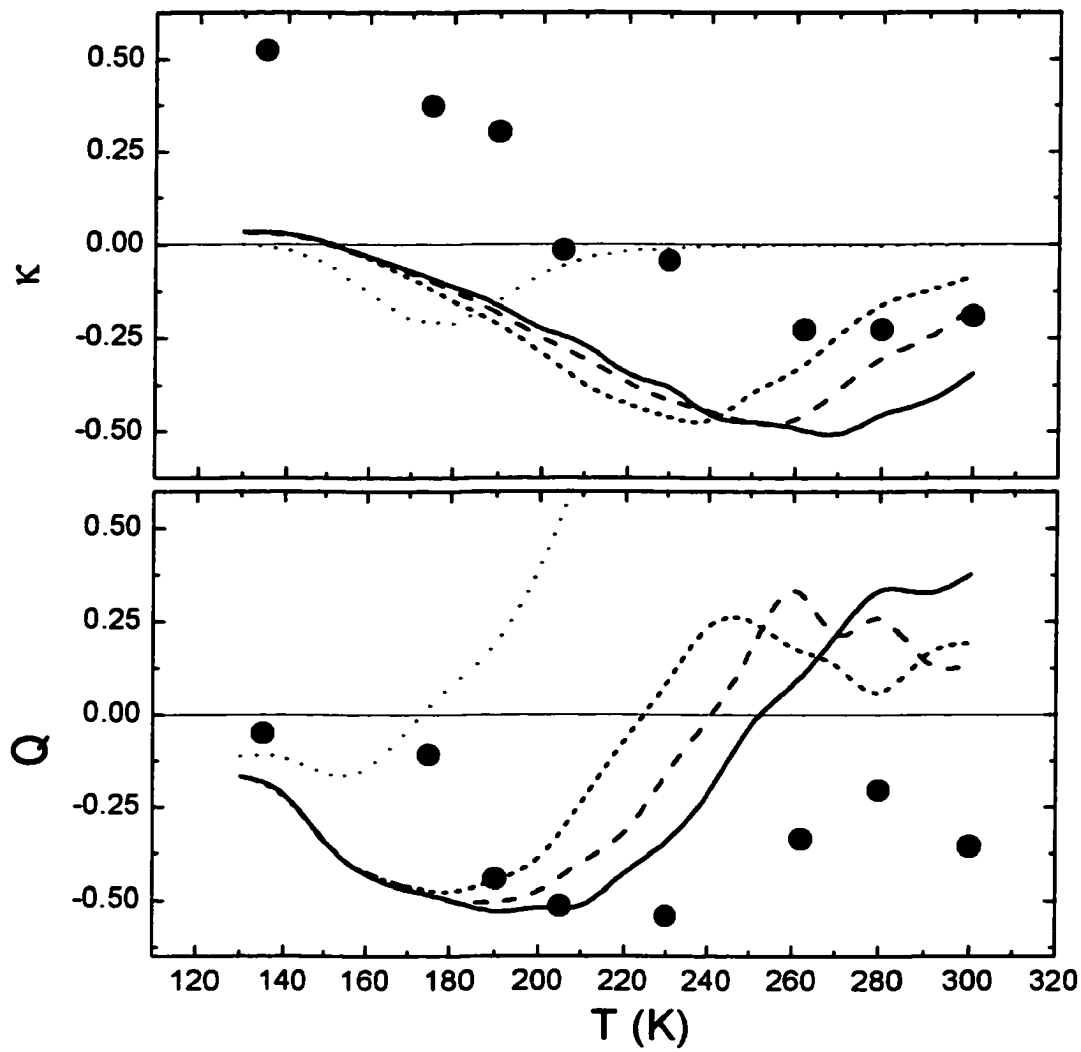
0.50
0.25
0.00
-0.25
-0.50
K
0.50
0.25
0.00
-0.25
-0.50
Q
120
140
160
180
200
220
240
260
280
300
320
T (K)

Figure 16

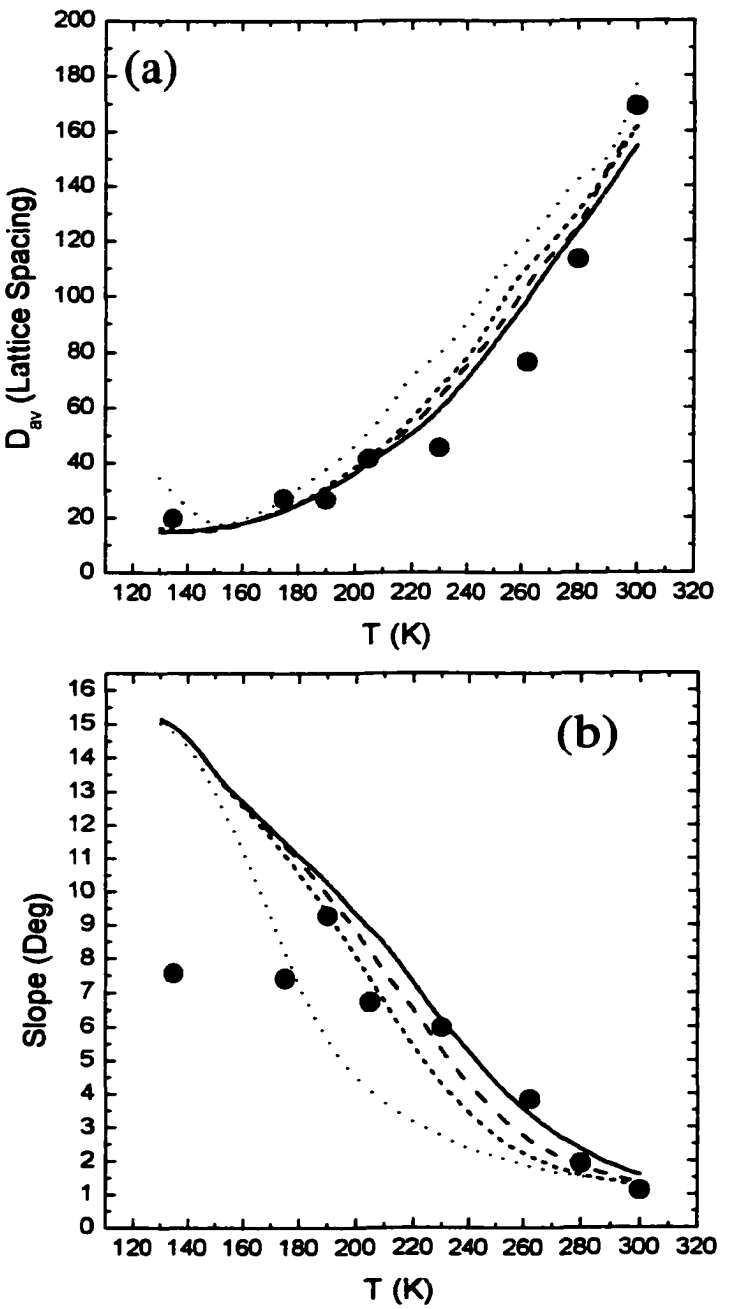

Figure 17

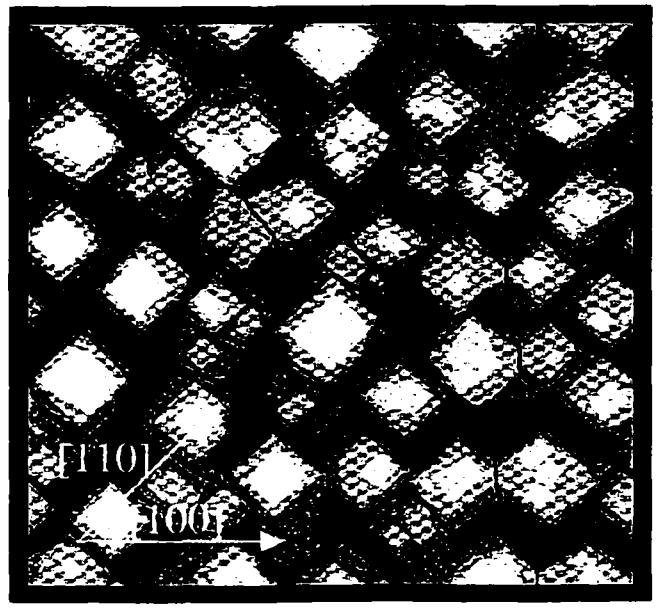

Figure 18

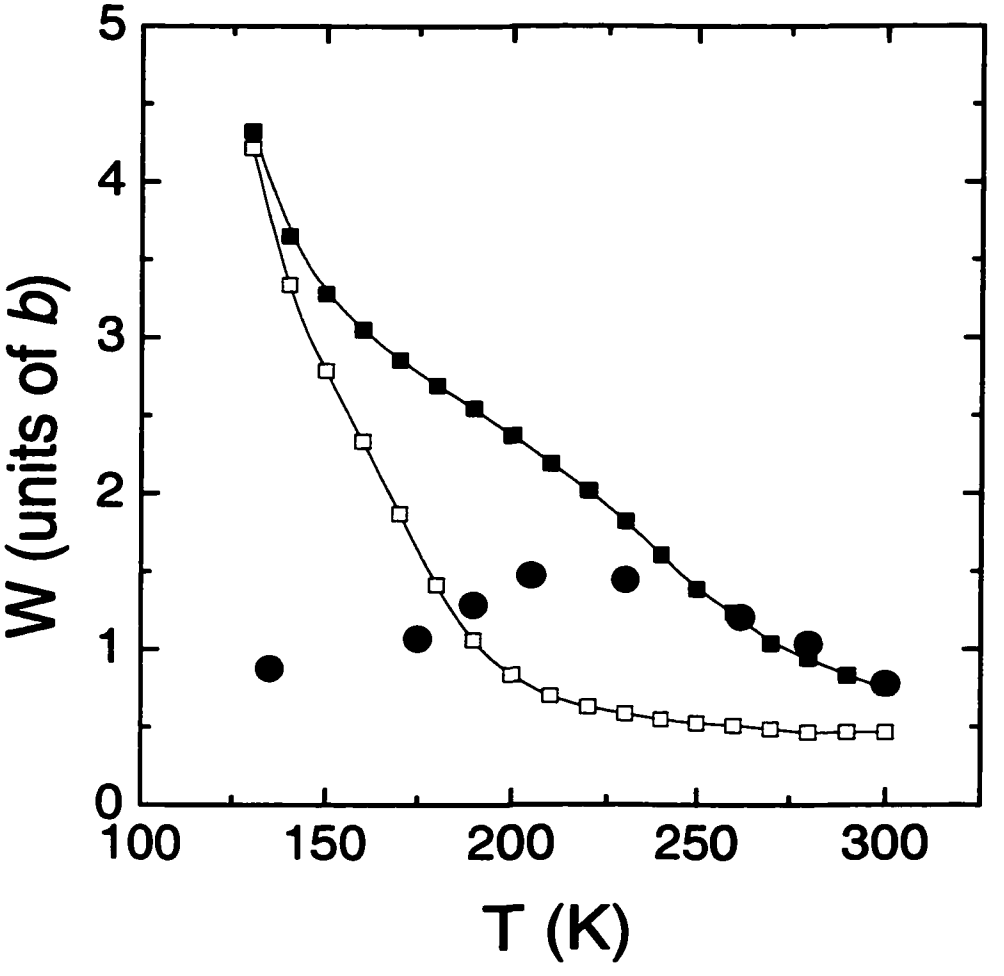

Figure 19

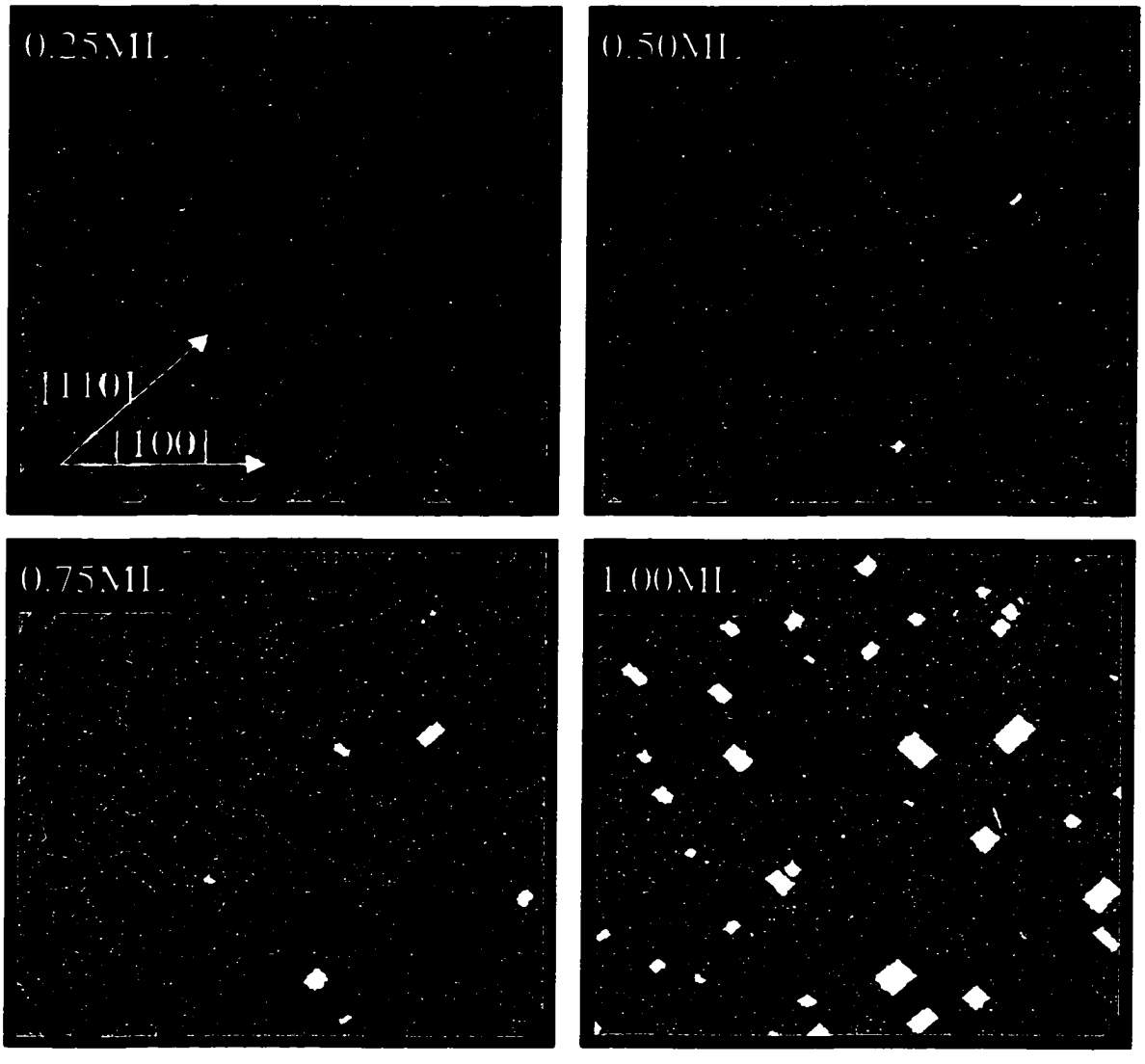

Figure 20

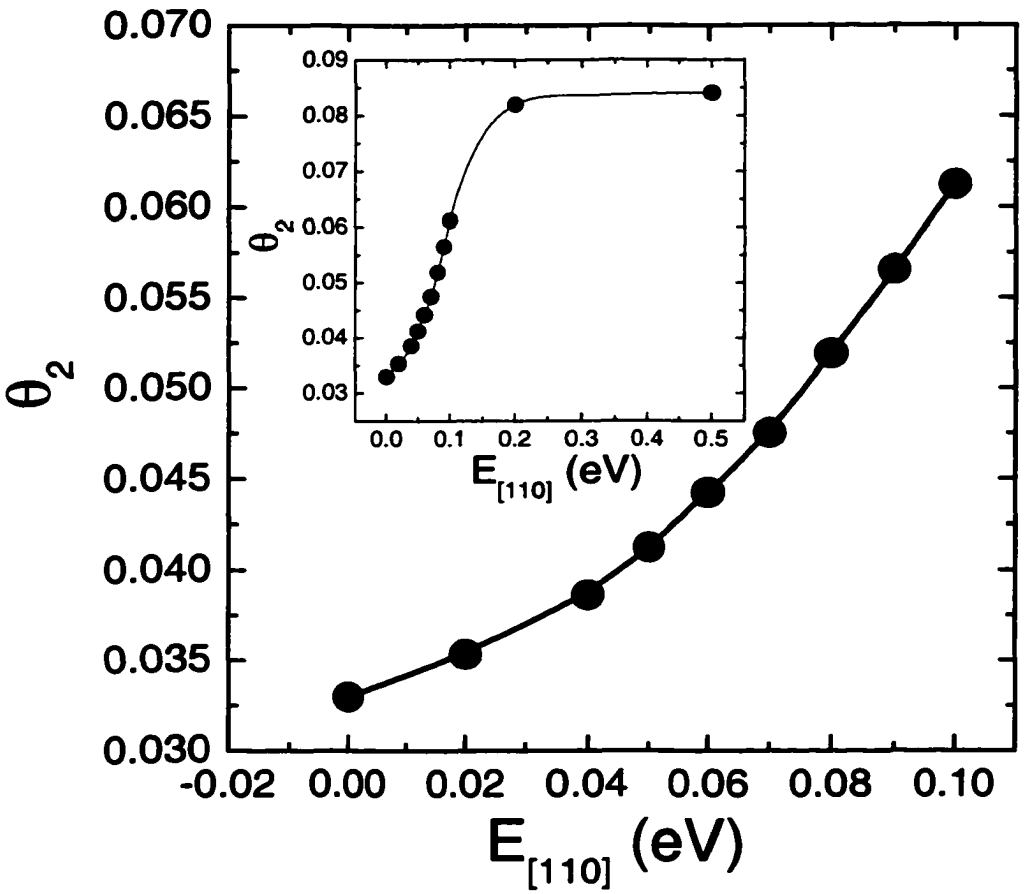
0.070
0.065
0.060
0.055
0.050
0.045
0.040
0.035
0.030
θ2
-0.02
0.00
0.02
0.04
0.06
0.08
0.10
E[110] (eV)
0.09
0.08
0.07
0.06
0.05
0.04
0.03
θ2
0.0
0.1
0.2
0.3
0.4
0.5
E[110] (eV)

Figure 21

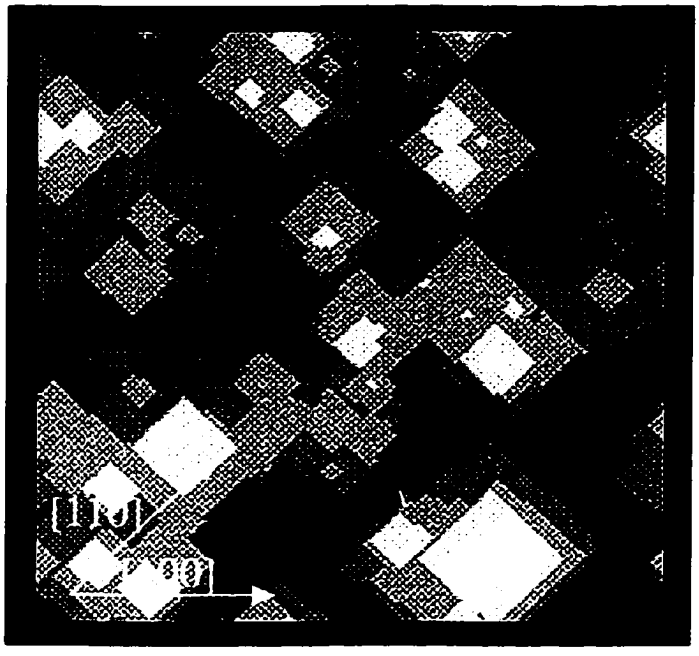

Figure 22

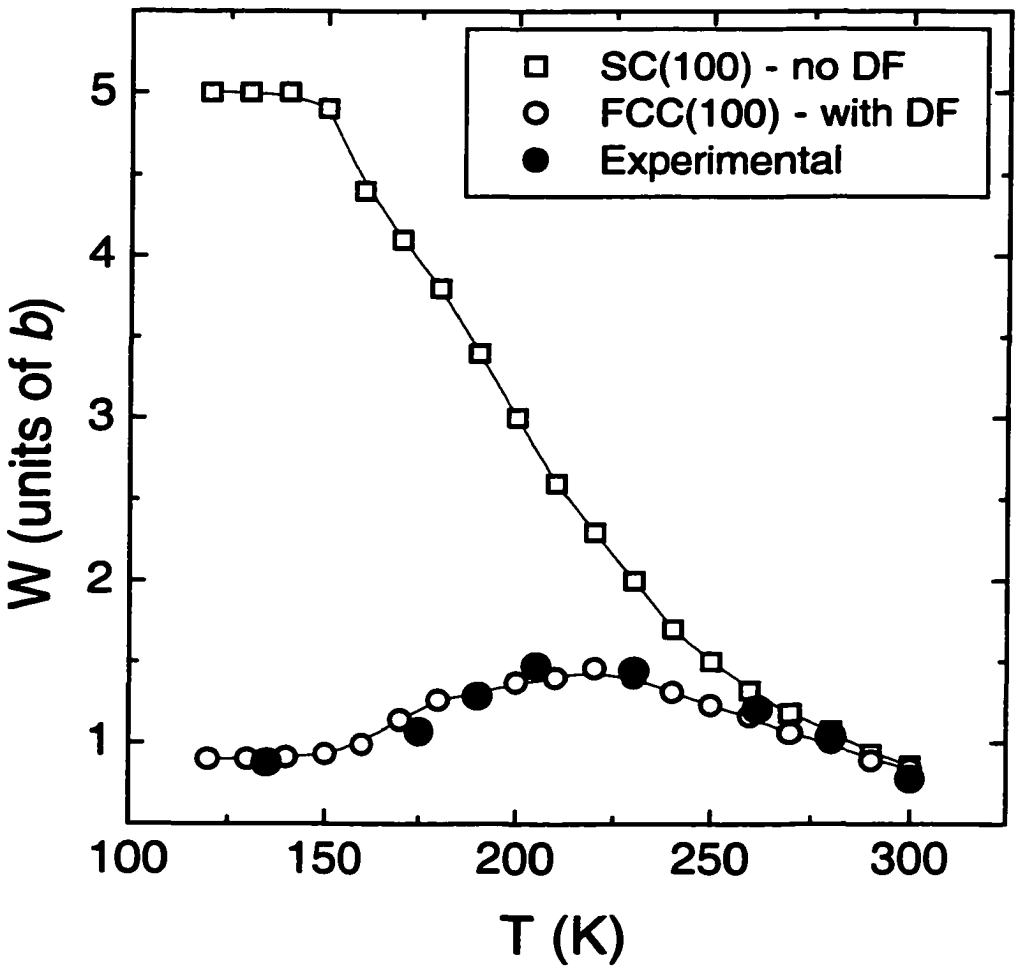
SC(100) - no DF
FCC(100) - with DF
Experimental
W (units of b)
T (K)
1
2
3
4
5
100
150
200
250
300

Figure 23

5. INTERLAYER MASS-TRANSPORT WITH A NON-UNIFORM STEP-EDGE BARRIER: AG/AG(100)

A paper to be submitted to Surface Science.

K.J. Caspersen, A.R. Layson, C.R. Stoldt, P.A. Thiel, and J.W. Evans

H. Wedler, S. Frank, R.J. Behm

Abstract

Interlayer transport is analyzed in the Ag/Ag(100) system, and shown to be consistent with a non-uniform (Ehrlich-Schwoebel) step-edge barrier. We present VTSTM data for second layer nucleation for both deposition of ~1ML films at fixed flux and temperature, T (200, 250, or 300K), and also for tailored two-stage deposition experiments. In the latter, we first create large near-square islands by deposition at higher T, and then populate the second layer by a subsequent deposition at lower T. Behavior is interpreted using an atomistic model for film growth which incorporates different step-edge barriers, E_{se}, at close-packed [110] step-edges, and at kinked or open [100] step edges. We set $E_{se}[100] \approx 0$meV (based on semi-empirical analyses), and find that $E_{se}[110] \approx 70$meV, consistent with a recent estimate from analysis of multilayer growth.

I. Introduction

Early FIM studies of homoepitaxial metal systems [1] revealed the presence of an additional activation barrier to downward diffusion at step edges (relative to the barrier for terrace diffusion). This is commonly referred to as the Ehrlich-Schwoebel or step-edge (SE)

barrier. Villain [2] first emphasized the crucial role of SE barriers in producing unstable growth of epitaxial films on "perfect" low-index single-crystal substrates, as manifested by "mound formation". These SE barriers result in reflection of diffusing adatoms from descending steps, and biased incorporation at ascending steps. This produces a (destabilizing) net lateral mass current in the uphill direction. Metal(100) homoepitaxial systems seem to have small SE barriers (often ~10% of the terrace diffusion barrier), in contrast to metal(111) homoepitaxial systems [3]. Nonetheless, even small barriers produce mound formation, and control the morphology of multilayer films. Thus, accurate determination of these barriers is important.

Analytic mean-field theories have been developed [4,5] and applied [5,6] for 2^{nd} layer nucleation in systems with uniform SE barrier. However, in some cases (particularly for irreversible island formation), fluctuation effects cause dramatic deviations from these mean-field predictions [7]. One strategy which has been applied to avoid these complications is direct simulation of growth using simple atomistic models with a uniform SE barrier and which realistically treat submonolayer deposition [8,9]. The SE barrier is treated as a free parameter, which is adjusted to match observed behavior in initial stages of multilayer growth (e.g., the 2^{nd} layer coverage after deposition of 1ML, or the roughness after deposition of a few layers).

However, analysis of experimentally observed growth behavior for metal(111) systems [10], and recently for Ag/Ag(100) [11], has favored the existence of distinct SE barriers at step edges with different local configurations. Specifically, for Ag/Ag(100), it is anticipated that the SE barrier is negligible along kinked, or open, [100] step edges, but significant along close-packed [110] step edges. This scenario is consistent with the

predictions of earlier theoretical studies using semi-empirical potentials for Ag/Ag(100) and other metal(100) homoepitaxial systems [12-14]. Note however that more precise *ab-initio* treatments still have difficulty estimating such small barriers [15].

Thus, even for the "simple" Ag/Ag(100) system, a more refined analysis of interlayer diffusion is required going beyond the treatments assuming a uniform SE barrier. Such an analysis is presented in this paper by combining results from variable-temperature scanning tunneling microscopy (VTSTM) experiments (see Sec.II) with kinetic Monte-Carlo simulations of appropriate atomistic models. We analyze two types of complementary experiments. The first (Sec.III) involves deposition of ~1ML films with fixed flux (F) and substrate temperature (T), so the evolving submonolayer morphology includes a mixture of different types of step edges, and the effective SE barrier is a mixture of those for open and closed steps. The second (Sec.IV) involves preparing near-square submonolayer islands (with primarily [110] step edges) by a first deposition at higher T, and then performing subsequent deposition at lower T to assess 2nd nucleation on the prepared islands. Now, the effective SE barrier is mainly controlled by that of close-packed step edges. Thus, the two experiments are complementary and can be used to assess the consistency of SE barrier estimates. Some concluding remarks are provided in Sec.V.

II. Experimental Details

The 200K and 250K experiments in Sec. III and the first experiment is Sec. IV were performed at the University of Ulm using a home-built beetle type VTSTM designed for operation at various temperatures in the range from 115 K up to 500 K, details described elsewhere [16]. The 300K experiment in Sec. III and the second experiment in Sec. IV were performed at Iowa State University using Omicron VTSTM [17]. At both sites pure Ag was

deposited on to the (100) surface of a single Ag crystal under Ultra High Vacuum (UHV). The fluxes used were as noted below. Also at both sites the surface was cleaned by repeated cycles of Ar^+ ion sputtering followed by annealing. The images were taken as soon after deposition as possible, and on as broad of terrace as possible. This was done to reduce post-deposition restructuring and effects generated by step edges.

III. Second-Layer Nucleation During Deposition of ~1ML films

A. Film Morphology and Modeling

During the initial stages of film growth, deposited atoms diffuse across the surface irreversibly nucleating new islands and aggregating with existing islands [3]. Below θ_T will denote the (total) film coverage in monolayers (ML). In the low-coverage precoalescence regime, islands have compact near-square shapes with close-packed [110] step-edges. The compactness reflects efficient edge diffusion [3], and the squareness reflects the preferred equilibrium shape [18]. Coalescence of islands, which becomes prevalent for θ_T~0.3ML, produces some kinked or open step edges. Above θ_T~0.5ML, ramified clusters of coalesced islands are formed with a substantial population of kinked step edges. Some of these persist as the coverage approaches 1ML, where the first layer is occupied apart from a remaining isolated irregular vacancy regions [11].

We describe this behavior using a model for irreversible island formation with active edge diffusion [11]. We incorporate terrace diffusion with the known activation barrier of $E_d \approx 0.40$eV. For edge diffusion, atoms reaching island edges (either by diffusion or direct deposition) are typically moved instantaneously to the closest doubly-coordinated kink site where they are irreversibly incorporated. This choice reflects the rapid diffusion of adatoms along close-packed step-edges (with a barrier of only $E_e \approx 0.25$eV [15]), and also active

rounding of kink sites. The latter is necessary to avoid a shape-instability in island growth, and to achieve the compact island shapes observed at least down to 200K. In this model, we include distinct SE barriers for closed and kinked step edges as free parameters. We set all attempt frequencies for intra- and inter-layer diffusion to equal $\nu \approx 10^{13}$/s.

It is clear that second layer nucleation will be controlled by some average of the SE barriers for closed and kinked step edges (cf. Sec.I), since significant populations of both occur particularly in the post-coalescence and percolation regimes. Thus, it is important that the model accurately describes the relative populations of these different step edges. Otherwise estimates of the SE barriers would be compromised. We believe, however, that this aspect of the growth morphology is quite robust and described well by the above model (which contains no parameters describing edge diffusion to which the relative populations of step edges are sensitive).

B. Results

Estimated 2nd layer coverages (θ_2) after deposition of ~1ML films with F≈0.0065 ML/s are shown in Fig.1 for a deposition temperature of 200K, and Fig.2 for 250K (followed by a quench to freeze the morphology). More specifically, in each experiment, images of a number of regions of the surface were obtained, and θ_T and θ_2 were assessed for each. These pairs are shown on the plots, with the area of the symbol scaled with the area of the associated image. Also shown in Fig.1 and Fig.2 are the predictions of our model for θ_2 versus θ_T (with the appropriate F and T) choosing $E_{se}[100]=0$ and for various choices of $E_{se}[110]$ (shown). A consistent best fit of the data for both temperatures is achieved by

setting $E_{se}[110] \approx 0.07$eV. (Note that the two high θ_2-points in Fig.1 for low θ_T come from images on particularly narrow terraces, and are thus likely corrupted.)

We also performed a ~1ML deposition experiment at 300K with F≈0.02ML/s , and assessed from a single (large) region the second layer coverage as $\theta_2 \approx 0.059$ ML just after deposition (for $\theta_T \approx 1.02$ ML). See Fig.3a. In Fig.4 we show the model predictions θ_2 under these conditions. The simulations were carried out on a lattice constructed to be the same size as the experimental image, therefore the solid black circles represents the average simulated θ_2 and the open circles represent the statistical fluctuations indicative of this image size. Hence if the statistical fluctuations generated simulation are consistent with experiment the experimental value should not deviate by more than two standard deviations (σ) of the θ_2 distribution, and by inspection of Fig.4 leaves a range of possibly consistent $E_{se}[110]$ values of 0.07eV-0.10eV with the median being 0.85eV.

In the above 300K experiment, there was no quench following deposition, and the second layer coverage was observed to decrease significantly on the time scale of ~1hr (Fig.3b). The decay is associated with an Ostwald ripening process where second layer islands dissolve and their atoms are captured by the edges of first layer vacancies [18]. In the above analysis, we use the value of θ_2 at a time (denoted by "t=0") immediately after deposition, and thus extrapolate the curve in Fig.3 back to this time. To extrapolate the data to t=0 we fit the θ_2 data to an exponential decay curve ($\theta_2=0.0036+0.056\exp[-t/78.6]$) and then determined that $\theta_2=0.059$ML. Since θ_2 decays most quickly for short t, it is important to obtain the first STM image at a time t_1 soon after deposition. In the current experiments,

$t_1 \approx 13$ min., greatly improving on previous data with $t_1 \approx 45$min. [9,11], although θ_2-behavior in both data sets is consistent.

IV. Second-Layer nucleation for Two-Stage Deposition

In the first experiment, 0.16ML of Ag was first deposited at a higher temperature of 270K (with F≈0.0033ML/s), then the sample was cooled to 195K (taking 5-10min.), and second deposition of 0.03ML performed (using the same F). STM imaging was then performed at 125K after further cooling. The focus of the analysis here was on whether or not "small" second layer islands nucleated on top of "large" first layer islands, rather than consideration of the 2nd layer coverage. Specifically, for each first layer island size, we compare the total population of such islands with the sub-population of these islands upon which second layer islands were nucleated. We plot in Fig.5a the fraction, f, populated on top versus first layer island size (S_1), akin to analyses in [4-6]. Note that population on top with multiple islands effectively does not occur under these conditions (due to the low second dose). Also note that the simulations are, in a sense, immediately quenched to 0K therefore any post-deposition cluster diffusion is neglected, also the STM may have difficulty in resolving very small islands. Therefore the smallest islands (i.e. dimers) are not counted as islands, for they are quite small and dimer diffusion maybe active between the end of deposition and the first STM scan (typically 10-20 minutes).

In the second experiment, 0.20ML of Ag was first deposited at 320K (with F≈0.002ML/s), then the sample was cooled to 235K and another 0.30ML was deposited (with F≈0.02ML/s). In this case (mainly because of the high second dose), most first layer islands are populated on top, and many have more than one second layer island. See Fig.5b.

Thus, here it is natural to plot the coverage on top if islands (θ_{top}) versus S_1. Experimental and simulated images of this second experiment are shown in Fig.6.

Results from these simulations are also shown in Fig.4 choosing $E_{se}[100]=0$ and for various choices of $E_{se}[110]$. For the first experiment the best fit appears to be $E_{se}[110]\approx 0.06$eV. And likewise for the second experiment $E_{se}[110]\approx 0.06$eV appears to be the best fit. Note that statistics are poor for f and θ_{top} for S_1 far larger than the average, due to the limited population of such islands. Also one may observe that for in f and θ_{top} appear to have a maximum at the approximately the point where the statistics begin to diverge. This is not a coincidence, it means that for an island to reach this large size it must be made up of two (or more) islands that have coalesced. These large islands will have a large number of [100] edges due to the coalescence process, and therefore they will have a smaller average E_{se} than normal shaped islands decreasing f and θ_{top}.

V. Comments and Conclusions

First, we compare our best estimate of the close-packed step edge barrier, $E_{se}[110]\approx 70$meV, with those of semi-empirical predictions. Consistency with our previous multilayer studies either exploring the T-dependence of the roughness of 25ML films [11], or monitoring kinetic roughening at various T [19]. We have already noted that some of these studies determined a negligible barrier for open, or kinked, step edges [12-14]. Most studies focus on assessing the barrier for perfect close-packed [110] step edges (which is taken as the lower of the barriers for direct hopping or exchange processes). Estimates for $E_{se}[110]$ from the latter are 85meV from EMT [20], 114meV also from EMT [13], 110meV from EAM-FDB [14], and 30meV from EAM-VC [14]. *Ab-initio* GGA studies yield 100meV for

hopping, but 0meV for exchange [14,15], although with considerable uncertainty (±50meV). We believe our current estimate of 70meV obtained from comparing experiment with appropriate modeling to be the most reliable.

As an aside, we should note that previous atomistic modeling of growth experiments using models with a uniform SE barrier extracted estimates of E_{se}≈25-30meV [9,17]. This effective value can be thought of as some non-trivial weighted average of E_{se}[100]≈0meV and E_{se}[110]≈70meV.

In our modeling, we have assumed equal prefactors or attempt frequencies for intra- and inter-layer diffusion. EAM-FBD calculations indicate that the prefactor is a factor~3 higher for the latter [14]. Obviously, the choice of prefactor affects the estimate of E_{se} (higher prefactors yielding higher E_{se}). Some recent studies have suggested that dramatic differences can occur in these prefactors for metal(111) homoepitaxial systems [21,22]. There is no clear evidence of such an effect for Ag/Ag(100), and more refined modeling of this system should perhaps first incorporate a more detailed description of step edge structure and barriers before attempting to assess differences in prefactors.

We also are aware that the island shapes described here are growth, not equilibrium, island shapes [23]. Growth shapes are the correct choice for the second layer nucleation (Sec. III), however for double deposition (Sec IV) there is a chance for the islands to equilibrate between depositions. While the cold temperature in the first experiment may preclude this, the relatively high temperatures in the second experiment may allow the islands to equilibrate significantly. Where the equilibrated island shape is not exactly square but rather square-like with rounded corners [24]. This means that the equilibrated island will have more open edges and therefore an overall smaller average E_{se} and this feature could

account for the apparently small $E_{se}[1\,1\,0]$ seen in the second experiment. Currently we a focusing on this by employing tailored simulations where atoms are deposited on one island at a time where the shape of the island is an imput parameter.

Acknowledgments

KJC, ARL, CRS, PAT and JWE were supported for this work by NSF Grant CHE-0078596. Their work was performed at Ames Laboratory, which is operated for the U.S. Department of Energy by Iowa State University under Contract No. W-7405-Eng-82. SF gratefully acknowledges a fellowship of the Deutsche Forschungsgemeinschaft (DFG) within the Graduiertenkolleg 'Molekulare Organisation und Dynamik an Grenz- und Oberflächen.

References

[1] G. Ehrlich and H. Hudda, J. Chem. Phys. **44**, 1039 (1966); R.L. Schwoebel and E.J. Shipsey, J. Appl. Phys. **37**, 3862 (1966).

[2] J. Villain, J. Physique I **1**, 19 (1991).

[3] *Morphological Organization in Epitaxial Growth and Removal*, edited by Z. Zhang and M.G. Lagally (World Scientific, Singapore, 1997).

[4] J. Tersoff, A.W. Denier van der Gon, and R.M. Tromp, Phys. Rev. Lett. **72**, 266 (1994).

[5] J.A. Meyer, J. Vrijmoeth, H.A. van der Vegt, E. Vlieg, and R.J. Behm, Phys. Rev. B **51**, 14790 (1995); P. Smilauer and S. Harris, *ibid*, **51**, 14798 (1995).

[6] K. Bromman, H. Brune, H. Roder, and K.Kern, Phys. Rev. Lett. **75**, 677 (1995).

[7] J. Rottler and P. Maass, Phys. Rev. Lett. **83**, 3490 (1999); J. Krug, P. Politi, and T. Michely, Phys. Rev. B **61**, 14037 (2000); S. Heinrichs, J. Rottler, and P. Maass, *ibid*, **62**, 8338 (2000).

[8] M.C. Bartelt and J.W. Evans, Phys. Rev. Lett. **75**, 4250 (1995); J.G. Amar and F. Family, Phys. Rev. B **52**, 13801 (1995).

[9] C.-M. Zhang, M.C. Bartelt, J.-M. Wen, C.J. Jenks, J.W. Evans, and P.A. Thiel, Surf. Sci. **406**, 178 (1998).

[10] M. Henzler, T. Schmidt, and E.Z. Luo, in *The Structure of Surfaces IV* (World Scientific, Singapore, 1994); J. Jacobsen, K.W. Jacobsen, P. Stoltze, and J. Norskov, Phys. Rev. Lett. **74**, 2295 (1995).

[11] K.J. Caspersen, C.R. Stoldt, A.R. Layson, M.C. Bartelt, P.A. Thiel, and J.W. Evans, Phys. Rev. B **63**, 085401 (2001).

[12] Ch. Teichert, Ch. Ammar, and M. Klaua, Phys. Stat. Sol. A **146**, 223 (1994).

[13] J. Merikoski, I. Vattulainen, J. Heinonen, and T. Ala-Nissila, Surf. Sci. **387**, 167 (1997).

[14] U. Kurpick and T.S. Rahman, Phys. Rev. B **59**, 11014 (1998).

[15] B.D. Yu and M. Scheffler, Phys. Rev. Lett. **77**, 1095 (1996); Phys. Rev. B **55**, 13916 (1997).

[16] S. Günther, Ph.D. dissertation, Universität Ulm (1995).

[17] C.R. Stoldt, K.J. Caspersen, M.C. Bartelt, C.J. Jenks, J.W. Evans, and P.A. Thiel, Phys. Rev. Lett. **85**, 800 (2000).

[18] P.A. Thiel and J.W. Evans, J. Phys. Chem. B **104**, 1663 (2000).

[19] A.R. Layson, C.R. Stoldt, K.J. Caspersen, M.C. Bartelt, J.W. Evans, and P.A. Thiel, Bull. APS **45**, 203 (2000).

[20] P. Stoltze, J. Phys. Cond. Matter **6**, 9495 (1994).

[21] K.R. Roos and M.C. Tringides, Phys. Rev. Lett. **85**, 1480 (2000), which is reanalyzed by J. Krug, Phys. Rev. Lett. (Comment, 2001) incorporating fluctuation effects, and suggesting roughly equal prefactors.

[22] A. Steltenpohl and N. Memmel, Phys. Rev. Lett. **84**, 1728 (2000).

[23] For metal(100) homepitaxial systems, there is a subtle distinction between growth shapes versus equilibrium shapes of isolated near-square islands. If edge diffusion and kink rounding are very efficient, but kink escape is negligible on the time scale of island growth, then growing shapes are near-square or near-rectangular with at most one kink per edge. In contrast, equilibrium shapes have corners, which are quite rounded at higher T [18]. In our two-stage deposition experiments, it is difficult to determine the extent of equilibration either during the first deposition, or during cooling for the second deposition. Indeed it is possible that a quasi-equilibrium shape corresponding to an intermediate T is "frozen in".

[24] C. Rottman and M. Wortis, Phys. Rev. B **24**, 6274 (1981).

Figure Captions

Figure 1. θ_2 versus θ_T at 200K with F=0.0065ML/s. The experiments are solid dots, where the area of the dot represents the area of that particular STM image relative to the other images. Solid lines represent the simulations, where the value of the E_{se}[110] for a particular simulation is labeled. (Note: only half of the simulations are labeled, however the E_{se}[110] for the unlabeled simulation is the median between the two labeled simulations surrounding it.)

Figure 2. θ_2 versus θ_T at 250K with F=0.0065ML/s. The experiments are solid dots, where the area of the dot represents the area of that particular STM image relative to the other images. Solid lines represent the simulations, where the value of the E_{se}[110] for a particular simulation is labeled. (Note: only half of the simulations are labeled, however the E_{se}[110] for the unlabeled simulation is the median between the two labeled simulations surrounding it.)

Figure 3. An $100\times100nm^2$ STM image (a) and a plot of θ_2 versus θ_T (b) for a 1.02ML Ag/Ag(100) film deposited at 300K. (Note: the image was scanned 13 minutes after deposition.)

Figure 4. A plot showing simulated θ_2 versus E_{se}[110] for 1.02ML Ag/Ag(100) films deposited at 300K with F≈0.02ML/s. Where solid circles represent the average simulation values and the open circles are average simulation values plus or minus 2σ. The dashed line at θ_2=0.059 is the experimental value. Therefore the shaded region represents consistency between experiment and simulation values.

Figure 5. (a) A plot of f vs. S_1 for Ag/Ag(100) films for an initial deposition of 0.16ML at 270K with F≈0.0033ML/s, and a final deposition of 0.03ML at 195K with F≈0.0033ML/s. (b) A plot of θ_{top} vs. S_1 for Ag/Ag(100) films for an initial deposition of 0.20ML at 320K with F≈0.002ML/s, and a final deposition of 0.30ML at 235K with F≈0.02ML/s. Where for both (a) and (b) the solid lines represent simulations with various $E_{se}[110]$ and the open circles represent experimental data.

Figure 6. An STM (a) and simulated (where $E_{se}[100]$=0.07eV) (b) 100×100nm^2 image of a Ag/Ag(100) film generated from an initial deposition of 0.20ML at 320K with F≈0.002ML/s, and a final deposition of 0.30ML at 235K with F≈0.02ML/s.

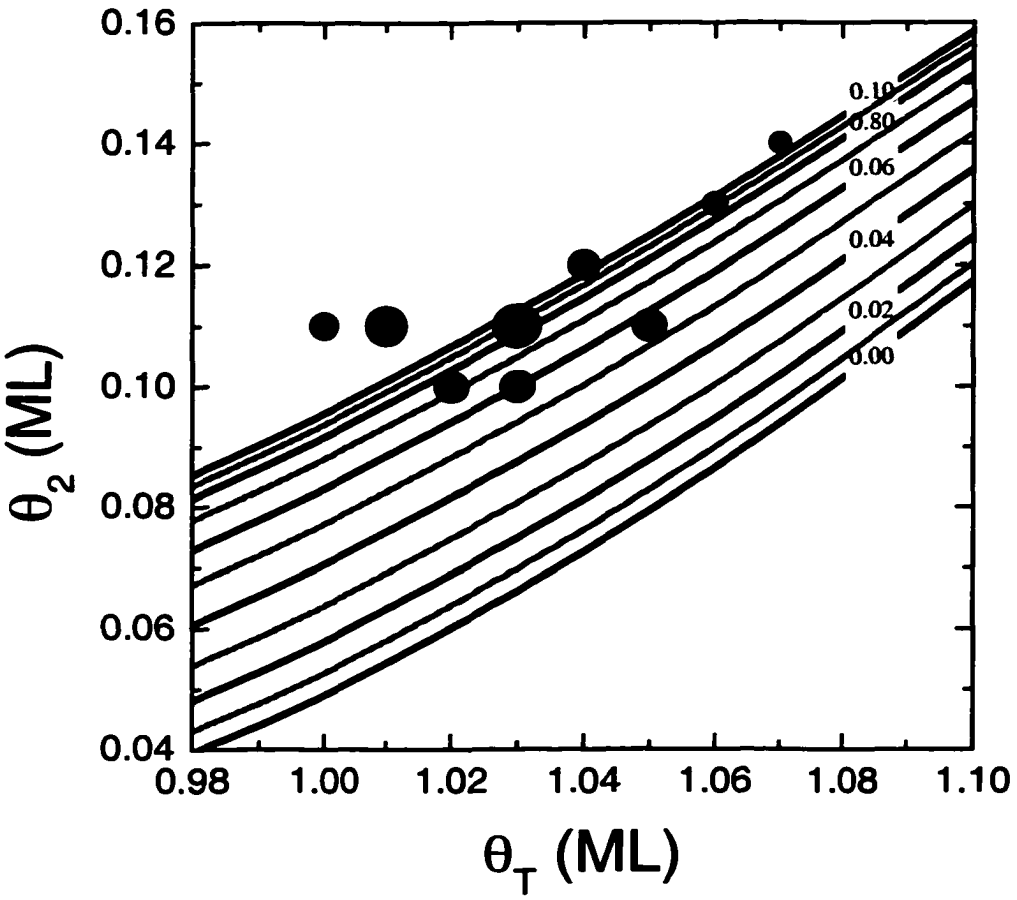
0.16
0.14
0.12
0.10
0.08
0.06
0.04
0.98
1.00
1.02
1.04
1.06
1.08
1.10
θ2 (ML)
θT (ML)
0.10
0.80
0.06
0.04
0.02
0.00

Figure 1

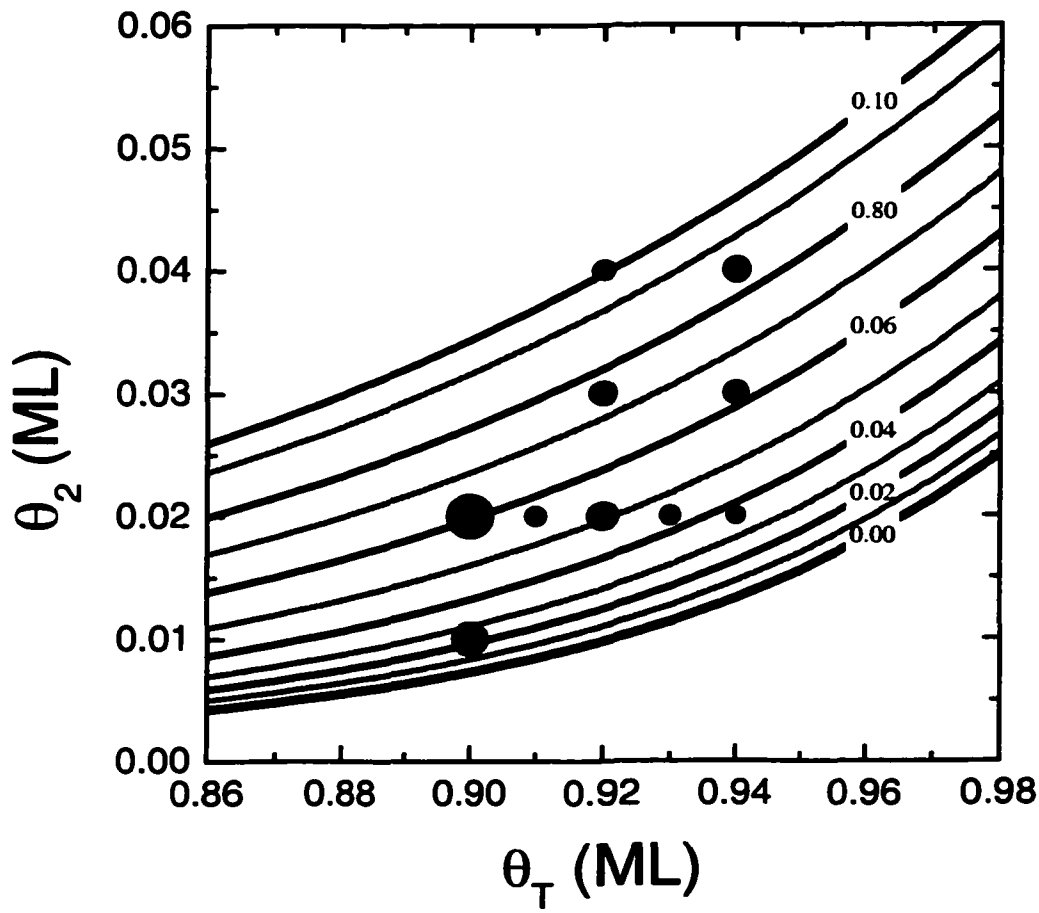
0.06
0.05
0.04
0.03
0.02
0.01
0.00
θ2 (ML)
0.10
0.80
0.06
0.04
0.02
0.00
0.86
0.88
0.90
0.92
0.94
0.96
0.98
θT (ML)

Figure 2

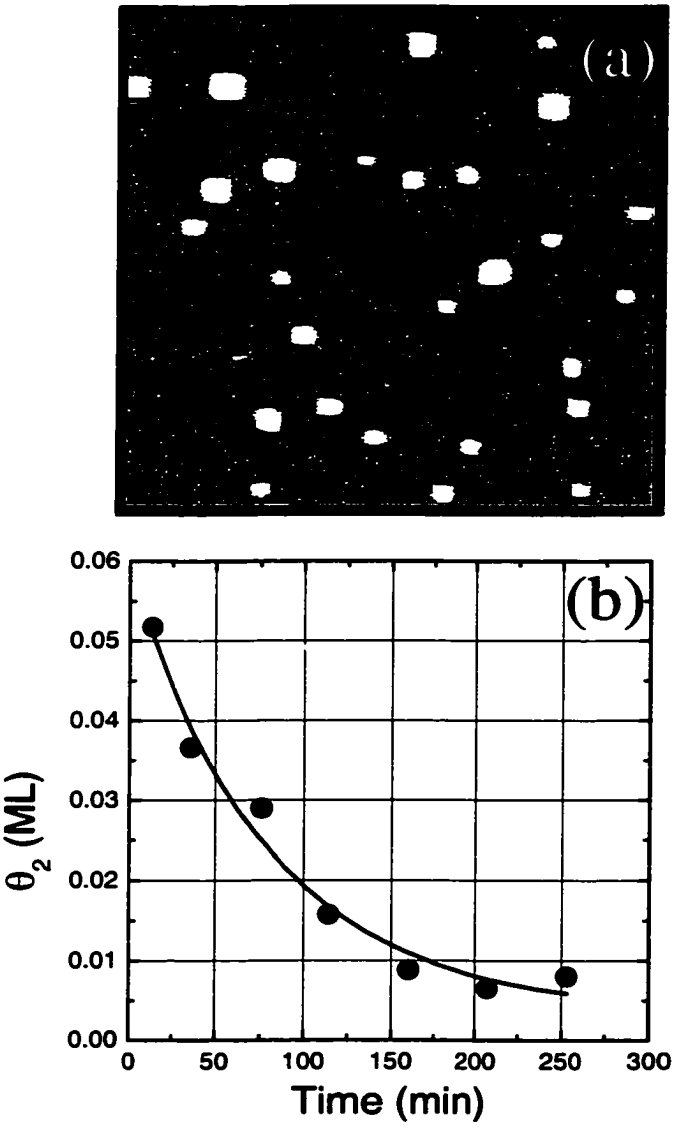
(a)
(b)
0.06
0.05
0.04
0.03
0.02
0.01
0.00
θ2 (ML)
0
50
100
150
200
250
300
Time (min)

Figure 3

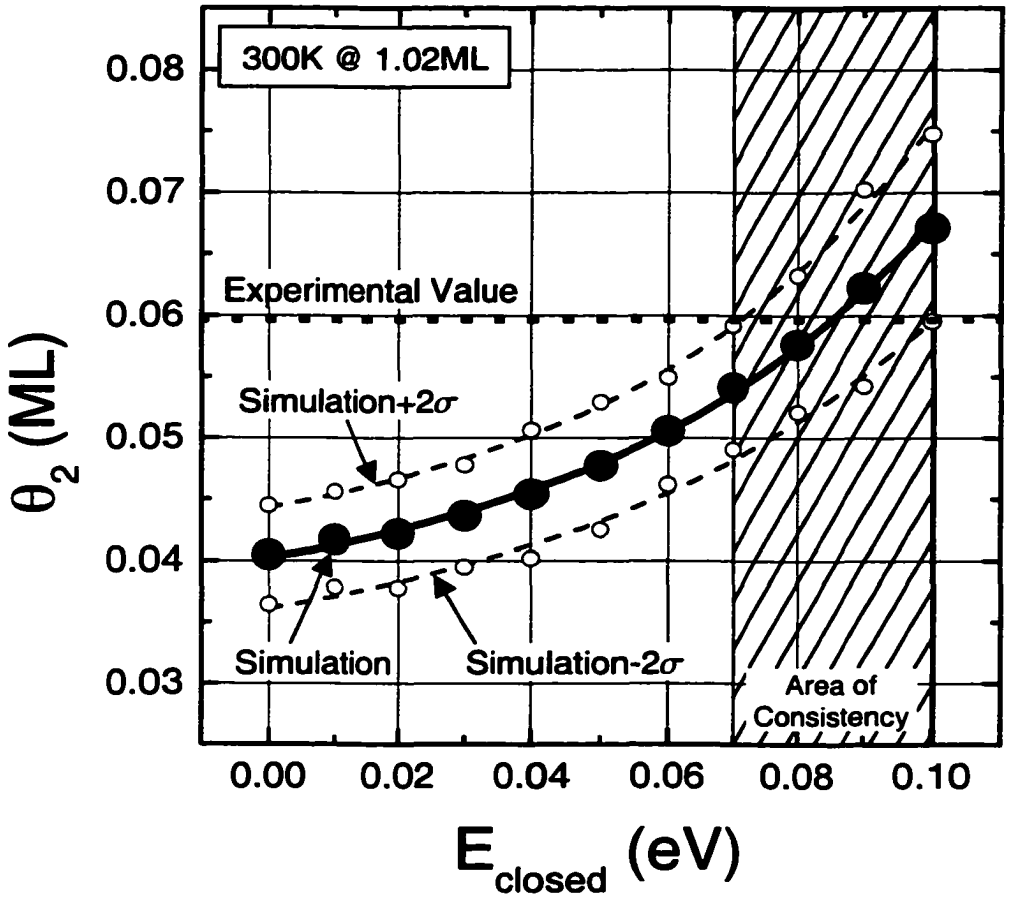
300K @ 1.02ML
Experimental Value
Simulation+2σ
Simulation
Simulation-2σ
Area of Consistency
θ2 (ML)
0.08
0.07
0.06
0.05
0.04
0.03
0.00
0.02
0.04
0.06
0.08
0.10
Eclosed (eV)

Figure 4

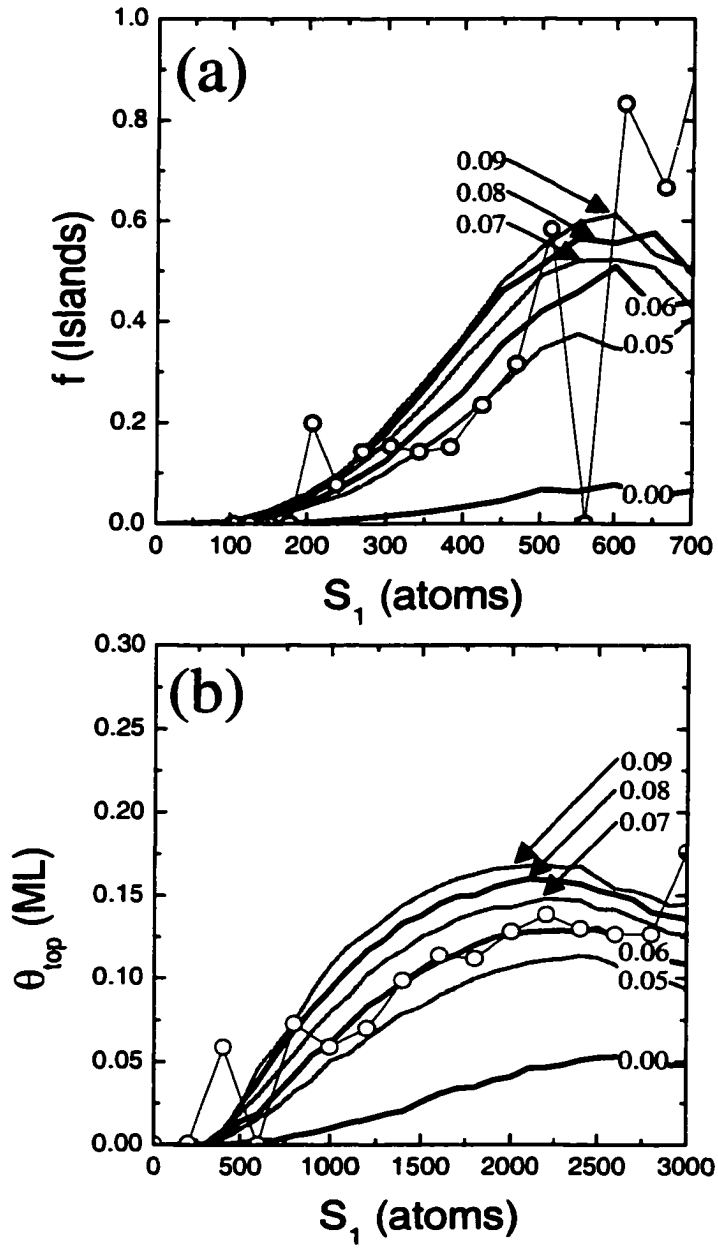
(a)
f (Islands)
S1 (atoms)
0.09
0.08
0.07
0.06
0.05
0.00
(b)
θtop (ML)
S1 (atoms)
0.09
0.08
0.07
0.06
0.05
0.00

Figure 5

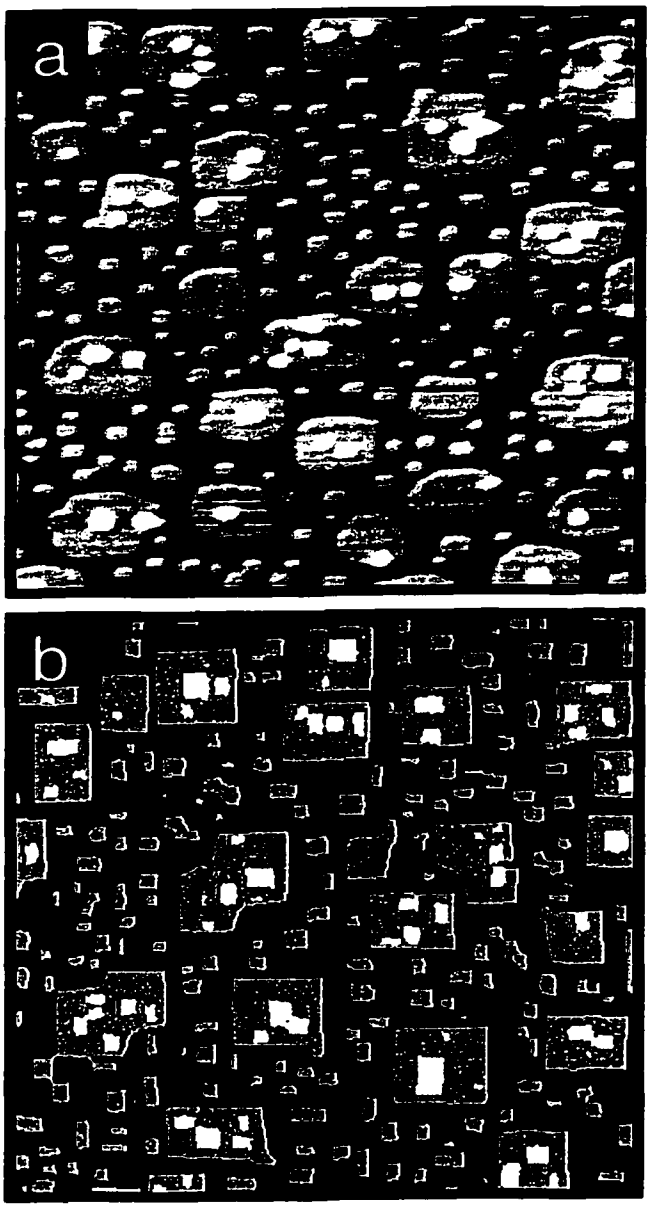

Figure 6

6. EVOLUTION OF MOUNDS DURING METAL(100) HOMOEPITAXY: CHARACTERIZATION OF THREE CONSECUTIVE GROWTH REGIMES

A paper to be submitted to Physical Review Letters.

K.J. Caspersen, A.R. Layson, C.R. Stoldt, V. Fournee, P.A. Thiel, and J.W. Evans

Abstract

A combination of variable-temperature scanning tunneling microscopy (VTSTM) studies and realistic atomistic modeling for Ag/Ag(100) homoepitaxy reveals three distinct growth regimes at higher temperatures: initial transformation from 2D islands to 3D mounds; mound steepening (with slow mound coarsening and rapid film roughening); and finally asymptotic slope selection (concurrent with a complex mound ordering, annihilation, and coalescence dynamics). These regimes are compressed at lower temperatures.

Text

The evolution of complex patterns in physical systems occurs in a variety of phase separation and domain boundary driven coarsening processes. Examples can be found in alloy systems, complex fluids, and surface adlayers [1]. There is considerable experimental and theoretical interest in analyzing these patterns, often focussing on long-time asymptotic behavior. The latter is of particular interest as it typically falls into one of a few "universality classes" determined by the basic characteristics of the process (symmetry, domain degeneracy, dimension) rather than by the finer details [1]. Another example receiving much attention recently is "mound" formation during epitaxial growth [2-11], a phenomenon of

significance for various thin film deposition technologies. An extra complication here, which is not yet fully understood, is a subtle interplay between the observed lateral coarsening of the array of mounds, and the kinetic roughening of growing film [9-11]. In fact, many aspects of the intricate morphological "landscapes" developing in these growing films have yet to be carefully examined or fully understood.

Villain [2] noted that step-edge (SE) barriers to downward transport of adatoms induce unstable growth in epitaxial films: diffusing adatoms tend to be reflected from descending steps and incorporated at ascending steps, producing a destabilizing lateral mass current, J_{up}, in the uphill direction. This results in the formation of "mounds" which coarsen laterally while their height increases (so the film roughens). Their side slopes increase initially, but may stabilize if there is a downhill current, J_{down} (e.g., due to "downward funneling" of depositing atoms) which can counterbalance J_{up} [12]. While some aspects of coarsening behavior are similar to 2D systems [1], there are complications associated with the 3D topology [10]. Also, the SE barrier strength and details of periphery diffusion are known to influence coarsening [11]. Most theoretical studies have attempted to elucidate asymptotic behavior of idealized models in the regime of mound slope selection. Comparisons with experiment (often for only a single temperature and limited range of film thickness) should be scrutinized, as clarified below.

In this Letter, we provide a comprehensive and realistic picture of kinetic roughening and mound coarsening for Ag/Ag(100) film growth, including the dependence on temperature (T). This is achieved by closely integrating high-resolution LEED studies (up to 10-15 monolayers or ML), VTSTM studies (up to 60-100 ML), and appropriate atomistic modeling (up to ~2000ML). As expected, initial growth is fairly smooth at 300K, and

rougher for lower T due to kinetic barriers to smoothing which derive from small SE barriers (but see [6]). We find that the opposite is true for thick films! More generally, we characterize film growth for higher T in terms of an initial "smooth" regime (2D islands become 3D mounds), an extended "pre-asymptotic" regime of mound steepening (slow mound coarsening and rapid roughening), and an "asymptotic" regime of slope selection (often not accessed experimentally). The regimes are compressed and less well distinguished at lower T, where slope selection is more rapid. Modeling elucidates key aspects of atomistic processes underlying growth (e.g., non-uniform SE barriers, inhibited kink rounding below 200K influencing island shape and thus downward transport). It also reveals subtle aspects of morphological evolution in the asymptotic regime including complex mound ordering, annihilation, and coalescence dynamics, which reflects strong up-down symmetry breaking (an unexpected feature not addressed in recent continuum formulations of mounding) [9,10].

The experiments were performed in a UHV chamber with base pressure $<10^{-10}$ Torr. Films were produced by evaporative deposition of Ag onto the Ag(100) single-crystal surface between 190K and 300K – the temperature regime of mound formation, with a flux of F≈0.02ML/s. Nanostructure evolution was monitored with an Omicron VTSTM. Specifically, we determine the film roughness, W (in units of the interlayer spacing b=2.04A), and the height-difference correlation function $H(\underline{r})$ (mean-square height difference vs. lateral separation, $\underline{r}$). Oscillations in the latter reflect a partially ordered array of mounds, the first maximum (and minimum) roughly corresponding to the mean mound "radius" L_R (and "diameter" L_D). We also directly determine the mound density, N_m, and thus the mean mound separation $L_S=1/\sqrt{N_m}$. For the initial stage of growth, VTSTM statistics for $H(\underline{r})$ are poorer, so we instead extract lateral correlation lengths, $L_C \propto 1/d^*$, where d^* is

the inverse ring diameter of LEED profiles obtained during deposition in a separate UHV chamber.

First, we describe the key VTSTM results for kinetic roughening, interpretation of which is facilitated by comparison with simulation results from our atomistic modeling described below. Experimental data (symbols) and simulation results (curves) for W versus coverage, θ, are shown in Fig.1 for various T. At 300K, one can clearly distinguish regimes of initial "smooth" growth up to ~30ML (consistent with previous studies [13]), rapid "pre-asymptotic" roughening up to ~1500ML (during which mounds steepen), and subsequent "asymptotic" slope selection (as checked in simulations) with slower roughening. Note that the onset and nature of true asymptotic scaling is unclear. Also, the possibility of smooth growth followed by rapid roughening might be gleaned from previous simulations [14] and experiments [13]. The three regimes are compressed upon reducing T, so that asymptotic behavior is already achieved by ~100ML at 190K. This is understood since smaller islands and mounds result in a more rapid increase in slope, and thus earlier slope selection (although selected slopes are somewhat higher at lower T [15]).

Roughening behavior can be described in terms of an effective or local exponent, $\beta_{eff} = d(\ln W)/d(\ln\theta)$, which varies strongly with θ for higher T, but less so at 190K. From simulations, β_{eff} has low values in the initial regime (e.g., $\beta_{eff} \approx 0.2$ at 300K), high values in the pre-asymptotic regime (which peak at $\beta_{eff} \approx 0.8$ at 300K, 0.75 at 260K, 0.65 at 230K, and 0.45 at 190K), and lower "asymptotic" values of $\beta_{eff} \approx 0.3$ at 190K, and ~0.25 for higher T. Just using the experimental data superficially suggests that $\beta_{eff} \approx 0.5$-0.6 for 230-300K, and $\beta_{eff} \approx 0.4$ at 190K.

Next, we describe the lateral mound coarsening behavior. The effective coarsening exponent is defined as $n_{eff}=d(\ln L)/d(\ln\theta)$, where L measures lateral size (see above). Limited statistics preclude precise analysis, but experimental values for L_D, L_R, and L_S in the range of 5ML to 60-120ML (Fig.2a) indicate that n_{eff} varies much less with θ than does β_{eff}, and generally give values for n_{eff} consistent with each other, and with simulation predictions (Fig.2b): $n_{eff}\approx 0.18$ (0.19) for 260K, ≈ 0.18 (0.17) for 230K, and a somewhat higher $n_{eff}\approx 0.2$-0.3 (0.19) at 190K, from experiment (simulation). Our key observation is that coarsening is much slower than kinetic roughening up to ~100ML. We note some discrepancies for 190K where STM data is poorer [16], and that L-values from simulation are somewhat above experiment for 230-260K.

There are limitations in the STM analysis. The microscope tip cannot fully probe the floor of narrow and deep valleys (cf. the Zeno effect [17]) resulting in a potential underestimation of W, and an excessively positive skewness of the film height distribution [15]. This effect is likely significant at 230K where mounds are fairly small and growth from 25-100ML is roughest: the experimental W=1.9 at 100ML (not shown in Fig.1) is well below the simulated value. Also, there are ambiguities in "mound" identification at low θ for all T, and for all θ at 190K [16].

Finally, we comment briefly on LEED results for coarsening in the initial stage of growth. Based on behavior of L_C, we find that $n_{eff}\approx 0.20$ (up to ~10ML) at 190K, $n_{eff}\approx 0.19$ (up to ~15ML) at 230K, and $n_{eff}\approx 0.3$ (up to ~7ML) at 260K. This increase in the initial n_{eff} with T is compatible with simulation results up to ~10ML (where $n_{eff}\approx 0.20$ at 190K and

230K, and $n_{eff} \approx 0.22$ at 260K), but differs from behavior for the subsequent pre-asymptotic regime.

Next, we describe our atomistic modeling of the growth process. It incorporates the following key steps: deposition of atoms randomly at four-fold hollow sites of a fcc(100) surface according to downward funneling deposition dynamics [12,15]; terrace diffusion of isolated adatoms with attempt frequency $\nu=10^{13}s^{-1}$ and activation barrier $E_d=0.40$eV for interlayer hops; an additional SE barrier of E_{se} exists for downward hops at step edges. Adatoms irreversibly nucleate (immobile dimer) islands, and irreversibly aggregate with existing islands. In our simplest "instantaneous kink rounding" (IKR) model [15], adatoms reaching island edges move immediately to double-bonded kink sites, even if this involves kink rounding. We first modeled growth assuming a uniform SE barrier, E_{se}, but find that it must vary from 0.035eV at 230K, to 0.06eV at 300K, to fit the data. This demonstrates the existence of a non-uniform ES barrier. Motivated by semi-empirical studies of energetics [18], we select $E_{se}=0$eV along open or kinked step edges, and adjust $E_{se}=E_{[110]}$ along [110] close-packed step edges to match growth. Fig.3 shows the optimum choice of $E_{[110]}=0.07$eV matching experimental W(25ML) for $T \geq 230$K.

We claim that the IKR model fails for low T, as it artificially maintains square islands. Indeed, the predicted W is too high, due to the "high" ES barrier at the [110] edges of the square islands. Kink rounding is likely inhibited at low T producing irregular island shapes with a higher population of kinked step edges having no ES barrier. Thus, we introduce a modified "finite kink rounding" (FKR) model to reflect limited kink rounding as controlled by a barrier E_{kr} (which must exceed the low 0.25eV barrier for hopping along perfect [110] step edges). Fig.3 shows that W for 25ML films at low T depends very

sensitively on E_{kr}, which is selected as 0.41eV (for $\nu_{edge}=10^{12}s^{-1}$) to match observed behavior. To summarize, re-entrant smooth growth of ~25ML films at low T is in part due to enhanced downward funneling (as shown by the IKR model [15]), and in part due to irregularization of islands given E_{se}=0eV along kinked step edges.

Our FKR model reproduces the key features of roughening and mound coarsening observed for growth up to 60-100ML (see Fig.4 and Fig.s 1 & 2). Thus, we believe it reliably predicts growth for thick films, including the extended mound steepening regime, and the transition to (and evolution in) the slope selection regime. The following discussion focuses on these regimes, comparing predicted behavior with various existing concepts and theories for mound coarsening. These theories employ evolution equations for the coarse-grained film height, $h(\underline{x}, t)$, vs. lateral position $\underline{x}$ at time t, in terms of a lateral mass flux, $\underline{J}$. For the FKR model, one expects that

$$\partial h/\partial t = F - \nabla\cdot\underline{J} + \eta, \text{ where } \underline{J} = \underline{J}_{NE}(\underline{m}) + \lambda\,\nabla A(m^2) + D_4\,\nabla\,\nabla^2 h + D_6\,\nabla\,\nabla^2\,\nabla^2 h + \ldots, \quad (1)$$

where η is a noise term. The non-equilibrium current, $\underline{J}_{NE}$, increases linearly for small slopes, $\underline{m}=\nabla h$ (Villain's instability), but then decreases vanishing at selected slopes reflecting the four-fold symmetry of the fcc(100) surface [10,12]. The 2nd term in $\underline{J}$ breaks up-down symmetry. It was introduced in [5] for metal(100) systems, and its general dependence on $m^2=\underline{m}\cdot\underline{m}$ discussed in [17]. The 3rd term includes the Mullin's contribution (absent here) to equilibration via surface diffusion where bond-breaking is operative, and another contribution due to the stochastic nature of nucleation [17]. The last term was introduced in [5] to account for the partial "equilibrating" influence of terrace diffusion in the regime of irreversible island formation (as in our models).

Pre-asymptotic Mound Steepening Regime: In this regime, slope selection not achieved, and one can plausibly use a simpler form for J_{NE} with no zeros, but which must decrease like 1/m, for large m (as narrow terraces restrict J_{NE}) [3,9]. Analysis of (1) then produces rapid roughening with $\beta=1/2$, and slow coarsening with $n_{eff}=1/4$ for $D_4>0$, or $n_{eff}=1/6$ for $D_4=0$ (and $D_6>0$) [9]. Thus, a low $n_{eff}\approx 0.18$ in experiment and in the FKR model indicates that D_6 term dominates in this steepening regime for the Ag/Ag(100) system, consistent with the irreversible nature of island formation. [Note that escape of edge adatoms from kink sites also drives a larger n_{eff} [8], but this process is not operative in our system.] Experimental roughening is rapid, indicating that the above analysis captures the key features of growth, but one cannot say $\beta=1/2$. A more general perspective (from previous simulations [14]) which applies here is that coarsening is slow when steepening is operative, due to competition between these processes.

Asymptotic Slope-Selection Regime: Values of exponents $\beta \approx n_{eff}$ from 0.25-0.3 indicate that the D_4-term in (1) is significant in this regime. The trend of (slightly) higher n_{eff} for lower T contrasts previous simulation studies where inhibited kink rounding produced lower n_{eff} [11]. However, the non-uniform SE barrier in our system can produce distinct behavior.

In the FKR model, we observe a roughly isotropic distribution of mounds at the beginning of this regime, from which develops *ordered 1×1 patches of mounds* with square bases along the close-packed directions (Fig.5). Correspondingly, the power spectrum of the distribution of mound centers evolves from an isotropic ring to a four-fold symmetric pattern (Fig.5), and D_{av} in [110] and [100] step directions start equal, but ultimately differ by $\sim\sqrt{2}$

(Fig.2b). This behavior should be contrasted with that of systems with up-down symmetry where a *checkerboard pattern of alternating mounds and pits* (inverted mounds) develops, and evolution is enslaved to the dynamics of rooftop or valley floor "defects" [10]. Morphologies for Ag/Ag(100) instead have strong up-down symmetry breaking, with valley floors (which separate most mounds) greatly favored over rooftops. Mound dynamics for Ag/Ag(100) also differs from [10]. For disordered arrays of square mounds, corner-to-corner coalescence seems to predominate. However, ordered 1×1 regions of side-by-side mounds display a more complex and cooperative dynamics: fluctuations in size of adjacent mounds trigger annihilation of the smaller neighbor, leading to corner-to-corner coalescence (and other synchronous annihilation) events. See Fig.6. Corner-to-corner coalescence requires considerable disruption of the 1×1 ordered pattern.

In summary, we have presented a detailed picture of distinct growth regimes in Ag/Ag(100) homoepitaxy. Prolonged mound steepening occurs, followed by slope selection with up-down symmetry breaking controlling long-time dynamics. This work was supported by NSF grant CHE-0078596 at Ames Laboratory-USDOE operated by ISU under Contract No.W-7405-Eng-82.

References

[1] A.J. Bray, Adv. Phys. **43**, 357 (1994).

[2] J. Villain, J. Phys. I (France) **1**, 19 (1991).

[3] M.D. Johnson *et al.*, Phys. Rev. Lett. **72**, 116 (1994).

[4] H.J. Ernst *et al.*, Phys. Rev. Lett. **72**, 112 (1994); L.C. Jorritsma *et al.*, *ibid*, **78**, 911 (1997);

J.-K. Zuo and J.F. Wendelken, *ibid*, **78**, 2791 (1997).

[5] J.A. Stroscio *et al.*, Phys. Rev. Lett., **75**, 4246 (1995).

[6] C.R. Stoldt *et al.*, Phys. Rev. Lett. **85**, 800 (2000).

[7] G. Constantini *et al.*, Phys. Rev. Lett. **86**, 838 (2001).

[8] T. Michely *et al.* Phys. Rev. Lett. **86**, 2589 (2001).

[9] L. Golubovic, Phys. Rev. Lett. **78**, 90 (1997).

[10] M. Siegert, Phys. Rev. Lett. **81**, 5481 (1998); D. Moldovan and L. Golubovic, Phys. Rev. B **61**, 6190 (2000).

[11] S. Schinzer *et al.*, Surf. Sci. **439**, 191 (1999); J.G. Amar, Phys. Rev. B **60**, R11317 (1999);

L. H. Tang *et al.*, Eur. Phys. J. B **2**, 409 (1998).

[12] M.C. Bartelt and J.W. Evans, Phys. Rev. Lett. **75**, 4250 (1995); Surf. Sci. **423**, 189 (1999).

[13] W.C. Elliott *et al.*, Phys. Rev. B **54**, 17938 (1996).

[14] P. Smilauer and D.D. Vvedensky, Phys. Rev. B **52**, 14263 (1995).

[15] K.J. Caspersen *et al.*, Phys. Rev. B **63**, 085401 (2001).

[16] In 190K experiments, n_{eff} derived from L_S and $L_D \approx 2L_R$ differ, and spatial heterogeneity develops in thicker films perhaps due to heterogeneous or non-normal flux. This effect (absent in simulations) degrades $H(\underline{r})$, although L_R is generally more robust than L_D.

[17] P. Politi and J. Villain, Phys. Rev. B **54**, 5114 (1996).

[18] C. Teichert *et al.*, Phys. Stat. Sol. A **146**, 223 (1994); U. Kurpick and T.S. Rahman, Phys. Rev. B **57**, 2482 (1998).

Figure Captions

Figure 1. W vs. coverage, θ, for growth at different T (shown). Experimental data (symbols) and FKR model predictions (curves from bottom to top - on right - with increasing T).

Figure 2. Lateral mound size, L, vs. coverage, θ, for growth at 190K, 230K, 260K (bottom to top): (a) experimental: L_S (€) <L_D (O); island densities at 0.1ML are used to anticipate L_D for lower θ where mounds are ill-defined; $L_R \approx L_D/2$ (<L_S) is not shown; (b) FKR model: L_S (gray curves), and L_D along close-packed steps (black dashed) and open steps (black solid).

Figure 3. W vs. T for 25ML films predicted by the FKR model for various kink rounding barriers, E_{kr} (shown). Experimental values are also shown as symbols.

Figure 4. Film morphologies (50×50 nm^2) at 230K from: (a) STM experiment; (b) FKR model.

Figure 5. Mound ordering at 190K in the FKR model for 100ML (130×130 nm^2) and 5000ML (300×300 nm^2) films; [100] steps are horizontal. Insets: power spectrum for mound centers.

Figure 6. Complex mound dynamics within ordered 1×1 patches at 230K in the FKR model. Images are 35×35 nm^2. Coverage increments are 50ML.

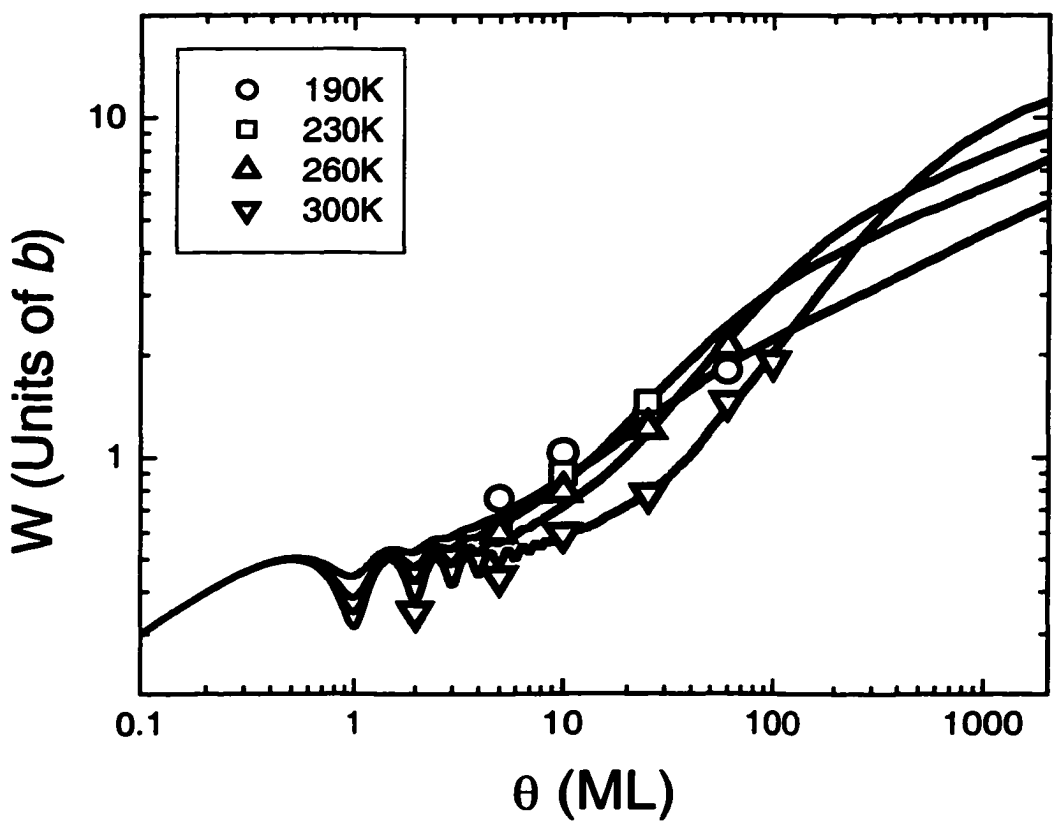

Figure 1

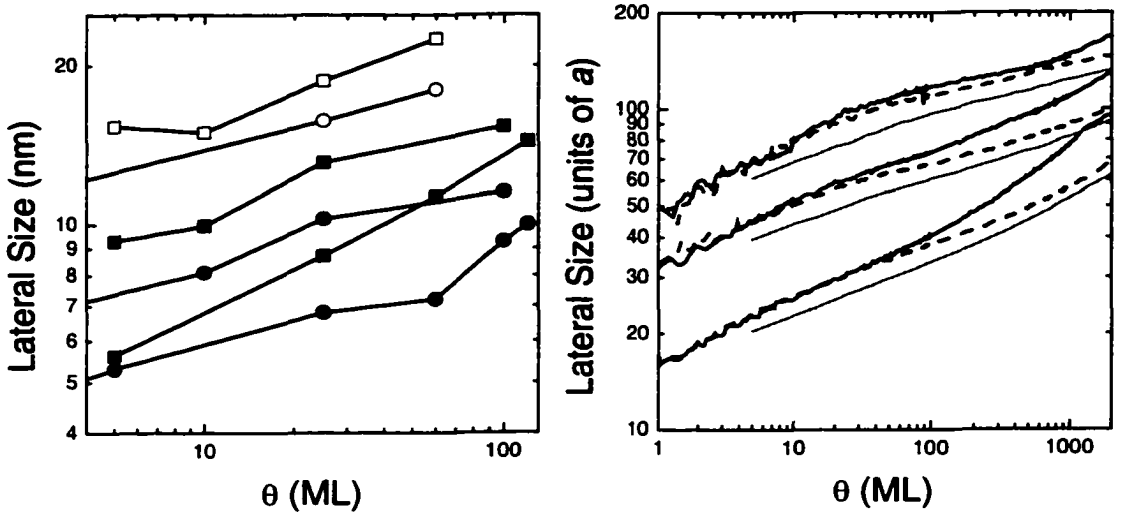
Lateral Size (nm)
20
10
9
8
7
6
5
4
10
100
θ (ML)
Lateral Size (units of a)
200
100
90
80
70
60
50
40
30
20
10
1
10
100
1000
θ (ML)

Figure 2

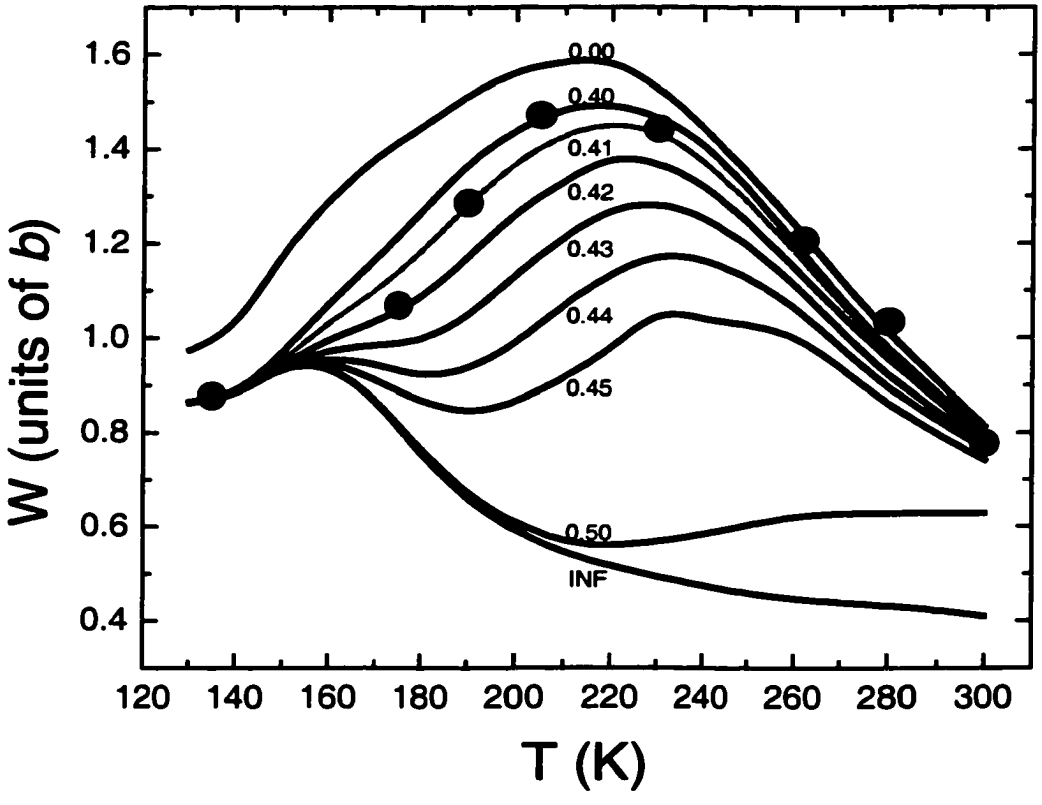
W (units of b)
T (K)
1.6
1.4
1.2
1.0
0.8
0.6
0.4
120
140
160
180
200
220
240
260
280
300
0.00
0.40
0.41
0.42
0.43
0.44
0.45
0.50
INF

Figure 3

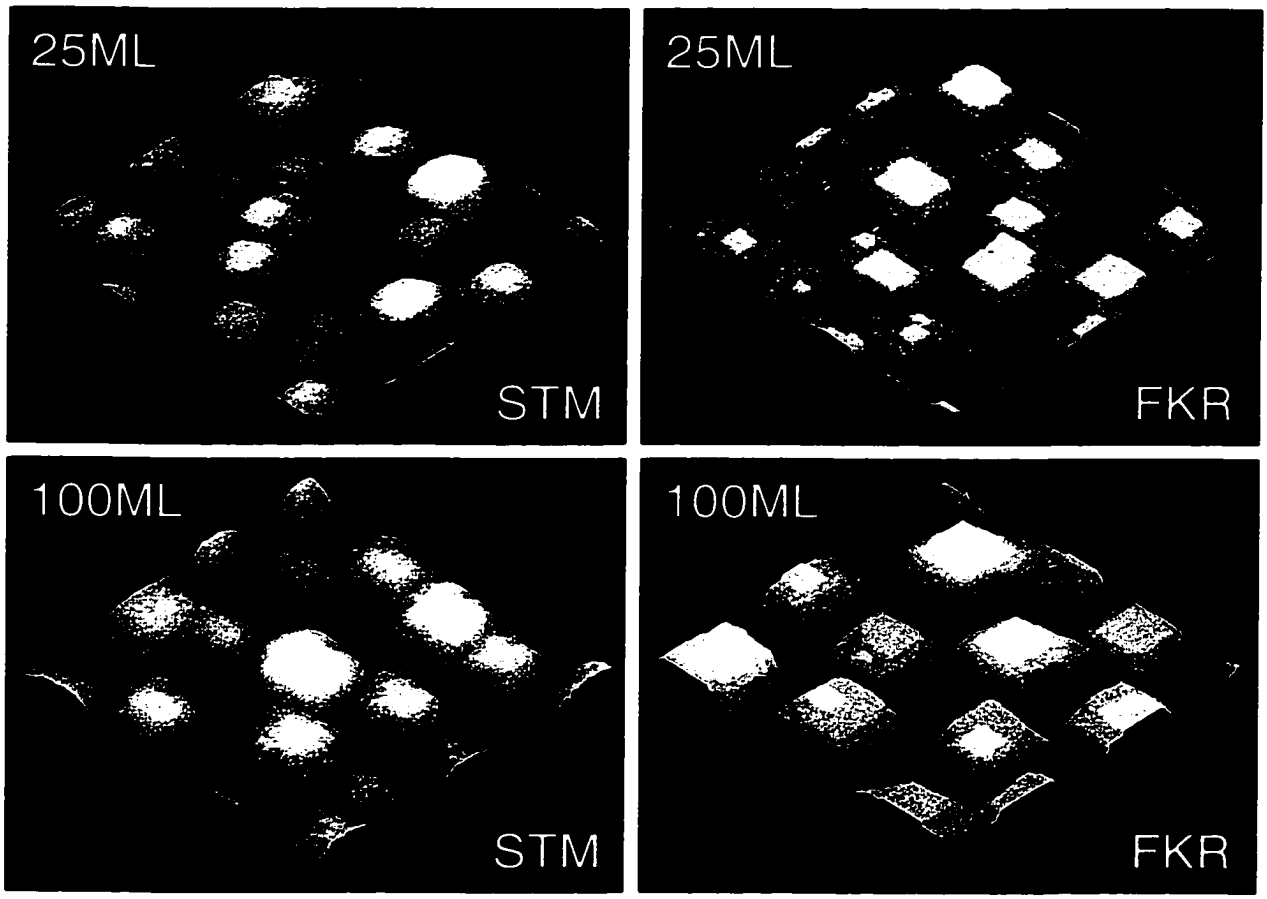

Figure 4

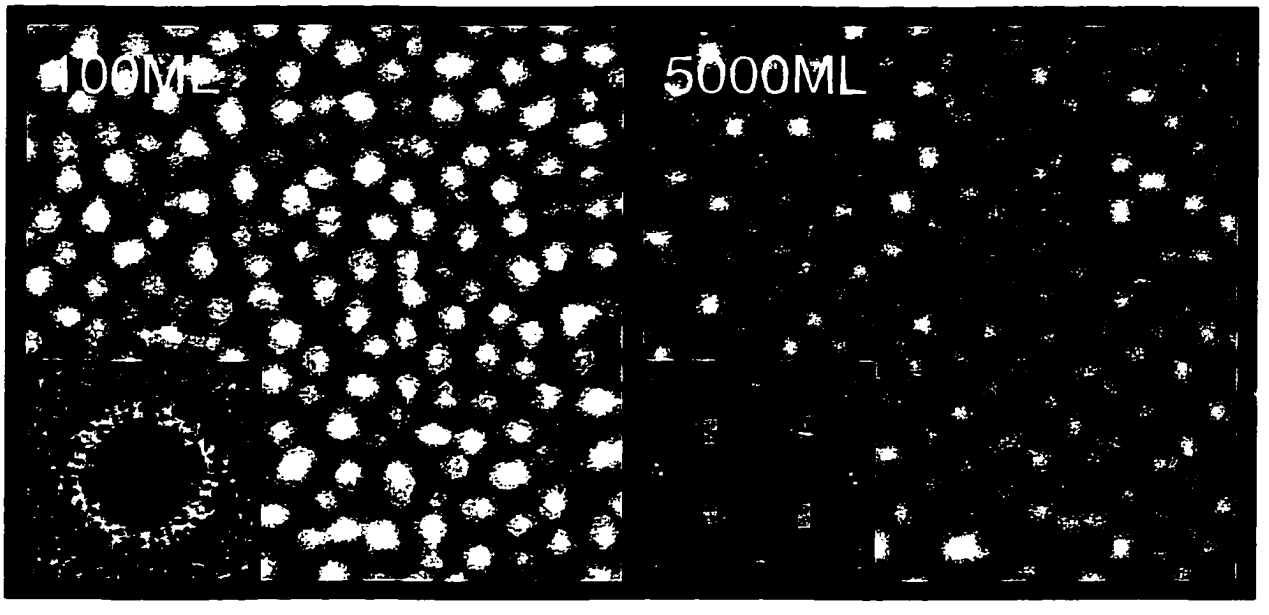

Figure 5

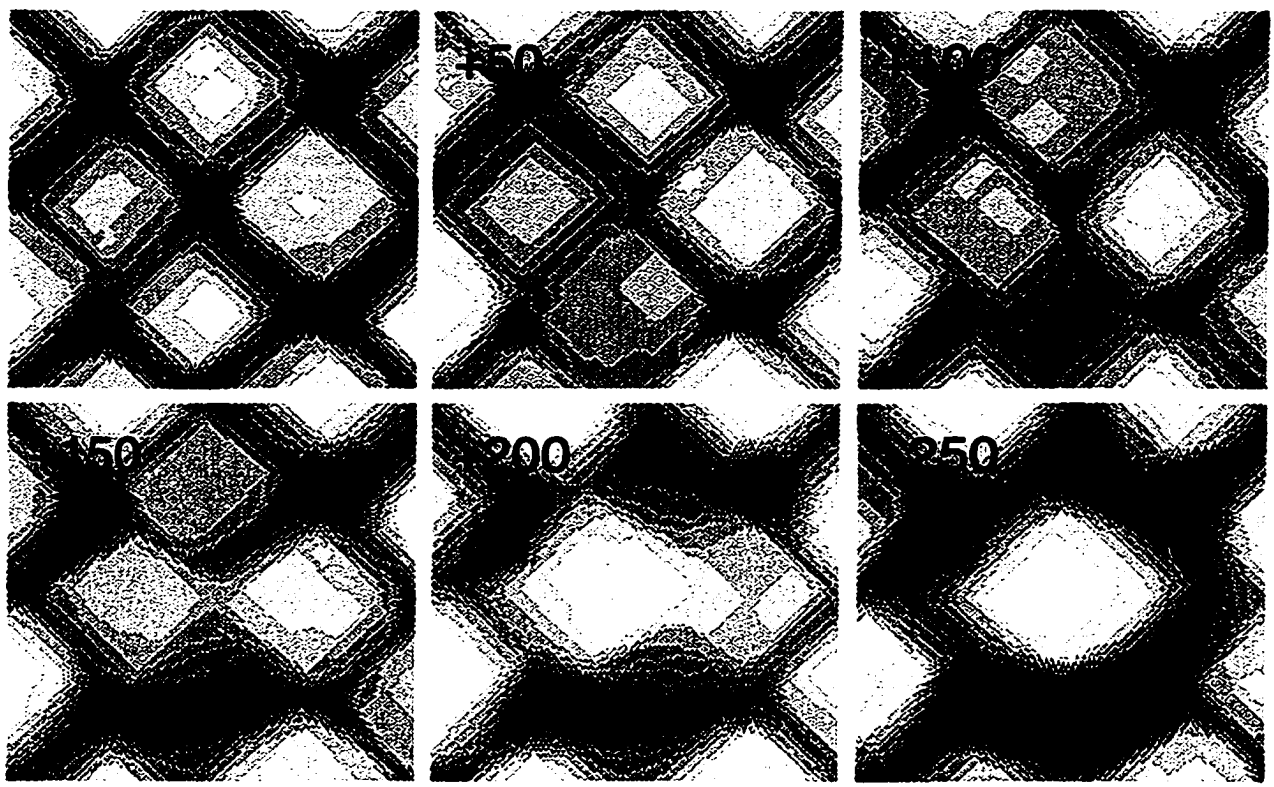

Figure 6

7. REALISTIC ATOMISTIC MODELING OF MOUND FORMATION DURING MULTILAYER GROWTH: METAL(100) HOMOEPITAXY

A paper to be published in the 2001 Proceedings of the North Atlantic Treaty Organization's Workshop for Advanced Research-Atomic Aspects of Epitaxial Growth.

K.J. Caspersen and J.W. Evans

Abstract

A realistic atomistic lattice-gas model is developed which describes the key features of film morphologies observed for multilayer growth of Ag/Ag(100) in the temperature range 175-300 K corresponding to "mound formation". The model accounts for irreversible formation of islands in each layer mediated by terrace diffusion, growth coalescence of islands within each layer, a non-uniform step edge barrier inhibiting downward transport, and restricted rounding of kinks by adatoms at island edges (at lower temperatures).

1. Introduction

The last decade has seen intensive activity in atomistic modeling of epitaxial film growth, to a large extent driven by detailed scanning tunneling microscopy (STM) data available for both homo and heteroepitaxial systems [1]. Some efforts have addressed the long standing problem of describing island formation in the initial stages of growth, a process involving random deposition, and subsequent terrace diffusion, leading to nucleation of new islands and aggregation with existing islands. Recent studies have focused on describing subtle correlations between island sizes and separations (which control the size distribution)

[2], and on the structure of islands (which reflect the degree of shape equilibration via periphery diffusion) [3,4]. Appropriate characterization of film morphology during multilayer growth is relatively recent. A key observation of Villain [5] is that an additional Ehrlich-Schwoebel (ES) or step-edge barrier [6] to downward transport of adatoms induces unstable growth characterized by the formation of multilayer island stacks or "mounds".

The presence of an ES barrier means that diffusing adatoms tend to be reflected from descending step edges and incorporated at ascending steps, thus producing a destabilizing mass current, $\underline{J}_{up}$, in the uphill direction [5,7]. The slopes of the sides of the resulting mounds initially increase, but may stabilize if there is a downhill current, $\underline{J}_{down}$, which can counterbalance $\underline{J}_{up}$ [8,9]. For metal(100) homoepitaxy, $\underline{J}_{down}$ results from downward funneling of atoms deposited at step edges and at nanoprotrusions to lower four-fold hollow adsorption sites [9]. Some theoretical studies of multilayer growth have utilized evolution equations for the coarse-grained film height, h. These PDE's incorporate the change in h due to deposition (which includes noise), and also due to surface mass flow [10]. The latter includes contributions from $\underline{J}_{up}$ and $\underline{J}_{down}$, as well as additional "relaxation terms" associated with surface diffusion, and also terms reflecting up-down symmetry breaking. However, the precise form and relative strength of these terms is often unclear, so quantitative modeling of specific systems requires an alternative approach.

Thus, our strategy is to develop realistic atomistic lattice-gas models tailored to metal(100) homoepitaxy, systems where the formation of mounds is well established [11-15]. Specifically, we develop a sequence of models to treat progressively more complex aspects of growth [9,14,15]. At each new level of modeling, there is an additional relevant process (affecting film morphology), the rate for which is determined by fitting model predictions to

experimental behavior. We thus obtain estimates for the activation barriers for terrace diffusion, for kink rounding at island edges, and for the non-uniform ES barrier. We believe that the resulting model is sufficiently robust to predict evolution of the film morphology during multilayer growth up to 1000's of multilayers.

2. Previous Models for Mound Formation in Metal(100) Homoepitaxy

2.1. SQUARE-ISLAND MODEL WITH UNIFORM ES BARRIER

Our simplest model applied to the submonolayer regime involves random deposition, and subsequent terrace diffusion, leading to irreversible nucleation and growth of near-square islands [16]. Here, the shape of individual islands is forced to be near-square by immediately placing aggregating atoms at a single kink site along the edge of isolated growing islands. This choice is motivated by the observed near-square islands in these systems, and by *ab-initio* calculations which reveal a low barrier of 0.25eV for diffusion along close-packed [110] step edges [17]. Also, islands coalescing due to growth are prescribed to continue growth as overlapping squares (but see below). A barrier of E_d=0.40eV for terrace diffusion (with attempt frequency $\nu=10^{13}s^{-1}$ per direction) is determined for Ag/Ag(100) by matching experimental island densities. For multilayer growth [9], the above process of square island formation occurs in each layer. Our modeling also incorporates downward funneling deposition dynamics, and a uniform ES barrier for the close-packed [110] step edges generated in the square-island model. This ES barrier is then determined to be 30meV by matching observed roughness for Ag/Ag(100), either for 1ML or multilayer films at some specific temperature, T [14,18]. With these parameters, the model reproduces the observed variation of RMS width of the film height distribution (i.e., the film roughness), W, with T for 25ML Ag/Ag(100) films deposited at 0.02ML/s between 140K and 300K (shown below)

[14]. However, the model fails in that it greatly underestimates the lateral size of mounds [15].

2.2. INSTANTANEOUS KINK ROUNDING (IKR) MODEL WITH NON-UNIFORM ES BARRIER

One key improvement in the IKR model relative to Sec.2.1. is to include a realistic treatment of growth coalescence of islands in each layer. In the IKR model [15], we do not demand square island shapes. However, we do still immediately place aggregating atoms at a nearby kink site on each side of isolated growing islands (allowing islands to have rectangular shapes), or at nearby kink sites in clusters of coalesced islands (allowing realistic growth of necks during corner-to-corner coalescence of islands). This might require rounding a kink site which occurs "instantaneously" with probability $P_{kr}=1$. See Fig. 1(a). Clearly in this model, growth creates a mixture of close-packed (or closed) [110] steps, and open (or kinked) steps. Implementing a uniform ES barrier fails to describe our extensive experimental data for roughening at different temperatures. Thus, motivated by predictions from semi-empirical energetics [19], we set the ES barrier along open step edges (E_{open}) to zero, and regard that along closed step edges (E_{closed}) as a free parameter. See Fig. 1(a). Adjusting E_{closed} to 70meV accurately reproduces the observed W versus T for 25ML Ag/Ag(100) films deposited at 0.02ML/s above 230K, as well as recovering the observed lateral dimension of mounds [15]. See Fig.2.

Our IKR model is particularly successful for higher T, where predicted morphologies are quite robust (given that kink rounding is efficient). However, it significantly overestimates W for lower T (whereas the simpler model of Sec.2.1. was "artificially" successful). This failure reflects the feature that the IKR model produces isolated islands with

compact (rectangular) shapes even at low T where kink rounding in Ag/Ag(100) may be inhibited. The latter inhibition should produce irregular island shapes [3], and thus kinked step edges with zero ES barrier and more efficient downward transport. To test this claim, we have also implemented a No Kink Rounding (NKR) model [15], representing the opposite extreme of IKR. The W's from the NKR model match experiment at around 130K, but are far too low for higher T where the model produces islands with an unphysical star-like shape. See Fig.2 and Fig.3.

3. Finite Kink Rounding (FKR) Model for Metal(100) Homoepitaxy

3.1 DETAILS OF THE FKR MODEL AND ALGORITHM

The challenge here is to implement a finite rate of corner rounding for atoms aggregating at the edge of islands on 1D terraces configured as shown in Fig. 1(b) [20]. (Other aggregating adatoms can reach kink sites "instantaneously" without kink rounding.) In fact, the adatoms in Fig. 1(b) rapidly diffuse along such 1D terraces. In the case of a significant additional kink rounding barrier, they achieve an "equilibrated" uniform probability distribution along the terrace (i.e., a probability of 1/L per site). Then, they can "leak" around kinks at a rate controlled by the kink rounding barrier, E_{kr} (which is expected to exceed the 0.25eV barrier for diffusion along [110] step edges [17]). Rather than follow the detailed motion of these edge atoms, our philosophy is to develop a more efficient algorithm mimicking the finite rate of kink rounding. Thus, each adatom reaching the 1D terrace in Fig. 1(b) either remains on the terrace (where it provides a "nucleus" for growth of the next layer, and thus possible destabilization of the island shape), or it is immediately moved around the kink to a doubly-bonded site with a suitable probability $P_{kr}<1$.

The kink rounding probability, $P_{kr} = R_{kr}/(R_{kr} + R_{agg})$, is determined by the relative magnitudes of the rate of kink rounding, R_{kr}, and the rate of aggregation, R_{agg}, of diffusing adatoms with the 1D terrace in Fig. 1(b). (The latter process leads to capture of previously aggregated adatoms before kink rounding.) From above, we naturally write $R_{kr} = 2\nu_{edge}\exp(-\beta E_{kr})/L$, where $\beta=(k_BT)^{-1}$ is the inverse temperature, and ν_{edge} is the attempt frequency for edge diffusion. We also make the approximate identification that $R_{agg} = L \cdot F/\rho_{edgesite}$, where F is the deposition flux (per site), and $\rho_{edgesite}$ is fraction of surface atoms in the film which are step edge atoms. Thus, this form for R_{agg} appropriately assumes a steady-state condition where all deposited atoms are captured at edge sites. It further assumes that the rate for capture at the 1D terrace in Fig. 1(b) is proportional to its length, L. This is an approximation, since the aggregation rate must depend on the details of the local film morphology, but it should reasonably describe typical behavior.

3.1. FKR MODEL RESULTS: AG/AG(100) HOMOEPITAXY

Simulation results for the FKR model in Fig. 2 show that W for 25ML Ag/Ag(100) films is extremely sensitive to the choice of E_{kr} for lower T, producing an estimate of E_{kr}=0.41eV (with an attempt frequency $\nu_e=10^{12}s^{-1}$ per direction). This shows that the decrease in W below 230K is due in part to downward funneling, and in part to the development of irregular islands (with kinked step edges facilitating easy downward transport). The typical lateral dimension of the mounds is relatively insensitive to E_{kr}, so the match between experiment and simulation seen for the IKR model is maintained. The match to local slope is improved in the FKR model (due to the lower W at lower T).

It is also of theoretical interest to examine the dependence of entire film morphology (rather than just W) on kink rounding barrier in the FKR model. See Fig. 3. For 25ML films,

islands and mounds have edges aligned with closed [110] steps for lower E_{kr} (0.41eV and below); they are fairly round for $E_{kr} \approx 0.5$eV, and irregular for high E_{kr}. A similar trend is observed for 1000ML films, except that for high E_{kr}, the overall shape of the mounds (which are composed of irregular islands) is surprisingly "geometrical", the mounds being "rotated" so that the edges are aligned with open [100] steps. Such morphologies have appeared in simulations of other NKR-type models [21].

Finally, in Fig. 4, we compare "mounded" morphologies of 25ML Ag/Ag(100) films deposited at 0.02ML/s as predicted by the FKR model with those observed in VTSTM experiments [14,15]. This comparison (as well as those in Fig. 2) indicates that the FKR model with our selected parameters does an excellent job in describing film morphologies between 190K and 300K.

4. Conclusions and Extensions

In summary, through a sequence of refinements, we have developed an atomistic model which reliably predicts the mounded morphologies of 25ML Ag/Ag(100) films deposited between 175K and 300K. In the process, we have estimated a terrace diffusion barrier of 0.40eV, a kink rounding barrier of 0.41eV, and ES barriers of 0meV for kinked step edges, and 70meV for closed [110] step edges. We believe that the model is sufficiently robust to predict kinetic roughening and mound coarsening up to 1000's of monolayers. Results, reported elsewhere [20], indicate three regimes of growth (well-defined at higher T): initial transformation from 2D islands to 3D mounds; extended mound steepening with slow coarsening and rapid roughening; and finally asymptotic slope selection with a complex mound dynamics reflecting strong up-down symmetry breaking. Behavior is quite distinct from that of "standard" continuum models incorporating up-down symmetry [22].

5. Acknowledgements

The authors thank Conrad Stoldt, Anthony Layson, and Patricia Thiel for access to experimental data, and Maria Bartelt for square-island model results. This work was supported by NSF Grants CHE-0078596 and EEC-0085604. It was performed at Ames Laboratory, which is operated for the U.S. Department of Energy by Iowa State University under contract No. W-7405-Eng-82.

6. References

[1] *Morphological Organization in Epitaxial Growth and Removal*, edited by Z. Zhang and M.G. Lagally (World Scientific, Singapore, 1998).

[2] M.C. Bartelt and J.W. Evans, *Phys. Rev. B* **54** (1996) R17359; M.C. Bartelt, A.K. Schmid, J.W. Evans, and R.Q. Hwang, *Phys. Rev. Lett.* **81** (1998) 1901.

[3] M.C. Bartelt and J.W. Evans, *Surf. Sci. Lett.* **314** (1994) L829; J. Zhong, T. Zhang, Z. Zhang, and M.G. Lagally, *Bull. Am. Phys. Soc.* **45** (2000) 506.

[4] A. Bogecivic, J. Stromquist, and B.I. Lundqvist, *Phys. Rev. Lett.* **81** (1998) 637.

[5] J. Villain, *J. Phys. I (France)* **1** (1991) 19.

[6] G. Ehrlich and F.G. Hudda, *J. Chem. Phys.* **44** (1966) 1039; L. Schwoebel and E.J. Shipsey, *J. Appl. Phys.* **37** (1966) 3682.

[7] M.D. Johnson, C. Orme, A.W. Hunt, D. Graff, J. Sudijono, L.M. Sander, and B.G. Orr, *Phys. Rev. Lett.* **72** (1994) 116; P. Politi and J. Villain, *Phys. Rev. B* **54** (1996) 5114.

[8] P. Smilauer and D.D. Vvedensky, *Phys. Rev. B* **52** (1995) 14263.

[9] M.C. Bartelt and J.W. Evans, *Phys. Rev. Lett.* **75** (1995) 4250; *Surf. Sci.* **423** (1999) 189.

[10] J. Krug, *Physica A* **263** (1999) 170; P. Politi, G. Grenet, A. Ponchet, and J. Villain, *Phys. Rep.* **324** (2000) 271.

[11] H.-J. Ernst, F. Fabre, R. Folkerts, and J. Lapujoulade, *Phys. Rev. Lett.* **72** (1994) 112; L.C. Jorritsma, M. Bijnagte, G. Rosenfeld, and B. Poelsema, *ibid*, **78** (1997) 911; J.-K. Zuo and J.F. Wendelken, *ibid*, **78** (1997) 2791.

[12] J.A. Stroscio, D.T. Pierce, M. Stiles, A. Zangwill, and L.M. Sander, *Phys. Rev. Lett.* **75** (1995) 4246.

[13] W.F. Elliott, P.F. Miceli, T. Tse, and P.W. Stevens, *Phys. Rev. B* **54** (1996) 17938.

[14] C.R. Stoldt, K.J. Caspersen, M.C. Bartelt, C.J. Jenks, J.W. Evans, and P.A. Thiel, *Phys. Rev. Lett.* **85** (2000) 800.

[15] K.J. Caspersen, C.R. Stoldt, A.R. Layson, M.C. Bartelt, P.A. Thiel, and J.W. Evans, *Phys. Rev. B* **63** (2001) 085401.

[16] M.C. Bartelt and J.W. Evans, *Surf. Sci.* **298** (1993) 421.

[17] B.D. Yu and M. Scheffler, *Phys. Rev. B* **55** (1997) 13916.

[18] C.-M. Zhang, M.C. Bartelt, J.-M. Wen, C.J. Jenks, J.W. Evans, and P.A. Thiel, *Surf. Sci.* **406** (1998) 178.

[19] C. Teichert, C. Ammar, and M. Klaua, *Phys. Status Solidi A* **146** (1994) 223; U. Kurpick and T.S. Rahman, *Phys. Rev. B* **57** (1998) 2482.

[20] K.J. Caspersen, A.R. Layson, C.R. Stoldt, V. Fournee, P.A. Thiel, and J.W. Evans, *Phys. Rev. Lett.* (2001) submitted.

[21] S. Schinzer, M. Kinne, M. Biehl, and W. Kinzel, *Surf. Sci.* **439** (1999) 191; J.G. Amar, *Phys. Rev. B* **60** (1999) R11317.

[22] M. Siegert, *Phys. Rev. Lett.* **81** (1998) 5481; D. Moldovan and L. Golubovic, *Phys. Rev. E* **61** (2000) 6190.

Figure Captions

Figure 1. (a) Schematic for the FKR model of irreversible nucleation and aggregation processes, and of interlayer diffusion processes with a non-uniform ES barrier. (b) Schematic illustrating the key processes and rates controlling the kink rounding probability, $P_{kr}=R_{kr}/(R_{kr}+R_{agg})$, for the configuration shown.

Figure 2. Results for the FKR model with terrace and interlayer diffusion parameters for Ag/Ag(100): dependence of the roughness, W, mound "diameter", D_{av}, and local slope (versus T) on kink rounding barrier, E_{kr}=0 (IKR), 0.40, 0.41 (grey), 0.42, 0.43, 0.44, 0.45, 0.50, ∞ (NKR) in eV.

Figure 3. Results for the FKR and NKR models showing the dependence of film morphology on E_{kr} (shown) for 25 ML films and 1000 ML films, deposited at 230K. Images are 102×102 nm^2 with open [100] steps aligned horizontally.

Figure 4. Comparison of morphologies of 25 ML Ag/Ag(100) films obtained by VTSTM at various T (shown) with those predicted by the FKR model. Image sizes are 100×80 nm^2 with close-packed [110] steps aligned horizontally.

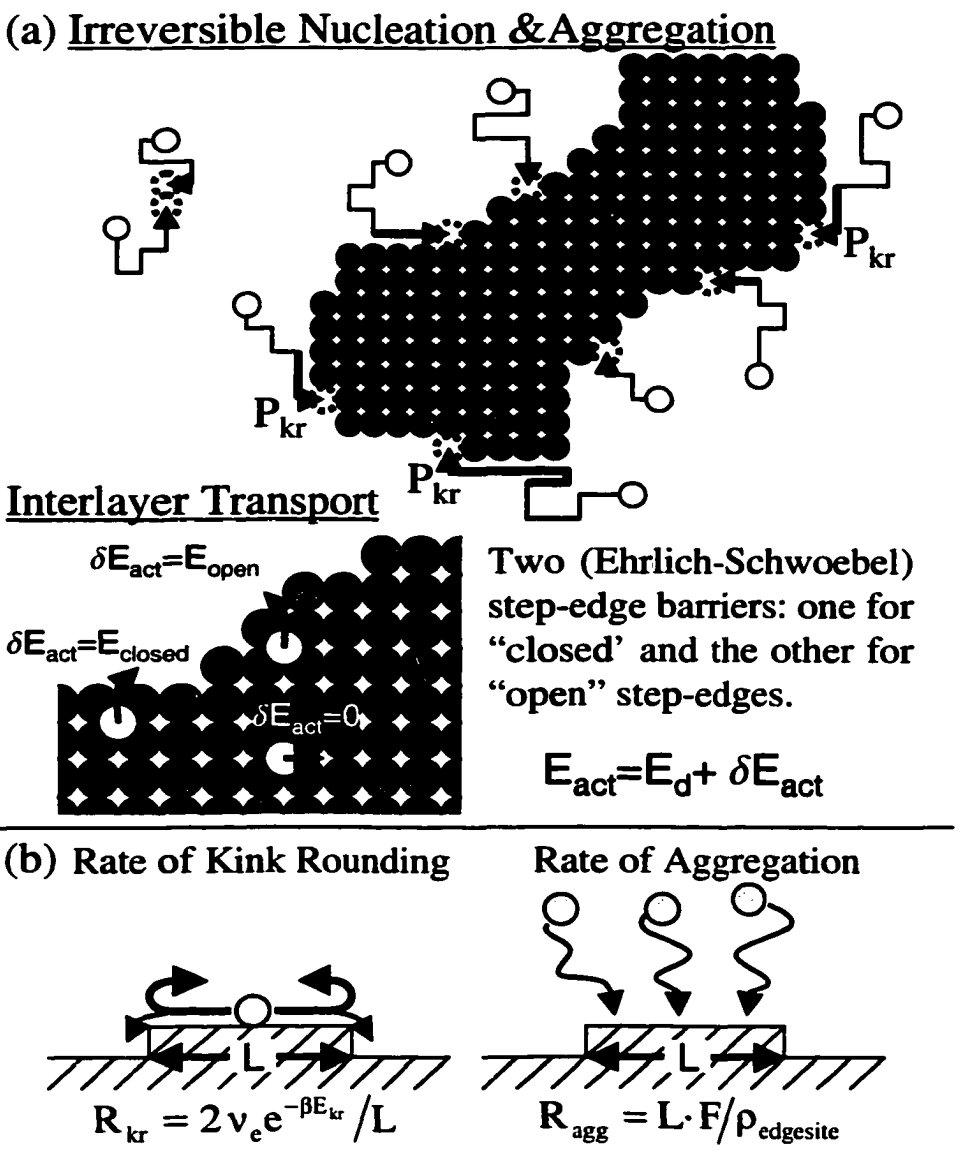
(a) Irreversible Nucleation &Aggregation
P_{kr}
P_{kr}
P_{kr}
Interlayer Transport
$\delta E_{act}=E_{open}$
$\delta E_{act}=E_{closed}$
$\delta E_{act}=0$
Two (Ehrlich-Schwoebel) step-edge barriers: one for "closed' and the other for "open" step-edges.
$E_{act}=E_d+\delta E_{act}$
(b) Rate of Kink Rounding
Rate of Aggregation
L
L
$R_{kr}=2\nu_e e^{-\beta E_{kr}}/L$
$R_{agg}=L\cdot F/\rho_{edgesite}$

Figure 1

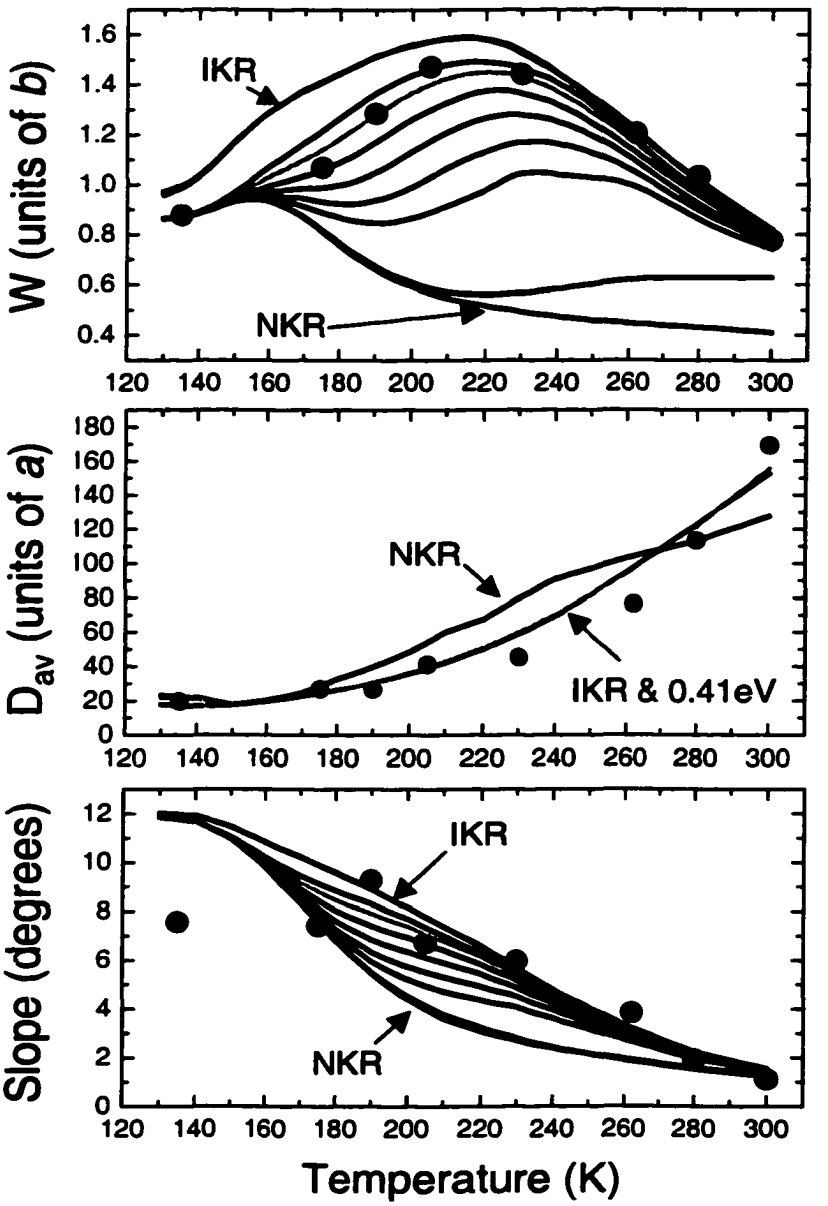
W (units of b)
IKR
NKR
D_av (units of a)
NKR
IKR & 0.41eV
Slope (degrees)
IKR
NKR
Temperature (K)

Figure 2

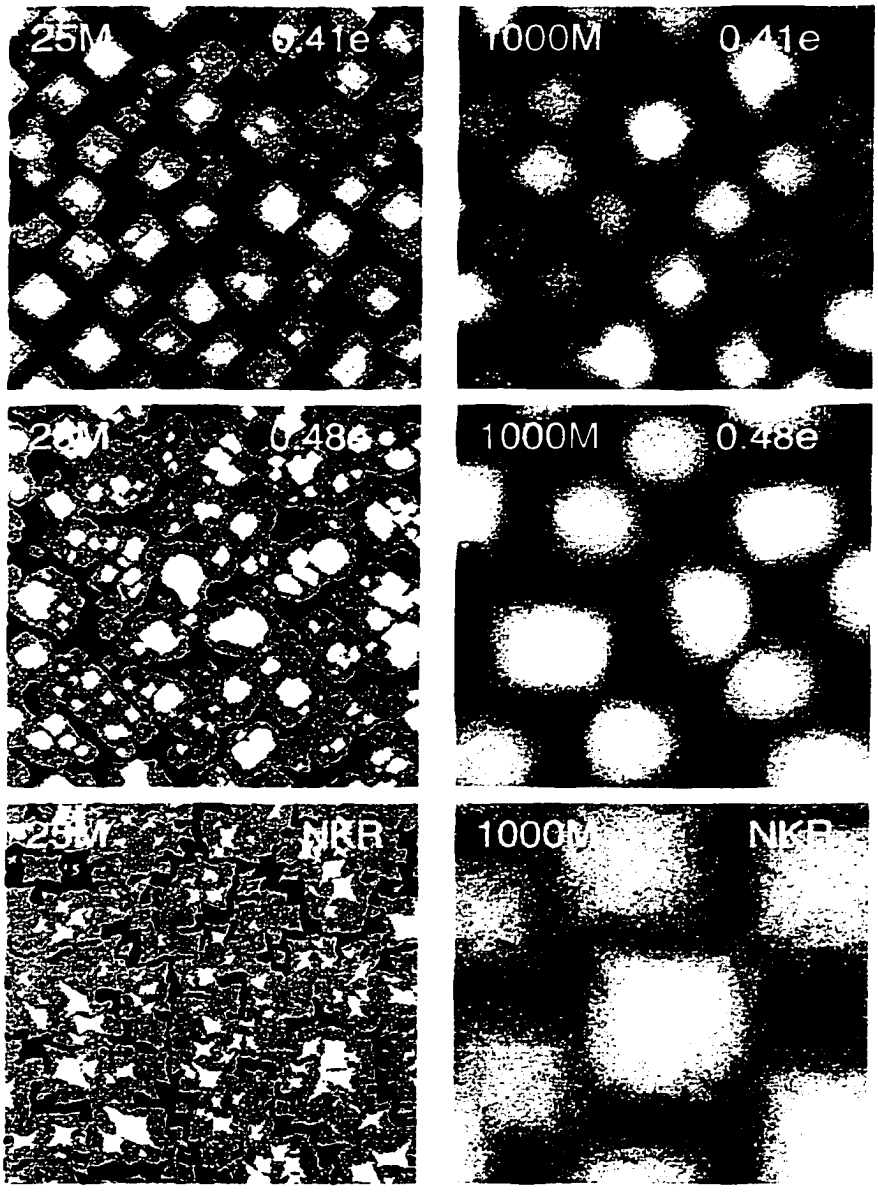

Figure 3

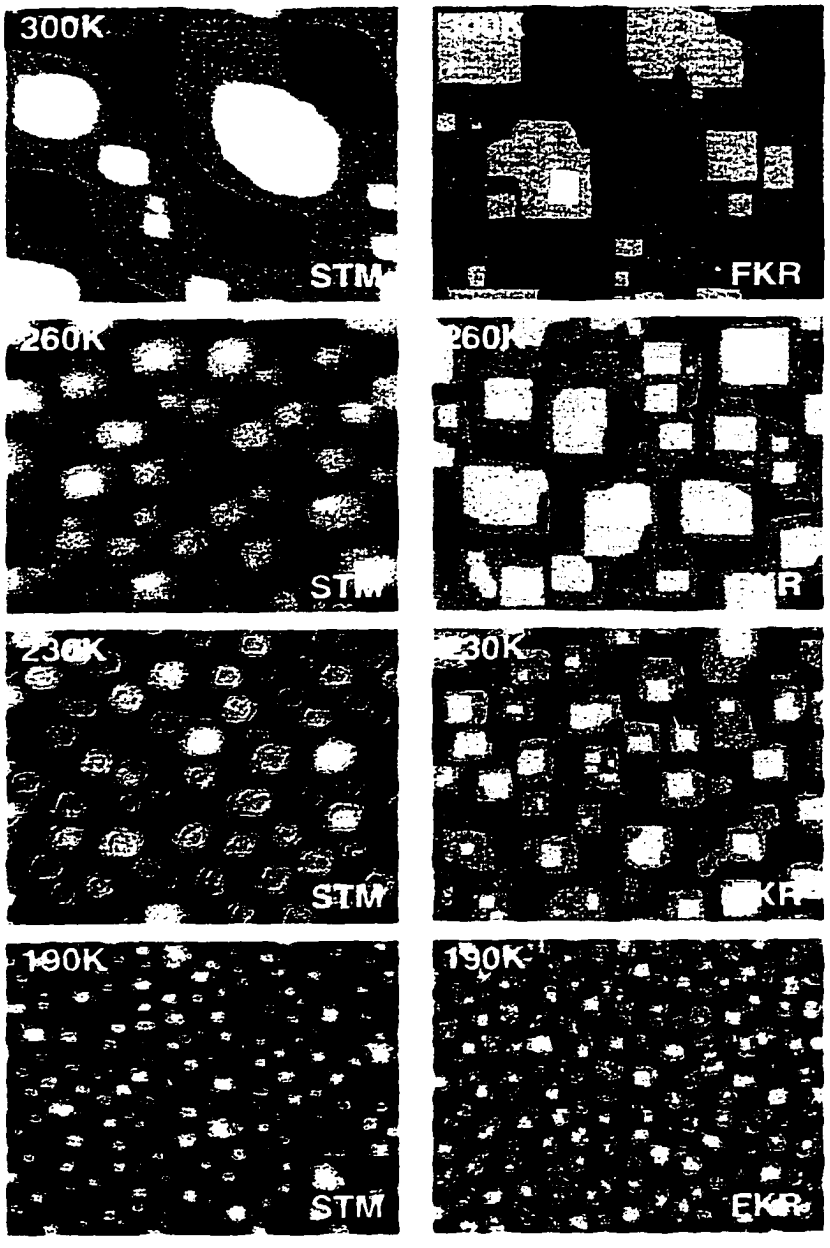

Figure 4

8. GENERAL CONCLUSIONS

The work presented here was a theoretical study of thin film nucleation and growth (focusing on Ag/Ag(100)). Here the nature of the deposition breaks detailed balance and drives the surface far from equilibrium. This means that kinetics processes, rather than bulk energetics, determine the surface morphology. To study the processes that dominate the growing film lattice gas models were developed that contained realistic diffusion pathways and deposition dynamics. Kinetic Monte-Carlo was used to simulate these models, after which they were compared with experimental data. These models containing only a fraction of all diffusion pathways still recovered the essential features of the experiment, and therefore lead to understanding relevant atomistic pathways that control surface growth.

ACKNOWLEDGEMENTS

I would like to express my gratitude to Professor Jim Evans who provided me knowledge and wisdom, he was, and is, a true mentor. I would also like to thank Professor Pat Thiel for guidance and support throughout my work here. Also I must thank Dr. Da-Jiang Liu for patience in answering, what must have seemed, like and endless barrage of stupid questions. Also where would I be with out the experiments generated by Dr. Conrad Stoldt and Dr. Tony Layson, who never did get to angry with me when I told them that the experiments were wrong and my simulations were right.

I thank Jack and Dana (and "little" Kyle) Hartwigsen for making Ames fun, and for being there when I needed them, but mostly for being true friends. I would also like to thank Beth Fatland who made three years of my life in Ames wonderful, even though she made the last six months hell. I would also like to thank her family: Roy, Janet, Melissa, Jamie, Linda, and the many others who took me in and made me fell at home. I would be remiss if I didn't thank Paul Bloom who suffered through all of this with me, even though he caused me to suffer at the end. Also, I thank Steve Gagnier (despite being a Vikings fan) for playing endless rounds of golf with me and putting up with me as a roommate. When it comes to golf I have to mention Scott McKinnly because even with the endless double and triple bogies I could still convince him play. Bridget Mahon, who left here before this place could corrupt her, deserves thanks for toiling through the first year with me. I also thank Dale "The Canadian" McLeod for showing me the ropes my first year (i.e. where to not eat lunch, which is the best golf course, which bar has the best special on a given night, etc.) Thankfully there we a number of people who made my stay in Ames and enjoyable one.

They include, but are not limited to, the people I listed above and Steve "The Chicken" Prescot, Arishika Prescot, Mike "The Complainer" Reynolds, Dave Klien, and Eric Hagberg. Obviously, I also thank my family and friends who even though they were not with me in person they were with me in spirit.

APPENDIX I. USING TEMPERATURE TO TUNE FILM ROUGHNESS: NON-INTUITIVE BEHAVIOR IN A SIMPLE SYSTEM

A paper published in Physical Review Letters.

C.R. Stoldt, K.J. Caspersen, M.C. Bartelt, C.J. Jenks, J.W. Evans, and P.A. Thiel

Abstract

Ag(100) homoepitaxy constitutes one of the simplest systems in which to study thin-film growth. Yet, we find that the roughness variation with temperature is extraordinarily complex. Specifically, as the deposition temperature is reduced from 300 to 50 K, the roughness of 25 monolayer films first increases, then decreases, then increases again. A transition from mound formation to self-affine (semi-fractal) growth occurs at ~135 K. The underlying mechanisms are postulated. An atomistic model incorporating these mechanisms reproduces the experimental data quantitatively.

Text

The surface morphologies of films grown by deposition on perfect substrates can reveal surprising features. Even if the equilibrium structure is simple, deposition can drive the system into an unanticipated variety of far-from-equilibrium forms, particularly at low temperatures, T, where equilibration is limited [1]. Important physical properties of such films depend sensitively on these morphologies, particularly on roughness. Prominent examples are magnetic properties of thin metal films, transitions in conductivity, superconductivity and localization in quench condensed films, and catalytic properties of

bimetallic thin films [1,2] Thus, a fundamental understanding of the atomic-scale processes that underlie film growth and their relationship to film morphology is a crucial goal, since it will enable control or "tuning" of film structure.

This goal has yet to be achieved even for simple growth systems. Homoepitaxy (self-growth) is at an extreme of simplicity, because thermodynamics requires that such a film grows as smoothly as possible within entropic limits, with each layer filling in sequence (for typical T). Naturally, one expects to see this type of evolution at high T, where kinetic barriers—especially those to interlayer diffusion—can be overcome. Certainly, deposition at lower T can produce rougher non-equilibrium structures ("kinetic roughening"). A traditional expectation is that the roughness will increase monotonically as the deposition temperature is lowered, and the system deviates farther from equilibrium. This view was prompted in part by the "rain model" for low T deposition, where randomly deposited atoms irreversibly stick at on-top adsorption sites in a simple cubic (SC) crystal geometry [3]. This model exhibits rough growth characterized by a Poisson height distribution, behavior which persists (in an SC geometry) whenever interlayer diffusion is inoperative. A contrasting view [1] is that films should grow smoother at lower T, due to the presence of smaller islands (atoms deposited on top are closer to edges where they can hop down, but this neglects slower terrace diffusion). Neither picture is supported by our results.

In reality, metal film growth is far more complex and challenging to understand. One example is the non-monotonic variation of roughness with temperature observed on substrates with threefold symmetry [4]. This anomalous behavior has been related to a transition from compact to irregular shapes of the large 2D islands formed, the increase in kink sites at island edges facilitating interlayer transport. On substrates with fourfold

symmetry, such as Ag(100), there is no comparable island shape transition. However, surprisingly smooth growth has been observed in metal(100) homoepitaxy at low temperature (~77K), as reflected by persistent diffraction intensity oscillations [5]. More recently, roughness was observed to increase from 300K to 200K for Ag/Ag(100) [6], but to decrease from 200 to 160K for Cu/Cu(100) [7]. While these fragments of experimental evidence for systems with fourfold symmetry have been tantalizing, they have been insufficient to provide a comprehensive picture for growth. This Letter provides the broad experimental picture that has been absent, including an assessment of behavior down to extremely low temperatures—where new surprises emerge! Tailored atomistic growth models are applied to test our interpretation of experimental observations.

The experiments reported here detail the temperature-dependence of multilayer homoepitaxy on Ag(100) between 300K and 50K. We use an Omicron Variable-Temperature Scanning Tunneling Microscope (VTSTM) in a UHV chamber with base pressure below 1×10^{-10} Torr. Films are formed by evaporation of pure Ag from an Omicron EFM3 UHV evaporator. After deposition, T remains fixed (± 5 K), and data is obtained from central portions of broad terraces in order to minimize the effect of step edges on data analysis (cf. Ref.[8]).

Figure 1 shows STM images of 25 ML Ag films grown on Ag(100) deposited at various T. In order to characterize the vertical morphology precisely, we discretize the continuous film height distribution obtained from STM by peak fitting using multiple Gaussian functions with a separation equal to the atomic interlayer spacing, b=2.04Å. The resulting surface roughness, W (RMS width of the height distribution in units of b), versus T, is shown in Fig. 2a. The temperature variation is remarkably complex. Specifically, the

roughness of 25-monolayer (ML) Ag films *increases* as T is reduced from 300K to 220K, then *decreases* as T is reduced further to 140K, and finally *increases* again for lower T (at least down to 50K).

To facilitate a more detailed characterization of film morphology, we provide some further background on possible growth modes. For metal homoepitaxy, roughening is often accompanied by the development of three-dimensional mounds with a well-defined characteristic lateral size [1,3,4,7]. Although other possibilities exist [9], this behavior is usually associated with the existence of an additional potential energy barrier, the Ehrlich-Schwoebel or step-edge barrier, which inhibits downward diffusion at step edges [10]. Further explanation is provided below. In many systems [3], an alternative to mounding is observed known as self-affine (semi-fractal) growth, which is characterized by a continuous spectrum of lateral lengths. A single system usually exhibits just one of these two types of behavior, and distinction between them is provided by examination of the height-height correlation function, H(**r**), i.e., the mean-square height difference for two points on the film surface versus their lateral separation, **r** [3].

Thus, we next examine H(**r**) vs. **r** for the STM data shown in Fig.1. Behavior at 230 K is plotted in the inset of Fig. 2b. The presence of oscillations indicates formation of somewhat ordered arrays of mounds. The first maximum (minimum) corresponds roughly to the average mound radius, R_{av} (separation or diameter, D_{av}). Figure 2b shows that R_{av} and D_{av} (= $2R_{av}$) decrease rapidly with decreasing T to about 205 K, after which they remain roughly constant. Oscillations in H(**r**) are apparent down to 175 K, but are gone by 135 K, suggesting a transition to self-affine growth. This claim is supported by examining the roughness exponent, α, determined from the roughness, W_L, for a range of short STM scans

of length L, and using $W_L \sim L^{\alpha}$ [3]. We find that $\alpha \approx 1$ for T>135 K (reflecting "regular" mounded morphologies), with α decreasing to < 0.5 below 135 K (reflecting self-affine morphologies). See Table I. Hence, two independent analyses of the film morphology support a transition from mound formation to self-affine growth in the range of 175-135 K. We also find that the average step density (or mean local slope), and the slope of mound sides, increase monotonically with decreasing T (Table I), observations which we shall exploit below in interpreting low T growth.

The behavior shown in Figs. 1-2 warrants a detailed discussion regarding the possible atomic processes responsible for the observed growth characteristics. This discussion below is split into the two temperature regimes for mounding and self-affine growth, respectively.

Mounding Regime at higher T: We propose that film structure at 175K and above is determined by three main processes: (i) intralayer terrace diffusion (with barrier E_d) leading to the irreversible formation [8] of near-square islands in each layer; (ii) downward interlayer diffusion inhibited by a small step edge barrier (of magnitude E_{se}); and (iii) "downward funneling" (DF) [11] or deflection of deposited atoms from step edges and other microportusions to lower four-fold hollow (4FH) adsorption sites. See Fig.3a. (DF results from the high kinetic energy acquired by atoms on approaching the surface.) Villain noted that the Ehrlich-Schwoebel barrier causes diffusing atoms to be reflected from descending step edges, enhancing their probability of capture at ascending step edges. This produces a lateral mass current in the uphill direction ($\mathbf{j}^{up}$) resulting in a growth instability (mounding) [10]. DF produces stabilizing downhill current ($\mathbf{j}^{down}$) which for sufficiently large slopes of mound sides can counterbalance the uphill current (i.e., $\mathbf{j}^{up}+\mathbf{j}^{down} \approx \mathbf{0}$), resulting in selection of these mound slopes [11]. See again Fig.3a.

At 300 K, the two diffusional processes are most important for films up to ~25ML. Terrace diffusion is highly active producing large lateral structures. Intralayer diffusion is also efficient, and allows atoms deposited in higher layers to readily reach lower layers perpetuating smooth growth. Only for thicker fims would mounds become well-developed.

As the deposition temperature is reduced from 300 K to about 200 K, the main effect on roughness comes from increasing inhibition of interlayer diffusion due to the presence of the small step-edge barrier. Atoms become less likely to reach lower layers and, as a result, mounds become more pronounced even by 25ML. This is reflected in an increase in W, which peaks between 230 and 205 K (Fig 2a), where the mounds are still nearly-square with broad, flat summits (see Fig. 1). At least at 230K (and below), we find that DF significantly influences mound morphology, inhibiting the growth of mound slopes already by 25 ML.

As temperature is reduced, a strong inhibition of terrace diffusion also occurs, leading to a significant decrease in feature size (see Fig.1 and Fig.2b), and a corresponding increase in step density. Below about 200 K, we propose that this increase in step edge density becomes the determining effect: it leads to an enhancement of the effect of the DF mechanism. DF acts to smooth the surface, as evidenced by the decrease in W below 230 K (Fig. 2a), and ultimately to induce a transition out of the mounding regime.

To test our understanding of the evolution of film structure in the mounding regime, we employ kinetic Monte Carlo (KMC) simulations of an atomistic model for homoepitaxial growth with an FCC(100) crystal geometry that incorporates the elements described above. This generic model has been presented previously [11], although at that time detailed experimental data for Ag/Ag(100) did not exist for comparison. From previous Arrhenius analyses of submonolayer island separation [8], and from *ab-initio* theory [13], we know E_d

≈0.38-0.45 eV. Interestingly, a consistent estimate of $E_d \approx 0.45$ eV follows from an Arrhenius analysis [3,11] of the mound separation data in Fig.2b. Here, we use E_d=0.40 eV. We estimate the step edge barrier to be 30 ± 5 meV from a fit to the value of W at 230 K reported above. All attempt frequencies were set to the value 10^{13}/s (cf. Ref.[8]). Hence, there remain no adjustable parameters in the model.

As shown in Fig.4a, this kinetic model reproduces very well the experimental W's between 300 and 135 K. It also reproduces the monotonic increase in slope with decreasing T, and a transition out of the mounding regime for lower T, trends seen in previous generic simulations [11]. Despite this success, we emphasize our simplifying assumptions: the step edge barrier is assumed uniform; isolated islands are square with [110] step edges, and do not restructure upon "collision" due to growth [17]. In reality, open [100] step edges are present, and E_{se} is likely lower for [100] than [110] edges [12], so our $E_{se} \approx 30$ meV is an effective value.

Finally, as a definitive test of our claim that DF produces the decrease in W below 220K, we have repeated these simulations with the same parameters, but for a SC crystal geometry with on-top adsorption sites where DF does not occur. The results reveal a monotonic increase in W for 25ML films as T decreases below 300K (achieving a Poisson value of W=5 *b* for low T).

Self-Affine Growth Regime at Lower T: Below 135 K, W increases again. Such a phenomenon has not been observed previously. Why does this occur? A key point is that the surface becomes increasingly irregular and local slopes become steeper at lower T (see Table I). Molecular Dynamics simulations of metal(100) homoepitaxy [14] indicate that in such situations, DF can breakdown, deposited atoms becoming captured on the sides of

microprotrusions rather than reaching lower 4FH sites, leading to formation of overhangs and internal defects (Fig.3b).

We have attempted to model growth in this regime, by starting from a "restricted downward funneling" (RDF) model, which should apply at 0 K. In this model, deposited atoms funnel downward, but can get stuck when they reach special types of sites which do not contain complete quartets of four supporting atoms. These "trap sites" contain at least three supporting atoms in the layer beneath; or two such atoms beneath and at least one in-layer neighbor; or one atom beneath and at least two in-layer neighbors (see Fig. 3b). For a 25ML film, one finds for RDF that $W^{RDF} = 1.41\ b$ (solid line in Fig.4b below 40K) and that the film has a significant density of internal voids, versus $W^{DF} = 0.74\ b$ (and no voids) for standard DF.

The next challenge is to extend this model to describe the T-dependence of W in the range up to 135K where terrace diffusion is inoperative. The key point here is that on the irregular structures formed during film growth at low T, there are many other thermally activated interlayer hopping processes, with low barriers, E_{act}, which can be operative and affect film morphology. For example, consider a "micropyramid" with sides corresponding to {111} microfacets. Atoms on such facets are thermally mobile even down to 40K [1], which can lead to a novel downward transport pathway. With this in mind, we augmented the above RDF model by incorporating various interlayer hopping processes for atoms with low coordination number, m, as follows: hopping is instantaneous for m<3; E_{act}=0.10eV for m=3 (or 0.15eV for three supporting atoms); E_{act}=0.25eV for interlayer hops with m=4 and 5. See Fig.3d. Attempt frequencies are set to $10^{12}\ s^{-1}$. These choices are motivated by the known attempt frequency and terrace diffusion barrier (0.10eV) for Ag/Ag(111) [1], and by

semi-empirical studies of other activation barriers. As T increases from 0 K, these processes turn on in sequence according to the hierarchy of energetic barriers, leading to the stepwise variation in W for a 25 ML film shown in Fig. 4b. Consequently, our model recovers the general experimental trend between 135 and 50 K.

Thus, a picture emerges that idealized DF provides a reasonable description of deposition dynamics at temperatures above 100K, because either the film morphology is locally smooth enough to make breakdown rare, or when breakdown occurs, low barrier interlayer diffusion processes are active which can bring deposited atoms to lower 4FH sites.

All of the data presented above are for 25ML films. How would our observations depend upon film thickness? The qualitative variation of W vs. T should remain the same up to at least 100ML, as is in fact predicted by our simulation models. However, since the film roughens at different rates for different T, such features as the temperature for maximum roughness shift (higher with 0). There is much current interest [1,15,16] in characterizing kinetic roughening, usually described by the relation $W \sim \theta^{\beta}$, the coarsening of lateral mound dimensions described by D_{av} (or R_{av}) ~ θ^{n}, and the relationship between these. Our results will be reported in detail elsewhere. But here we note that at 230K, where initial mound formation is most pronounced (and 25ML films are roughest), analysis of growth up to 100ML reveals that roughening occurs much more quickly than coarsening (n is slightly below 0.2, whereas β is roughly 0.4 or higher initially). This behavior is consistent with our simultaneous observation of slow slope selection during growth (at 230K), and recent theoretical analyses of such growth regimes [16].

In summary, we have shown that the simple system, Ag/Ag(100), exhibits the most complex variation of W vs. T yet observed in any metal homoepitaxial system. Atomistic

simulations support the following characterization of the deposition and diffusion processes controlling observed behavior: a small step edge barrier leads to mound formation at the higher temperatures; downward funneling at step edges triggers smoother growth and ultimately a transition to self-affine morphologies at lower T (where step edges are more prevalent); and, finally, the breakdown of funneling on small steep microprotrusions leads to rougher growth at very low T. This work was supported by NSF Grant CHE-9700592, and performed at Ames Laboratory, which is operated for the USDOE by ISU under Contract No. W-7405-Eng-82. MCB was supported by the USDOE (BES) under Contract No. DE-AC04-94AL85000.

References

[1] *Morphological Organization in Epitaxial Growth and Removal*, Z. Zhang and M.G. Lagally, Ed.s (World Sci., Singapore, 1998).

[2] *Magnetism on a Microscopic Scale*, MRS Bull., **20**, no. 10 (1995); K.L. Ekinci and J.M. Valles, Phys. Rev. B **58**, 7347 (1998).

[3] A.-L. Barabasi and H.E. Stanley, *Fractal Concepts in Surface Growth* (University Press, Cambridge, 1995).

[4] R. Kunkel *et al.*, Phys. Rev. Lett. **65**, 733 (1990); F. Tsui *et al.*, *ibid* **76**, 3164 (1996).

[5] W.F. Egelhoff and I. Jacob, Phys. Rev. Lett. **62**, 921 (1989).

[6] W.C. Elliot *et al.*, Phys. Rev. B **54**, 17938 (1996).

[7] H.-J. Ernst *et al.*, Phys. Rev. Lett. **72**, 112 (1994).

[8] C.-M. Zhang *et al.*, Surf. Sci. **406**, 178 (1998).

[9] M.V.R. Murty and B.H. Cooper, Phys. Rev. Lett. **83**, 352 (1999); J.G. Amar and F. Family, *ibid*, **77**, 4584 (1996).

[10] J. Villain, J. Phys. I (France) **1**, 19 (1991).

[11] M.C. Bartelt and J.W. Evans, Phys. Rev. Lett. **75**, 4250 (1995); Surf. Sci. **423**, 189 (1999).

[12] U. Kurpick and T.S. Rahman, Phys. Rev. B **57**, 2482 (1998).

[13] B.D. Yu and M. Scheffler, Phys. Rev. Lett. **77**, 1095 (1996).

[14] C.L. Kelchner and A.E. DePristo, Surf. Sci. **393**, 72 (1997).

[15] M. Siegert, Phys. Rev. Lett. **73**, 5481 (1998); L.-H. Tang, P. Smilauer, and D.D. Vvedensky, Euro. Phys. J. B **2**, 409 (1998); J.G. Amar, Phys. Rev. B **60**, R11317 (1999).

[16] L. Golubovic, Phys. Rev. Lett. **78**, 90 (1997); P. Politi and A. Torcini, J. Phys. A (2000).

Table Captions:

1. Variation of the roughness exponent, α, the average local slope, ϕ_{av}, and the slope of mound sides, ϕ_{md}, (in degrees) with T for 25 ML Ag/Ag(100) films.

Figure Captions:

Figure 1.Differentiated 100×100nm^2 STM images of 25 ML Ag/Ag(100) films deposited with F≈0.02ML/s at various temperatures (shown). The vertical scale is expanded.

Figure 2.Properties of 25 ML Ag/Ag(100) films deposited with F≈0.02ML/s at T≤300K. (a) Roughness W (solid circles) in units of interlayer spacing, b=2.04Å; (b) Average mound separation, D_{av} (solid circles) and radius, R_{av} (solid squares). Solid curves guide the eye, error bars indicate statistical uncertainty (excluding systematic tip effects, expected at low T). Inset: H(**r**) at 230K; arrows indicate R_{av} and D_{av}.

Figure 3. Schematics: (a) mound formation - step edge reflection (SER), downward funneling (DF), and associated lateral mass currents; (b) restricted downward funneling (RDF) with a top view of some trap sites (# supports / # in-layer atoms); (c) low-barrier downward hops.

Figure 4. MC simulation results for: (a) mound formation up to 300K (solid curve); (b) RDF with low barrier hops up to 135 K (solid curve). Expt data are open squares.

T	54K	135K	175K	230K	280K
α	0.50	0.93	1.05	1.07	----
ϕ_{av}	14.0	10.6	10.4	8.4	2.7
ϕ_{md}	16.0	12.0	12.2	9.6	3.2

Table 1

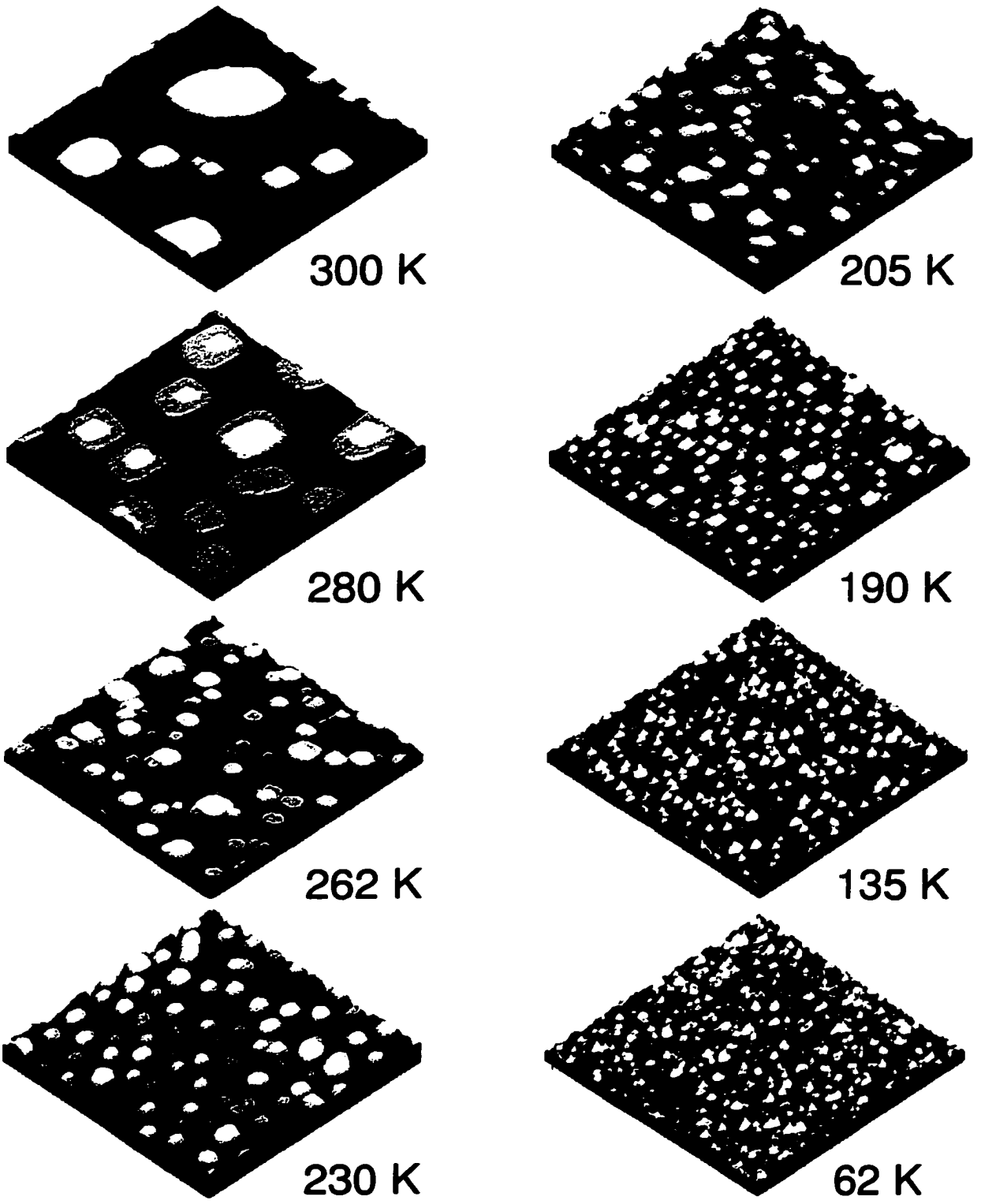

Figure 1

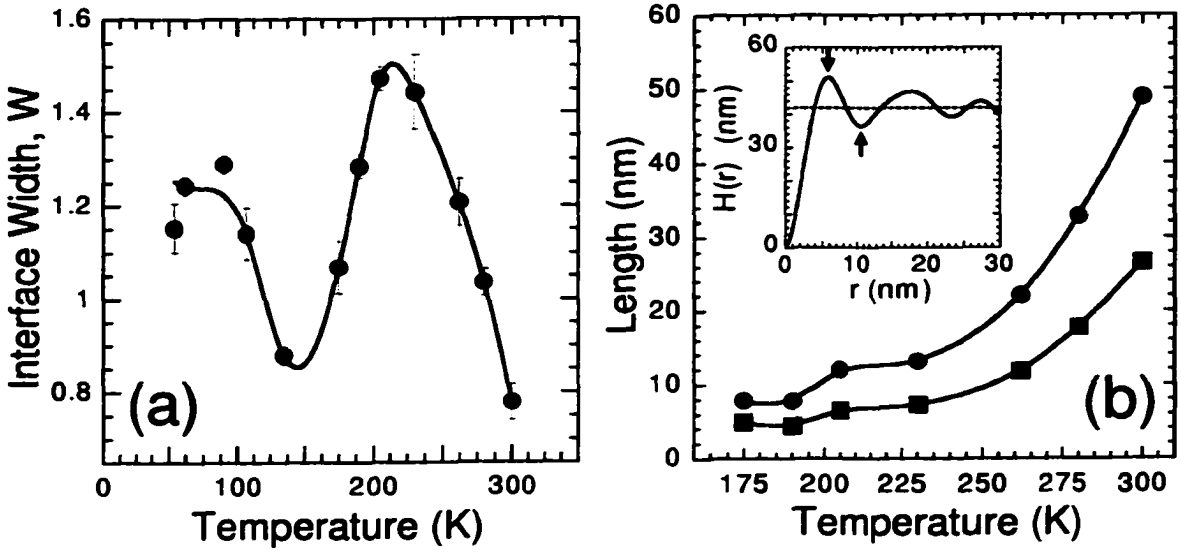
Interface Width, W
1.6
1.4
1.2
1
0.8
(a)
0
100
200
300
Temperature (K)
Length (nm)
60
50
40
30
20
10
0
H(r) (nm)
60
30
0
0
10
20
30
r (nm)
(b)
175
200
225
250
275
300
Temperature (K)

Figure 2

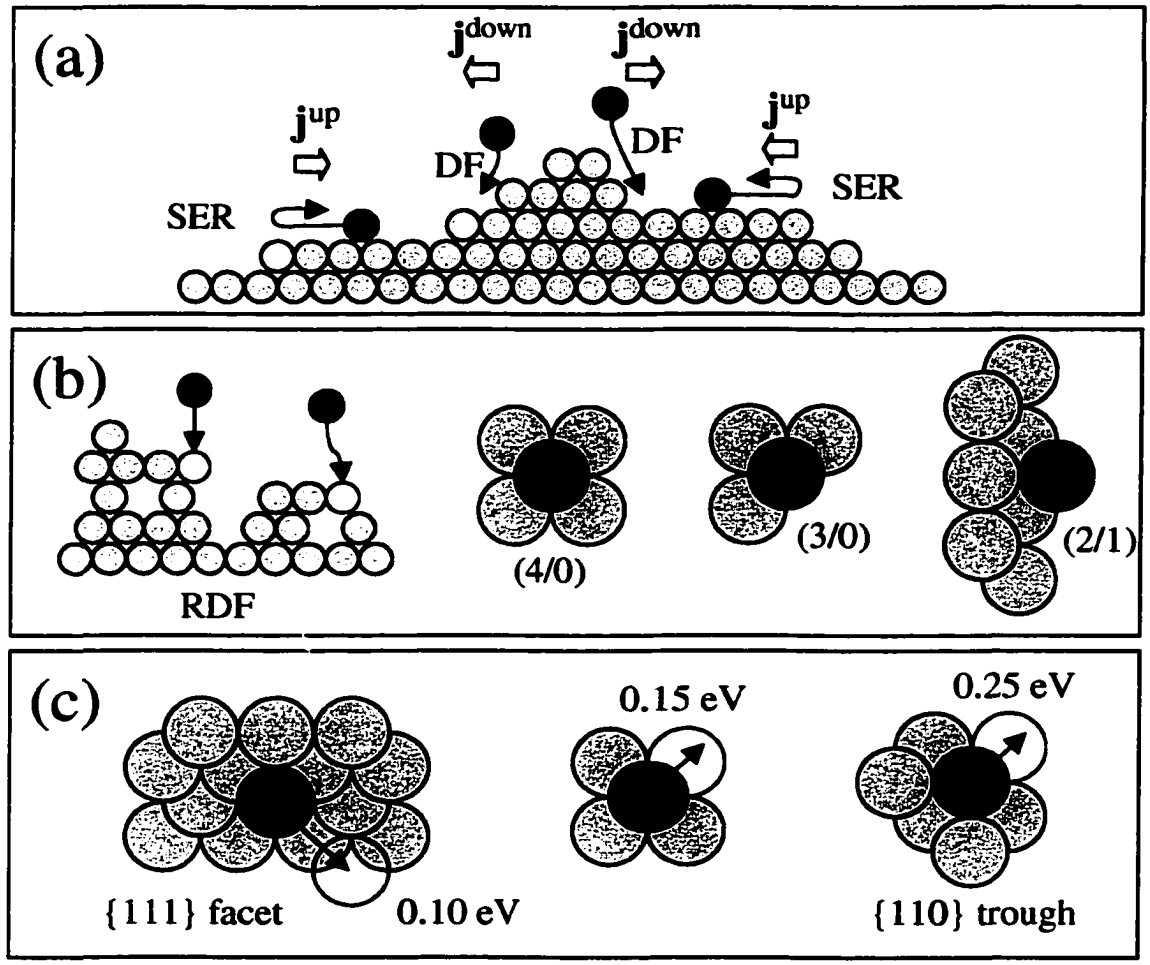
(a)
j^down
j^down
j^up
j^up
DF
DF
SER
SER
(b)
RDF
(4/0)
(3/0)
(2/1)
(c)
0.15 eV
0.25 eV
{111} facet
0.10 eV
{110} trough

Figure 3

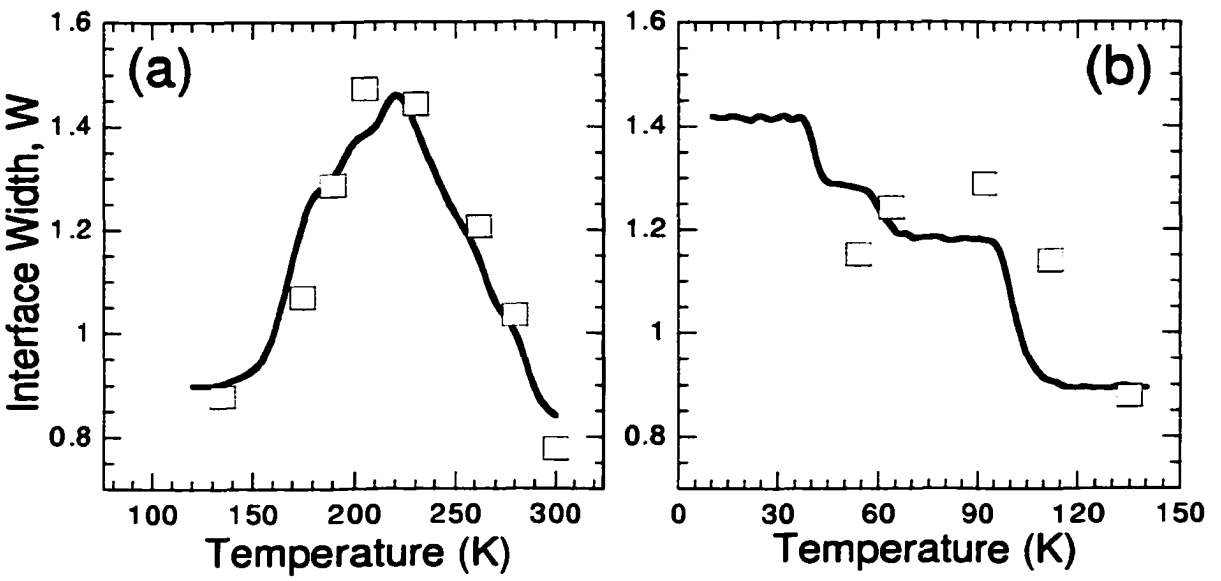
(a)
(b)
Interface Width, W
1.6
1.4
1.2
1
0.8
100
150
200
250
300
0
30
60
90
120
150
Temperature (K)
Temperature (K)

Figure 4

APPENDIX II. MODELING OF METAL(100) HOMEPITAXIAL FILM GROWTH AT VERY LOW TEMPERATURES

A paper published in the Volume 619 of the Symposium Proceedings of the Materials Research Society.

K.J. Caspersen, C.R. Stoldt, P.A.Thiel, and J.W. Evans

Abstract

We model the growth of Ag films deposited on Ag(100) below 140K. Our recent Variable-Temperature Scanning Tunneling Microscopy (VTSTM) studies reveal "smooth growth" from 120-140K, consistent with earlier diffraction studies. However, we also find rougher growth for lower temperatures. This unexpected behavior is modeled by describing the deposition dynamics using a "restricted downward funneling" model, wherein deposited atoms get caught on the sides of steep nanoprotrusions (which are prevalent below 120K), rather than always funneling down to lower four-fold hollow adsorption sites. At 0K, where no thermal diffusion processes are operative, this leads to the formation of *overhangs* and *internal defects* (or *voids*). Above 40K, low barrier interlayer diffusion processes become operative, producing the observed smooth growth by 120K. We also discuss how the apparent film morphology mapped out by the STM tip "smears" features of the actual film morphology (which are small at low temperature), and also can lead to underestimation of the roughness.

I. Introduction

Traditionally, the roughness of deposited homoepitaxial films (of a given thickness) was expected to increase with decreasing temperature (T), due to enhanced kinetic barriers to smoothing [1,2]. One well-known exception is "re-entrant" smooth growth at low T in the Pt/Pt(111) system [3], but this behavior is due to a transition from compact to fractal islands (which facilitates downward transport). Perhaps more surprising is the "smooth growth" at liquid nitrogen temperatures observed in diffraction studies [4,5] of metal(100) homoepitaxial growth, for which there is no analogous island shape transition. This smooth growth, and observed long-range lateral spatial correlations (i.e., narrow diffraction profiles) in the submonolayer regime, were associated with "transient mobility" of "hot" deposited adatoms (noting that thermal terrace diffusion is inoperative at low T) [4]. Such transient mobility was not found in molecular dynamics (MD) studies [6], and instead it was proposed that smooth growth was due to "downward funneling" of depositing atoms to lower four-fold hollow sites in the fcc(100) geometry [6]. The narrow profiles have been attributed to intralayer "clumping" of atoms deposited nearby other adatoms facilitated by low-barrier edge diffusion processes [7].

Our recent VTSTM studies [8] of the morphology of 25ML Ag films deposited on Ag(100) do in fact find "re-entrant" smooth growth (i.e., roughness increases as T is lowered to 220K, but then decreases again until 140K). This is consistent with the earlier diffraction studies [4,5]. However, our studies also reveal rougher growth for lower T, the explanation of which is the focus of this paper. Motivated in part by recent MD studies [9], we propose that the latter feature is due to "restricted downward funneling (RDF)", where deposited atoms get caught on the sides of steep nanoprotrusions (which are prevalent below 120K). In Sec.II,

we analyze this model for growth at 0K. Next, in Sec.III, we introduce certain low-barrier thermal diffusion processes that are operative above 40K. This reproduces the additional smoothing observed experimentally by 120K. Some discussion of model behavior is provided in Sec.IV. In Sec.V, we compare the actual film morphology with that probed by STM tip. Conclusions are provided in Sec. VI.

We focus on the behavior of the surface roughness, W, of the growing film. Let P_j denote the (normalized) population in layer j of "surface atoms", by which we mean those atoms which are at the top of each vertical column of atoms in the fcc(100) geometry. Then, one has $W^2 = \Sigma_j (j-j_{av})^2 P_j$, where $j_{av} = \Sigma_j j P_j$ is a measure of the mean film height. This W is measured in units of the interlayer spacing, b = 2.04 Å for Ag(100). One can also consider the skewness, $\kappa = W^{-3} \Sigma_j (j-j_{av})^3 P_j$, and the kurtosis, $Q = W^{-4} \Sigma_j (j-j_{av})^4 P_j - 3$ (which measures the amount of the height distribution in the tail, relative to a Gaussian distribution).

II. "Restricted Downward Funneling" Model for Growth at 0K

The idea behind this model is that depositing atoms can be captured or trapped at sites with:

(i) four supporting atoms, i.e., four-fold hollow adsorption sites in the fcc(100) geometry;

(ii) three supporting atoms, i.e., one supporting atom is "missing" compared with (i);

(iii) two supporting atoms, provided there are one (or more) in-layer neighbors;

(iv) one supporting atom, provided there are two (or more) in-layer neighbors.

More specifically, in the RDF model, an atom impinging on the surface funnels downward until reaching one of the above trap sites. In contrast, for pure downward funneling (DF), the atom continues further down until reaching a four-fold hollow site. See Fig. 1 for schematics

of DF, RDF, and the above trap sites. Note that in the RDF model of homoepitaxial growth, the formation of overhangs and internal defects or voids is possible, as seen in MD studies [9].

Next, we consider the behavior of the roughness, W, for the growing film. Fig.2a shows W versus the thickness or coverage, θ (in monolayers, ML), for RDF and for DF. For a 25ML film, one finds for RDF that $W^{RDF} = 1.41\ b$ versus a much smaller $W^{DF} = 0.74\ b$ for standard DF. The defect density of thick (100ML) films is 28.4% for RDF (versus 0% for DF). See Fig. 2b.

III. Growth Between 0K and 140K: Low Barrier Interlayer Diffusion

The next challenge is to extend the RDF model to describe the T-dependence growth (and specifically of W) up to 140K where terrace diffusion is still inoperative. (The barrier for terrace diffusion is 0.4eV with a prefactor of $10^{13}\ s^{-1}$, implying a hop rate below $0.04\ s^{-1}$ at 140K.) The key point to be made here is that on the irregular structures formed during film growth at low T, there are many other thermally activated *interlayer* hopping processes with low barriers, E_{act}, which can be operative and affect film morphology. For example, consider a "micropyramid" with sides corresponding to {111} microfacets. Atoms on such facets are thermally mobile even down to 40K [1], which can lead to a novel downward transport pathway.

With this in mind, we have augmented the above RDF model by incorporating various interlayer hopping processes for atoms with <u>low</u> coordination number, m, as follows: hopping is instantaneous for m<3; E_{act}=0.10eV for m=3 (or 0.15eV for three supporting atoms); E_{act}=0.25eV for interlayer hops with m=4 and 5. See Fig.3. Attempt frequencies are set to $10^{12}\ s^{-1}$. These choices are motivated by the known attempt frequency and terrace

diffusion barrier (0.10eV) for Ag/Ag(111) [1], and by semi-empirical studies of other activation barriers. Terrace diffusion, involving hopping out of four-fold hollow sites, is still inoperative. One other significant choice in the model is whether to allow adatoms to pass through sites with low coordination, as e.g., is necessary to hop from the {111}-faceted sides of a mesa-like microprotrusion to the top. Our model I has no restriction on the coordination of sites visited, and thus allows climbing "up and over". In contrast, in our model II, sites visited must have coordination m>2, which forbids climbing up on top of mesas, so adatoms diffuse "up and back". The latter is consistent with the additional "large" step-edge barrier which exists at the edge of Ag islands on Ag(111).

As T increases from 0K, these interlayer diffusion processes turn on in sequence according to the hierarchy of energetic barriers. This leads to the step-wise variation of W versus T for a 25ML film shown in Fig. 4 for an (experimental) deposition flux of F=0.040ML/s. Our models recover the general trend in the experimental data (also shown) between 50K and 135K. Note that in model I, W does not always decrease with increasing T. This is due to the fact that activation of certain interlayer diffusion processes can lead to some atoms climbing uphill rather than downhill. From the simulations, we also extract the T-dependence of other aspects of film morphology, e.g., the density of internal defects (Fig.5a), and the skewness and kurtosis of the surface (Fig.5b) of 25ML films. The negative skewness and positive kurtosis for low T correspond to a film surface with deep narrow crevasses, a feature which disappears at higher T. Thus, a picture emerges that idealized DF provides a reasonable description of deposition dynamics at temperatures above 100K, because either the film morphology is locally smooth enough to make breakdown of DF rare,

or when breakdown occurs, low barrier interlayer diffusion processes are active can bring deposited atoms to lower 4FH sites.

IV. Discussion

To elucidate the behavior of film growth, one can consider a coarse-grained description of the evolution of the film height, $h(\underline{x},t)$, at various lateral positions, $\underline{x}$, according to

$$\partial/\partial t\, h = F/\rho - \nabla\cdot\underline{J} + \eta, \qquad (1)$$

where F is the deposition flux, ρ is the film density (ρ=1 being defect free), $\underline{J}$ is the lateral mass flux of adatoms on the surface, and η is the uncorrelated deposition noise. For the DF model, one has ρ=1 and $\underline{J} \approx -cF\nabla h$, so (1) becomes the linear Edwards-Wilkinson equation [7,10]. Here W increases logarithmically with θ=Ft, and the skewness and kurtosis vanish. For RDF, one has ρ<1, and furthermore expects that $\rho=\rho_0(1+d|\nabla h|^2)$. Since $\underline{J}$ should retain the form for DF with reduced c (due to reduced downward funneling), then (1) adopts the non-linear KPZ form. For 2+1 dimensional models in the KPZ-class such as RDF for 0K growth, random deposition at four-fold hollow sites (RD4FH) [10] and ballistic deposition [BD], one expects that $W\sim\theta^{\beta}$ with $\beta\approx0.24$. This applies in the experimentally relevant coverage range for RD4FH, but not for RDF where the effective $\beta\approx0.06$ at 100ML (or for BD). We presume that this is in part because of a very weak non-linearity for RDF with $d \approx -0.081$. The feature of a very slow crossover to true asymptotic KPZ behavior is familiar from studies of other growth models with internal defects [11]. However, all these models display similar behavior of the skewness, κ (kurtosis, Q), which vary from –0.55 to –0.44 (1.03 to 0.74) for RDF, -0.38 to –0.41 (0.26 to 0.32) for RD4FH, and –0.70 to –0.33 (1.78 to 1.04)

for BD in the 25-100ML range. For the models of Sec.III incorporating interlayer diffusion, behavior for higher T (around 140K) is similar to that for pure downward funneling. This highlights the fact that thermal diffusion on the surface is still limited, not including terrace diffusion or detachment from step edges (which produce rather different behavior). In all these models, the above equation predicts self-affine morphologies for the growing film, consistent with experimental observations and with simulations.

V. Tip-Probed Versus Actual Film Morphology

Finally, we comment on a generic issue as regards using STM to probe film morphology. For low temperatures, where the film surface has small, steep nanoprotrusions, one expects that the STM tip can not fully probe the surface, and thus produces a mollified morphology. In particular, one expects that the roughness, W, can be underestimated. To illustrate this point, we also show in Fig.2 the reduced W for the RDF model of growth at 0K, as measured by a conical tip with slope $s=\Delta y/\Delta x=1$. (In this analysis, the tip is lowered at each point, $\underline{x}$, above the surface until it contacts the surface. See Fig. 6.) Another perspective comes from comparing the actual morphology of a simulated film, the modified morphology of the simulated film mapped out by conical STM tips with various apex angles, and an actual VTSTM image of a film grown at the same T. This is done in Fig.7 for film growth at about 50K, where we note that the simulated morphology from a tip a fifth as steep as that used above reasonably reflects the actual measured experimental morphology.

VI. Conclusions

Our simple RDF model, augmented by low-barrier interlayer diffusion processes, succeeds in producing the basic behavior observed by VTSTM for the roughness of Ag films deposited on Ag(100) between 50K and 140K. Of course, various refinements of the model

are possible to incorporate, e.g., some downward funneling from the trap sites with less than four supporting atoms, "knockdown" of incompletely supported adatoms by depositing atoms, intralayer edge diffusion, and a more accurate and diverse selection of barriers of interlayer diffusion processes. However, we believe that our simplified model captures the essential features of low T growth.

Acknowledgements

This work was supported by NSF Grant CHE-9700592, and performed at Ames Laboratory which is operated for the USDOE by Iowa State University under Contract No. W-7405-Eng-82.

References

[1] *Morphological Organization in Epitaxial Growth and Removal*, edited by Z. Zhang and M.G. Lagally (World Scientific, Singapore, 1998)

[2] Another inappropriate view found in Ref.[1] is that smoother growth at low T is simply due to the presence of smaller islands from which deposited atoms can more easily descend; cf. Ref.[8].

[3] R. Kunkel, B. Poelsema, L.K. Verheij, and G. Comsa, Phys. Rev. Lett. **65**, 733 (1990).

[4] W.F. Egelhoff and I. Jacob, Phys. Rev. Lett. **62**, 921 (1989).

[5] D.K. Flynn-Sanders, J.W. Evans, and P.A. Thiel, Surf. Sci. **289**, 77 (1993); J. Vac. Sci. Technol. A **7**, 2162 (1989).

[6] J.W. Evans, D.E. Sanders, P.A. Thiel, and A.E. DePristo, Phys. Rev. B **41**, 479 (1990).

[7] M.C. Bartelt and J.W. Evans, Surf. Sci. **423**, 189 (1999); G. Vandoni, C. Felix, R. Monot, J. Buttet, W. Harbich, Surf. Sci. **320**, L63 (1994); M. Breeman, unpublished.

[8] C.R. Stoldt, K.J. Caspersen, M.C. Bartelt, C.J. Jenks, J.W. Evans, and P.A. Thiel, Phys. Rev. Lett., submitted (2000).

[9] C. Kelchner and A.E. DePristo, Surf. Sci. **393**, 72 (1997).

[10] H.C. Kang and J.W. Evans, Surf. Sci. **271**, 321 (1992)

[11] M. Schimschak and J. Krug, Phys. Rev. B **52**, 8550 (1995); S. Das Sarma, C.J. Lanczycki, S.V. Ghaisas, and J.M. Kim, Phys. Rev. B **49**, 10693 (1994).

Figure Captions

Figure 1. 1+1 dimensional schematics of: (a) downward funneling: (b) restricted downward funneling: (c) bird's eye view of trap sites (black circles) of types (i)-(iii).

Figure 2. (a) Roughness, W, versus θ for RDF and DF. The *thin* dotted lines show W estimated by the STM tip (see Sec.V). (b) Cross-section of a film grown by RDF.

Figure 3. Bird's eye view of various low-barrier interlayer diffusion processes: hopping on a {111} microfacet; hopping down from a site with three supporting atoms; hopping down a {110} type trough.

Figure 4. W versus T for a 25ML film according to model I (dashed line) and model II (solid line), with the choice of barriers indicated in Fig.3 and the text. Symbols denote experimental estimates of W, with error bars indicating the statistical uncertainty. In all cases, F=0.040ML/s.

Figure 5. Temperature dependence for 25ML films of: (a) the density of internal defects; (b) the skewness and kurtosis. Results are shown for model I (dashed line) and model II (solid line).

Figure 6. Schematic of a STM scan: solid dark line represents the real surface; dashed line represents the surface mapped out by the STM tip.

Figure 7. Comparison of simulated tip-mapped and STM morphologies. s-values are shown.

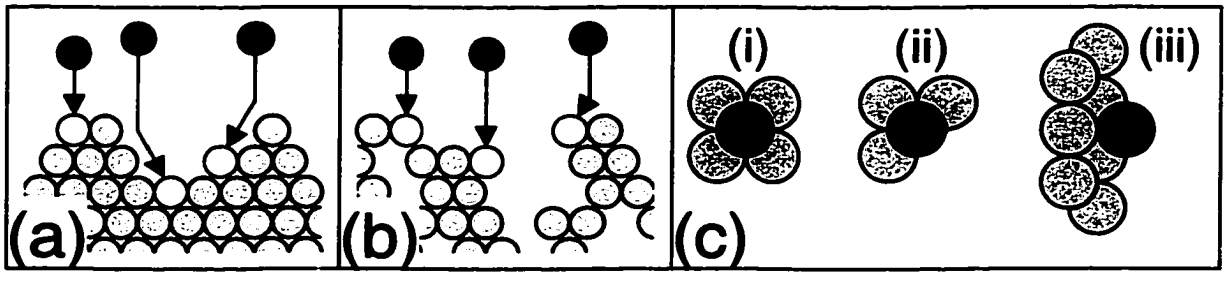

Figure 1

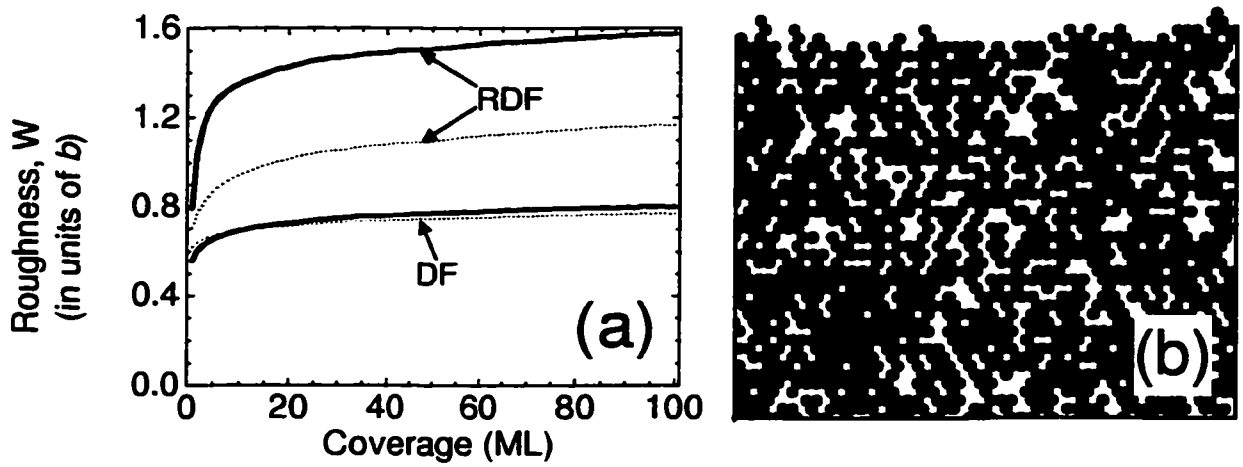
Roughness, W
(in units of b)
1.6
1.2
0.8
0.4
0.0
0
20
40
60
80
100
Coverage (ML)
RDF
DF
(a)
(b)

Figure 2

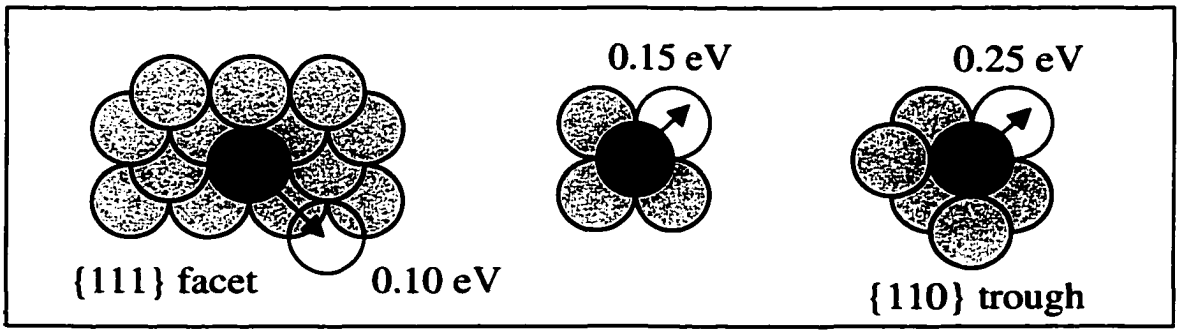

Figure 3

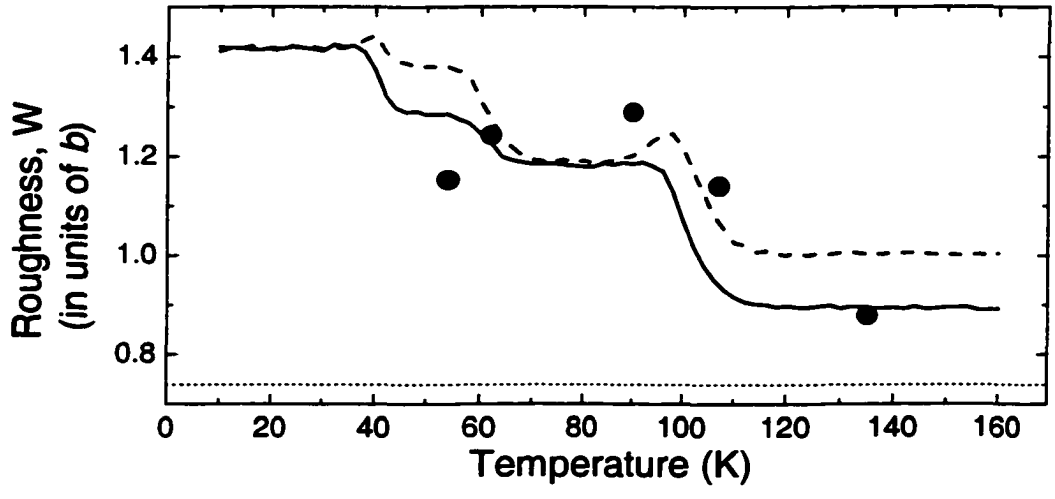
Roughness, W
(in units of b)
1.4
1.2
1.0
0.8
0
20
40
60
80
100
120
140
160
Temperature (K)

Figure 4

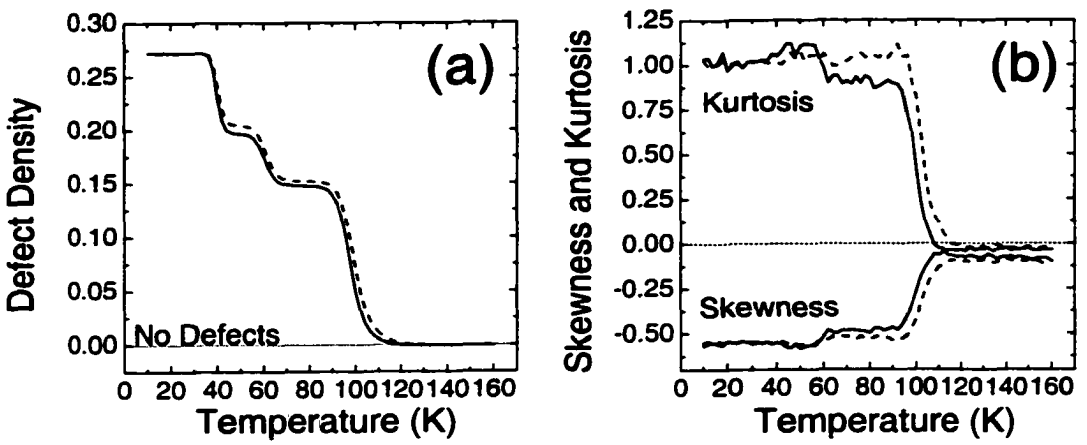
(a)
Defect Density
0.30
0.25
0.20
0.15
0.10
0.05
0.00
No Defects
0 20 40 60 80 100120140160
Temperature (K)
(b)
Skewness and Kurtosis
1.25
1.00
0.75
0.50
0.25
0.00
-0.25
-0.50
Kurtosis
Skewness
0 20 40 60 80 100120140160
Temperature (K)

Figure 5

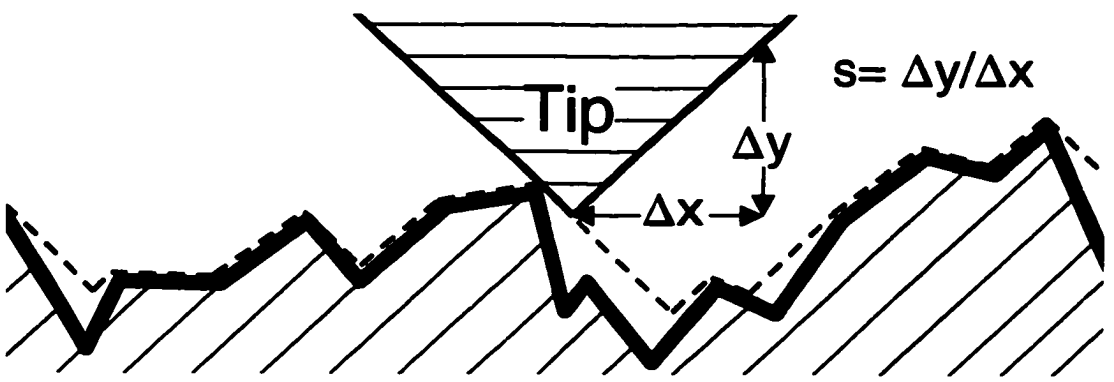

Figure 6

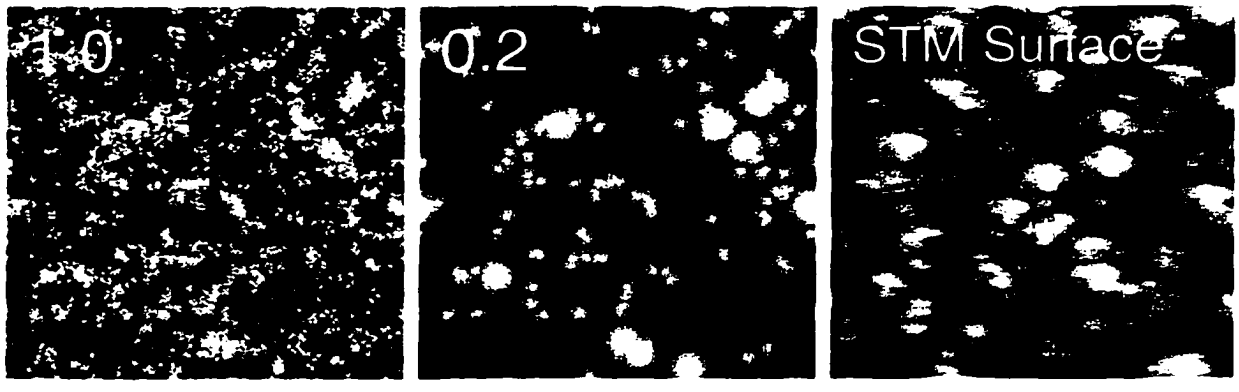

Figure 7

APPENDIX III. THE DISCRIPTION OF A TESSELATION ALGORITIM

Most of the data discussed in this thesis had to do with average quantities, such as the average feature height (i.e. the roughness (W)) or the average feature separation (D_{av}). However, these features (mounds) have local characteristics as well. The height versus the area of the mound, the shape of the valleys between the mounds, and the size and number of the neighboring mounds are all examples of quantities dependent on the local characteristics of a mound. To study these local characteristics one must be able to define a mound. And this is the focus of this appendix, to describe an algorithm that was designed to tessellate the surface into individual mounds (Fig.1). Where this algorithm consists of four major parts: The Determination of all the peaks on the surface, the grouping the peaks into tops of mounds, and finally growing the tessellation around the mound tops

1. The Determination of the Peaks

The first part is quite straightforward to implement. Initially all the islands on the surface are determined (An island is a group of atoms that are all in the same layer and all connected by nearest neighbor connectivity (Fig.1)). Then if the island has no atoms on top of it is deemed a peak, conversely if there is an atom on top of it is not a peak (Fig.2).

2. The Grouping of Peaks

The second part of the algorithm is the most complicated. The main idea is to group the peaks such that a convex region can be formed around them so that the entire area of the convex region remains on one level (Fig.3) this then is the top of a mound. To do this first the connectivity of the peaks must be determined then a rule must be implemented to group the peaks into the top of mounds. The connectivity rule states that two peaks are connected if

the lines connecting the four lateral maxima (up, down, left, right) stay on the same plane (Fig.4a) or if the lines cross another peak in the same level as the two peaks (Fig.4d). Thus if the lines between the maxima go up (Fig.4c,f) or down (Fig.4b,e) a level the two peaks are not connected.

To obtain this convex region an observation was made, that if a set of peaks forms a convex region then all the peaks in the set must be mutually connected. Thus the last part of this section is to group the mounds into mutually connected sets. The first step was two order the peaks by decreasing connectivity, this was done in order to assure the largest possible convex (mutually connected) regions. To determine the convex region a two-dimensional lattice was constructed in which the columns and rows are labeled by the peak with maximum connectivity and all the connecting peaks. A one is placed in a lattice site if column labels of the columns and rows was connected (one placed down the diagonal as well). Then all the columns were added up if all the column sums were equal then all the peaks were determined part of the same mound. However, if the column sums were not equal then the column and row from the peak with the lowest summed total connectivity was eliminated. Then the columns were summed again, if all the column sums were equal then the remaining peaks were deemed to be the top of the same mound, if not the process was repeated until all the columns summed to the same number (example in Fig.5).

3. Tesselation Growth

It is straightforward to form the tessellation once the tops of the mounds have been determined. Where the tessellations grow outward from the peaks absorbing the area it comes in contact with into the mound, provided the area does not belong to another mound. Also they only grow one layer art a time. This means that tesselations only grow for at one

particular surface height at any one time, when that height is completely absorbed into specific mounds do the tesselations begin growing in the layer below. This prevents mounds with exceptionally large peaks from dominating the total surface area. An example of this growth process is shown in Fig.6.

Figure Captions

Figure 1. An example of a surface morphology (a) and the morphology after it has been tessellated (b).

Figure 2. A schematic showing mound peaks.

Figure 3. A schematic showing a peaks grouped into a convex mound top.

Figure 4. Examples of mound peaks with varying connectivity.

Figure 5. An example of the iterative process of determining the largest possible convex region of connectivity.

Figure 6. An schematic of the tessellation growth process.

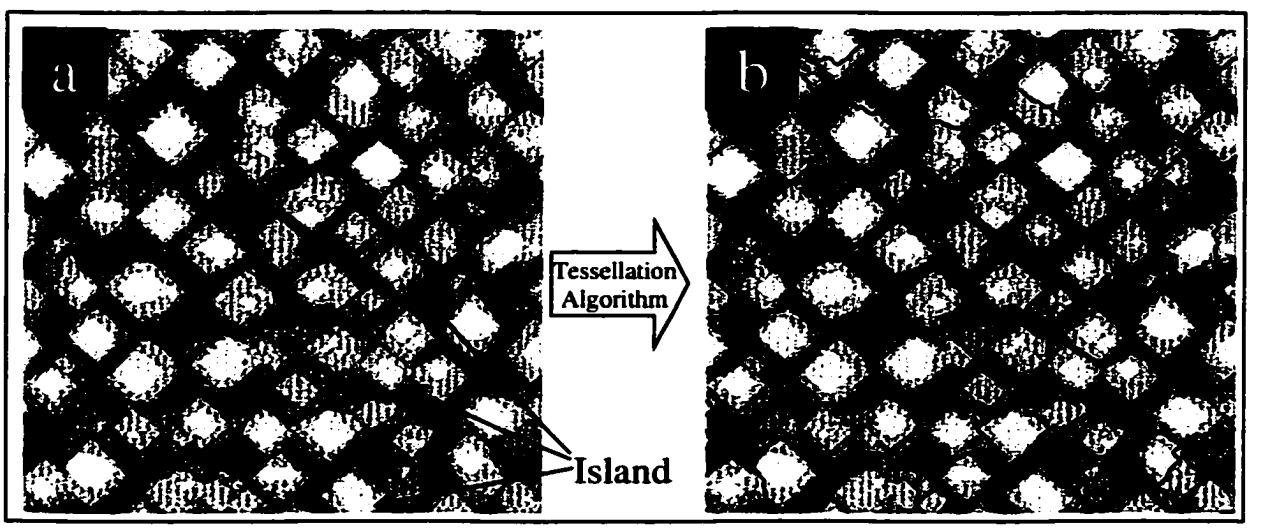

Figure 1

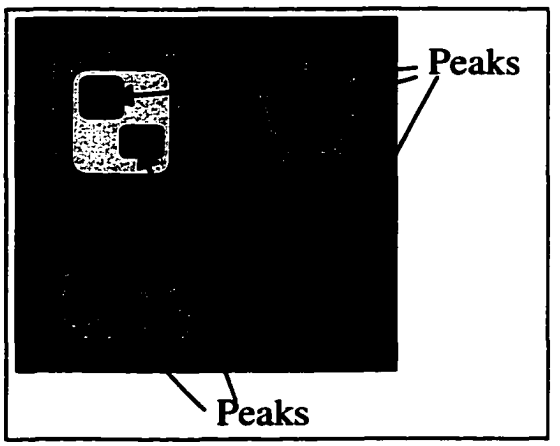

Figure 2

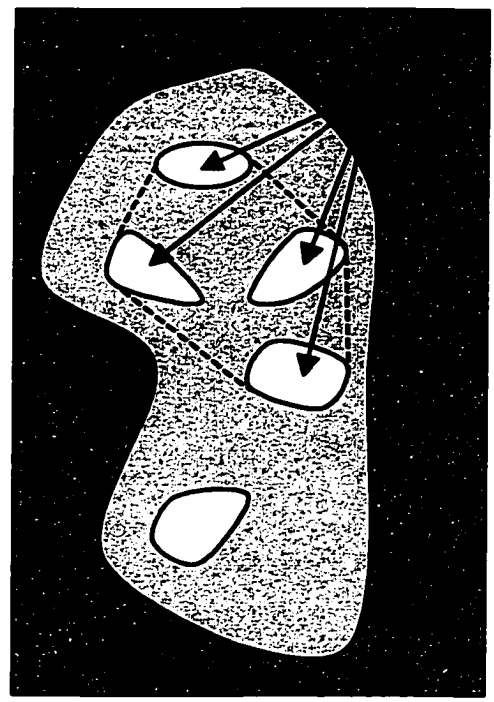

Figure 3

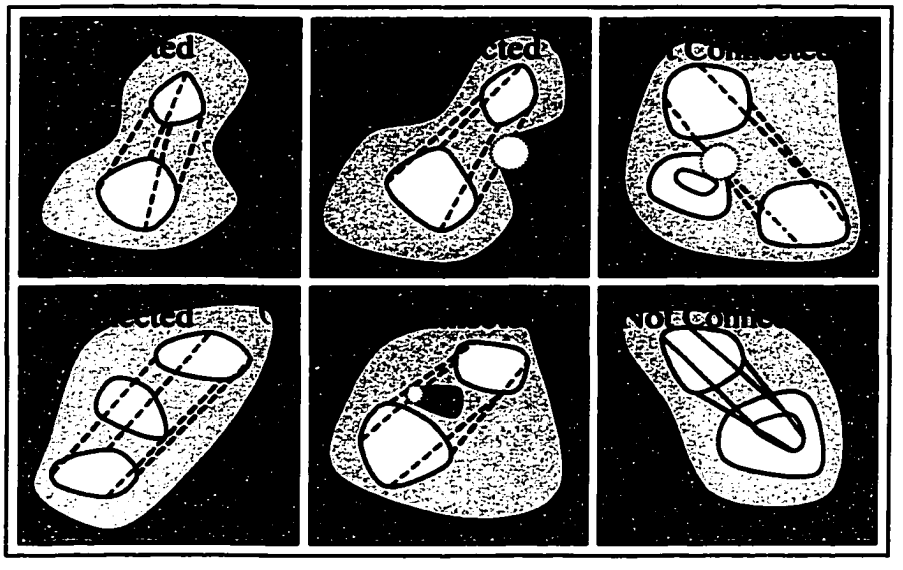

Figure 4

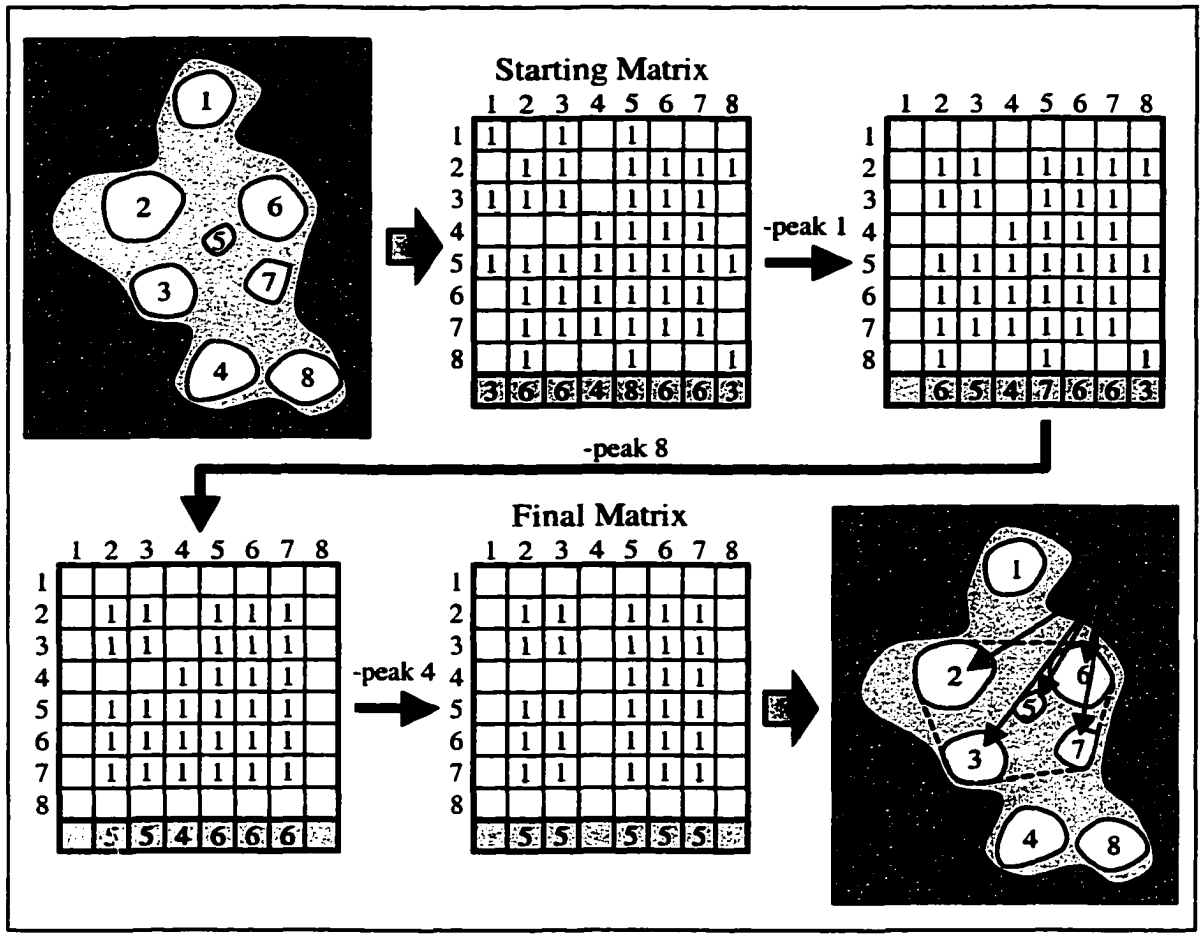

Figure 5

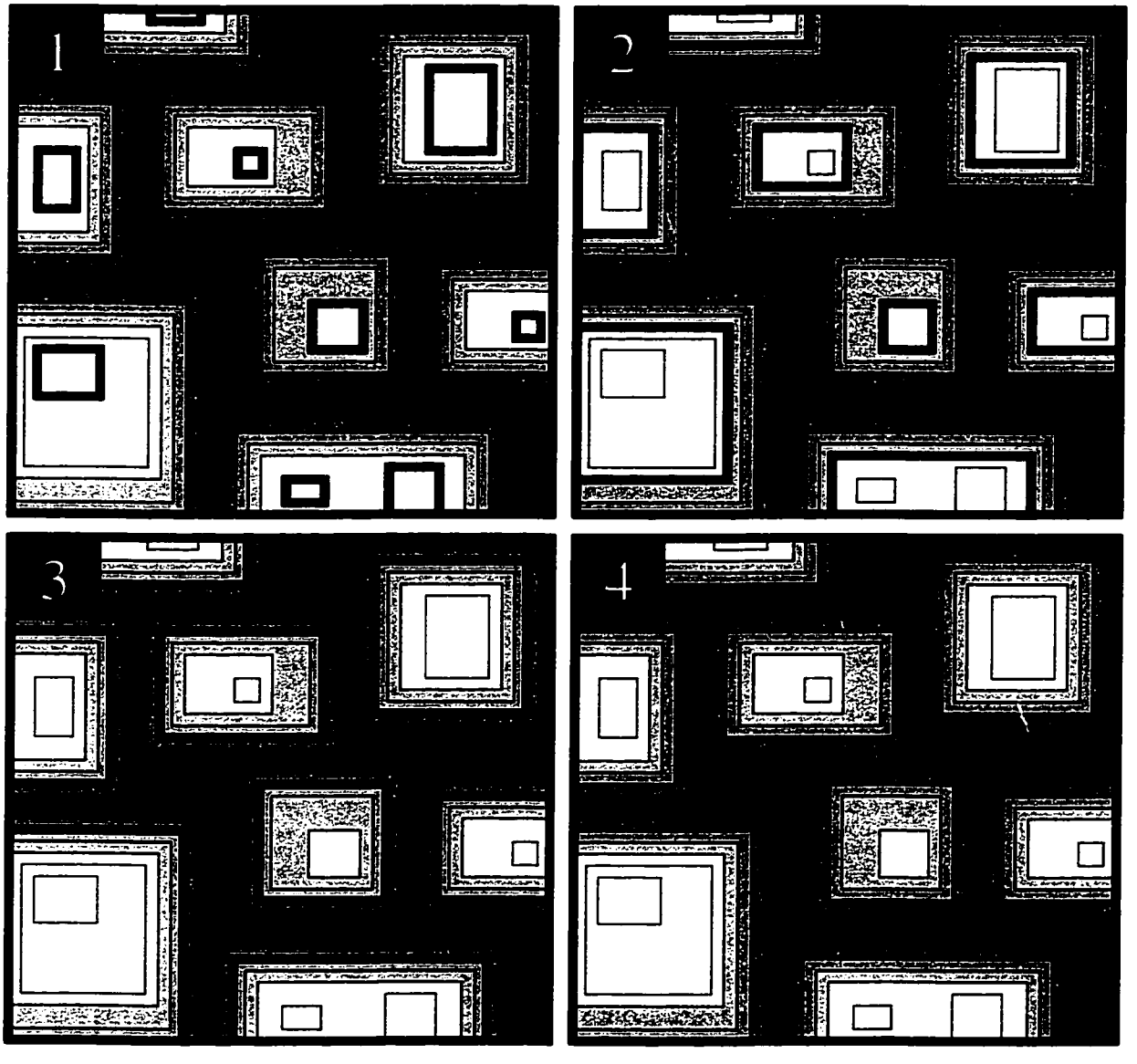

Figure 6